THE BOUNDARY LAYER OF ACCRETION DISKS

DISSERTATION

der Mathematisch-Naturwissenschaftlichen Fakultät
der Eberhard Karls Universität Tübingen
zur Erlangung des Grades eines
Doktors der Naturwissenschaften
(Dr. rer. nat.)

vorgelegt von
Marius Hertfelder
aus Ostfildern

Tübingen

2017

Gedruckt mit Genehmigung der Mathematisch-Naturwissenschaftlichen Fakultät der Eberhard Karls Universität Tübingen.

Ohana *means family.*
Family means nobody gets left behind, or forgotten.

— Lilo & Stitch

ABSTRACT

The accretion of matter is a powerful source of energy which is responsible for the brightest astrophysical objects and events in the Universe. In the majority of cases, this process is accompanied by the formation of an accretion disk surrounding the gravitating object. This is a consequence of angular momentum conservation which prevents the matter from radially falling towards the center. Instead, the material gathers on circular orbits which are determined by the balance of gravitation and the centrifugal force.

Accretion disks play an important role in astrophysics and can be found around a variety of objects. As a result of different mechanisms in the disk, the material generates friction. In a differentially rotating disk this means exchange of angular momentum and consequently transport of mass. While the matter is spiraling inwards, it continually looses energy which is radiated away from the surface of the disk.

At the inner edge of the accretion disk, the material makes contact with the stellar surface. It has to adopt the angular velocity of the star which is smaller than the disk velocity. The region where the matter is slowed down is called the Boundary Layer (BL). It has a radial extent of about 1% of the stellar radius. Due to the large energy dissipation during the deceleration, the BL can reach luminosities comparable to the disk. Thus, the existence of the BL and its properties can be well examined by observations.

From a theoretical point of view, the BL is still poorly understood. It is the aim of this work to shed light upon the non-magnetic BL of accretion disks around white dwarfs and young stars. For this purpose, the problem is approached in different ways, each of which treats a subset of issues concerning the BL.

Within the one-dimensional radial approximation, the radiation characteristics of the BL are investigated. The luminosity and a simple BL spectrum are calculated and can be compared to observations. A more sophisticated approach involves the modeling of a vertical structure at each radius, using the density and temperature data from the 1D simulations. Hereby, more detailed synthetic spectra are created and compared to real observations.

A major part of this work concerns the vertical structure of the BL. It is still unclear where the disk material is decelerated and how far it spreads over the surface of the star. In a two-dimensional spherical approach, these questions are addressed and it is assessed whether the competing concept of the Spreading Layer is a valid depiction of the star-disk interface. By comparison with previous simulations, it is evaluated whether the 1D model is a sufficient approximation for certain questions.

Recent investigations have sparked the exploration of BL instabilities in the equatorial plane. It is analyzed through two-dimensional simulations under which conditions the supersonic velocity drop in the BL is prone to instabilities and how oblique shock waves make an impact on the angular momentum and mass transport in the BL.

ZUSAMMENFASSUNG

Akkretionsscheiben spielen eine große Rolle in der Astrophysik. Sie bilden sich immer dann, wenn ein Stern (oder ein schwarzes Loch) Materie aus der Umgebung durch seine Gravitationswirkung einfängt. Schon die kleinste Rotation des Gases führt zur Bildung einer Scheibe, in der die Materie langsam auf das Zentralobjekt zu spiralt, um von diesem aufgesammelt (akkretiert) zu werden. Bei diesem Einspiralen wird Gravitationsenergie freigesetzt, was zu einer Energieabstrahlung führt, welche die des zentralen Sterns bei weitem übersteigen kann.

Am Innenrand von Akkretionsscheiben um Sterne lagert sich das Gas auf dem Stern an und muss dazu die Geschwindigkeit der Sternoberfläche annehmen. Diese ist im Allgemeinen sehr viel langsamer als die Rotationsgeschwindigkeit der Scheibe, welche näherungsweise mit keplerscher Geschwindigkeit rotiert. Die Abbremsung des Materials führt zu einer enormen Energiefreisetzung, die maximal (bei einem nicht-rotierenden Stern) die Hälfte der gesamten Akkretionsleuchtkraft betragen kann. Da diese Energie innerhalb eines räumlich sehr kleinen Bereichs freigesetzt wird, sind die Temperaturen hier üblicherweise deutlich höher als in den äußeren Scheibengebieten. Somit kann die Existenz einer Grenzschicht im Prinzip gut über Beobachtungen untersucht werden.

Von theoretischer Seite ist die Struktur dieser Grenzschicht noch immer nicht ausreichend verstanden. Im Rahmen der vorliegenden Dissertation soll darum die nicht-magnetische Grenzschicht von Akkretionsscheiben um weiße Zwerge und junge Sterne mit Hilfe von numerischen Simulationen erforscht werden.

Zunächst wird die Grenzschicht in der eindimensionalen radialen Näherung untersucht, wobei der Fokus auf den Strahlungseigenschaften dieser Region liegt. Aus den Ergebnissen der Simulationen lassen sich die Leuchtkraft und detaillierte Strahlungsspektren der Grenzschicht bestimmen. Diese Daten werden anschließend mit Beobachtungen verglichen.

Ein wesentlicher Teil der Arbeit besteht in der Untersuchung der vertikalen Struktur der Grenzschicht. Hierbei ist von besonderem Interesse, wo das Material aus der Scheibe an Geschwindigkeit verliert und wie es sich auf dem Stern ausbreitet. Zur Klärung dieser Fragen werden zweidimensionale, achsialsymmetrische Rechnungen angefertigt. Diese werden weiterhin mit 1D Ergebnissen verglichen. Dadurch kann die Aussagekraft und eventuelle Limitierungen des eindimensionalen Modells bestimmt werden.

In den letzten Jahren kam vermehrt die Frage nach der Viskosität in der Grenzschicht auf. Dieser Aspekt wird durch zweidimensionale Rechnungen in der Scheibenebene betrachtet. Es wird untersucht, unter welchen Umständen der steile Geschwindigkeitsabfall in der Grenzschicht die Entstehung von Instabilitäten begünstigt. Letztlich stehen die Auswirkungen der erzeugten Schockwellen auf den Drehimpuls- und Massentransport im Fokus.

CONTENTS

1 | INTRODUCTION

For millions of years, organisms have relied on the seemingly inexhaustible energy delivered by the Sun as their source of life. Plants, animals and, evolution's most complex achievement, mankind, have thrived on the warmth that the Sun, yet millions of kilometers away, bathes the Earth in. Our central star gains its immense power through nuclear fusion as myriads of other stars, which appear as small gleaming dots in the night sky, do as well. We can observe the vehemence of nuclear fusion and fission also on the Earth, whether good or bad. There is, however, a process which surpasses even nuclear fusion in the amount of energy liberated per unit mass: The accretion of a gram of hydrogen onto a neutron star of solar mass yields an energy release which is almost 100 times the energy produced by nuclear fusion. Moreover, accretion is by no means a rare event but an ubiquitous phenomenon that appears in a multitude of astrophysical situations. It is therefore no surprise that it has fascinated scientists for centuries and also plays a vital role in our studies. Accretion is the point where we start to dive into the subject of this thesis.

Accretion is powered by gravity, which also fuels the most luminous objects in the Universe. As matter approaches an object of mass M and size R, it gains energy because it falls into the potential well of the gravitating object and is accelerated. Apart from the distance, the energy obtained depends on the ratio M/R. Compact objects such as neutron stars or white dwarfs are therefore interesting laboratories for the study of these kinds of processes since they feature a high mass and a small radius. Accretion of matter is frequently accompanied by a disk which surrounds the central object. In any such case, the reason for the formation of an accretion disk is a non-vanishing angular momentum of the material that is accreted. As a consequence of angular momentum conservation, the matter can not fall directly onto the object but rather forms a disk in which it circles around the gravitating center. Stable orbits in the disk are given by the balance of gravitation and the centrifugal force and their associated angular velocity is said to be Keplerian,

$$\Omega_K(r) = \sqrt{\frac{GM_*}{r^3}}, \tag{1.1}$$

where G, M_* and r are the gravitational constant, the stellar mass and the distance from the stellar center, respectively. For realistic disks, there is a small deviation from Eq. (1.1) since the pressure is not constant and pressure gradients act as additional forces. Those forces are directed inwards at the beginning of the accretion disk near the star, and outwards at the surface of the star and in the disk.

Equation (1.1) describes a differential rotation and therefore every accretion disk exhibits a non-zero shear rate,

$$\text{shear rate} = r\frac{d\Omega}{dr}. \tag{1.2}$$

If the accretion disk is composed of a viscous medium, the shearing leads to angular momentum transport and energy dissipation through friction. The source of the viscosity is not necessarily of molecular kind but can be any process which seeks to damp out the shearing motion of the gas and thus act like a genuine viscosity on macroscopic scales. As a consequence, the gas perpetually looses angular momentum and slowly moves towards the center of the disk on a spiral path. The main characteristic of an accretion disk is therefore that mass is traveling to the center and angular momentum is transported outwards (Jeffreys, 1924; Weizsäcker, 1948; Lynden-Bell and Pringle, 1974; Pringle, 1981; Verbunt, 1982; Frank et al., 2002). This situation changes, however, when the accretion disk physically connects to the star, as we will see in Chapter 2. While the material is moving inwards in the disk, it constantly looses energy due to the viscous shearing. This energy comes from the gravitational energy that the material gains by falling into the potential well of the star. It is transfered into heat and eventually radiated away from the surface of the accretion disk.

The viscosity plays an essential role in the local structure of the disk and it determines the time scale on which accretion occurs (*viscous time scale*). The actual mechanism which is responsible for the observed viscosity, however, still is a matter of debate and ongoing research. The obvious choice, ordinary molecular viscosity, has been ruled out a long time ago. Considering typical values for the particle density and collisional cross section in accretion disks, the molecular viscosity yields a time scale which is several times the age of the Universe and thus greatly exceeds the typical lifetime of accretion disks of a few million years. It is likely a mixture of several processes, each of which operates under certain conditions at different locations in the disk. The magnetorotational instability (MRI), found in regions with magnetic Prandtl numbers of order unity, is probably the most famous of these processes (Velikhov, 1959; Chandrasekhar, 1960; Balbus and Hawley, 1991, 1998; Balbus, 2003; Balbus and Lesaffre, 2008), but may not always work (e.g. Stoll and Kley, 2014). The term MRI describes a phenomenon which appears in magnetic disks with decreasing angular velocity profile $\Omega(r)$ and creates turbulence that acts like a genuine viscosity on macroscopic scales. It has been demonstrated both by local (Brandenburg et al., 1995; Hawley et al., 1995, 1996; Stone et al., 1996; Brandenburg, 2001; Sano et al., 2004) and by global numerical simulations (Armitage, 1998; Hawley, 2000, 2001; Hawley and Krolik, 2001; Stone and Pringle, 2001) that the MRI induces a turbulent state which enables a considerable angular momentum transport in the disk. Shakura and Sunyaev (1973) have shown that for any process which creates turbulence in the disk, the kinematic viscosity ν can be parametrized by

$$\nu = \alpha c_s H, \tag{1.3}$$

where all the, possibly unknown, details of the mechanism are absorbed into the parameter α. The sound speed c_s and the disk scale height H are

supposed to be the typical velocity and size of a turbulent eddy. If α can not be derived theoretically, numerical simulations can aid to determine the effective value (e.g. Gammie, 1998; Brandenburg, 1998; King et al., 2007). Equation (1.3) is utilized in the great majority of accretion disk simulations.

Binary star systems are important representatives of the existence of an accretion disk. About one half of all stars reside in binary systems (van Albada and Blaauw, 1967; Martynov, 1971; Jaschek and Gómez, 1970). The reason for the increased occurrence in multistar systems is the joint development history. Stars form in groups in dense regions within molecular clouds of the interstellar medium (Stahler and Palla, 2005) and are surrounded by several other young stars. The main characteristic of binary systems lies in the fact that mutual exchange of mass influences the evolution of the individual stars (Paczyński, 1971). If one star fills up its Roche lobe due to an increasing radius after leaving the main sequence, additional growth causes an overflow and mass transfer via the inner Lagrangian point to the companion (Martynov, 1971). The Roche lobe describes the region where the material is gravitationally bound to the star. Another process which leads to the exchange of mass between the two stars is the mass loss from the surface via a stellar wind. In both cases, a significant amount of material can be transfered to the companion where it accumulates in an accretion disk due to its non-zero angular momentum. The evolution of such a disk is illustrated in Fig. 1.1: An initial stream of gas leads to the formation of a ring around the accreting companion. Due to the viscous shearing, the ring spreads whereby mass is primarily transported inwards and angular momentum is transported outwards (Lynden-Bell and Pringle, 1974). After some time, a disk forms and connection of the disk material and the stellar surface is established. Obviously, in a binary system the size of the accretion disk is limited by the Roche lobe of the accreting star. In close binary systems such as SS Cygni, the disk has a radial extent of about 50 stellar radii (Giovannelli et al., 1983; Martinez-Pais et al., 1994).

The class of binary star systems comprises a multitude of configurations consisting of two stars. Out of these, cataclysmic variables (CVs) are of special interest since they feature a luminous accretion disk and show time-dependent behavior such as outburst and light curve oscillations. CVs are very close binaries with an orbital period of the order of hours. They are composed of a white dwarf (WD) which has about one solar mass and a lighter star that has a late spectral class (e.g. Warner, 1995; Giovannelli, 1985). The lighter star fills its Roche lobe and transfers mass to the WD where it accumulates in an accretion disk. The luminosity of accretion depends on how compact the accreting object is:

$$L_{acc} = \frac{GM_* \dot{M}}{R_*} \tag{1.4}$$

Here, $G, M_*, \dot{M}$ and R_* are the gravitational constant, stellar mass, mass accretion rate and stellar radius, respectively. Since WDs have about the mass of the Sun, yet only the radius of the Earth, the luminosity of an accretion disk surrounding such objects is comparably high. The mass accretion rate typically lies in the range of 10^{-11} to 10^{-8} solar masses per year (Patter-

son, 1984). CVs are subdivided into four categories which characterize the outburst behavior of the system (Maran, 1992):

- classical novae

- recurrent novae

- dwarf novae

- nova-like object

The term *outburst* describes a considerable increase in luminosity compared to the system's quiescence state. Depending on how often such outbursts occur and what shape they assume, systems can be assigned to the above classes. While the time scale of outbursts stretches from days to years, there are two additional phenomena in CVs which are responsible for fast light curve oscillations in the range of seconds. These dwarf nova oscillations (DNOs) and quasi-periodic oscillations (QPOs) are attractive since variations on such short time scales are very likely associated with the very inner parts of the accretion disk or the WD itself. However, the cause of these rapid oscillations is still poorly understood (e.g. Warner, 2004; Warner and Woudt, 2005; Pretorius et al., 2006).

The study of young stars is another large astrophysical field where accretion disks play an essential role. Since the molecular clouds in which protostars are formed exhibit an angular momentum of a few percent of the gravitational energy (Goodman et al., 1993), the residual material accumulates in a disk around the newly born star. In some cases (*HL Tau, DG Tau*), these disks can be spatially resolved by conducting interferometric observations (e.g. Beckwith et al., 1990). Their radial extent is comparable to the size of the solar system and can reach radii of up to 1000 astronomical units. Young stars obtain a considerable amount of mass from the disk (5-10 %, Frank et al. 2002) which is why the mass accretion rates in disks around young stars are rather large and yield values of 10^{-7} (T Tauri stars, Hartmann et al., 1993) or even 10^{-4} (FU Ori outburst, Reipurth, 1990) solar masses per year. These disks, then named *protoplanetary disks* will later be the birthplace of planets (e.g. Pollack et al., 1996; Durisen et al., 2007; Weidenschilling, 1977; Yorke and Bodenheimer, 1999; Eisner et al., 2005).

In both of the above mentioned cases, disks around WDs in CVs and disks around protostars, the star frequently possesses a magnetic field. Different manifestations of the accretion process then occur depending on the magnitude of the magnetic field: For weak field strengths, the accretion disk reaches all the way to the stellar surface and the material enters the stellar surface in the equatorial plane. This is considered the case of the non-magnetic boundary layer and the topic of this thesis. With increasing field strength, the accretion disk is truncated and matter finally moves on magnetic field lines towards the stellar surface. Here, a supersonic shock occurs and high energetic radiation (hard X-rays) is emitted. For very strong magnetic fields, no disk at all forms and the matter is purely accreted via magnetic field lines.
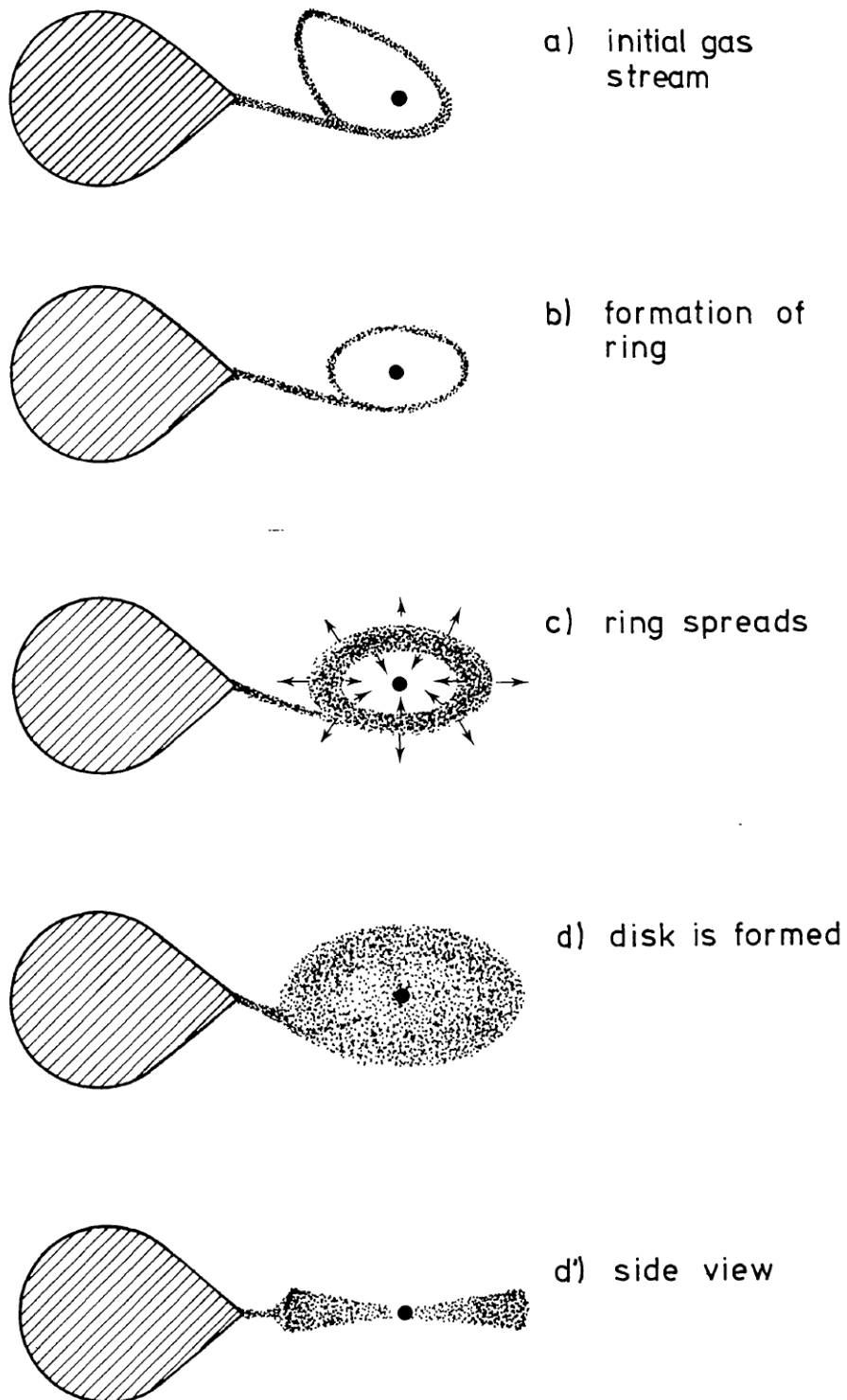
a) initial gas stream

b) formation of ring

c) ring spreads

d) disk is formed

d') side view

Figure 1.1: Sketch of the evolution of an accretion disk in a binary system (credits: Verbunt, 1982).

2 | CONTEXT

In this chapter I introduce the Boundary Layer which is the main research topic of this thesis. The problem can be tackled by different approaches which differ mainly in dimensionality. I will bring up the Spreading Layer (SL), an alternative concept for the disk-star interface, and delineate the main differences between the BL and the SL. Finally, I move the topic towards applications and describe three cases in which the BL plays an essential role for the whole system.

2.1 THE BOUNDARY LAYER

INTRODUCTION In the accretion disk, the gas is required to rotate with the Keplerian angular velocity in order to remain on stable orbits (see Eq. 1.1). This causes a high rotation velocity for the innermost regions of the disk. The stellar surface, in contrast, exhibits a lower rotation velocity of in general $\lesssim 50\% \Omega_K(R_*)$ (Shapiro and Teukolsky, 1983). Thus, a supersonic velocity difference appears at the point where the gas from the disk meets the surface of the star. Due to the viscosity present in this region, the gas from the disk is rapidly slowed down and smoothly connects to the stellar rotational velocity. The region between the stellar surface and the maximum of the angular velocity, i.e. $d\Omega(r)/dr = 0$, is called the BL (see Fig. 2.1 for an illustration). During the deceleration, a large part of the kinetic energy of the gas is converted into heat and emitted from the system by radiation. The proportion of the energy loss depends on the rotation rate of the star and can be calculated by (Kluźniak, 1987)

$$L_{BL} = \frac{1}{2} \left(1 - \frac{\Omega_*}{\Omega_K(R_*)} \right)^2 L_{acc}. \tag{2.1}$$

In case of a non-rotating star, the luminosity of the BL therefore just equals the luminosity of the whole accretion disk ($L_{disk} = 0.5 L_{acc}$). From simulations (e.g. Hertfelder, 2017) as well as simple theoretical analysis (Frank et al., 2002), it is evident that the width of the BL is tiny. It amounts to approximately 1% of the stellar radius for the case of WDs. Since a great deal of energy is emitted in a small region, the generated radiation is hard and clearly visible as UV and X-ray contributions to the spectrum of the system. This explains the great importance of the BL. In Fig. 2.1, the *dynamical* width of the BL is displayed (Δr). The energy dissipation, however, occurs over a larger area of approximately 10% of the stellar radius due to the radiation transport (see Fig. 2.2). This region is usually called the *thermal* BL (Regev and Bertout, 1995; Popham and Narayan, 1995). While the gas is decelerated in the equatorial plane of the WD, the problem is dynamically one-dimensional and only dependent on the radial distance from the star. At
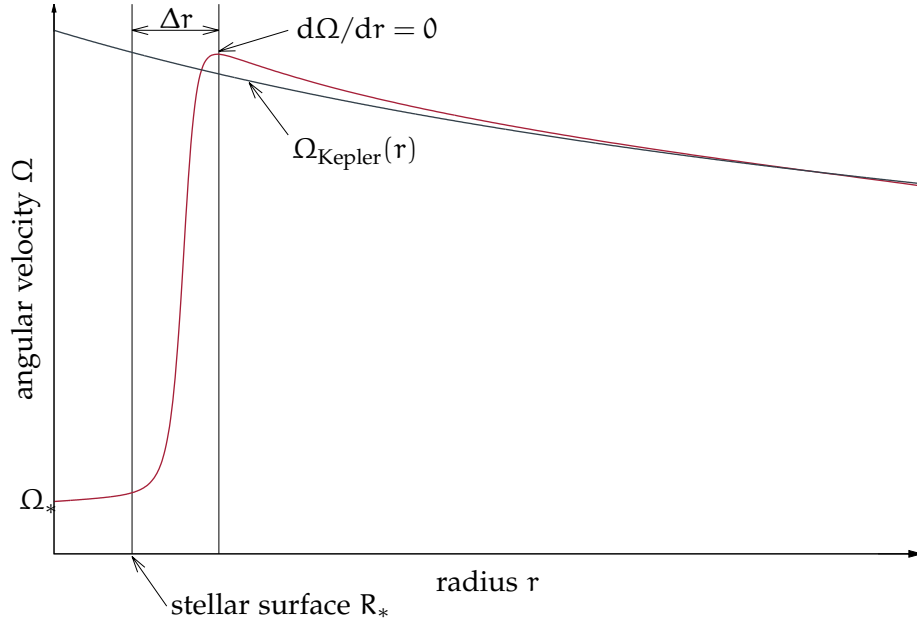
Figure 2.1: Sketch of the angular velocity $\Omega(r)$ in the BL and the accretion disk. The solid black line represents the Keplerian angular velocity $\Omega_K(r)$ which results from the balance of gravitation and the centrifugal force. The red line is the result from numerical simulations similar to Hertfelder et al. (2013).

some point during or after the deceleration, however, the gas leaves the midplane and moves towards the poles on the surface of the WD. Consequently the BL is an intrinsically (at least) two-dimensional problem. Owing to its complexity, the BL has nevertheless been treated in different 1D approximations, where only the radial or the vertical dependence of the variables is considered. Two-dimensional simulations are still rare. Simple time scale estimates were among the first efforts to understand the processes in the BL (Lynden-Bell and Pringle, 1974; Pringle, 1977; Tylenda, 1977, 1981; Pringle and Savonije, 1979).

RADIAL MODELS Within the purely radial approximation, the equations of the BL in cylindrical coordinates are vertically integrated and axisymmetry is assumed. The vertical velocity is set to zero and the gas is decelerated and absorbed by the star in the equatorial plane. Due to the vertical integration, the 3D flow variables are partly replaced by 2D equivalents. The mass density, for instance, is substituted by the surface density Σ which is given by

$$\Sigma = \int_{-\infty}^{\infty} \rho\,dz = \sqrt{2\pi}\rho(z=0)H, \tag{2.2}$$

where a Gaussian profile for ρ is assumed in the vertical direction. H denotes the pressure scale height and is a measure for the thickness of the disk. The temperature and the velocities are midplane quantities in the 1D model, whereas the pressure is a vertically integrated 2D pressure. The vertical direction cannot be ignored since it is important for the cooling of the disk
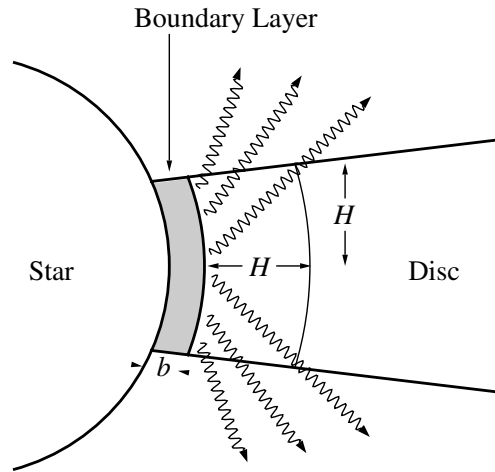
Figure 2.2: Side view of the star-disk system with an optically thick BL. The width of the dynamical BL is given by b. The thermal BL extends approximately one scale height H deeper into the disk. The sketch is not drawn to scale. (credits: Frank et al., 2002)

and the BL. Thus, the vertical structure is approximated by an estimate of the vertical optical depth (Hubeny, 1990).

The radiation characteristic of the BL crucially depends on the mass accretion rate of the system. In the BL, the gas is radially accelerated towards the star. This results in a decrease of the surface density which can drop to such an extent that the region becomes optically thin. In this case, the gas density is not large enough so that the generated radiation can undergo several absorption and emission processes which are necessary for a thermalization of the radiation. The system is thus not in thermodynamical equilibrium. Since a considerable amount of energy is released, optically thin BLs of WDs are very hot with temperatures of the order of the virial temperature ($\sim 10^8$ K). The radiation corresponding to such high temperatures are soft and hard X-rays (~ 10 keV). These conditions are met for CVs in quiescence with low mass accretion rates of 10^{-12} to $10^{-10} M_\odot$/yr (Warner, 1987). Observations of such systems (e.g. Mukai and Patterson, 2004; Pandel et al., 2003, 2005) could be well reproduced by theoretical predictions (e.g. Pringle and Savonije, 1979; Tylenda, 1981; King and Shaviv, 1984; Shaviv, 1987; Narayan and Popham, 1993; Popham, 1999). It is, however, not yet clear how the hard X-rays are generated. Pringle and Savonije (1979) suggested the production via strong shocks, whose existence in the BL is controversial due to the strong shearing. Another possible explanation is given by the evaporation of the inner parts of the disk and the formation of a corona-like shell (Liu et al., 1995; Medvedev and Narayan, 2001; Meyer and Meyer-Hofmeister, 1994). Recent observations of VW Hyi in quiescence (Liu et al., 2008) seem to disagree with this theory.

For higher mass accretion rates, $\dot{M} \gtrsim 10^{-10} M_\odot$/yr (Pringle and Savonije, 1979; Tylenda, 1981), the BL is assumed to be optically thick and the temperatures on the surface are predicted to be of the order of $\sim 10^5$ K (Pringle, 1977; Syunyaev and Shakura, 1986). The radiation of optically thick BLs is mostly thermalized and resembles a black body spectrum. Higher accretion

rates occur in CVs during outburst states, when values between 10^{-9} and $10^{-8} M_{\odot}/yr$ are reached (Warner, 1987; Cannizzo et al., 1988). Observations of such events (e.g. Cordova et al., 1980; Mauche, 2004b) demonstrate the validity of numerical predictions (e.g. Popham and Narayan, 1995; Obach and Glatzel, 1999), also for optically thick BLs.

MULTIDIMENSIONAL MODELS   The downside of the one-dimensional BL models is that either the vertical or the radial velocity is assumed to be zero. This approximation is known to limit the scope of the 1D approach (Ferland et al., 1982). Therefore, evolutionary numerical simulations in two dimensions under the assumption of axisymmetry have been performed soon after the first 1D efforts. Robertson and Frank (1986) and Kley and Hensler (1987) conducted the first calculations of this kind. They assumed an adiabatic flow and either instantly released the energy generated by viscosity or did not perform any cooling. Accordingly, the disk and the BL became either very thin or were puffed up considerably. More realistic 2D simulations have been performed by Kley (1989a,b, 1991), who implemented a two-temperature radiation treatment incorporating the flux-limited diffusion approximation (Levermore and Pomraning, 1981; Levermore, 1984). The results indicate that an optically thick BL is surrounded by a hot corona. At the same time, first models for rotating stars have been simulated. However, due to the limited amount of computing resources, the grid resolution and the simulation times were limited. More recent BL simulations feature a higher resolution, but treat only adiabatic flows and a small domain in the direct vicinity of the star (Fisker and Balsara, 2005; Fisker et al., 2006). Magnetic fields have been included in 2D by Küker et al. (2003) for protostars and for CVs in 3D by Armitage (2002), who used a low numerical resolution and short dynamical time scales. Axisymmetric long-term simulations for the case of protostars have been run for different accretion rates by Kley and Lin (1996, 1999). They found that for accretion rates below $10^{-7} M_{\odot}/yr$, the BL is optically thin. For high accretion rates, $\dot{M} \approx 10^{-5} M_{\odot}/yr$, a thermal instability led to states of outburst similar to the FU Ori outbursts.

More recently, detailed calculations of the BL around neutron stars in low mass X-ray binaries (LMXB) have been made by Babkovskaia et al. (2008). However, they included only a small patch around the star. Balsara et al. (2009) have simulated the BL around a WD employing a somewhat artificial treatment of the dissipation function, similar to the very first multi-dimensional efforts. Radiation processes were not taken into account. The accretion via magnetic field lines and also the classical BL were investigated in three-dimensional simulations by Romanova et al. (2012). As a source of viscosity, the magnetorotational instability is explicitly simulated. These models do, however, not include an implementation of radiation transport.

Non-axisymmetric phenomena such as spiral-shaped shock waves have been suggested by Pringle and Savonije (1979) for the accretion onto WDs and by Kluzniak and Wilson (1991) for the neutron star case. This field has been explored heavily in the last few years and the possibility of a wave-mediated angular momentum transport has been proposed (Belyaev and Rafikov, 2012; Belyaev et al., 2012, 2013a,b; Hertfelder and Kley, 2015; Belyaev, 2017).

VISCOSITY IN THE BL Several problems arise in connection with the viscosity in the BL. We will first assume that the mechanism for the angular momentum transport creates local turbulence and its impact on the fluid can be described by a classical α-viscosity (Shakura and Sunyaev, 1973). Then, attention must be payed to the transition of the mean free path of the turbulence (or the maximum eddy size). In the BL, the stabilization of the gas shifts from centrifugal to pressure forces and hence the radial pressure scale length becomes smaller than the vertical one. The vertical pressure scale height is usually taken as the maximum eddy size in the disk. Thus it has been argued that the α-viscosity prescription of the disk cannot be deployed in the BL (Papaloizou and Szuszkiewicz, 1994; Narayan et al., 1994; Kato and Inagaki, 1994; Godon, 1995). A popular workaround for this problem has been developed by Papaloizou and Stanley (1986), who employed a viscosity prescription that considers the smaller of the radial or the vertical length scale:

$$\nu = \alpha c_s \left(\frac{1}{H^2} + \frac{(dp/dr)^2}{p^2} \right)^{-1/2} \tag{2.3}$$

This expression for the viscosity has been used for the BL several times (e.g. Popham and Narayan, 1995).

Many of the early BL calculations have yielded supersonic infall velocities (e.g. Papaloizou and Stanley, 1986; Kley, 1991; Popham and Narayan, 1991). Pringle (1977) pointed out that supersonic infall causes difficulties concerning causality and is thus to be considered unphysical. Information about the stellar boundary, such as the star's rotation velocity, travel upstream no faster than the speed of sound. This knowledge is required by the gas at the inner disk edge and therefore the radial velocity must be less than the sound speed in order to acquire consistent results. Supersonic infall can be avoided by including so called causality factors in the viscosity formula (Shakura and Sunyaev, 1988; Godon, 1995; Narayan, 1992; Popham and Narayan, 1992). A slightly different approach has been pursued by Kley and Papaloizou (1997), who implemented a relaxation time scale for the shearing component of the viscous stress tensor (see also Papaloizou and Szuszkiewicz, 1994). By choosing the right relaxation time, they were able to limit the infall to subsonic velocities. Causality preserving factors have not been used lately since for typical α-values in BL simulations, supersonic velocities rarely occur.

The greatest problem, however, is probably the assumption of local turbulent stresses that is associated with the utilization of an α-like viscosity. As pointed out by Godon (1995) and Abramowicz et al. (1996) and recently shown by Pessah and Chan (2012), if the angular velocity increases with radius, $d\Omega/dr > 0$, the MRI is effectively damped out and the associated angular momentum transport oscillates around zero. Since this situation clearly applies for the BL, we do not expect to obtain sufficient AM transport through the MRI. There have been various alternative transport mechanisms proposed, among them the Kelvin-Helmholtz instability (Kippenhahn and Thomas, 1978), the baroclinic instability (Fujimoto, 1993), and the Tayler-Spruit dynamo (Tayler, 1973; Spruit, 2002; Piro and Bildsten, 2004a), none of which have yet been proven to efficiently transport mass and AM in the BL. Recently, a promising candidate for the transport has been

proposed and investigated. According to this theory, the steep velocity drop in the BL is prone to the sonic instability (Glatzel, 1988; Belyaev and Rafikov, 2012), which is an instability of a supersonic shear layer, much like the Papaloizou-Pringle instability (Papaloizou and Pringle, 1984; Narayan et al., 1987). Acoustic waves are excited in the BL as a consequence of the sonic instability and AM can be transported by these modes in an efficient way. This has been demonstrated for 2D flows (Belyaev et al., 2012; Hertfelder and Kley, 2015), 3D flows in cylindrical coordinates (Belyaev et al., 2013a), and even for 3D magnetohydrodynamical flows (Belyaev et al., 2013b). The wave mediated AM transport implies that this process is intrinsically non-local since the waves can potentially travel a long way before they dissipate and release the AM to the fluid. Therefore, it is problematic to describe the AM transport in the BL by means of a local viscosity like the α-model. As a consequence of the BL instability, incompressible modes such as gravity or Rossby modes might be excited at the surface of the star (Belyaev, 2017). The concept of the sonic instability has also been applied to the spreading layer theory (see Sec. 2.2), where it might overcome the viscosity problem on the stellar surface (Philippov et al., 2016).

2.2 THE SPREADING LAYER

The spreading layer (SL) is an alternative concept for the interface between the disk and the star which has originally been developed by Inogamov and Sunyaev (1999, 2010) for neutron stars. The main difference between the BL and the SL concerns the order of deceleration and polar spreading: In the BL theory, the gas is first slowed down in the equatorial plane where it looses its energy and then slowly spreads on the surface of the star. Within the SL rationale, the material from the disk is vertically spread on the surface of the star by the ram pressure. Due to the turbulent friction between the hot gas and the cold and dense stellar layers below, it is slowed down and the energy is liberated in two rings above and beyond the stellar equator (see Fig. 2.3). The position and the width of the two rings (or belts) is determined by the mass accretion rate. The larger $\dot{M}$ is, the wider the belts are and the closer they are shifted towards the poles. Thus, the majority of the SL luminosity comes from these two belts. In the equatorial plane, in contrast to the BL, the luminosity is minimal. The authors argue that a deceleration in the disk midplane does not occur since the angular momentum stabilizes the gas against the gravitation of the star. Not until it moves to the poles does the gas loose this stabilization.

The gas in the active belts on the stellar surface is dominated by radiation pressure. Since in this medium the sound speed is considerably larger than in a plasma without radiation, the rotational motion is only moderately supersonic ($\mathcal{M}_\varphi \sim 5$). Furthermore, the meridional distribution is subsonic for the same reason, which is important concerning the causality of the SL and the choice of an apt model for the friction. Once the gas leaves the radiating belt towards the pole, its azimuthal velocity drops to zero and the material contracts and builds a cold thin layer which barely radiates. It slowly
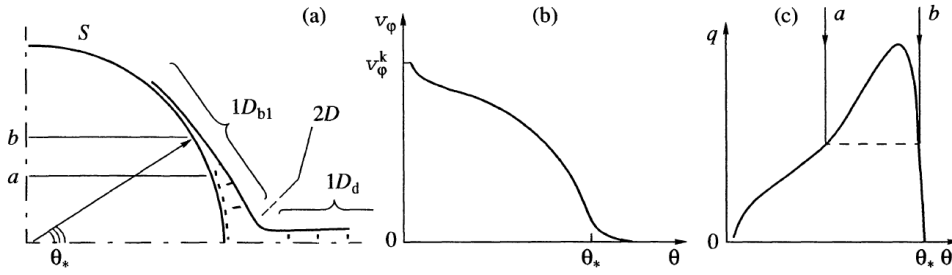
Figure 2.3: The spreading layer (from Inogamov and Sunyaev, 1999): (a) The stellar surface is denoted by S, the one-dimensional SL by $1D_{b1}$, the two-dimensional transition region between disk and SL by 2D and the one-dimensional disk by $1D_d$. (b) The velocity in azimuthal direction, v_φ, as a function of the latitude θ. The gas is mainly rotating in a belt of width $0 < \theta < \theta_*$. In the case of a non-rotating star, matter outside this belt has almost no rotation velocity. (c) The local radiative flux q as a function of latitude. The arrows enclose the region of increased luminosity. Their location is also marked in panel (a).

spreads on the whole star and comes to rest beneath the hot, active layers with which it then interacts viscously.

A major problem of the SL theory is the deceleration of the material on the surface of the neutron star. In absence of an anomalous viscosity, the molecular viscosity on the neutron star is much too small to considerably slow down the gas from the disk. Additionally, more recent investigations by Inogamov and Sunyaev (2010) revealed that the fast rotating material spins up the outer layers of the star. Therefore, the energy release would occur rather deep in the star ($\sim 10^4$ cm). Another problem lies in the fact that it is difficult or even impossible to distinguish between the BL and the SL from an observer's point of view. On the one hand, the radiating belts are located close to the stellar equator for low mass accretion rates and their vertical size is comparable with the classical BL. On the other hand, in case of a high mass accretion rate ($L_{BL} \approx L_{Edd}$), the BL is also expected to engulf the whole star (Popham and Sunyaev, 2001). In both cases, it will be nearly impossible to tell the two concepts apart by looking at the observations.

Although initially developed for neutron stars, the theory of the SL has been adapted to CVs by Piro and Bildsten (2004a,b). In this case, the luminosity of the innermost region is much smaller and the position of the rings deviates from the midplane only for high accretion rates, as for instance during outbursts. Suleimanov and Poutanen (2006) have extended the SL model to account for different chemical compositions of the accreted material and included effects of general relativity.

2.3 IMPORTANCE

While the BL plays an important role in every system where accretion on a central object occurs, there are some cases where a better understanding of the BL could explain long outstanding problems or push the knowledge in the latest research. I will shortly outline these situations below:

- THE WD CASE: The simulation of the BL around a WD is a challenging task. Due to the large mass and small radius, the WD has a small radial scale height and the BL is very narrow. Hence a large numerical resolution has to be chosen in order to sufficiently resolve these regions. Accordingly, the demands for computational resources are exceptionally high. WDs in CVs show several interesting features, such as recurring periods of outburst and quiescence and rapid oscillations of the light curve (DNOs, QPOs). It is to be assumed that the BL is particularly involved in such phenomena due to its vicinity to the stellar surface. The mechanism of the AM transport is supposed to be of vital importance.

- PLANETARY ACCRETION: A protoplanet in a protoplanetary disk will likely open a gap and accrete the majority of its mass through a circumplanetary disk. The thermal energy of the protoplanet likely depends on how the material from the disk is transported to the planet, i.e. on the BL of the circumplanetary disk. It is interesting to investigate the conditions that lead to a large energy deposit in the protoplanet by the BL and to differentiate it from the opposite case, where most of the accretion energy is radiated away. In this first *hot-start* case, the protoplanet will be inflated and driven to high luminosities through the energy deposit from the BL. In contrast, the second or *cold-start* case is characterized by a considerably less luminous protoplanet. These two scenarios are presently discussed (e.g. Owen and Menou, 2016).

- THE YOUNG STAR CASE: The complexity of simulations of the BL around a young star lies between the WD and the protoplanet case. The ratio of stellar mass and radius is much smaller than for a WD but larger than for a protoplanet. Young stars can have very high accretion rates and thus the BL is expected to be completely optically thick. Furthermore, the high accretion rates will allow to test the scenario by Popham and Sunyaev (2001), according to which the BL engulfs the star at very high $\dot{M}$. Young stars also experience outburst phases, which are named after the prototype system FU Orionis. The role of the BL in this process is still unclear. Finally, the hot/cold-start scenarios which we discussed in connection with protoplanetary disks also applies to young stars and is important for the evolution of the star, the disk and the planetary system.

3 | A I M S

Despite strong efforts for over 30 years, the BL is still poorly understood from a theoretical point of view and several questions remain unanswered. It is the aim of this thesis to shed more light upon the BL mystery by addressing some of the key issues in BL research. For that purpose, the work plan is subdivided into three stages which approach the BL with different geometrical assumptions. Various numerical schemes and codes are developed, adapted and employed for each stage. The results of the individual parts of the thesis interact with one another and thus finally draw the big picture of the BL.

The first stage involves one-dimensional radial models of the BL around a WD which resides in a cataclysmic variable system. A numerical code developed by the author will be extended by the inclusion of radiation energy in the one-temperature approach and radiation pressure. Since the BLs around WDs are very hot, these additions are important in order to obtain consistent results. The aim of the first part is to compute the radial density and temperature distribution in the BL. This data is then employed as an input for detailed vertical structure models at each radius which are computed using the stellar-atmosphere method in collaboration with Prof. Dr. Klaus Werner and Dr. Valery Suleimanov of our institute. The acquired detailed radiation spectra of BLs around WDs will be compared to observations of CV systems. Simultaneously, a second approach to compare the theory with observations will be pursued in collaboration with the group of Professor Solen Balman from the Middle East Technical University in Ankara. The luminosity of the BL is derived from the 1D radial models and their dependence on the stellar mass, stellar rotation rate and mass accretion rate is thoroughly investigated. I will search for a way to overcome the ambiguity which is omnipresent when comparing theoretical results with observations: Different choices of parameters yield almost identical BL luminosities.

During the second stage, I will deal with the BL around WDs in the two-dimensional vertical approach. Perhaps the most important unanswered question concerns the vertical structure of the BL. I will analyze the flow properties in the vicinity of the star and on the stellar surface. I aim to determine where the gas is decelerated from Keplerian rotation to the stellar rotation rate—in the equatorial plane or somewhere on the stellar surface. Since the deceleration is accompanied by energy dissipation which accounts for the BL luminosity, this question is important for the emergent spectrum. The wider the dissipation region, the softer the spectrum will be, for instance. The radiation characteristics also depend on the mixing of the disk material with the stellar layers. Therefore, I will track the evolution of the disk material on the stellar surface and its interplay with the layers beneath. I will finally be able to make a statement whether the competing concept of the SL is a possible scenario or can be ruled out for the star-disk interface.

Another essential goal is the comparison of the 2D results with the 1D radial model. If I find that the luminosity and surface temperature of the 1D model matches the more elaborate 2D approach, this would result in a huge simplification. One-dimensional simulations, which are fast, easier to set up and more stable, could be conducted for the purpose of comparing spectra with observations. In extension to the radiation treatment in the 1D approach, I will employ a two-temperature radiation model, where the radiation energy is an independent variable with an evolutionary equation which is closed by the flux in the flux-limited diffusion approximation.

The third part of the thesis comprises two-dimensional simulations of an infinitesimally thin BL in the disk plane. Previous simulations of the BL almost always considered axial symmetry. This is, in principle, a reasonable approximation since perturbations by the secondary in CVs, for instance, are usually very small. However, it has been found that under certain conditions the supersonic drop of the angular velocity in the BL is prone to the sonic instability which triggers oblique shock waves. This mechanism efficiently transports mass and angular momentum through the BL. I will investigate if these instabilities are a general BL phenomenon which occurs under typical conditions. Therefore, a more physical approach than in recent publications is pursued and the mechanism is tested for the BL around a young star. One important consequence of the wave mediated AM transport is that the process is non-local and it is possible that energy and AM are transported away from their point of origin. A major aim thus entails analyzing where the BL energy is dissipated and whether the main drawback of the SL theory (the still undetermined mechanism which decelerates the gas on the stellar surface) can be mitigated within this picture. Another important task will be to examine if we are able to condense what we learn about this specific AM transport into a simple prescription which can be used for later 2D simulations in order to save resources, energy and time. Furthermore, there might be a connection to observed variability phenomena like FU Ori outbursts, DNOs or QPOs.

4 | PUBLICATIONS

In this chapter, the publications which seek to answer the questions posed in Chapter 3 and have been written in the context of this thesis are presented. The papers are reproduced with permission from Astronomy & Astrophysics, © ESO, and Proceedings of Science.

In Hertfelder et al. (2013) [1], we investigate one-dimensional radial models of the BL around WDs including radiation energy and pressure. Both the stellar mass and the stellar rotation rate are varied and the impact of the parameter variation on the BL is analyzed. The results of these simulations are used in Suleimanov et al. (2014) [2] for the modeling of the EUV spectra of optically thick BLs. For this purpose, the radiation-hydrodynamical BL models are divided into a number of rings. For each ring the stellar-atmosphere method is employed to calculate a structure model along the vertical direction. The final spectra take into account Doppler broadening and limb darkening and are compared to SS Cyg and U Gem.

A different approach is pursued in Hertfelder (2017) [3] where the luminosity of the BL around a WD is computed from 1D radial models. Among the varied parameters are the stellar mass, rotation rate and mass accretion rate. A large number of models is computed and evaluated. A distinction between the X-ray luminosity and the total luminosity is made and particularly the dependence on the stellar rotation rate is investigated. A paper in collaboration with Armin Nabizadeh and Prof. Solen Balman of the Middle East Technical University (Ankara) in which the derived luminosities are compared to SS Aur is in preparation.

Meanwhile, in Hertfelder and Kley (2015) [4] the BL instabilities in the disk midplane have been investigated within the 2D planar approach. The parameters for the BL around a protostar are used and the simulations are started from realistic 1D radial profiles which have been calculated similar to Hertfelder et al. (2013). An ideal equation of state is assumed and radiation transport in the disk and radiative cooling from the disk surfaces are considered. No ad hoc prescription for the viscosity is applied in the BL.

Recently, the major question of the vertical structure of the BL around WDs has been answered in Hertfelder and Kley (2017) [5]. In the 2D vertical model including the radiation energy in the two-temperature approach and the flux-limited diffusion approximation, the polar spreading and mixing of the disk material is analyzed. By comparing the results with the 1D radial approach, the connection to Hertfelder et al. (2013) has been established and the circle has been closed, resulting in a complete and consistent treatment of the topic of this thesis.

---

1 Published in Astronomy & Astrophysics.
2 See footnote 1.
3 Accepted for publication in Proceedings of Science.
4 See footnote 1.
5 Accepted for publication in Astronomy & Astrophysics.

The boundary layer in compact binaries

Marius Hertfelder[1], Wilhelm Kley[1], Valery Suleimanov[2,3], and Klaus Werner[2]

[1] Institut für Astronomie und Astrophysik, Abt. Computational Physics, Auf der Morgenstelle 10, 72076 Tübingen, Germany
  e-mail: marius.hertfelder@gmail.com
[2] Institut für Astronomie und Astrophysik, Abt. Astronomie, Sand 1, 72076 Tübingen, Germany
[3] Kazan (Volga region) Federal University, Kremlevskaya 18, 420008 Kazan, Russia

ABSTRACT

Context. Disk accretion onto stars leads to the formation of a boundary layer (BL) near the stellar surface where the disk makes contact with the star. Although a large fraction of the total luminosity of the system originates from this tiny layer connecting the accretion disk and the accreting object, its structure has not been fully understood yet.
Aims. It is the aim of this work to obtain more insight into the BL around the white dwarf in compact binary systems. There are still many uncertainties concerning the extent and temperature of the BL and the rotation rate of the white dwarf.
Methods. We perform numerical hydrodynamical simulations, where the problem is treated in a one-dimensional, radial approximation (slim disk). The turbulence is described by the α parameter viscosity. We include both cooling from the disk surfaces and radial radiation transport. The radiation energy is treated in a one-temperature approximation.
Results. For a given $\dot{M}$ our results show a strong dependence on the stellar mass and rotation rate. The midplane and the effective temperature rise considerably with increasing stellar mass or decreasing stellar rotation rate. Our simulations also show that the radiation energy and pressure are indeed important in the BL. However, some models show a low optical depth in the BL, making it necessary to find a better representation for optically thin regions.
Conclusions. The combination of a high mass and a small radius, characteristic of white dwarfs, can lead to an enormous energy release in the BL, provided the WD rotates slowly. Since the radial extent of BLs is typically very small (about 0.02 to 0.05 R_*), this leads to surface temperatures of a few hundred thousand Kelvin. All of our models showed subsonic infall velocities with Mach numbers of <0.4 at most.

Key words. accretion, accretion disks – binaries: close – white dwarfs – methods: numerical – hydrodynamics

1. Introduction

Accretion of matter on compact objects via a disk is a ubiquitous phenomenon in astrophysics and can be observed in a variety of systems such as protostars, close binary systems, and active galactic nuclei. Since accretion disks appear very frequently in astrophysical situations, they have been studied extensively and several analytical models of stationary disks assuming axial symmetry and neglecting the vertical direction (the equations have been vertically integrated) have been constructed (e.g. Shakura & Sunyaev 1973; Lynden-Bell & Pringle 1974; Pringle 1981; Verbunt 1982). The vertical structure was investigated afterwards with the help of these models (e.g. Meyer & Meyer-Hofmeister 1982).

While about one half of the accretion energy is released over almost the whole radial extent of the accretion disk, the other half is still stored in terms of kinetic energy of the gas near the surface of the central object. Only when the flow reaches the surface of the star is it slowed down from the Keplerian rotation rate to the rotation of the star, which will usually be much slower. This tiny region with a radial extent of less than one percent of the stellar radius where the accretion disk connects to the central object is called the boundary layer (BL). Since a great deal of energy is released in a spatially restricted area, the BL can get very hot and might account for the observed soft and hard X-ray and UV emission in several cataclysmic variable systems (e.g. Cordova et al. 1981a,b; Cordova & Mason 1984). It is therefore of great importance when it comes to

understanding star-disk systems. The first models of the BL were stationary calculations or estimates of timescales that were made under various assumptions by different authors (Lynden-Bell & Pringle 1974; Pringle 1977; Tylenda 1977, 1981; Pringle & Savonije 1979; Regev 1983). However, because of the simplification made there have been debates concerning the consistency of these models with the observations (e.g. Ferland et al. 1982). The first evolutionary calculations were performed soon afterwards (Robertson & Frank 1986; Kley & Hensler 1987; Kley 1989a,b, 1991; Godon et al. 1995), and for the first time allowed non-stationary phenomena like instabilities to be investigated. Among the first analytical studies of the BL were the efforts of Bertout & Regev (1992) and Regev & Bertout (1995), who dealt with the one-dimensional, stationary equations by using the method of matched asymptotic expansions (MAE).

Most of the one-dimensional BL models focus on the radial evolution of the variables, where an infinitesimal thin disk is connected directly to the star. The vertical velocity is set to zero and the fast moving accretion flow is slowed down within the midplane of the disk and accreted by the star. The deceleration of the gas in the BL is accomplished by a mechanism that is not yet fully understood (cf. Pessah & Chan 2012; Belyaev et al. 2012). Here, we assume a viscous medium and use the classical α-parametrisation from Shakura & Sunyaev (1973). The radiation emitted by the BL strongly depends on the mass accretion rate of the accreting object. For rather low mass accretion rates ($\dot{M} \leq 10^{-10}\,M_\odot$/yr, Warner 1987), the BL is optically thin, reaching very high temperatures ($\sim 10^8$ K) and emitting soft and

hard X-rays in the case of cataclysmic variables (e.g. Mukai & Patterson 2004; Pandel et al. 2003, 2005, King & Shaviv 1984; Shaviv 1987; Narayan & Popham 1993; Popham 1999). An optically thick BL, on the contrary, shows a lower temperature of about 10^5 K (Pringle 1977; Syunyaev & Shakura 1986; Popham & Narayan 1995) and emits radiation that is mostly thermalized and resembles a black body spectrum (see e.g. Cordova et al. 1980; Mauche 2004).

It should be noted that in addition to the above-mentioned radial models, there are also one-dimensional models that investigate the vertical flow of the gas in the near proximity of the star. Here, it is assumed that the gas spreads around the star because of the ram pressure in the BL. In contrast to the radial models, the gas is not slowed down in the midplane of the disk, but rather on the whole surface of the star. This alternative model is called the spreading layer (Inogamov & Sunyaev 1999, 2010). While this model was originally designed for the BL of a neutron star, Piro & Bildsten (2004a,b) adapted it for cataclysmic variables systems. The spreading layer concept was extended by Suleimanov & Poutanen (2006), who included general relativity and different chemical compositions of the accreted matter.

In contrast to these 1D models, a number of multidimensional studies of the BL have been performed, mostly under the assumption of axial symmetry. Full radiation hydrodynamical simulations of that kind were performed by Kley (1989a,b, 1991), but only very few dynamical timescales could be followed in low spatial resolution. In recent years, local BL models with higher resolution have been presented by Fisker & Balsara (2005) and Fisker et al. (2006) for the purely adiabatic cases. Calculations including magnetic fields have been done in 2D by Küker et al. (2003) and in 3D by Armitage (2002), though with only low resolution and short dynamical timescales. Additional 2D simulations were performed by Kley & Lin (1996, 1999) for protostars, by Babkovskaia et al. (2008) for neutron stars in LMXB, or by Balsara et al. (2009), who simulated the BL around a white dwarf and used a simplified energy dissipation function without radiation transport. Three-dimensional magnetohydrodynamical simulations including magnetospheric accretion were performed by Romanova et al. (2012), but without the inclusion of radiation transport. Non-axial-symmetric phenomena were investigated only very recently by Belyaev et al. (2012), though only with an isothermal equation of state.

In this paper we focus on the BL structure around white dwarfs in compact binaries such as cataclysmic variable systems. Despite the existing multidimensional studies, we opted for new one-dimensional models because of the moderate computational effort. These are made more realistic by including radiation transport in the radial direction and local cooling in the vertical direction. To allow variability studies, we solve the time-dependent equations. This extends the approach of Popham & Narayan (1995), who solved the stationary equations (see Sect. 4.4 for more details). Furthermore, we have implemented force and dissipation terms of the radiation field and a quasi-two-dimensional radiation transport to treat the radiation field consistently in our calculations, where the radiation pressure (energy) is comparable to the thermal pressure (energy). This work is the first step and will be used to expand the simulations to more dimensions. The results presented in this paper will be used to calculate synthetic, theoretical spectra and thereby considerably narrow the regimes for various parameters of binary systems, like the stellar rotation rate of the white dwarf. More detailed theoretical spectra and observational consequences will be presented in a subsequent paper.

The paper itself is organized as follows: in Sect. 2, an overview of the used equations and assumptions is given, and basic physics of the models is described. Section 3 is devoted to the numerical methods that were utilized in order to solve the equations. In Sect. 4, the models are presented and discussed. We conclude with Sect. 5.

2. Equations

In this section, we present the one-dimensional, vertically integrated Navier-Stokes equations used in the numerical code. Although one-dimensional BL calculations are certainly not sufficient to describe the structure of the BL, they are adequate to model the emitted energy, since the gas is slowed down in the midplane before it engulfs the star (e.g. Kley 1989b).

2.1. Vertical averaging

The 1D equations of motion are obtained through vertical integration of the Navier-Stokes equations over the z coordinate. Assuming a Gaussian profile for the three-dimensional density ρ in the vertical direction, the surface density is given by

$$\Sigma = \int_{-\infty}^{\infty} \rho \, \mathrm{d}z = \sqrt{2\pi}\rho_c(r)H. \tag{1}$$

Here, ρ_c denotes the mass density in the midplane and H is the pressure scale height, which is a measure of the vertical extent of the disk. If we also assume hydrostatic balance and an isothermal equation of state in the vertical direction, the pressure scale height reads

$$H = \frac{c_s}{\Omega_K}, \tag{2}$$

where c_s denotes the (isothermal) sound speed, and $\Omega_K = \sqrt{GM_*/r^3}$ the Keplerian angular velocity (G is the gravitational constant and M_* is the mass of the star).

In our 1D approximation, the vertical component of the velocity vector $\boldsymbol{u}$ is assumed to be negligible. Formally, this can no longer be true in the regions where the gas leaves the midplane and spreads to the poles of the star.

2.2. Continuity equation (conservation of mass)

The vertically integrated continuity equation in polar coordinates is then given by

$$\frac{\partial \Sigma}{\partial t} + \frac{1}{r}\frac{\partial (r\Sigma u_r)}{\partial r} = 0, \tag{3}$$

where u_r denotes the velocity component in the radial direction.

2.3. Equations of motion (conservation of momentum)

The vertically integrated equations of motion read

$$\Sigma\left(\frac{\partial u_r}{\partial t} + u_r\frac{\partial u_r}{\partial r} - \frac{u_\varphi^2}{r}\right) = -\frac{\partial p}{\partial r} + \frac{1}{r}\frac{\partial (r\sigma_{rr})}{\partial r} - \frac{1}{r}\sigma_{\varphi\varphi}$$
$$- \Sigma\frac{GM_*}{r^2} + \frac{\kappa_R \Sigma}{c}\boldsymbol{F}, \tag{4}$$

in the radial direction and

$$\Sigma\left(\frac{\partial u_\varphi}{\partial t} + u_r\frac{\partial u_\varphi}{\partial r} + \frac{u_r u_\varphi}{r}\right) = \frac{1}{r^2}\frac{\partial (r^2\sigma_{r\varphi})}{\partial r} \tag{5}$$

in the azimuthal direction. Here p denotes the vertically integrated thermal pressure and κ_R and F are the Rosseland mean opacity and the radiative flux, respectively, which we will describe in detail in the next section. The term $\frac{\kappa_R \Sigma}{c} F$ acts as a radiative force on the material; σ denotes the vertically integrated viscous stress tensor with the components $\sigma_{rr}, \sigma_{\varphi\varphi}$ and $\sigma_{r\varphi}$ (Papaloizou & Stanley 1986), where we assume a vanishing bulk viscosity.

2.4. Energy equation (conservation of energy)

Since the temperatures in the BL region around white dwarfs are expected to be very hot even if they are optically thick (the temperature is of the order of 10^5 Kelvin, Pringle & Savonije 1979; Tylenda 1981), radiation pressure and radiation energy play an important role in our models and cannot be ignored. Instead of simultaneously solving one equation for the gas energy and one for the radiation energy separately (called the two-temperature approximation[1]), we chose a different approach in order to speed up the calculations. In this so-called one-temperature radiation transport (see e.g. Flaig et al. 2010), we add the two equations for the gas and the radiation energy and obtain

$$\rho \frac{\mathrm{d}}{\mathrm{d}t}\left(\varepsilon + \frac{E}{\rho}\right) = -P\nabla u + \left[\sigma_{ij} - \mathcal{P}_{ij}\right]\nabla_i u_j - \nabla F, \tag{6}$$

where $\varepsilon, E, P, \mathcal{P}$ and F denote the specific thermal energy of the gas, the radiative energy density, the 3D thermal pressure of the gas, the radiation pressure tensor, and the radiative flux, respectively.

The assumption of a local thermodynamic equilibrium is justified for optically thick regions, as is the one-temperature approach (see e.g. Kuiper et al. 2010). Since we concentrate here on high mass accretion rates during outbursts, the BL will stay optically thick even for slow stellar rotation rates. In the approximation of local thermal equilibrium (LTE), the radiation energy simplifies to read $E = aT^4$, where a is the radiation constant and T is the gas temperature.

In addition to the one-temperature approximation, we use the flux-limited diffusion approximation (FLD; Levermore & Pomraning 1981; Levermore 1984), which allows us not to consider an equation for the radiative momentum. The radiation flux is then set to

$$F = -\frac{c\lambda}{\kappa_R \rho}\nabla E = -\frac{\lambda c 4aT^3}{\kappa_R \rho}\nabla T, \tag{7}$$

where λ is a dimensionless number called the flux-limiter. Here, we adopt the formulation by Levermore & Pomraning (1981),

$$\lambda = \frac{1}{R}\left(\coth R - \frac{1}{R}\right), \tag{8}$$

$$R = \frac{|\nabla E|}{\kappa_R \Sigma E}. \tag{9}$$

For the given flux-limiter, the corresponding approximation for the radiation pressure tensor reads (Levermore 1984)

$$\mathcal{P} = \frac{E}{2}\left[(1 - f_{\mathrm{Edd}})\mathcal{I} + (3f_{\mathrm{Edd}} - 1)\,nn\right]. \tag{10}$$

---

[1] Although often used, this term might be misleading since the radiation energy cannot be described by any temperature if no LTE is assumed.

Here, $\mathcal{I}$ is the identity tensor of rank 2, $n = (\nabla E)/|\nabla E|$ is the unit vector parallel to the gradient of E, and the Eddington factor is given by

$$f_{\mathrm{Edd}} = \lambda + \lambda^2 R^2. \tag{11}$$

This approximation reflects the correct behaviour of the radiation pressure tensor in the optically thick regime where it is isotropic and $E/3$, and in the optically thin regions where its absolute value parallel to ∇E is E. If one considers a purely isotropic radiative pressure tensor, a approximation in the flux-limited diffusion theory is given by $\mathcal{P} = \lambda E \mathcal{I}$ (Commerçon et al. 2011). Our simulations showed that the difference between Eq. (10) and the purely isotropic approximation is in general very small.

Furthermore, if we assume that the radiation pressure tensor is diagonal (Eddington approximation) and use the relation between the specific thermal energy and temperature $\varepsilon = c_v T$, the energy equation in the one-temperature approximation becomes after a vertical integration

$$\begin{aligned}
&\left[\Sigma c_v + 4aT^3 \cdot \widetilde{H}\right]\left(\frac{\partial T}{\partial t} + u_r\frac{\partial T}{\partial r}\right) + 4aT^4 \cdot \frac{1}{r}\frac{\partial(ru_r)}{\partial r} = \\
&\quad -p\frac{1}{r}\frac{\partial(ru_r)}{\partial r} - \mathcal{P}_{ij}\nabla_i u_j \\
&\quad + 2\nu\Sigma\left[\left(\frac{\partial u_r}{\partial r}\right)^2 + \left(\frac{u_r}{r}\right)^2\right] + \nu\Sigma\left(r\frac{\partial\Omega}{\partial r}\right)^2 - \frac{2}{3}\nu\Sigma\left(\frac{1}{r}\frac{\partial(ru_r)}{\partial r}\right)^2 \\
&\quad - 2\sigma_{\mathrm{SB}}T_{\mathrm{eff}}^4 + \widetilde{H}\frac{1}{r}\frac{\partial}{\partial r}\left[\frac{16\sigma_{\mathrm{SB}}\lambda}{\kappa_R\Sigma}r\widetilde{H}T^3\frac{\partial T}{\partial r}\right],
\end{aligned} \tag{12}$$

where σ_{SB} is the Stefan-Boltzmann constant, T_{eff} the effective temperature, κ_R the Rosseland opacity, and $\widetilde{H} = \sqrt{2\pi}H$. The second line describes the pressure work exerted by the thermal and radiative pressure. The third line contains viscous dissipation, where ν denotes the kinematic viscosity. The last line describes emission of radiation from the disk surface and diffusion of the radiative flux in the disk midplane. By this means we employ a quasi-2D radiation transport.

To close the set of equations, we need some constitutive relationships. For the equation of state, we use the ideal gas law. The vertically integrated pressure then reads

$$p = \frac{\Sigma R_G T}{\mu}, \tag{13}$$

where $R_G = k_B/m_H$ with k_B being the Boltzmann constant, m_H the mass of hydrogen, and μ is the mean molecular weight. In order to take the radiation pressure effects into account, we have defined an effective sound speed (Krumholz et al. 2007)

$$c_{\mathrm{eff}} = \sqrt{\frac{\gamma p + (4/9)\cdot E\cdot\widetilde{H}\cdot(1 - \mathrm{e}^{-\kappa_R\rho\Delta r})}{\Sigma}}. \tag{14}$$

The factor $(1 - \mathrm{e}^{-\kappa_R\rho\Delta r})$ (Δr is the width of a cell) is used to interpolate between the optically thick region, where the radiation pressure increases the effective sound speed since it contributes to the restoring force and optically thin regions, where radiation pressure plays no role.

For the opacity we use Kramer's law,

$$\kappa = \kappa_0(\rho/\mathrm{g\ cm}^{-3})(T/\mathrm{K})^{-3.5}, \tag{15}$$

where $\kappa_0 = 5 \times 10^{24}\ \mathrm{cm}^2\ \mathrm{g}^{-1}$. If the temperature is high enough for the gas to be fully ionized, we can assume a lower threshold for the opacity given by free electron scattering processes

(Thomson scattering). The corresponding opacity has the constant value $\kappa_{\text{Thomson}} = 0.335 \, \text{cm}^2 \, \text{g}^{-1}$ (assuming a hydrogen mass fraction of $X = 0.675$ for the gas composition) and is added to Kramer's opacity. Because we estimate the local cooling of the disk via a blackbody radiation of temperature T_{eff}, we need a relation that links the effective temperature to the temperature in the midplane of the disk. Therefore, we employ the relation by Hubeny (1990) which is a generalisation of the grey atmosphere (e.g. Rybicki & Lightman 1986) and approximates the optical depth in the vertical direction of the disk. The relations read (Suleymanov 1992)

$$T^4 = \tau_{\text{eff}} T_{\text{eff}}^4 \tag{16}$$

$$\tau_{\text{eff}} = \frac{3}{8}\tau_{\text{R}} + \frac{\sqrt{3}}{4} + \frac{1}{4\tau_{\text{P}}}, \tag{17}$$

where τ_{R} and τ_{P} ($\tau = \kappa\rho H = \frac{1}{2}\kappa\Sigma$) are the Rosseland and the Planck mean optical depth (see also Kley & Crida 2008).

2.5. Viscosity

The mechanism that accounts for the angular momentum transport in the BL region is still a matter of concern (Papaloizou & Szuszkiewicz 1994; Narayan et al. 1994; Kato & Inagaki 1994; Godon 1995). The most likely driving force for the anomalous viscosity in accretion disks with magnetic Prandtl numbers of the order of unity is the magneto-rotational instability (e.g. Balbus & Lesaffre 2008) that gives rise to the onset of turbulence (Balbus & Hawley 1991, 1998; Balbus 2003) which acts like a genuine viscosity on macroscopic scales. However, this cannot be the case for the BL, since the magneto-rotational instability is effectively damped out for a increasing rotation profile $\Omega(r)$ (Godon 1995; Abramowicz et al. 1996). For lack of a better representation, we assume that the angular momentum transport in the BL is managed by turbulence of some kind (cf. Pringle 1981). In that case we can use the classic α-prescription by Shakura & Sunyaev (1973), which is a parametrisation for the stresses caused by turbulence in an accretion disk and therefore is still valid for MRI unstable disks, provided that a viable value for the numerical parameter α is given. This α ansatz, which is a frequently used expression for the disk viscosity is written as

$$\nu = \alpha c_{\text{s}} H, \tag{18}$$

where $c_{\text{s}} = \sqrt{p/\Sigma}$ is the isothermal sound speed. Unless stated otherwise, Eq. (18) was used to calculate the viscosity in our models. In the BL, the radial pressure scale height becomes smaller than the vertical one. This is considered in the viscosity prescription by Papaloizou & Stanley (1986), which reads

$$\nu = \alpha c_{\text{s}} \left[\frac{1}{H^2} + \frac{(\text{d}p/\text{d}r)^2}{p^2} \right]^{-1/2}. \tag{19}$$

We used Eq. (19) when we compared our calculations with that of Popham & Narayan (1995) in Sect. 4.4.

3. Numerical methods

3.1. General remarks

The partial differential equations, Eqs. (3)–(5) and (12), are discretized on a fixed Eulerian grid using the finite differences method and propagated in time using a semi-implicit-explicit

scheme. For this purpose a new framework, guided by the ZEUS code by Stone & Norman (1992), has been programmed completely from scratch and tested extensively before it was used to perform the calculations. To ensure a formal second-order accuracy in time and space, we employed a staggered grid in space (see e.g. Tscharnuter & Winkler 1979) and a multistep procedure for the time integration (operator-splitting, e.g. Hawley et al. 1984). The computational domain typically ranges from one to two stellar radii, $\mathcal{D} = [R_*, 2\,R_*]$, and is divided into 512 logarithmically spaced grid cells.

3.2. Implicit methods

For some source terms, a special treatment for the time integration is necessary, because using a time-explicit scheme would constrain the time step considerably and slow down the simulations. Hence those parts of the equations, namely the radial diffusion (radiation transport) and the viscous torques and forces, have to be solved with an implicit scheme that does not limit the time step if we are looking for a stationary solution. In contrast to an explicit time integration, the equations are now solved assuming the value of the physical quantity at the new time step $n + 1$. This leads to a system of linear equations, which can be written as a matrix-vector multiplication in a space of dimension N, where N is the number of active grid cells. However, this system can become very large if we are using a large number of cells. Fortunately, in our one-dimensional case the use of this implicit method only leads to a tridiagonal matrix, and the equations can be solved easily.

3.3. The time step

One undesirable feature of explicit numerical methods in hydrodynamics is the limitation of the largest possible time step (Courant et al. 1928). It must be limited with respect to the characteristics of the system according to the relation known as the CFL condition,

$$\Delta t = f_{\text{C}} \cdot \min_j \left[\frac{\Delta r_j}{|u_j| + c_{\text{s},j}} \right], \tag{20}$$

where Δr_j is the extent of the cell j, u_j its velocity, and $c_{\text{s},j}$ the sound speed. The minimum of all active cells is taken. Typically, we use a Courant factor $f_{\text{C}} = 0.8$ in Eq. (20).

3.4. Boundary and initial conditions

The modelling of the BL surrounding a star is a classical boundary value problem, meaning that the solution we try to obtain must satisfy not only the partial differential equations but also the boundary conditions because of the finite space domain. In mathematical terms those conditions are given as either Dirichlet or Neumann boundary conditions where either a value or the normal derivative of a variable is specified.

Physically speaking, at the outer boundary of our computational domain, we have to allow for an incoming mass flux that corresponds to the accretion of matter. Additionally, we require the angular velocity to be Keplerian $\Omega(r_{\text{out}}) = \sqrt{GM/r_{\text{out}}^3}$ and consider a pressure correction. At the inner boundary, where the stellar surface is located, we set the angular velocity of the gas to the stellar rotation rate $\Omega(r_{\text{in}}) = \Omega_*$, i.e. we impose a no-slip boundary condition in φ-direction. Instead, the radial velocity is

not set to zero, but rather to a small but finite fraction of the Keplerian velocity,

$$u_r(r_{\rm in}) = \mathcal{F}\sqrt{GM_*/r_{\rm in}}, \tag{21}$$

in order to enable a mass flux out of the domain. For $\mathcal{F}$ we choose a value much smaller than one, typically 10^{-5}. This open inner boundary is necessary to avoid the accumulation of mass and allow for accretion onto the star. The value of $\mathcal{F}$ determines how much of the stellar interior is taken into account in the simulation. The extreme case of $\mathcal{F} = 0$ would imply that the whole star is considered which does not make sense in this type of simulation. Our choice of $\mathcal{F}$ ensures that a sufficient part of the stellar envelope is contained in the domain but not too much, otherwise the temperatures become too high and slow down the simulations. For testing purposes we have varied $\mathcal{F}$ and do not find any differences in the results despite a small shift in radius.

The stellar radiation is taken care of by including the flux $F_* = \sigma_{\rm SB}T_{\rm eff}^4$ in the radiative diffusion routine as an inner boundary condition. Because the temperature at $r_{\rm in}$ is inside the star, it is not known a priori and cannot be specified. Hence, a simple zero gradient condition for the temperature is assumed in all other routines that require a temperature. Previous studies suggest that the thermal boundary condition at the star is of great importance for the BL (Regev & Bertout 1995; Godon et al. 1995). We would like to point out that the influence of the incoming flux is virtually nil, as test calculations have shown. Apart from the Dirichlet conditions that have been shown above, for most other physical variables we imposed zero gradient boundary conditions, which means that the normal derivative at the boundary equals zero (Neumann type).

Initially, we have to prescribe values for all variables. Here, it is vital to ensure that the initial conditions are compatible with the boundary conditions and are physically reasonable. We have found that a reliable set of initial conditions is given by the Shakura & Sunyaev (1973) disk solution (see e.g. Frank et al. 2002, for a compact representation), even though they are not completely consistent with all boundary conditions. To avoid any problems in this context, we have interpolated both regions smoothly. For a given stellar mass M_*, radius R_*, temperature T_*, and rotation rate ω_*, the solution will be given by the mass inflow rate $\dot{M}$ and the viscosity parameter α.

3.5. Model parameters

In this paper, we focus on the BL around the white dwarf in cataclysmic variable systems, and investigate its structure. We computed several models, where we vary the mass of the white dwarf and its rotation rate. We ran the simulations with the following three masses, $M = 0.8\,M_\odot$, $1.0\,M_\odot$, and $1.2\,M_\odot$, which are typical white dwarf masses in cataclysmic variables. Another important parameter that also determines the entire amount of energy released in the accretion disk and BL is the radius of the star. Here we used the mass-radius relation from Nauenberg (1972). We imposed an effective temperature of $T_* = 50\,000$ K that is, for example, consistent with the estimates of Sion et al. (2010) for SS Cyg, where a mass accretion rate of $\dot{M} = 1.51 \times 10^{-8}\,M_\odot/\mathrm{yr}$ was assumed. Since we are interested in the thermodynamics of the BL, the rotation rate of the white dwarf is an important parameter. It determines how much energy is dissipated in the BL region and therefore has a major influence on the temperature. We simulated a variety of models where the white dwarf is non-rotating ($\Omega_* = 0$), fast rotating ($\Omega_* = 0.8\Omega_{\rm K}$), and in between. We took $\alpha = 0.01$ for the viscosity parameter

throughout, which is probably too small a choice for the disk. In the BL, however, the viscosity is supposed to be far smaller than in the disk. Test calculations with $\alpha = 0.1$ showed no major structural differences compared to the models presented here, except for the inflow velocity that reaches the sonic point for models with high mass and low rotation rates. If we use Eq. (19) instead of the classical α ansatz for the viscosity, the sonic point is hit only for greater values of α. To avoid unphysical, supersonic infall velocities, it is possible to include a causality preserving factor (e.g. Narayan 1992).

4. Results

4.1. The $1.0\,M_\odot$ model

First, we will describe the basic properties of the BL for our standard model of a one solar mass white dwarf. In doing this, we are going to emphasise the dependence of the structure and thermodynamics on the rotation rate of the central star, a parameter whose exact value is still unclear in many systems. We usually show five different stellar rotation rates (a fraction of $\{0.0, 0.2, 0.4, 0.6, 0.8\}$ of the Keplerian rotation rate at the stellar surface) and use the abbreviation $\omega := \Omega_*/\Omega_{\rm K}(R_*)$.

4.1.1. Dynamic structure of the disk

Figure 1 shows the angular rotation rate of the gas in units of the Keplerian rotation rate, $\Omega_{\rm K} = \sqrt{GM_*/r^3}$. We can clearly see that outside the BL, for $r/R_* \gtrsim 1.2$, the gas rotates with the Keplerian angular velocity. When moving farther inwards, the gas rotates slightly super-Keplerian in order to compensate the large inward-pointing pressure gradient that is present in this region. Not until the gas is at a distance of less than a percent of the stellar radius does its angular velocity decrease to connect smoothly to the stellar rotation rate. The more the angular velocity differs from the Keplerian value, the more the gas loses radial stabilisation via the centrifugal force. This is, however, compensated by a large, now outward-pointing pressure gradient since the star has a much higher temperature and density and so the pressure is much higher than in the BL. Although the connection between the angular velocity of the gas and the star does not involve discontinuities, the angular velocity strongly changes in a very small region. The width of the BL is defined as the distance from the star (here R_*) to the point where the radial derivative of $\Omega(r)$ vanishes. We note that this point does not in general coincide with the point where $\partial/\partial r(\Omega/\Omega_{\rm K}) = 0$. Table 1 gives an overview of the width of the BL for different stellar rotation rates. We also note that R_* is not defined unambiguously owing to the continuous transition to the star, and the observed width may depend on the value of $\mathcal{F}$, see Eq. (21). With an increasing stellar rotation rate, the width of the BL decreases up to $\omega = 0.2$ at first. After that, however, it gets wider again. In general, the width of the BL is governed by the viscosity, which in turn depends on the temperature and the surface density for the case of an α-prescription. An increasing temperature and surface density leads to a broadening of the BL region. A look at Fig. 4, which shows the temperature in the midplane of the disk, indicates, that the temperature in the disk decreases with increasing stellar rotation rate. This behaviour is in line with our expectations, since a faster moving star means less friction and therefore less heating. As a consequence of this overall temperature variation with ω, the faster rotation of the star, the smaller the width of the BL; however, the surface density rises with increasing ω, as can be seen in the inset in Fig. 3, because of an increasingly inefficient
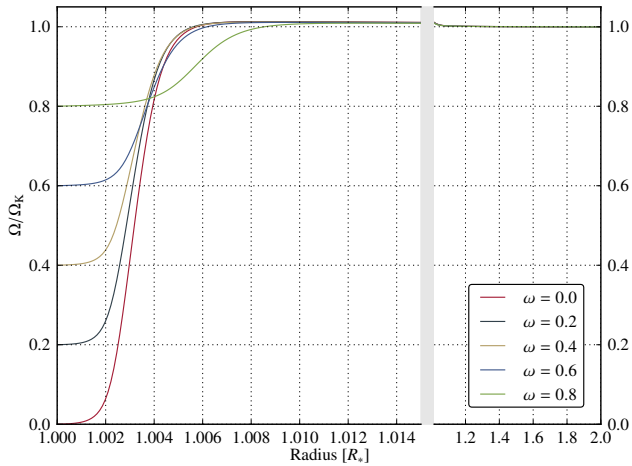
Fig. 1. Angular velocity $\Omega = u_\varphi/r$ in terms of the Keplerian angular velocity for a central star with mass $M_* = 1.0 \, M_\odot$ and five different stellar rotation rates Ω_*, denoted by $\omega = \Omega_*/\Omega_K(R_*)$. The plot depicts two regions separated by a light grey bar that differ in the radial scaling and enable us to show both the rapid variation in the BL and the constant overall trend.

Table 1. Width of the BL for $M_* = 1.0 \, M_\odot$ and different stellar rotation rates $\omega = \Omega_*/\Omega_K(R_*)$.

ω	$\Delta r \, [R_*]$	$u_\varphi^{max} \, [\mathrm{cm \, s^{-1}}]$	$\beta = \frac{\Omega_{max}}{\Omega_K(r_{max})}$
0.0	0.0074	493×10^6	1.013
0.2	0.0072	493×10^6	1.012
0.4	0.0074	492×10^6	1.012
0.6	0.0079	492×10^6	1.011
0.8	0.0104	490×10^6	1.008

Notes. By definition, the BL ranges from the surface of the star to the point where $\partial\Omega(r)/\partial r = 0$, i.e. where it has a maximum. Additionally, the absolute value of $u_\varphi = \Omega \cdot r$ at r_{max} is given as u_φ^{max}.

mass transport through the disk (more mass can accumulate in the disk). This is the reason for the turnaround of the trend at $\omega = 0.2$, when the BL starts to become broader again. Another interesting feature is the comparatively large width of the BL for $\omega = 0.8$ that stands out both in Table 1 and Fig. 1, and does not match the shape of the other models. This effect is caused by a slightly different temperature evolution, as can be seen in the inset in Fig. 4. Here, as a result of reduced friction and hence less energy release, the green line (representing $\omega = 0.8$) is missing a peak (compared to the other curves) and is wider than most other temperatures over a small region.

The Mach number of the gas, which is defined as the quotient of the radial velocity and the speed of sound $\mathrm{Ma} = |u_r|/c_s$ is shown in Fig. 2. Since the radial velocity is negative throughout the computational domain, in principle the Mach number outlines the velocity of the radially inward-falling material. While the gas is moving inwards with a rather low velocity over most parts of the disk, there is a distinct maximum of the radial velocity in the BL. What drives the material to move inwards more rapidly in the BL is the loss of angular momentum caused by friction in the disk. Hence the radial velocity is increasing strongly in the BL region, as can be observed in the inset in Fig. 2. After peaking in the BL, the radial velocity decreases again as the gas approaches the surface of the star. Here, the gas slows down as it settles onto the atmosphere of the star, where
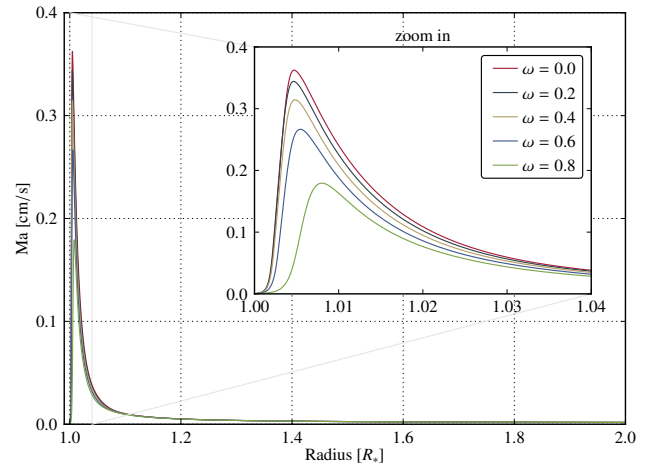
Fig. 2. Radial Mach number of the gas for a stellar mass of $1.0 \, M_\odot$. The Mach number is defined as a quotient of radial velocity and the sound speed $\mathrm{Ma} = |u_r|/c_s$. The different colours correspond to the different stellar rotation rates $\omega = \Omega_*/\Omega_K(R_*)$. The smaller box inside the graph is a zoom in of the inner edge; the light grey frame denotes the zoom area.
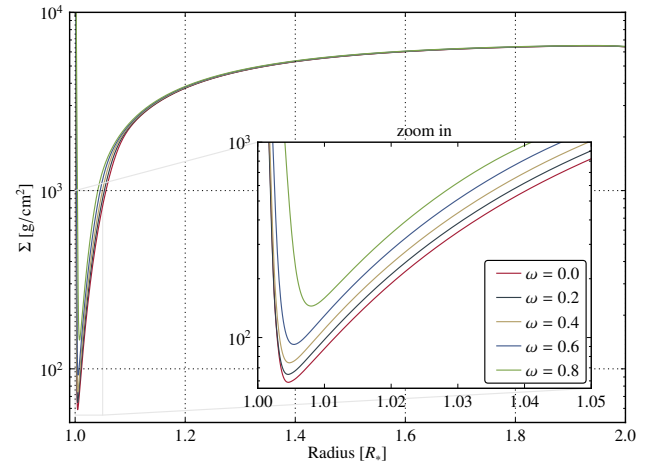

Fig. 3. Surface density $\Sigma \sim \rho H$ (log-scale) of the disk and a stellar mass of $1.0 \, M_\odot$ for five different stellar rotation rates $\omega = \Omega_*/\Omega_K(R_*)$. The inset is a zoom in of the inner edge; the light grey frame denotes the zoom area.

the individual layers are stabilized by the pressure (hydrostatic balance). The inflow velocity of the gas depends on how much angular momentum can be removed from the material, which in turn is dependent on the strength of the shearing. Accordingly, the faster the stellar rotation rate, the weaker is the shearing in the disk and hence the radial velocity should decrease with increasing stellar rotation rate in the BL. We can observe this trend in Fig. 2 where we can also see that the radial velocity is clearly subsonic throughout the computational domain and especially in the BL. Thus there are no problems concerning causality (e.g. Pringle 1977) in our simulations because of the small value of α.

4.1.2. Thermal structure of the disk

In the previous section, we looked closely at the dynamical structure of the disk and the BL, which is determined by the radial and azimuthal velocities. From an observational point of view,
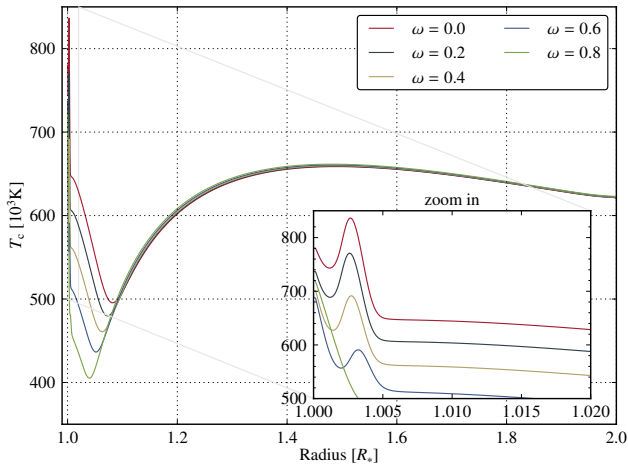
Fig. 4. Temperature T_c in the midplane of the disk, i.e. $z = 0$, for $M_* = 1.0\,M_\odot$. The five models displayed differ in the stellar rotation rate $\omega = \Omega_*/\Omega_K(R_*)$. The inset is a zoom in of the inner edge; the light grey frame denotes the zoom area. The small peak in the inset is a clear indication of a hot BL.

Fig. 5. Effective temperature T_{eff} of the disk, calculated according to Eq. (16). The plot shows five different models, all of which have the same stellar mass of $1.0\,M_\odot$, but different stellar rotation rates $\omega = \Omega_*/\Omega_K(R_*)$. The plot depicts two regions separated by a light grey bar that differ in the radial scaling and enable us to show both the narrow but very distinct peak of the effective temperature in the BL and the nearly constant behaviour in the disk all in one graph.

however, we are much more interested in the thermodynamics of the disk, since the quantity that we can actually observe, the emitted radiation, depends on the temperature; therefore, we will now explore the surface density and the temperature structure of our models.

The surface density Σ for the $1.0\,M_\odot$ model is shown in Fig. 3. We can observe a heavy depletion of material in the BL. The surface density drops by approximately two orders of magnitude compared to the weakly varying value in the disk. If we go farther in, the surface density rises rapidly since we encounter the surface of the star which has a density that is orders of magnitudes higher than in the disk. The reason for the strong decrease of the surface density in the BL is the aforementioned increase in inflow velocity. Since for the equilibrium state the mass accretion rate $\dot{M}$ is constant throughout the disk (see also Fig. 9 below), a local increase in inflow velocity leads to a reduced density at this point. The BL resembles a bottleneck with a higher velocity and a lower density. In the disk the distinction between models with different values of ω is very small; it is more pronounced in the BL. The models with a slower rotating star have a smaller surface density in the BL that is accounted for by the greater inflow velocity.

Even more interesting than the density structure is the temperature of the disk. In our one-dimensional models, we distinguish between the temperature in the midplane of the disk T_c and the effective or surface temperature, which is close to the disk temperature at $\tau \approx 1$. Figure 4 shows the midplane temperature for $M_* = 1.0\,M_\odot$ and five different stellar rotation rates. The local heat production is proportional to the square of the shear. Hence in the disk the temperature decreases with increasing radius r. In the BL, Ω reaches its maximum and the shear in the gas vanishes; therefore, there is a location in the disk where the viscous dissipation vanishes and the local heating is approximately zero (apart from pressure work). For that reason, the temperature must drop in the region where $\partial\Omega/\partial r = 0$, so in or near the BL. The minimum of T_c does, however, not coincide with the maximum of Ω, since heat is transported radially through the disk via advection and radiation. Furthermore, the cooling of the disk through emission of radiation depends on the local optical depth and hence is different at each location. On the other hand, after
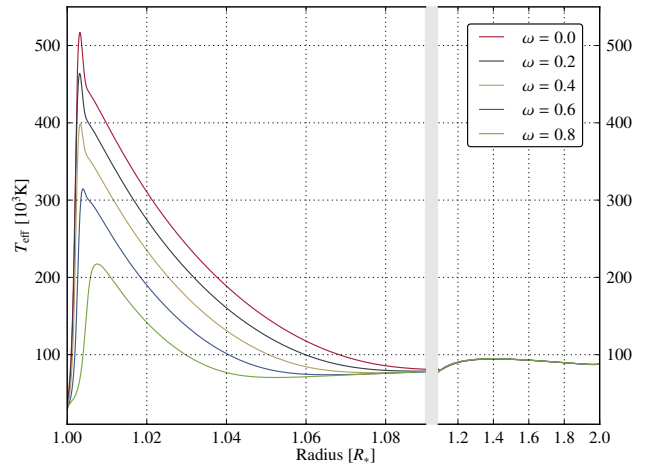
the zero-gradient point of Ω, the shearing is very strong where the angular velocity connects to the stellar rotation rate. As a consequence, the temperature again rises, whereby the considerably declined surface density compensates the strong shearing to some extent. The little peak in T_c, which is located very close to the star in the BL, is a result of the heat production in the BL (see the inset in Fig. 4) and is a clear indication of a hot BL. The influence of the stellar rotation rate on the temperature is twofold. In the disk, the temperature is slightly hotter for faster stellar rotation rates because of the larger surface density. This trend is reversed in the area of the BL, where a smaller rotation rate causes more shear and supersedes the influence of the surface density. A special case is obviously given for very fast rotating stars, as can be seen in Fig. 4 for $\omega = 0.8$, where the BL is broader and is missing a peak in the midplane temperature. The overall temperature regime of 400 000 to 840 000 Kelvin is very hot.

While the temperature shown in Fig. 4 corresponds to the temperature in the midplane of the disk, we are particularly interested in the emergent spectrum from the disk, which – in the LTE approximation – is determined by the temperature on the surface, see Eq. (16). The effective temperature T_{eff} is shown in Fig. 5 for the $M_* = 1.0\,M_\odot$ case. For outer parts of the simulation domain, T_{eff} changes only slightly and the difference in temperature between various choices of ω is hardly noticeable. The reason for the almost constant behaviour of the effective temperature in the disk is the strong increase in the BL that somewhat masks the variation in the disk. While the midplane temperature changes at most by a factor of 2 over the whole simulation area, the effective temperature changes considerably more, by a factor of 4–5. This is caused by a strong drop in the optical depth in the BL by several orders of magnitude due to the drop of the surface density. While, generally, the accretion disk is optically thick, under certain circumstances, the BL can become optically thin, since the dilution of matter is severe in this region. While the shear and the energy production are confined to a small region called the dynamical BL, the release of the produced energy occurs over a slightly wider area, called the
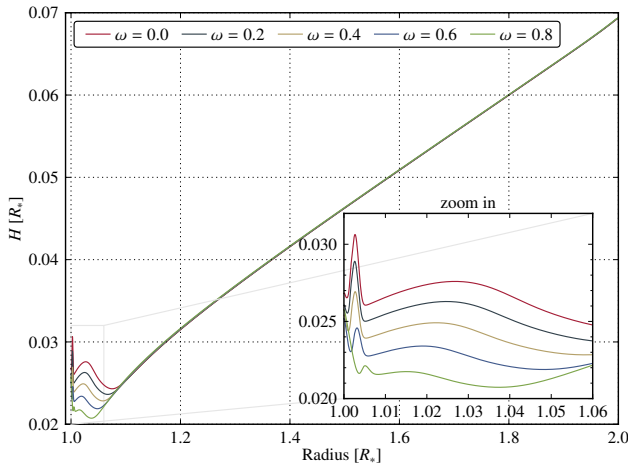
Fig. 6. Scale height H (see Eq. (2)) of the disk for $M_* = 1.0\,M_\odot$ and five different stellar rotation rates $\omega = \Omega_*/\Omega_K(R_*)$. The disk is obviously very thin and not flared. In the BL, it is puffed up to some extent, which is, however, not unexpected. The inset is a zoom in of the inner edge; the light grey frame denotes the zoom area.

thermal BL (Regev & Bertout 1995; Popham & Narayan 1995). Therefore, the peak in Fig. 5 is less intense than the one in Fig. 4, but instead it is wider because of the radial diffusion. According to what has already been said above, the magnitude of the peak of T_{eff} in the BL depends on the stellar rotation rate to the effect that a slower rotating star causes more shear in the BL, hence a higher energy dissipation and eventually a higher effective temperature.

Finally, we investigate the vertical extent of the disk. According to Sect. 2.1, a measure for the height is the variable H, which is the point where the density drops by a factor of $1/\sqrt{e}$ compared to the midplane density. The scale height $H(r)$ is depicted in Fig. 6 for the 1.0 $M_\odot$ model. The disk in the system is, according to our simulations, rather thin with an aspect ratio $h = H/r$ of roughly $h = 0.029$ (arithmetic mean) and has a slope of $dH/dr \approx 0.05$. In the region of the BL, the disk height increases noticeably because of the strong growth of temperature in the BL that causes a high pressure which puffs up the disk in the innermost region. Figure 6 confirms the picture of the BL being a bottleneck that we introduced earlier. When approaching the BL from the outside, the disk first starts to get thinner and thinner until it suddenly grows in height. In the disk the vertical extent is nearly identical for different ω, but in the BL it clearly depends on the stellar rotation rate. The faster the star spins, the less puffed out the BL is. We have already pointed out, that the temperature depends on the stellar rotation rate. Since the pressure depends on the temperature, the scale height in the BL changes with different stellar rotation rates.

4.2. Dependence on the stellar mass

After having discussed the basic properties of the BL using the example of a solar mass white dwarf, we now focus on the dependence of the BL on the stellar mass. First, we will again examine the dynamical structure of the BL (see Table 2 and Fig. 1[2]). The shape of the angular velocity profile is identical for

---

[2] Additional figures can be found at: http://www.tat.physik.uni-tuebingen.de/~hertfelder/BL2013.

Table 2. Width of the BL for three different stellar masses and the stellar rotation rates of $\omega = 0.0$ and $\omega = 0.8$.

Model	Δr [R_*] $\omega = 0.0$	Δr [R_*] $\omega = 0.8$	u_φ^{max} [cm s^{-1}] $\omega = 0.0$
$M_* = 0.8\,M_\odot$	0.0086	0.0134	391×10^6
$M_* = 1.0\,M_\odot$	0.0074	0.0104	493×10^6
$M_* = 1.2\,M_\odot$	0.0066	0.0084	638×10^6

Notes. By definition, the BL ranges from the surface of the star to the point where $\partial\Omega(r)/\partial r = 0$, i.e. where it has a maximum.

each of the three stellar masses. There is, however, a difference in the width of the BL. The higher the stellar mass, the less broad is the BL. Table 2 shows the width of the BL for the three different stellar masses and two different stellar rotation rates, along with the maximum value of Ω for $\omega = 0.0$. Here it becomes more obvious that the width of the BL strongly depends on the mass of the central star. The absolute value of the angular velocity also depends on the stellar mass and varies significantly. The reason for the decreasing width of the BL is the mass radius relation of white dwarfs. The more massive the star is, the smaller the stellar radius R_* is. This causes a non-linear variation of gravity and so affects the width of the BL. The Mach number stays more or less the same and the inflow occurs subsonically throughout all models.

The dynamical structure is affected by the mass of the central star, and also the thermodynamics of the BL. To gain more insight into this dependence, we first consider the surface density Σ for the different models. The general trend of the 0.8 and 1.2 $M_\odot$ models is closely related to that shown in Fig. 3. We note, however, that the more massive the central star is, the higher the surface density in the BL and in the disk is, for the same reason as for the decrease of the BL width, namely a lower effective viscosity. If the viscosity becomes smaller, the transport of matter through the disk is not as effective as it is for a higher viscosity because the shear viscosity drives the accretion of matter. Thus, more matter can accumulate in the disk and the surface density rises. Again, the minima of Σ are located at different radii, corresponding to different widths of the BL. Apart from these features, the evolution of the surface density looks identical for different stellar masses. The midplane temperature, on the other hand, shows considerable differences in magnitude between the three models. As Table 3 shows, the 1.2 $M_\odot$ model is hotter than the 0.8 $M_\odot$ by a factor of 1.7 throughout the BL and the disk. This is due to the higher surface density in the high stellar mass model. Since the viscous dissipation is proportional to the surface density, an increasing Σ ensures an increase in the midplane temperature. This effect prevails, although the viscosity is, as we have seen, smaller than in the low mass models.

A direct comparison is shown in Fig. 7, where we have plotted T_c for the three different stellar masses and $\omega = 0.4$ in one single diagram. This makes it clear how the midplane temperature increases overall with increasing stellar mass.

Table 3 also describes the effective temperature T_{eff} for the three different masses, whose general trend is given by Fig. 5. As we have expected, the more massive the central star is, the higher the effective temperature of the BL (and also the disk) is and the harder the radiation emerging from the BL is, because of the ratio of stellar mass and radius, which exclusively determines the total amount of accretion energy that is released in the disk and the BL. The total luminosity that can be extracted from the

Table 3. Illustration of the midplane and effective temperature for the models with 0.8 and 1.2 $M_\odot$.

Midplane temperature T_c		peak [K]	
M_* [$M_\odot$]	Ω_* [Ω_K]	BL	disk
0.8	0.0	640 000	520 000
	0.2	590 000	520 000
	0.4	520 000	520 000
	0.6	450 000	520 000
	0.8	no peak	520 000
1.2	0.0	1 140 000	900 000
	0.2	1 060 000	900 000
	0.4	950 000	900 000
	0.6	820 000	900 000
	0.8	650 000	900 000

Effective temperature T_{eff}		peak [K]	
M_* [$M_\odot$]	Ω_* [Ω_K]	BL	disk
0.8	0.0	400 000	64 000
	0.2	360 000	64 000
	0.4	300 000	64 000
	0.6	235 000	64 000
	0.8	165 000	64 000
1.2	0.0	690 000	125 000
	0.2	625 000	125 000
	0.4	540 000	125 000
	0.6	440 000	125 000
	0.8	300 000	125 000

Notes. The table states the maximum temperatures both in the disk and in the BL for each stellar rotation rate.

process of accretion on a body with mass M and radius R is given by

$$L_{acc} = \frac{GM\dot{M}}{R},\tag{22}$$

where $\dot{M}$ is the mass accretion rate and G the gravitational constant. The luminosity of the BL is at most one half of L_{acc}. Therefore, the greater the relation M_*/R_*, the higher the effective temperature. The inverse mass-radius-relation of white dwarfs enhances L_{acc} even more. We can also see that the width of the thermal BL follows the trend of the dynamical BL. With increasing stellar mass, the width of the peak of T_{eff} decreases. Again, we have plotted all three stellar masses in one diagram (Fig. 8) that emphasizes the points mentioned above. To give an overview of the radiation energy that corresponds to these temperatures, we focus on two models that are located at the opposite edges of the parameter space. The $\omega = 0.0, 1.2\,M_\odot$ model peaks at nearly 700 000 Kelvin. This corresponds to a black body radiation spectrum where the maximum of the distribution is located at a photon energy of 300 eV. The other model, where the parameters are given by $\omega = 0.8, 0.8\,M_\odot$, peaks at an effective temperature of about 170 000 Kelvin. This corresponds to a photon energy of 73 eV at the maximum of the black body spectrum. The effective temperature, or in other words, the spectrum emerging from the BL, is obviously a good way to try to determine the actual mass of the white dwarf in cataclysmic variable systems.

Finally, we want to have a look at the vertical structure of the disk. The scale height H of the different models again follows the trend of Fig. 6. The aspect ratio of the 0.8 $M_\odot$ model
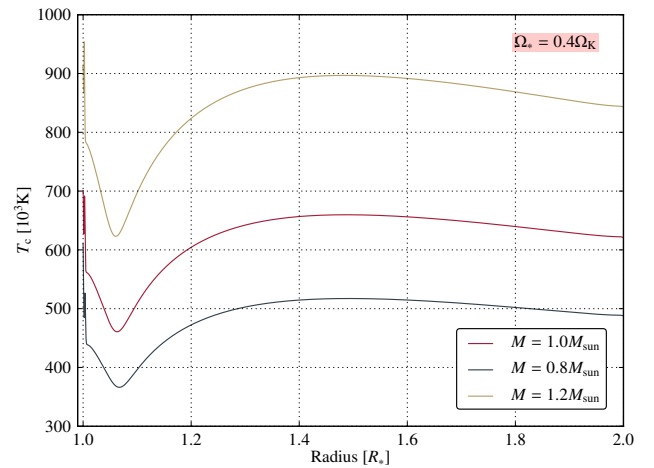

Fig. 7. Comparison of the temperature in the disk midplane T_c of the three different models with stellar masses of 1.0, 0.8, and 1.2 $M_\odot$. The stellar rotation rate Ω has been chosen to amount to $0.4\Omega_K$, as an illustrative case. It is clearly observable that with increasing stellar mass the temperature in the disk also rises.
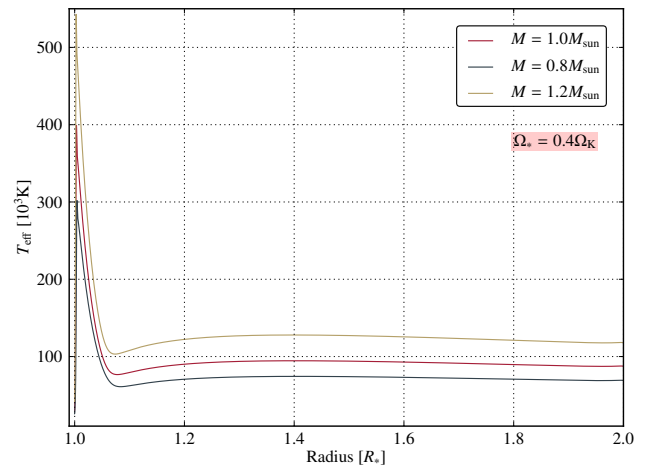

Fig. 8. Analogous to Fig. 7, we compare the effective temperatures of the three different stellar masses (1.0, 0.8, and 1.2 $M_\odot$) in this plot. Again, $\Omega = 0.4\Omega_K$ has been chosen as an example of the stellar rotation rate. We note that the effective temperature rises with increasing stellar mass.

is $H/r \approx 0.032$, while the model with 1.2 $M_\odot$ is slightly thinner with $H/r \approx 0.026$. The solar mass model lies in between with $H/r \approx 0.029$, as has been said earlier. We can therefore deduce that with increasing stellar mass, the vertical extent of the accretion disk diminishes. This also holds true for the BL, even though the midplane temperature is much higher in the high mass model and accordingly the pressure will try to puff out the BL with much more force. However, the gravitational field of the central star exerts a force against the pressure and is strong enough to outrange it. The disks are still not flared for all three stellar masses.

4.3. Mass accretion rate and angular momentum flux

For a stationary state the continuity Eq. (3) reduces to $\dot{M} = -2\pi r\Sigma u_r$, where $\dot{M}$ is the constant mass accretion rate that represents the amount of mass flowing through an annulus at a
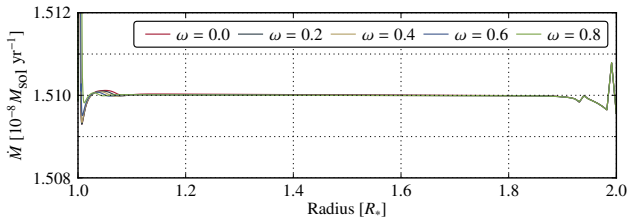
Fig. 9. Mass accretion rate $\dot{M} = -2\pi r \Sigma u_r$ for $M_* = 1.0\,M_\odot$ and five different stellar rotation rates $\omega = \Omega_*/\Omega_K(R_*)$. The imposed value equals $\dot{M} = 1.51 \times 10^{-8}\,M_\odot$ yr^{-1}. Since $\dot{M}$ is constant in a stationary state, this plot is also an indication that a good equilibrium has been reached.

Fig. 10. Normalized angular momentum flux $j = \dot{J}/\dot{J}_*$, where $\dot{J}$ is given by Eq. (23) and $\dot{J}_* = \dot{M}R_*^2\Omega_K(R_*)$ is the advective angular momentum flux at the surface of the star. Displayed is a stellar mass of $1.0\,M_\odot$ and five different stellar rotation rates in Keplerian units ω. We note that j should be constant in a stationary state.

given radius per time. Since we imposed a mass accretion rate of $\dot{M} = 1.51 \times 10^{-8}\,M_\odot$/yr at the outer boundary, we require $\dot{M}$ to attain this value throughout the disk if a steady state is reached. The mass accretion rate after a simulation time of about 10 000 orbits at $r = R_*$ is shown as an example in Fig. 9 for the $1.0\,M_\odot$ model. At first glance, the attained equilibrium state looks very good and stable. The maximum deviation from the imposed value is only about 4% for the heaviest white dwarf. The most constant $\dot{M}$ is reached for the models that correspond to $\omega = 0.8$. Apart from the inner and outer boundary, where $\dot{M}$ matches the imposed value to an accuracy of far less than one percent, the agreement between the simulation and the imposed value is perfect. This holds true for any of the three stellar masses. However, with decreasing stellar rotation rate and increasing stellar mass the mass accretion rate starts to deviate slightly from the constant value of $1.51 \times 10^{-8}\,M_\odot$/yr. The deviations near the outer boundary, however, are induced by the boundary conditions.

Another quantity that should attain a constant value in the steady state, is the angular momentum flux $\dot{J}$. It plays the role of an eigenvalue in the stationary equations, whose value has to be determined while solving the set of equations (Popham & Narayan 1995; Kley & Papaloizou 1997). In our model, the total angular momentum flux is composed of the angular momentum carried in with the accreting material, and the angular momentum transported by shear viscosity. Therefore, it is given as

$$\dot{J} = \dot{M}r^2\Omega + 2\pi r^2\sigma_{r\varphi}. \tag{23}$$

Usually, the angular momentum (AM) flux is displayed as the normalized, dimensionless j, which is $\dot{J}$ from Eq. (23) divided by the advective AM flux at the surface of the star, $\dot{J}_* = \dot{M}R_*^2\Omega_K(R_*)$. This value is shown in Fig. 10 for the $1\,M_\odot$ star. Again, good equilibrium states have been reached, since the deviations of j are very small. We also note the same trend as for the mass accretion rate: with increasing stellar mass and decreasing stellar rotation rate the deviations gain in strength. Since j is an eigenvalue in the stationary equations, it should be constant throughout the domain. For convenience, $\dot{M}$ is defined to be positive when mass is flowing to the center of the accretion disk and $\dot{J}$ is positive for inward-moving angular momentum (see Eq. (23)). Therefore, the net flux of angular momentum is directed inward and the absolute value is slightly above the advected angular momentum at the stellar surface and equals the accreted angular momentum of the star. The mean values of the normalized total angular momentum fluxes for $\omega = 0.0$ and $\omega = 0.8$ are given in Table 4, along with the numerical value of the corresponding $\dot{J}_*$ in cgs-units. These values of j correspond very nicely with those found by other numerical calculations, for example by Popham & Narayan (1995) who obtained a value of $j = 1.01$ for a $0.6\,M_\odot$ mass white dwarf with a radius
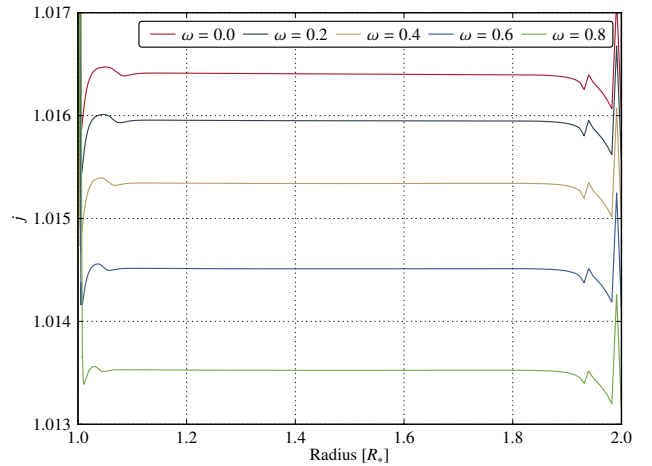
of 8.7×10^8 cm and a mass accretion rate $\dot{M} = 10^{-8}\,M_\odot$ yr^{-1}. Other deviations from the parameters used here are the usage of a different viscosity prescription and $\alpha = 0.1$. We have run a test calculation with their set of parameters and were able to reproduce j nearly perfectly.

The advected AM flux is pointing inward throughout the disk since the radial velocity u_r only attains negative values, that is, matter is only moving to the center of the disk. The transport of AM due to shear viscosity, on the other hand, changes its direction at the zero-gradient location, which is the radius where $\partial\Omega/\partial r = 0$ (and also the beginning of the BL, coming from the outside). Thus, in the disk, angular momentum is transported outward by the shear viscosity, while in the BL, it is transported inward. The sum of $\dot{J}_{\rm adv}$ and $\dot{J}_{\rm visc}$ remains constant. This means that in the disk, where $\dot{J}_{\rm visc} < 0$, the advected angular momentum flux must be greater than the total flux, $\dot{J}_{\rm adv} > \dot{J}$. In the BL, however, the viscous AM flux becomes positive and therefore $\dot{J}_{\rm adv} < \dot{J}$. At the inner boundary, $\dot{J}_{\rm adv}$ drops to nearly zero because u_r drops to nearly zero. Hence, $\dot{J}_{\rm visc}$ must be approximately equal to $\dot{J}$ although there is only very weak shearing. Here, $\nu\Sigma$ becomes very large, since the radial velocity is very small and the temperature is very high, which produces a high viscosity. If we compare the models with different stellar masses, we find that $\dot{J}_*$ gets smaller with increasing stellar mass (see Table 4). Two points affect the absolute value of $\dot{J}_*$ for different stellar masses. On the one hand, there is the mass-radius-relation of white dwarfs, meaning that with increasing mass, the stellar radius gets smaller. On the other hand, with increasing stellar mass, the Keplerian angular velocity also increases. Both effects together cause $\dot{J}_*$ to decrease only weakly with increasing stellar mass. The values of j also decrease with increasing stellar mass. While $\dot{J}_{\rm adv}$ gets slightly bigger with increasing stellar mass ($\dot{M}$ is equal for all models and equals the imposed value while the angular velocity increases), $\dot{J}_{\rm visc}$ also has to be larger to yield a smaller value of j. The reason for the increasing AM transport by viscosity is that the disk has a higher surface density and midplane temperature and thus a greater viscosity. We also observe a clear trend concerning the various values of j for different stellar rotation rates ω and constant stellar mass. With increasing stellar rotation rate Ω_*, j clearly decreases, as it also does with

Table 4. Normalized angular momentum flux j for three different stellar masses and two different stellar rotation rates.

Model	$j(\omega = 0.0)$	$j(\omega = 0.8)$	$\dot{J}_*$ [cm^2 g s^{-2}]
$M_* = 0.8\,M_\odot$	1.0187	1.0155	2.6088×10^{35}
$M_* = 1.0\,M_\odot$	1.0164	1.0135	2.5846×10^{35}
$M_* = 1.2\,M_\odot$	1.0140	1.0119	2.3915×10^{35}

Notes. The numbers shown are a constant fit to the results.

increasing stellar mass and constant rotation rate. Both trends were also found by Popham & Narayan (1995). From Eq. (23) we deduce that in the disk, $\dot{J}_{\text{adv}}$ must be nearly the same for every ω. In the BL, by contrast, it increases with higher stellar rotation rate since Ω does not drop as much. It is harder to make a reliable point concerning $\dot{J}_{\text{visc}}$. In the disk, however, both the midplane temperature and the density are slightly greater for increasing ω (see Figs. 3 and 4), yielding a higher viscosity and hence a greater $\dot{J}_{\text{visc}}$. This explains the smaller values of j in the disk. In the BL, however, the situation is not as clear, since the surface density increases with ω while the midplane temperature decreases.

4.4. Comparison with other BL models and equatorial radius increase

In this section we put our simulations in context with other work, that has been done in the field of BLs. As has been mentioned before, our results are closely related to those presented in Popham & Narayan (1995, hereafter PN95), at least qualitatively. However, the approach we took is quite different from this work. While Popham & Narayan have used the time-independent equations and performed stationary calculations, we have also propagated the physical quantities in time. Therefore, we are able to study time-dependent phenomena as well and we are not limited by the prerequisite that a stationary state exists for the given choice of parameters. Also, as we have seen in the last section, the BL is in permanent motion, even though most physical quantities do not change perceptibly. We have seen this by analysing the constant parameters $\dot{M}$ and j. Other differences involve the treatment of the radiation in the equations. While the authors of the quoted publication have taken care of the radiation field by adding an expression to the gas pressure, hence defining a total pressure, we have explicitly added the radiation force term in the momentum equation and a special pressure work term in the energy equation, both in the flux limited diffusion approximation. Although both approaches are identical in the optically thick limit, this is not necessarily the case for the optically thin and transition regions.

In order to compare our results quantitatively with the computations of Popham & Narayan (1995), we ran a set of simulations with the same parameters, the basis of which is their standard model. It is composed of a 0.6 $M_\odot$ white dwarf with a radius of 8.7×10^8 cm and a mass accretion rate of $\dot{M} = 10^{-8}\,M_\odot$/yr. The white dwarf does not rotate and they used a special viscosity prescription (see Eq. (19)) and a α-parameter of 0.1. For the standard model, we found a dynamical BL width of $\Delta r = 1.017\,R_*$, which is exactly the same as in PN95, and an AM flux of $j = 1.004$, as opposed to $j_{\text{PN95}} = 1.00994$. The dynamical quantities, viz. Ω and u_r, match the calculations of PN95 very closely ($\sim 1\%$). Only the peak value of the infall velocity deviates by about 10%. The peak position, on the other hand, is accurate to about 0.4%. The good agreement is also reflected

in the thermodynamical quantities, namely the disk and the surface temperatures T_c and T_{eff}. The second has a peak value in the BL of 227 000 K and about 54 000 K in the disk. Both temperatures agree to approximately one percent with the results of PN95. While the peak position of the midplane temperature T_c accurately matches that of PN95, our T_c as a whole is about 30% hotter. It is, however, T_{eff} that determines the emergent spectra of the BL and the disk, and since we find a very good match here, we conclude that our simulations are in very good agreement with the results of PN95.

Starting from the standard model described above, we performed the same Ω_* parameter study as in Popham & Narayan (1995). We have done this in particular to state an important point that has not been taken into account in the simulations shown above. Since the white dwarf flattens out considerably with increasing Ω_*, in principal we have to consider an equatorial radius increase. The radius of a rotating white dwarf in turn has to be calculated from stellar structure simulations. However, one finds (see e.g. Hachisu 1986) that for moderately rotating white dwarfs ($\omega \lesssim 0.8$), R_* increases at most by a factor of ~ 1.4. The change in stellar radius affects the effective temperature of the BL and the disk through Eq. (22), yielding slightly smaller values. This is in agreement with the standard solution for accretion disks, where the radius enters the effective temperature to the power $-3/4$. Because of the non-linear variation of gravity, the width of the BL also changes somewhat. Owing to the minor effect of the small radius increase and since the majority of white dwarfs are supposed to be slow rotators (Livio & Pringle 1998; Sion & Godon 2012), we have neglected this effect in the simulations above. Nevertheless, we want to illustrate the equatorial radius increase on the basis of the fastest rotating white dwarf in the aforementioned Ω_* study, which has a rotation rate in terms of the fraction of the breakup rotation rate of $\omega = 0.86$.

The width of the dynamical BL changes from $\Delta r \approx 1.018\,R_*$ for the model with equatorial radius increase (M1, $R_* \approx 1.25 \times 10^9$ cm) to $\Delta r \approx 1.017\,R_*$ for the model without an increase in radius (M2), i.e. $R_* = 8.7 \times 10^8$ cm. This is a variation of about one per mill. The difference concerning the normalized AM flux j between both models is even smaller, where $j_{\text{M1}} = 1.0038$ and $j_{\text{M2}} = 1.0033$. The agreement of the angular velocities is very good, as can be seen from the width of the BL. The radial velocities of both models do match each other very closely, as well. However, the absolute peak value of M2 is about 15% greater than that of M1. If instead we compare the Mach numbers, the deviation shrinks to about 1%, but the differing radii manifest themselves more obviously in the disk and effective temperature of the models. Thus, the disk temperature T_c of model M2 is about 30% higher throughout the whole domain which comes to approximately 40 000 K. This is due to the greater gravitational pull for smaller radii. We also find the same 30% deviation in the surface temperature T_{eff}, although here it accounts for only 13 000 K because of the lower temperature regime of the surface temperature. Apart from this vertical shift, both graphs are identical, meaning that the peak is at the same location and the thermal BL has the same radial extent. Model M1 peaks at $\sim 65\,000$ K in the BL.

Godon et al. (1995) used a time-dependent spectral numerical code and performed one-dimensional calculations of the BL that are closely related to ours. The aim of their simulations was to investigate the influence of the thermal inner boundary condition, which can lead to both cool and hot BLs, depending on whether the temperature is held fixed at the inner boundary or the flux of the star is fed into the computational domain. We have performed a simulation for the case of flux BC with the

same parameter choice as in Godon et al. (1995), their model 3, and were able to reproduce the results very closely.

4.5. Simulations with larger domain

For the Navier-Stokes equations it is still uncertain whether the same solution is reached for a small, bounded domain as for an unbounded domain. Of course, we cannot simulate our problem on an unbounded domain. We can, however, prove that the solution we presented above does not depend on the choice of the domain. In order to do this, we ran a test simulation, where we enlarged the computational domain by a factor of 10, so that it reaches from $r = 1 R_*$ up to $r = 10 R_*$. Except for the number of grid cells, all parameters were chosen according to the $0.8 M_\odot, 0.4 \Omega_K$ model. We find a nearly perfect agreement between the models with the small and the large domain. Differences are, apart from the boundaries, nearly imperceptible, except for the disk temperature, where the larger domain overestimates the peak temperature in the BL by approximately 5%. This is, however, due to the lower resolution of the model in this region.

Finally, to show the agreement of our models with the standard solution for accretion disks by Shakura & Sunyaev (1973), we compare our results with the analytically derived formulae for thin accretion disks. Since these equations are supposed to be a good approximation in the disk, we used the model with the large domain for the comparison, so that we could also compare both solutions in the disk over a farther region. The equations of a Shakura-Sunyaev-type solution can, for example, be found in Frank et al. (2002). In these equations, we have modified the typical factor $[1-(R_*/R)^{1/2}]$ by a factor of the form $[1-j(R_*/R)^{1/2}]$, where j is the normalized angular momentum flux. The solution cuts off not at R_*, but a little farther outside ($\sim 1.02 R_*$). We find that the S-S-type solution provides a very good approximation of the physical variables in the disk. In the BL the standard solution is insufficient. We also find that the surface temperature of our simulation peaks at $r = 1.4092 R_*$ in the disk (there is also a far more distinct peak in the BL). The S-S standard solution for the surface temperature reads

$$T(r) = \left\{ \frac{3GM_*\dot{M}}{8\pi r^3 \sigma_{SB}} \left[1 - j \left(\frac{R_*}{r} \right)^{1/2} \right] \right\}^{1/4} . \qquad (24)$$

If we plug $j = 1.0175$ into Eq. (24), which is the normalized angular momentum flux for this simulation, we find that the above function $T(r)$ has a maximum at $r \approx 1.4093$. Thus, our simulation is in perfect agreement with the theoretically derived formula. The temperature in Eq. (24) peaks at a value of $T_{max} \approx 0.475 T_*$, where T_* is defined by $T_* = \left(\frac{3GM_*\dot{M}}{8\pi R_*^3 \sigma_{SB}} \right)^{1/4}$. According to (24), for our model this means that the temperature peaks at $T_{max} = 74\,406$ K. The simulation shows a temperature of $T = 74\,335$ K of the peak of the surface temperature in the disk. Again, this is in perfect agreement with the theoretical value. Having matched the other quantities of our simulations against the S-S standard solution as well, we come to the conclusion that outside the BL, our simulations are perfectly described by the standard solution.

5. Summary and conclusion

We have presented new models of the structure of the BL around white dwarfs in compact binary star systems. One-dimensional, time dependent radial models have been constructed which include radiative diffusion in the radial direction, vertical cooling from the disk surfaces, and radiative pressure effects.

For a fixed mass accretion rate of $\dot{M} = 1.51 \times 10^{-8} M_\odot/$yr, which corresponds to systems in outburst, we have analysed the BL for different masses and rotation rates of the white dwarf.

The strong shear in the BL region leads to an enormous energy release and to surface temperatures of a few hundred thousand Kelvin. For a non-rotating white dwarf (with $1 M_\odot$) the maximum temperature is about $500\,000$ K, while for a star rotating with $\omega = 0.8$ of the break-up velocity the maximum is about $200\,000$ K. Hence, knowledge of the white dwarf mass, for example through a dynamical mass estimate of the binary star, and of the mass accretion rate, allows an estimate of the stellar rotation rate through the observed peak temperatures. Radial diffusion of energy leads to a more extended thermal BL with a width of typically 0.02 to 0.05 R_*. The models for slow rotation showed a tendency for instability due to the very high temperatures, small vertical thicknesses, and resulting low optical depths.

For the viscosity we use the α-parametrisation with $\alpha = 0.01$. For this value, the radial velocity remains subsonic throughout with maximum radial Mach numbers of 0.35 for $\omega = 0$ and 0.18 for $\omega = 0.8$. A higher value of $\alpha = 0.1$ left the disk structure unchanged and Mach numbers close to unity within the BL.

Varying the stellar mass leads to hotter BL for larger masses (and smaller radii) and cooler BL for smaller masses. Hence, when trying to infer stellar parameter through an analysis of the BL radiation one is faced with an ambiguity that models with different combinations of R_* and ω_* may yield similar peak temperatures. There is the indication, however, that the width of the thermal BL is different in these cases, such that the model spectra will lead to different results. In this paper we did not calculate synthetic, theoretical spectra for our numerical models, but leave that for a future paper.

The validity of our simulations has been demonstrated convincingly by comparing the results with related calculations and with the standard solution for thin accretion disks by Shakura & Sunyaev (1973). We found very good agreement with our results, both in the disk where the standard solutions holds true, and in the BL, where we were able to reproduce basic features shown in other works and match their results to an accuracy of about one percent for the dynamical and observed quantities. We also showed that our results are independent of the computational domain and the resolution. Simulations that have the same parameters, except for the simulation area, do match each other perfectly.

An equatorial radius increase due to a flattening of a fast rotating white dwarf in our simulations showed the following results. Even for the unlikely case of a rotation rate of 86% of the breakup rotation rate, the variation of the physical quantities that differ most is in the range of 30%, according to whether we take the flattening into account or not. The width of the thermal BL, which is also important for the emergent spectra, does not change perceptibly, however. For a $0.6 M_\odot$ white dwarf, the shift in the effective temperature is of the order of $10\,000$ K.

Analysing the data of our simulations, we also found that the consideration of radiation energy is indeed necessary in our models. We see this from the radiation pressure $P_{rad} = aT^4/3$, which becomes comparable to the thermal pressure P in the BL and even exceeds it by a factor of the order of unity for a small radial extent. If P_{rad} is not taken into account in the simulations, the effective temperature peaks at far higher temperatures and

the width of the thermal BL is distinctly smaller because of the lack of the widening effect of $P_{\rm rad}$.

Owing to the slim disk approximation, our models do not allow us to answer the question of how the material settles onto the central white dwarf. This question can only be answered by two dimensional r-z simulations, similar to those by Balsara et al. (2009) but with radiative transport (Kley 1991). The strong shear in the BL can lead to unstable behaviour when considering the φ-direction, as described by Belyaev et al. (2012) for isothermal disks. This behaviour could not be found in our simulations as they are purely radial. The next step would be to extend these to two-dimensional r-φ disks.

References

Abramowicz, M., Brandenburg, A., & Lasota, J.-P. 1996, MNRAS, 281, L21
Armitage, P. J. 2002, MNRAS, 330, 895
Babkovskaia, N., Brandenburg, A., & Poutanen, J. 2008, MNRAS, 386, 1038
Balbus, S. A. 2003, ARA&A, 41, 555
Balbus, S. A., & Hawley, J. F. 1991, ApJ, 376, 214
Balbus, S. A., & Hawley, J. F. 1998, Rev. Mod. Phys., 70, 1
Balbus, S. A., & Lesaffre, P. 2008, New Astron. Rev., 51, 814
Balsara, D. S., Fisker, J. L., Godon, P., & Sion, E. M. 2009, ApJ, 702, 1536
Belyaev, M. A., Rafikov, R. R., & Stone, J. M. 2012, ApJ, 760, 22
Bertout, C., & Regev, O. 1992, ApJ, 399, L163
Commerçon, B., Teyssier, R., Audit, E., Hennebelle, P., & Chabrier, G. 2011, A&A, 529, A35
Cordova, F. A., & Mason, K. O. 1984, MNRAS, 206, 879
Cordova, F. A., Nugent, J. J., Klein, S. R., & Garmire, G. P. 1980, MNRAS, 190, 87
Cordova, F. A., Jensen, K. A., & Nugent, J. J. 1981a, MNRAS, 196, 1
Cordova, F. A., Mason, K. O., & Nelson, J. E. 1981b, ApJ, 245, 609
Courant, R., Friedrichs, K., & Lewy, H. 1928, Math. Ann., 100, 32
Ferland, G. J., Pepper, G. H., Langer, S. H., et al. 1982, ApJ, 262, L53
Fisker, J. L., & Balsara, D. S. 2005, ApJ, 635, L69
Fisker, J. L., Balsara, D. S., & Burger, T. 2006, New Astron. Rev., 50, 509
Flaig, M., Kley, W., & Kissmann, R. 2010, MNRAS, 409, 1297
Frank, J., King, A., & Raine, D. 2002, Accretion Power in Astrophysics (Cambridge University Press)
Godon, P. 1995, MNRAS, 277, 157
Godon, P., Regev, O., & Shaviv, G. 1995, MNRAS, 275, 1093
Hachisu, I. 1986, ApJS, 61, 479
Hawley, J. F., Smarr, L. L., & Wilson, J. R. 1984, ApJS, 55, 211
Hubeny, I. 1990, ApJ, 351, 632
Inogamov, N. A., & Sunyaev, R. A. 1999, Ast. Lett., 25, 269
Inogamov, N. A., & Sunyaev, R. A. 2010, Astron. Lett., 36, 848
Kato, S., & Inagaki, S. 1994, PASJ, 46, 289
King, A. R., & Shaviv, G. 1984, Nature, 308, 519
Kley, W. 1989a, A&A, 208, 98
Kley, W. 1989b, A&A, 222, 141
Kley, W. 1991, A&A, 247, 95
Kley, W., & Crida, A. 2008, A&A, 487, L9
Kley, W., & Hensler, G. 1987, A&A, 172, 124
Kley, W., & Lin, D. N. C. 1996, ApJ, 461, 933
Kley, W., & Lin, D. N. C. 1999, ApJ, 518, 833
Kley, W., & Papaloizou, J. C. B. 1997, MNRAS, 285, 239
Krumholz, M. R., Klein, R. I., McKee, C. F., & Bolstad, J. 2007, ApJ, 667, 626
Kuiper, R., Klahr, H., Dullemond, C., Kley, W., & Henning, T. 2010, A&A, 511, A81
Küker, M., Henning, T., & Rüdiger, G. 2003, ApJ, 589, 397
Levermore, C. D. 1984, J. Quant. Spectr. Rad. Transf., 31, 149
Levermore, C. D., & Pomraning, G. C. 1981, ApJ, 248, 321
Livio, M., & Pringle, J. E. 1998, ApJ, 505, 339
Lynden-Bell, D., & Pringle, J. E. 1974, MNRAS, 168, 603
Mauche, C. W. 2004, in Rev. Mex. Astron. Astrofis. Conf. Ser. 20, eds. G. Tovmassian, & E. Sion, 174
Meyer, F., & Meyer-Hofmeister, E. 1982, A&A, 106, 34
Mukai, K., & Patterson, J. 2004, in Rev. Mex. Astron. Astrofis. Conf. Ser. 20, eds. G. Tovmassian, & E. Sion, 244
Narayan, R. 1992, ApJ, 394, 261
Narayan, R., & Popham, R. 1993, Nature, 362, 820
Narayan, R., Loeb, A., & Kumar, P. 1994, ApJ, 431, 359
Nauenberg, M. 1972, ApJ, 175, 417
Pandel, D., Córdova, F. A., & Howell, S. B. 2003, MNRAS, 346, 1231
Pandel, D., Córdova, F. A., Mason, K. O., & Priedhorsky, W. C. 2005, ApJ, 626, 396
Papaloizou, J., & Szuszkiewicz, E. 1994, MNRAS, 268, 29
Papaloizou, J. C. B., & Stanley, G. Q. G. 1986, MNRAS, 220, 593
Pessah, M. E., & Chan, C.-k. 2012, ApJ, 751, 48
Piro, A. L., & Bildsten, L. 2004a, ApJ, 616, L155
Piro, A. L., & Bildsten, L. 2004b, ApJ, 610, 977
Popham, R. 1999, MNRAS, 308, 979
Popham, R., & Narayan, R. 1995, ApJ, 442, 337
Pringle, J. E. 1977, MNRAS, 178, 195
Pringle, J. E. 1981, ARA&A, 19, 137
Pringle, J. E., & Savonije, G. J. 1979, MNRAS, 187, 777
Regev, O. 1983, A&A, 126, 146
Regev, O., & Bertout, C. 1995, MNRAS, 272, 71
Robertson, J. A., & Frank, J. 1986, MNRAS, 221, 279
Romanova, M. M., Ustyugova, G. V., Koldoba, A. V., & Lovelace, R. V. E. 2012, MNRAS, 421, 63
Rybicki, G. B., & Lightman, A. P. 1986, Radiative Processes in Astrophysics (Wiley)
Shakura, N. I., & Sunyaev, R. A. 1973, A&A, 24, 337
Shaviv, G. 1987, Ap&SS, 130, 303
Sion, E. M., & Godon, P. 2012, Mem. Soc. Astron. It., 83, 539
Sion, E. M., Godon, P., Myzcka, J., & Blair, W. P. 2010, ApJ, 716, L157
Stone, J. M., & Norman, M. L. 1992, ApJS, 80, 753
Suleimanov, V., & Poutanen, J. 2006, MNRAS, 369, 2036
Suleymanov, V. F. 1992, Sov. Astron. Lett., 18, 104
Syunyaev, R. A., & Shakura, N. I. 1986, Sov. Astron. Lett., 12, 117
Tscharnuter, W. M., & Winkler, K.-H. A. 1979, Comput. Phys. Commun., 18, 171
Tylenda, R. 1977, Acta Astron., 27, 235
Tylenda, R. 1981, Acta Astron., 31, 267
Verbunt, F. 1982, Space Sci. Rev., 32, 379
Warner, B. 1987, MNRAS, 227, 23

**Astronomy
&
Astrophysics**

Modeling the EUV spectra of optically thick boundary layers of dwarf novae in outburst

V. Suleimanov[1,2], M. Hertfelder[1], K. Werner[1], and W. Kley[1]

[1] Institut für Astronomie und Astrophysik, Kepler Center for Astro and Particle Physics, Universität Tübingen, Sand 1,
72076 Tübingen, Germany
e-mail: suleimanov@astro.uni-tuebingen.de
[2] Kazan (Volga region) Federal University, Kremlevskaja str. 18, 420008 Kazan, Russia

ABSTRACT

Context. Disk accretion onto weakly magnetized white dwarfs (WDs) in cataclysmic variables (CVs) leads to the formation of a boundary layer (BL) between the accretion disk and the WD, where the accreted matter loses its excess kinetic energy and angular momentum. It is assumed that angular momentum is effectively transported in the BL, but the transport mechanism is still unknown.
Aims. Here we compute detailed model spectra of recently published optically thick one-dimensional radial BL models and qualitatively compare them with observed soft X-ray/extreme ultraviolet (EUV) spectra of dwarf novae in outburst.
Methods. Every considered BL model with given effective temperature and surface density radial distribution is divided into a number of rings, and for each ring, a structure model along the vertical direction is computed using the stellar-atmosphere method. The ring spectra are then combined into a BL spectrum taking Doppler broadening and limb darkening into account.
Results. Two sets of model BL spectra are computed, the first of them consists of BL models with fixed WD mass (1 $M_\odot$) and various relative WD angular velocities (0.2, 0.4, 0.6 and 0.8 break-up velocities), while the other deals with a fixed relative angular velocity (0.8 break-up velocity) and various WD masses (0.8, 1, and 1.2 $M_\odot$). The model spectra show broad absorption features because of blending of numerous absorption lines, and emission-like features at spectral regions with only a few strong absorption lines. The model spectra are very similar to observed soft X-ray/EUV spectra of SS Cyg and U Gem in outburst. The observed SS Cyg spectrum could be fitted by BL model spectra with WD masses 0.8−1 $M_\odot$ and relative angular velocities 0.6−0.8 break up velocities. These BL models also reproduce the observed ratio of BL luminosity and disk luminosity. The difference between the observed and the BL model spectra is similar to a hot optically thin plasma spectrum and could be associated with the spectrum of outflowing plasma with a mass loss rate compatible with the BL mass accretion rate.
Conclusions. The suggested method of computing BL spectra seems very promising and can be applied to other BL models for comparison with EUV spectra of dwarf novae in outburst.

Key words. accretion, accretion disks – stars: dwarf novae – radiative transfer – methods: numerical – X-rays: binaries

1. Introduction

The importance of energy release between an accretion disk and a central object with a surface was realized almost immediately (Lynden-Bell & Pringle 1974) after the introduction of modern accretion disk theory (Shakura & Sunyaev 1973). Later a similar one-dimensional (1D) boundary-layer (BL) theory was developed (Pringle 1977; Pringle & Savonije 1979; Tylenda 1981; Regev 1983; Bertout & Regev 1992; Regev & Bertout 1995; Godon et al. 1995; Popham & Narayan 1995). Here we mainly consider BLs around white dwarfs (cataclysmic variable stars (CVs), see review in Warner 2003) and describe a few key points of BL theory.

Depending on the accretion rate, $\dot{M}$, a BL can be optically thin ($\dot{M} < 10^{16}$ g s^{-1}) or optically thick ($\dot{M} > 10^{16}$ g s^{-1}) (Pringle & Savonije 1979). The BL optical thickness also depends on the mass and angular velocity of the white dwarf (WD), as well as on the value of turbulent viscosity in the BL (Popham & Narayan 1995; Collins et al. 2000a). For the description of optically thick BLs, two qualitatively different approaches were suggested, which reduced the problem to a 1D model. In the first approach, the BL is considered as the inner part of the

1D axi-symmetric accretion disk (Pringle & Savonije 1979; Regev 1983; Popham & Narayan 1995) with no vertical component of the velocity. The condition imposed on the BL at the inner boundary is that it rotates at the stellar equatorial velocity. Therefore, the accreting matter has to decelerate and release its excess energy in a relatively narrow (a few percent of the inner disk radius) ring. Most of this energy is radiated away, but part of it can be advected into the WD (Popham 1997; Godon 1997), deposited to the outflow (Mauche & Raymond 2000), and can accelerate the outer layers of the WD forming a fast rotating belt (Long et al. 2006). In contrast, in the second approach, the matter keeps its nearly Keplerian velocity at the central object's equator and spreads over the surface (Inogamov & Sunyaev 1999). The spreading matter loses its kinetic energy gradually due to friction with the more slowly rotating surface of the central star and radiates the released energy mainly in two bright high-latitude belts. Initially the spreading layer model was developed for BLs around neutron stars (Inogamov & Sunyaev 1999), but later it was extended to the WD case, too (Piro & Bildsten 2004b).

Together with the difference in geometry, the description of the viscosity, which provides a strong coupling of rings of matter

moving with different velocities and an effective thermal dissipation of the lost energy, is different in both approaches. In the first model the usual α prescription for accretion disks is used, which means that the $r\varphi$-component of the viscosity stress tensor is parameterized by the total pressure P at a given point as $w_{r\varphi} = \alpha P$ (Shakura & Sunyaev 1973) or, almost equivalently, a similar parametrization of kinematic viscosity, ν_α, is used. In the second approach the α viscosity is completely ignored and only the friction between the high-velocity spreading matter and the dense and relatively cool stellar envelope is considered. The corresponding component of the specific frictional force, $f_{sl} = \alpha_b \rho_b v_{sl}^2$, is again scaled using the matter density at the bottom of the spreading layer, ρ_b, and the relative spreading matter velocity, v_{sl} (Inogamov & Sunyaev 1999). The estimated value of α_b is relatively low, about 10^{-3} (Inogamov & Sunyaev 1999). Detailed consideration of this problem shows that the matter deceleration due to friction with the underlying stellar envelope is not trivial and has to be investigated more carefully (Inogamov & Sunyaev 2010).

It is clear from both viscosity descriptions that we do not know the physics of kinetic energy loss and angular momentum transfer in BLs (see, e.g., Kato & Inagaki 1994; Narayan et al. 1994; Godon 1995a). The magneto-rotational instability (MRI; Velikhov 1959; Chandrasekhar 1960; Balbus & Hawley 1991), which is usually considered as a physical realization of the α viscosity, cannot operate in the case of angular velocity decrease taking place in BLs (Godon 1995a). Recently, Belyaev & Rafikov (2012) and Belyaev et al. (2012, 2013) have suggested a new physical model for an angular momentum transport in BLs based on acoustic instabilities. Various hydrodynamical instabilities, beginning with simple shear instabilities (Kippenhahn & Thomas 1978), were also considered before as a way of angular momentum transport (see the review in Belyaev & Rafikov 2012).

Another important feature of BLs is their 3D nature. A full 3D treatment is important to account for a correct turbulent viscosity description. But BL models that use a parametrization of the turbulent viscosity could be considered as axisymmetric 2D models. The first attempts to describe the BL around the WD using a 2D time-dependent hydrodynamical approach were performed many years ago (Robertson & Frank 1986; Kley & Hensler 1987; Kley 1989). The importance of the viscosity prescription was also demonstrated (Kley 1991). Recently, this kind of computation was repeated with higher, albeit insufficient temporal and spatial resolution without (Fisker & Balsara 2005) and with rudimentary radiation treatment (Balsara et al. 2009). These investigations have confirmed that matter is spreading over the WD surface for optically thick BLs.

Astrophysical observations give the possibility to constrain the correct description of angular moment transport and energy dissipation in BLs. It is necessary to compare properties of a mature BL model with observed features. There are two ways for this kind of comparison. The first one is to investigate flux variability, which is probably connected with BLs, using a noise power spectrum approach, for instance van der Klis (1989). There are a lot of observational data about rapid flux variability in low-mass X-ray binaries (LMXBs), such as quasi-periodic oscillations (QPOs) and power density spectra (van der Klis 2000). The cumulative data about rapid variability of CVs, especially in the optical band, is even larger (see, e.g., Patterson 1981; Warner 1986, 2003; Warner & Pretorius 2008, and references therein). Two types of rapid oscillations were distinguished (Robinson & Nather 1979), namely high-degree coherent oscillations with relatively short periods ($\sim 7-70$ s) in dwarf

nova outbursts (DNOs), and less coherent quasi-periodical oscillations (QPOs) with longer periods (up to tens of minutes). The amplitudes of variability for both DNOs and QPOs are relatively low in the optical band (<0.01 mag). On the other hand, the amplitude of these oscillations in X-rays can be much greater (tens of percent, Cordova et al. 1984; Jones & Watson 1992). It is interesting that the coherent oscillations in SS Cyg are observed in soft X-rays, but not in hard X-rays (Swank 1979; Jones & Watson 1992). This fact supports the hypothesis that the coherent oscillations might be connected with an optically thick BL that could be responsible for the soft X-ray radiation of SS Cyg during outburst. There are a few relatively simple models to explain DNOs and QPOs (see, e.g., Popham 1999; Warner & Woudt 2002; Piro & Bildsten 2004a; Godon 1995b; Collins et al. 1998, 2000b), and part of them are connected with the existing BL models.

The second way is a comparison of observed emergent spectra of close binary systems with predicted spectra of accretion disks and BLs. Emergent spectra could be computed for BL models with the simple local α-viscosity, because those models consider energy release and predict some bolometric radiation flux distribution over the BL. BL model spectra in blackbody approximation were computed by many authors (see, e.g. Tylenda 1977; Kley 1991; Popham & Narayan 1995). The contribution of BL radiation to the FUV spectra of some CVs was also taken into account by computing models of BL rings using the stellar-atmosphere method (Godon & Sion 2011; Godon et al. 2012).

Luminous LMXBs (with $L > 0.05-0.1\,L_{Edd}$ with neutron stars show relatively soft and wide X-ray spectra, which can be represented to first approximation by two blackbodies with temperatures kT about 1 keV and 2.5 keV (Mitsuda et al. 1984). It is possible to assume that the first component corresponds to the accretion disk, and the second one corresponds to the BL. Study of X-ray variability helped to distinguish between these two components (Gilfanov et al. 2003; Revnivtsev & Gilfanov 2006). These authors extracted the spectra of the strongly variable component of the observed X-ray flux in a few LMXBs and found that they are very similar for all the investigated sources and that they can be described by a comptonized plasma spectrum with $kT \approx 2.4$ keV and electron scattering optical depth $\tau_e \approx 5-7$. They connected these high-variability components of the X-ray flux to the BL emission. The spectra of these components were described by model spectra of spreading layers (Suleimanov & Poutanen 2006). Another reference to the validity of the hypothesis that the BLs around neutron stars are spreading layers was presented by Revnivtsev et al. (2013). The high-variability spectral component of the X-ray transient source XTE J1701-462 keeps the same spectral shape when the bolometric luminosity varies by a factor of twenty. The maximum temperature of this component (Wien tail color temperature) is about $2.4-2.6$ keV and coincides with the maximum color temperature of the type I X-ray bursts of the same source. It is believed that the latest color temperature of a burst corresponds to the Eddington luminosity (see, e.g., review Lewin et al. 1993). Therefore, most probably, the BLs in LMXBs consist of a part of the neutron star surface that radiates at the Eddington limit with the emitting area being proportional to the luminosity, as it was predicted by the spreading layer model (Inogamov & Sunyaev 1999).

X-ray and extreme ultraviolet (EUV) radiation of CVs, which can be associated with BL emission, is much more diverse and a univocal interpretation is difficult (see, e.g., Patterson & Raymond 1985a,b). Blackbody approximation of the optically

thick BL model spectra predicts a luminous soft X-ray/EUV component with temperature 200−500 kK (Pringle & Savonije 1979; Popham & Narayan 1995; Collins et al. 2000a; Piro & Bildsten 2004b; Hertfelder et al. 2013) in the spectra of all high mass-accretion rate CVs without significant magnetic field (dwarf novae in outburst and nova-like stars). In fact, only a few of them have this kind of component in their spectra, e.g. SS Cyg and U Gem in outburst (Cordova et al. 1984). The X-ray spectra of other non-magnetic CVs are rather hard (van Teeseling & Verbunt 1994; van Teeseling et al. 1996) and can be described by the model of a cooling flow with temperatures kT from a few keV up to tens of keV (Done et al. 1995; Mukai et al. 2003; Baskill et al. 2005). This kind of radiation is natural for optically thin BLs (Pringle & Savonije 1979), or even for the inner hot accretion flow (Revnivtsev et al. 2012) to be expected for dwarf novae in quiescence, but requires some non-trivial explanation for high mass-accreting CVs, like V603 Aql (see, e.g. Patterson & Raymond 1985b). Formally, Popham & Narayan (1995) have found that the transition to the optically thin regime in the model BLs could be reached at sufficiently high mass accretion rates. But their results are questionable because they underestimated the Rosseland "true" opacity by at least two orders of magnitude, using Kramers opacity $k_{kr} = k_0 \rho T^{-3.5}$ cm^2 g^{-1} with $k_0 = 6.6 \times 10^{22}$. The more realistic coefficient is much larger, $k_0 = 5 \times 10^{24}$ (Frank et al. 2002).

At present time, soft X-ray/EUV components were found in four dwarf novae in (super-) outbursts: SS Cyg (Cordova et al. 1980a, 1984; Mauche et al. 1995; Mauche 2004), U Gem (Cordova et al. 1980b, 1984; Long et al. 1996), VW Hyi (Mauche 1996), and OY Car (Mauche & Raymond 2000). The high-inclination system OY Car shows mainly broad emission lines arising due to resonance scattering in the strong disk wind (Mauche & Raymond 2000). The high-resolution spectra of the other CVs, obtained by *EUVE* and *Chandra* observations, show numerous broad absorption- and emission-like details. These spectra are similar to soft X-ray spectra of supersoft X-ray sources (Lanz et al. 2005; Rauch et al. 2010) and also have to be modeled using stellar model-atmosphere methods. The first attempt to fit the soft X-ray spectrum of SS Cyg in outburst (Mauche 2004) by hot LTE model-atmosphere spectra showed the potential for success of this approach (Suleimanov et al. 2013).

With the work at hand, we start to model the various BL models using the stellar-atmosphere method and a comparison of the results with the properties of observed soft X-ray/EUV spectra of CVs mentioned above. Here we present the model spectra of particular 1D hydrodynamic BL models that were computed recently by Hertfelder et al. (2013).

2. Method

Our work is based on the 1D models of BLs between optically thick accretion disks and WDs that were computed in our previous work (Hertfelder et al. 2013). Models are considered in a cylindrical coordinate system (z, φ, R), being axisymmetric (independent of φ) and vertically averaged (over z-coordinate). They were computed for a fixed mass-accretion rate $\dot{M} = 1.5 \times 10^{-8}$ $M_\odot$ yr^{-1}, three different values of WD mass, $M_{WD} = 0.8$, 1, and 1.2 $M_\odot$, and five values of WD angular velocity, $\omega_{WD} = 0$, 0.2, 0.4, 0.6 and 0.8 ω_K, where ω_K is the Kepler angular velocity $\omega_K^2 = GM_{WD}/R^3$ at the WD radius R_{WD}. WD radii were calculated using the Nauenberg (1972) relation. An increase of equatorial radii due to rotation was ignored. A simple α prescription for the viscosity ν_α

was used according to Shakura & Sunyaev (1973), see details in Hertfelder et al. (2013):

$$\nu_\alpha = \alpha a^2 \omega_K^{-1}, \tag{1}$$

where a is the sound speed. We note that ω_K is taken for the current BL radius, however, the radial extension of model BLs is low and ω_K for a given model is almost constant. A relatively low value of the α parameter ($\alpha = 0.01$) is assumed for all models in order to avoid supersonic radial motions.

For every 1D model we consider the distribution of the following physical parameters along the radial coordinate R: effective temperature $T_{eff}(R)$ (or, equivalently, the total radiated flux $F_0(R)$), surface density $\Sigma_0(R)$, BL half-thickness $H_0(R)$, and rotation velocity $v_\varphi(R)$. The following steps have to be performed to compute the model emergent spectrum:

- Divide the BL model in a number of rings with equal luminosity.
- Compute a gray model for each ring along the vertical coordinate z.
- Starting from the gray model, compute a model of the each ring using model atmosphere methods together with the local emergent spectrum.
- Sum up the local spectra to a total BL spectrum taking the rotation of the rings into account.

This approach is almost identical to the one that was used for the computation of CV accretion disk spectra by many authors (Kriz & Hubeny 1986; Shaviv & Wehrse 1991; Suleymanov 1992; Wade & Hubeny 1998; Nagel et al. 2004). We understand that the local 1D method assumed here is rather crude. But we believe that it gives a reasonable first approximation, which is applicable to comparison with observations. This method is a first step to more sophisticated 2D models.

Accretion disk and BL in the 1D models presented by Hertfelder et al. (2013) are considered as a comprehensive structure, and the boundary between accretion disk and BL is blurred. However, the $T_{eff}(R)$ distributions have a local minimum at $R \approx 1.1 R_{WD}$. We adopted that radius as the boundary between the disk and the BL and studied the BLs at radii lesser than this boundary. We divided each BL model into a few (5−20) rings, and the particular radius R_j of a given ring with number j, for which a local vertical structure and local emergent spectrum are computed, is determined by the condition

$$F_0(R_j)\Delta R_j = F_0(R_j)(R_j^U - R_j^L) = \int_{R_j^L}^{R_j^U} F_0(R)\, dR, \tag{2}$$

where R_j^U and R_j^L are the radii of the upper and lower ring boundaries, respectively. We note that $R_{j-1}^U = R_j^L$.

We now describe the other steps of our method in more detail.

2.1. BL vertical structure. Gray atmosphere approach

The approach employed here is based on the numerical method used for modeling of accretion disk structures over the z coordinate as presented by Suleimanov et al. (2007 – see also Kriz & Hubeny 1986; Shaviv & Wehrse 1991; Suleymanov 1992; Wade & Hubeny 1998; Nagel et al. 2004). Some modifications are made and described additionally.

The vertical structure of each BL ring at radius R_j is determined by the ring parameters T_{eff}, Σ_0, H_0, and a set of differential

equations. The first one is the hydrostatic equilibrium equation

$$\frac{1}{\rho}\frac{dP}{dz'} = g_z = \frac{(z_1 - z')}{(1 + (z_1 - z')^2/R_j^2)^{1/2}}\,\omega_K^2(R_j),\tag{3}$$

where $P = P_g + P_{rad}$ is the total pressure, the sum of gas and radiation pressure, ρ is the matter density, z_1 is a parameter, the distance from the mid-plane to the highest point of the vertical model, and $z' = z_1 - z$ is the vertical coordinate, which is equal 0 at the highest point of the model.

The second equation is the energy-conservation law. The correct local energy generation rate dF/dz in accretion disks as well as in BLs is not known and a local version of the α approach is often used (see e.g. Suleimanov et al. 2007). Fortunately, local emergent spectra of optically thick accretion disks (and, therefore, the BL models considered here, too) are weakly dependent on details of the energy generation rate, so we took the simplest version (Shakura & Sunyaev 1973):

$$\frac{1}{\rho}\frac{dF}{dz'} = -2\frac{F_0}{\Sigma_0}.\tag{4}$$

Here F is the integral (bolometric) vertical flux at given height, $F_0 = \sigma_{SB}T_{eff}^4$, is the emergent integral flux. The energy conservation law has the integral (Shakura & Sunyaev 1973)

$$F(m) = F_0\left(1 - \frac{2m}{\Sigma_0}\right),\tag{5}$$

where the boundary condition $F(m = 0) = F_0$ is used. Here the Lagrangian coordinate m is determined by the equation

$$dm = \rho\,dz',\tag{6}$$

and, therefore,

$$\Sigma_0 = \int_{-\infty}^{+\infty} dm \approx 2\int_0^{z_1} \rho\,dz'.\tag{7}$$

We assumed a purely radiative transport of energy in z-direction, therefore, the third equation is the radiation transfer equation. For the gray approach we use the first moment of that equation

$$\frac{1}{\rho}\frac{dP_{rad}}{dz'} = \frac{\kappa_R F}{c},\tag{8}$$

where κ_R is the Rosseland opacity, which is determined as the greater value of electron scattering, $\sigma_e = 0.335$ cm^2 g^{-1}, and Kramers opacity, $\kappa_{kr} = 5 \times 10^{24}\rho T^{-3.5}$. The sum of these values is also relevant (Popham & Narayan 1995).

These equations are solved together with the ideal gas law

$$P_g = nkT,\tag{9}$$

where n is the total number density of particles. We assume full local thermodynamic equilibrium (LTE). Therefore, the local gas temperature T can be found from the integrated (over frequency) mean intensity J

$$J = \frac{3c\,P_{rad}}{4\pi} = B(T) = \frac{\sigma_{SB}T^4}{\pi}.\tag{10}$$

Here we used the following TE relations between radiation energy density ε_{rad}, integral mean intensity J, and radiation pressure:
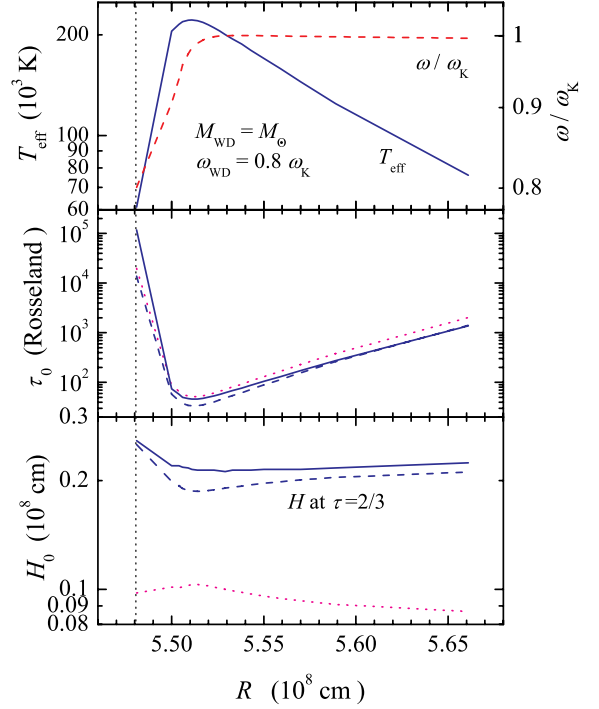
$$\varepsilon_{rad} = \frac{4\pi J}{c} = 3P_{rad}.\tag{11}$$

Fig. 1. Distribution of BL quantities along radius. The data are from the model with $M_{WD} = M_\odot$ and $\omega_{WD} = 0.8\,\omega_K$. The position of the WD surface at $R_{WD} = 5.48 \times 10^8$ cm is shown by the vertical dotted line. *Top panel*: shown is the effective temperature (solid curve) together with the relative angular velocity (dashed curve), as obtained from the 1D hydrodynamical model. These are the same for the atmosphere models. *Middle and bottom panels*: Rosseland optical half-thickness, τ_0, and geometrical half-thickness, H_0, for the model-atmosphere models (solid lines). The distributions obtained from the 1D hydrodynamical model (dotted curves) and the gray model (dashed curves) are also shown.

A solar chemical composition is assumed and all ionization states of the 15 most abundant chemical elements are taken into account. The relation between density ρ, total number density n, and electron number density n_e is found using Saha's equation for each considered ionization state.

We solve Eqs. (3) and (5–8) from the surface $z' = 0$ to the mid-plane $z' = z_1$ by using a shooting method with the boundary conditions

$$F(0) = F_0, \qquad \rho(0) = 0, \qquad P(0) = P_{rad}(0) = \frac{2}{3}\frac{F_0}{c}.\tag{12}$$

There is one additional parameter unknown at the outset: z_1. We find it by the dichotomy method on the range $(1-30)\,H_0$ using an additional boundary condition at the mid-plane

$$F(z' = z_1) = 0\tag{13}$$

or, equivalently,

$$m(z' = z_1) = \frac{\Sigma_0}{2}.\tag{14}$$

A comparison of optical depths and half-thicknesses of the 1D and the gray-approach models along z coordinate for one particular BL model ($M_{WD} = M_\odot$ and $\omega_{WD} = 0.8\,\omega_K$) is shown in Fig. 1 in the two bottom panels. It is clear that the new half-thickness of the BL model $H = z_1 - z(\tau_R = 2/3)$ is approximately twice as large as the thickness of the 1D hydrodynamic

Table 1. Parameters of the rings for the models with parameters $M_{\rm WD} = M_\odot$ and $\omega_{\rm WD} = 0.8, 0.6, 0.4, 0.2\,\omega_{\rm K}$.

R, 10^8 cm	$T_{\rm eff}$, 10^3 K	Σ_0, g/cm^2	H, 10^7 cm	τ_0	$\omega/\omega_{\rm K}$
5.493	154.4	499.6	2.188	230	0.839
5.513	219.6	140.4	1.866	34.1	0.987
5.522	209.4	152.9	1.882	40.3	0.998
5.543	180.3	207.1	1.945	71.1	1.000
5.604	109.5	466.8	2.059	404	0.998
5.482	241.2	376	2.36	79.8	0.652
5.505	298.0	83.4	1.938	13.9	0.999
5.515	283.2	93.5	1.889	15.7	1.003
5.534	253.8	121.1	1.905	23.1	1.002
5.610	144.1	363.1	2.094	187	0.999
5.479	302.6	306	2.565	51.2	0.475
5.499	356.6	68.3	2.395	11.4	0.994
5.512	333.1	75.7	2.205	12.7	1.005
5.538	302.9	101	2.089	16.9	1.004
5.623	170.1	330	2.145	125	0.999
5.478	349.7	264	2.998	44.1	0.299
5.498	410.0	62	3.115	10.3	0.992
5.515	372.7	69.3	2.619	11.6	1.006
5.540	331.5	85.2	2.272	14.2	1.004
5.708	188.9	648	2.554	203	0.997

Table 2. Parameters of the rings for the models with parameters $\omega_{\rm WD} = 0.8\,\omega_{\rm K}$ and $M_{\rm WD} = 1.2$ and $0.8\,M_\odot$.

R, 10^8 cm	$T_{\rm eff}$, 10^3 K	Σ_0, g/cm^2	H, 10^7 cm	τ_0	$\omega/\omega_{\rm K}$
3.865	222.2	565.6	1.370	179	0.829
3.873	304.3	164.7	1.187	30.6	0.961
3.886	284.1	176.7	1.180	36.5	0.993
3.895	253.0	227.2	1.204	56.9	0.993
3.936	150.5	559.9	1.275	356	0.991
7.044	113.8	461.3	3.166	299	0.848
7.065	167.9	147.7	2.784	46.2	0.965
7.092	156.8	156.0	2.788	55.1	1.002
7.114	139.5	192.0	2.850	83.9	1.004
7.205	84.37	426.8	3.026	482	1.001

Table 3. Parameters of the rings for the model with parameters $M_{\rm WD} = 0.8\,M_\odot$ and $\omega_{\rm WD} = 0.6\,\omega_{\rm K}$.

R, 10^8 cm	$T_{\rm eff}$, 10^3 K	Σ_0, g/cm^2	H, 10^7 cm	τ_0	$\omega/\omega_{\rm K}$
7.022	177.7	297	3.247	85.5	0.670
7.044	233.3	78.6	2.631	14.0	0.972
7.069	222.0	83.1	2.628	16.0	1.007
7.094	196.0	115	2.751	27.2	1.006
7.200	111.3	323	3.050	215	1.002
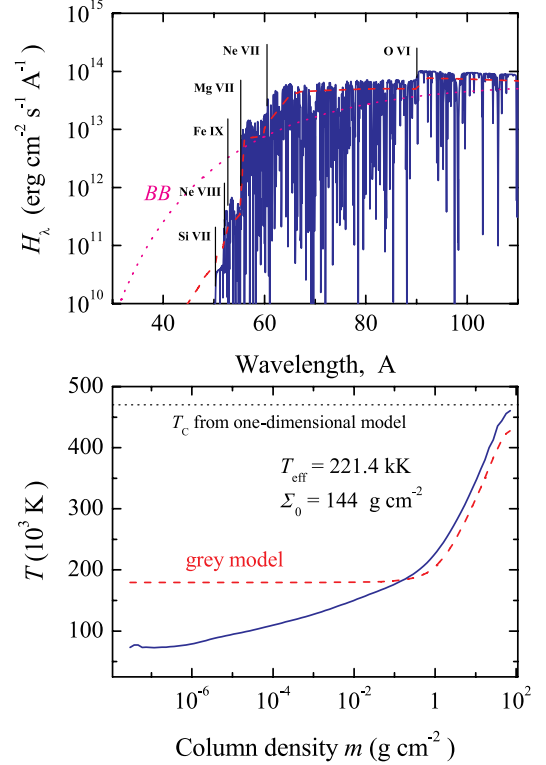
Fig. 2. *Top panel*: local spectra of the hottest ring of the same BL model as in Fig. 1 computed with (solid curve) and without (dashed curve) spectral lines taken into account. The blackbody spectrum corresponding to the effective temperature is shown by the dotted curve. *Bottom panel*: temperature structures of the model with lines (solid curve) and the gray model (dashed curve). The central temperature of the hydrodynamical 1D model is shown by the dotted line.

model (red dotted line). This is a well known factor (Shakura & Sunyaev 1973) because the half-thickness of 1D models is just the pressure scale height $H_0 = a\omega_{\rm K}^{-1}$, while the new thickness is given by the height of the photosphere. The effective temperatures are plotted in the top panel of Fig. 1, here the models agree by definition. The gray temperature structure of the hottest ring of the same BL model is shown in Fig. 2 (bottom panel). We note that this ring is a reference model for our illustration of the presented method. The parameters of the rings for all computed BL models with five rings are shown in Tables 1−3. The ring half-thicknesses, H, and the ring Rosseland optical depths, $\tau_0 = \int_0^{z_1} k_{\rm R}\,\rho\,{\rm d}z$, were computed by using the gray ring models.

Every computed gray vertical ring model is interpolated to a logarithmically equidistant column density grid with 98 depth points in the range from $\sim 10^{-7}$ g cm^{-2} to $\Sigma_0/2$. This interpolated ring model is used as a starting model for the calculation of a non-gray model and its emergent spectrum.

2.2. Boundary layer vertical structure. Model atmosphere approach

The non-gray model is determined by Eqs. (3) and (5), rewritten in the form

$$\frac{{\rm d}P_{\rm g}}{{\rm d}m} = g_z - g_{\rm rad}, \qquad (15)$$

where g_z and $g_{\rm rad}$ are defined by Eqs. (3) and (20). Here we again assume that energy is transferred by radiation alone and this is described by the radiation transfer equation at every considered frequency point

$$\mu \frac{{\rm d}I_\nu}{{\rm d}\tau_\nu} = I_\nu - S_\nu, \qquad (16)$$

where the monochromatic optical depth is determined from

$${\rm d}\tau_\nu = (\sigma_{\rm e} + k_\nu)\,{\rm d}m, \qquad (17)$$
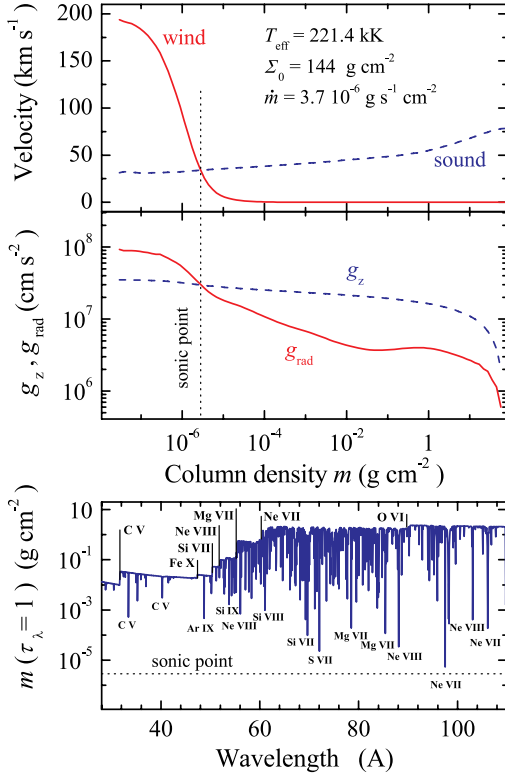
Fig. 3. *Top panel*: sound speed (dashed curve) and wind velocity (solid curve) distributions along depth in the ring model shown in Fig. 2. *Middle panel*: distributions of gravity (dashed curve) and radiative acceleration (solid curve) along depth. The position of the sonic point is marked by the dotted vertical line. *Bottom panel*: depths where the emergent spectrum forms ($\tau_\lambda = 1$). The position of the sonic point is marked by the dashed horizontal line.

and the source function can be expressed as

$$S_\nu = \frac{k_\nu}{\sigma_{\rm e} + k_\nu} B_\nu + \frac{\sigma_{\rm e}}{\sigma_{\rm e} + k_\nu} J_\nu. \tag{18}$$

Here $\mu = \cos\theta$ is the cosine of angle θ, which is the angle between the radiation transfer direction and the ring normal. Eq. (16) determines the specific intensity I_ν at given frequency and μ. The mean intensity J_ν and Eddington flux $H_\nu = F_\nu/4\pi$ are defined by

$$J_\nu = \frac{1}{2} \int_{-1}^{+1} I_\nu \, {\rm d}\mu, \qquad H_\nu = \frac{1}{2} \int_{-1}^{+1} \mu I_\nu \, {\rm d}\mu. \tag{19}$$

We took coherent electron scattering $\sigma_{\rm e}$ into account together with the free-free and bound-free opacities k_ν of all ions of the 15 most abundant elements using opacities from Verner & Yakovlev (1995) and Verner et al. (1996). Line blanketing was taken into account using ~25 000 spectral lines from the CHIANTI, Version 3.0, atomic database (Dere et al. 1997).

We solve the radiation transfer equation (16) at three values of $|\mu|$ using the short characteristics method (Olson & Kunasz 1987). The adopted μ values correspond to Chebyshev-Gauss quadrature abscissas to accurately compute the integrals in (19).

Radiative acceleration $g_{\rm rad}$ is determined by

$$g_{\rm rad} = \frac{4\pi}{c} \int_0^\infty [\sigma_{\rm e} + k_\nu] H_\nu(m) \, {\rm d}\nu. \tag{20}$$

A correct model has to satisfy the energy balance equation which can be written in two forms:

$$4\pi \int_0^\infty H_\nu(m) \, {\rm d}\nu = F_0 \left(1 - \frac{2m}{\Sigma_0}\right) \tag{21}$$

and

$$4\pi \int_0^\infty [\sigma_{\rm e} + k_\nu] [J_\nu - S_\nu] \, {\rm d}\nu = -\frac{2F_0}{\Sigma_0}. \tag{22}$$

Of course, the initial model does not satisfy the energy balance equation, having the relative flux error

$$\varepsilon_{\rm H}(m) = 1 - \frac{F_0(1 - 2m/\Sigma_0)}{4\pi \int_0^\infty H_\nu(m) \, {\rm d}\nu}, \tag{23}$$

and flux derivative error

$$\varepsilon_\Lambda(m) = 4\pi \int_0^\infty [\sigma_{\rm e} + k_\nu] [J_\nu - S_\nu] \, {\rm d}\nu + \frac{2F_0}{\Sigma_0}, \tag{24}$$

at each depth. It is possible to find corrections to the temperature $\Delta T(m)$ using two methods modified for a non-constant bolometric flux over the ring depth (Suleymanov 1992): the integral Λ-iteration together with a surface temperature correction for the optically thin parts of the atmosphere

$$\Delta T_\Lambda(m) = -\varepsilon_\Lambda(m) \left(\int_0^\infty \left[\frac{\Lambda_{\nu,{\rm diag}} - 1}{1 - \alpha_\nu \Lambda_{\nu,{\rm diag}}} \right] k_\nu \frac{{\rm d}B_\nu}{{\rm d}T} \, {\rm d}\nu \right)^{-1}, \tag{25}$$

where $\alpha_\nu = \sigma_{\rm e}/(k_\nu + \sigma_{\rm e})$, and $\Lambda_{\nu,{\rm diag}}$ is the diagonal matrix element of the Λ-operator, and the Avrett-Krook flux correction based on the relative flux error $\varepsilon_{\rm H}(m)$ for the optically thick parts of the ring model

$$\Delta T_{\rm H}(m) = -\frac{{\rm d}T}{{\rm d}m} \int_0^m \varepsilon_{\rm H}(x) \, {\rm d}x. \tag{26}$$

Both methods were described in detail by Kurucz (1970).

Then we find new values of the gas pressure using new $g_{\rm rad}$ and recalculate the densities. Subsequently, opacities are recalculated and the radiation transfer equations at all frequencies are resolved and a new temperature structure is computed. Then we recalculate the geometrical depth scale $z'(m)$ using the new densities. This procedure is performed up to convergence using our version of the computer code ATLAS (Kurucz 1970) that was modified to deal with high temperatures (Ibragimov et al. 2003; Suleimanov & Werner 2007; Suleimanov et al. 2013). We assumed LTE and accounted for pressure ionization effects using the occupation probability formalism (Hummer & Mihalas 1988), as described by Hubeny et al. (1994).

Because of the significant effect of spectral lines on the radiation force $g_{\rm rad}$, the atmosphere modeling approach is divided into two steps. In the first step we compute a continuum model without spectral lines, which provides the radiation force $g_{\rm rad} < g_z$ at all BL ring depths. The distributions of basic BL quantities for continuum ring models are presented in Fig. 1 by solid curves. Hydrostatic ring models cannot be computed when spectral lines are included, because then the radiation force $g_{\rm rad}$ becomes higher than the gravity g_z in the upper, optically thin (in continuum) layers of the models. Therefore, a line-driven wind has to arise from the BL surface, which is similar to the line-driven winds from hot stars (Castor et al. 1975; Kudritzki & Puls 2000). This kind of wind also exists for CV accretion disks (Drew & Verbunt 1985; Prinja & Rosen 1995; Proga et al. 1998).

2.2.1. Line-driven wind approach

Here, we are not interested in the properties of the wind itself, because it probably effects only the strongest spectral lines but not the continuum or moderate and weak spectral lines. In previous works (Ibragimov et al. 2003; Suleimanov et al. 2013), where hot WD model atmospheres were computed, the gas pressure was artificially fixed to 10% of the total pressure at the upper layers, where $g_{rad} > g_z$. The condition $P_{gas} = 0.1P$ was chosen because it was approximately correct at those atmospheric layers, where $g_{rad} \approx g_z$. This condition physically means that we assume some artificial wind velocity law that satisfies the imposed condition. Unfortunately, this simple approach is not working for the BL case because gravity g_z depends on the vertical coordinate z (it is constant for ordinary stellar atmospheres). Therefore, we develop another simple hydrodynamic approach which takes into consideration an expansion of the upper ring layers. This approach is not self-consistent as we do not include effects of motion in the radiation transfer. Thus we consider a hydrodynamical model for the ring upper layers but the radiation pressure force governing this expansion is computed for a formally static medium. This approach allows computing the model emergent spectra but the obtained wind properties such as the local mass-loss rate and wind-velocity distributions are not completely correct and cannot be considered as reliable results.

The considered approach is based on Euler's equation

$$\frac{d}{dz}(\dot{m}v + P_g) = -\rho(g_z - g_{rad}), \tag{27}$$

where $\dot{m}$ is the local mass-loss rate ($[\dot{m}]$= g s^{-1} cm^{-2}) and v is the gas velocity at given z. This equation can be rewritten as

$$\dot{m}\left(1 - \frac{a^2}{v^2}\right)\frac{dv}{dz} = -\rho(g_z - g_{rad}) - \rho\frac{da^2}{dz}, \tag{28}$$

where a is the sound speed connected with gas pressure and matter density by

$$P_g = \rho a^2. \tag{29}$$

Here we used the continuity equation for the plane 1D motion

$$\dot{m} = \rho v. \tag{30}$$

It is well known (see, e.g. Mihalas 1978) that a correct solution of Eq. (28) has to pass through a singular point with $|v| = a$, where the left and the right side of the equation vanish simultaneously. Therefore, these two conditions must be fulfilled in the singular point:

$$a^2 = v^2, \tag{31}$$

and

$$\frac{da^2}{dz} = -(g_z - g_{rad}), \tag{32}$$

or

$$C = \frac{da^2}{dz} + (g_z - g_{rad}) = 0. \tag{33}$$

We suggest the following scheme to compute a model of the BL ring with a line-driven wind. We take the model computed without lines as an initial model and solve the radiation-transfer equation with spectral lines taken into account. As a result we

obtain that the radiative acceleration g_{rad} is greater than the current gravity at the upper layers. At this stage we have the gas pressure $P_g(m)$ and the gas density $\rho(m)$ distributions from the continuum model, and the radiative acceleration $g_{rad}(m)$ and the gas temperature $T(m)$ distributions after the first temperature-correction iteration. The geometrical depth scale $z(m)$ and corresponding gravity g_z are connected with the gas density of the initial (continuum) model. Using these distributions we can find the sound-speed distribution $a(m)$ and its derivative $da(m)/dz$, and then find the depth m_c where Eq. (32) is satisfied. We know at this depth the wind velocity must be equal to the sound speed $a(m_c)$. Therefore, we can evaluate the local mass-loss rate

$$\dot{m} = \rho(m_c)\,a(m_c)/2 \tag{34}$$

using the continuity Eq. (30). Here we have taken into account that the correct gas density ρ_w in the singular point for the model with the wind must be half of that in the hydrostatic model ρ_{st}, see Eq. (27)

$$\dot{m}a + \rho_w a^2 = \rho_w a^2 + \rho_w a^2 = \rho_{st}a^2. \tag{35}$$

Using this mass-loss rate $\dot{m}$ we solve two ordinary differential equations

$$\frac{dP_w}{dz} = -\rho(g_z - g_{rad}) \tag{36}$$

and

$$\frac{dm'}{dz} = \rho, \tag{37}$$

where $P_w = \dot{m}v + \rho a^2$, on a new fine and equidistant geometrical depth grid z (50 000 points) from the midplane ($z = 0$) up to the surface ($m' = \Sigma_0/2$) with the boundary conditions $v = 0$, $m' = 0$, and $P_w(0)$, $\rho(0) = P_w(0)/a(0)^2$ at the midplane, using the shooting method. The current gas density is calculated using the current P_w

$$\rho = \frac{P_w}{2a^2} \pm \sqrt{\left(\frac{P_w}{2a^2}\right)^2 - \left(\frac{\dot{m}}{a}\right)^2}. \tag{38}$$

The plus sign is used for wind velocities below the sonic point and the minus sign in the supersonic part of the model. The wind velocity is found using the continuity Eq. (30). The necessary current values of the $g_{rad}(m')$ and $da^2(m')/dz = \rho d\,a^2(m')/d\,m'$ are found using a spline interpolation in the dependencies $g_{rad}(m)$ and $da^2(m)/dm$ known from the previous iteration, taking $m = \Sigma_0/2 - m'$.

Usually, the necessary conditions Eqs. (28) and (32) are not satisfied at the sonic point for the first tried initial condition for $P_w(0)$. Therefore, we find the necessary $P_w(0)$ with the dichotomy method. Usually, the correct initial value of the gas pressure at the midplane differs by a few percent from the gas pressure at the midplane found in the previous iteration. We adopt the two following numerical convergence criteria at the singular point

$$\frac{a - |v|}{a} < 10^{-2}, \qquad \frac{C}{g_z} < 10^{-2}.$$

After obtaining the solution, all quantities are interpolated on the model atmosphere column density grid m (98 points) which is used for the radiation transfer solution. Therefore, we have

a new distribution of the gas pressure $P_g = \rho a^2$ with the line-driven wind taken into account which is in accordance with the radiative acceleration g_{rad}. Then we find a new gas density distribution using the new P_g and the temperature distribution obtained after the temperature-correction iteration. For this aim the ideal gas Eq. (9) is used together with charge and number density conservation laws. Then the radiation transfer is re-solved and a new temperature correction is performed. The above described procedure to find a new gas-pressure distribution is repeated with a new radiative-acceleration distribution. There is only one difference. The local mass-loss rate is now calculated (see Eq. (34)) without division by 2 because the current model takes into consideration the line-driven wind.

This iteration scheme is converging and it is stable. As a result we get a self-consistent model of the BL ring and its emergent spectrum. Results of calculations for the reference ring model are presented in Figs. 2 and 3. The emergent spectrum (Fig. 2, top panel) is similar to hot stellar atmospheres with similar effective temperatures (see e.g. Suleimanov et al. 2013) and shows the same absorption edges as the continuum spectrum together with a forest of spectral absorption lines. The temperature structure (Fig. 2, bottom panel) differs significantly from the gray temperature distribution mainly because of line-blanketing effects. The final model's wind velocity law (Fig. 3, top panel) and the radiation force g_{rad} distribution (Fig. 3, middle panel) are shown together with the sound speed a and gravity g_z distributions. The sonic point is seen to be located at the upper ring layers ($m \approx 10^{-5}$ g cm^{-2}) and the corresponding mass-loss rate is sufficiently low ($\dot{m} \approx 10^{-5}$–10^{-6} g s^{-1} cm^{-2}). Formally, the sonic point is above the formation depths of even the strongest spectral lines (Fig. 3, bottom panel) and, therefore, the wind does not affect the spectrum.

2.3. Integral BL spectra

When the computation of all ring model spectra is finished, we integrate them over the BL radial coordinate with taken Doppler broadening due to ring rotation into account

$$L_\lambda = \cos i \int_{R_{in}}^{R_{out}} R \, dR \int_0^\pi I_{\lambda'}(\cos i) \, d\varphi$$

$$\approx \cos i \sum_{j=1}^{N_R} R_j \, \Delta R_j \sum_{k=1}^{N_\varphi} \Delta\varphi_k \, I_{\lambda'}(\cos i), \qquad (39)$$

where i is the inclination angle of the BL relative to the line of sight, $I_\lambda(\cos i)$ is the local specific intensity in the direction of the line of sight, N_R is the number of considered BL rings (5 or 20), and $N_\varphi = 100$ is a number of considered ring sectors. Here λ' is the Doppler shifted wavelength:

$$\lambda' = \lambda + \frac{v_\varphi(R)}{c} \sin i \cos\varphi. \qquad (40)$$

The azimuthal velocity distribution $v_\varphi(R)$ is taken from the 1D BL model. We note that integration is only performed over the visible BL part. We assume that we see only a quarter of the total BL surface, which is situated in front of the WD on the visible part of the disk, and that the visible part does not depend on the inclination angle. The change of the projection area of the BL's visible part is proportional to $\cos i$. Specific intensities for every ring model are computed using Eq. (16) for six angles relative to the normal: 0, 15, 30, 45, 60 and 75 degrees. Therefore, integral spectra can be computed for these inclination angles relative to the line of sight. We ignored any relativistic effects because they are low.
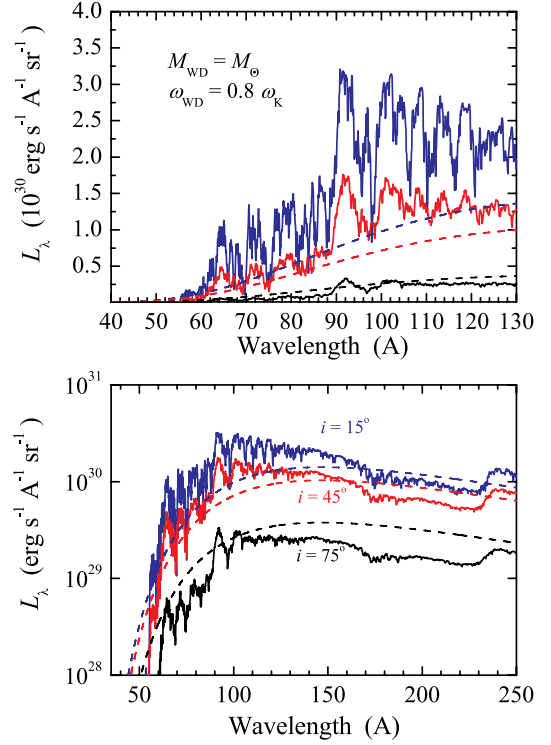
Fig. 4. Spectra of the BL model $M = M_\odot$, $\omega_{WD} = 0.8\,\omega_K$ for three inclination angles relative to the line of sight. The corresponding blackbody approximations are shown by dashed curves.
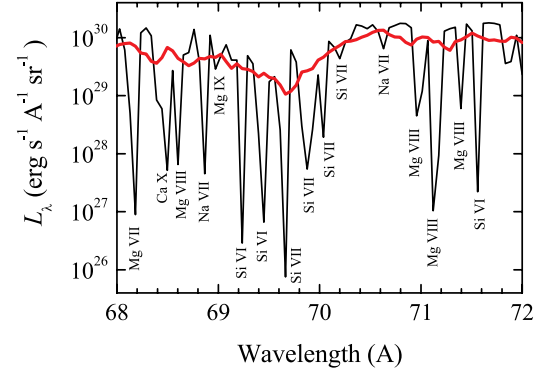

Fig. 5. Detail of the integral emergent fluxes of the same BL model as in Fig. 4 computed for $i = 0°$ (rotation does not affect the spectrum, thin black curve), and 15° (thick red curve).

3. Results

Using the method presented above, we computed spectra of several BL models. Examples of the integral reference BL model spectra for three angles are shown in Fig. 4. These spectra are calculated using the BL model partitioned in 20 rings. The spectra show broad absorption and quasi-emission features. The absorption features arise due to rotational broadening and blending as a result of many absorption lines at this place of the spectrum. The quasi-emission features are continuum sections with a low amount of absorption lines. These statements are illustrated by Fig. 5, where a narrow section of the integral spectra computed for $i = 0°$ and 15° are shown. In Fig. 4 the spectra computed in blackbody approximation are also shown. We focus attention on
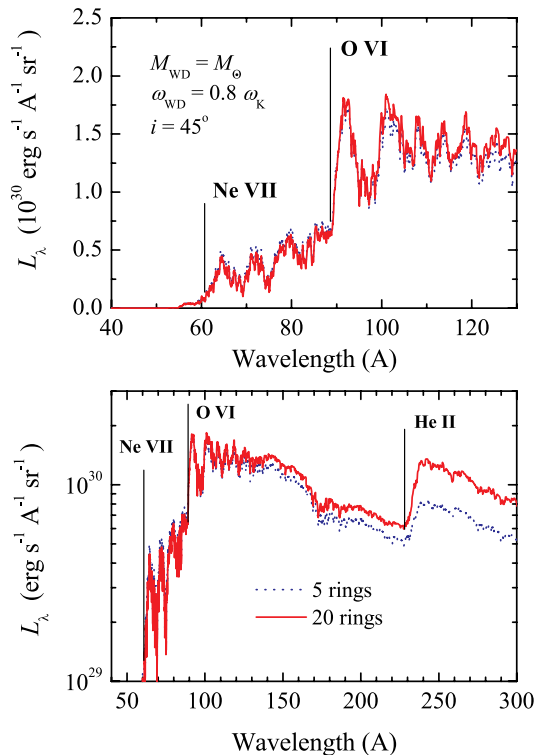
Fig. 6. Comparison of the spectra of the same BL model (see Fig. 4) computed using five (dotted curve) and twenty (solid curve) rings.
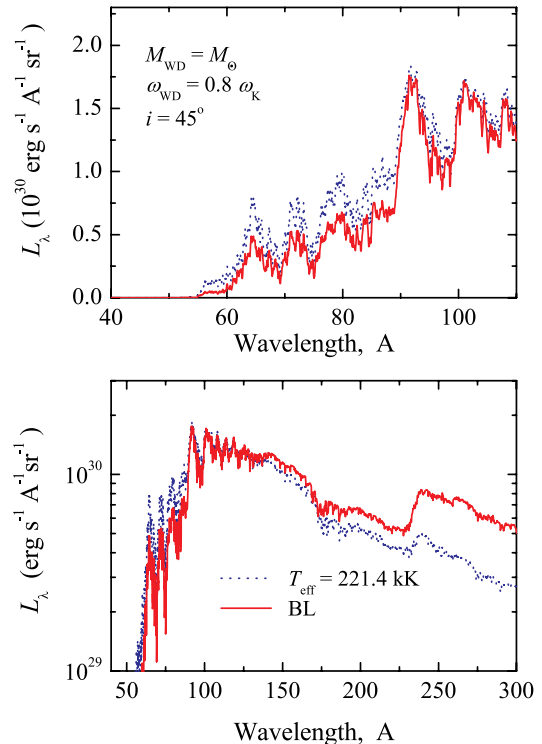
Fig. 7. Comparison of the BL model spectrum from Fig. 4 (solid curve) with the spectrum of the hottest ring (dotted curve) normalized to the flux at 100 Å.

the fact that the atmosphere-model intensities compared to the blackbody spectra are different for low and high inclination angles. This is the result of different limb-darkening laws for the ring atmospheres (the intensity is mainly concentrated along the normal) compared to the isotropic blackbody radiation.

We investigated the importance of the number of rings to describe the model spectra. In addition to the spectrum of the BL reference model presented above, we computed the spectrum of the same model using five rings. A comparison of both spectra is shown in Fig. 6. The difference is significant at wavelengths longer than 120−130 Å, but the spectra are almost identical at the shorter wavelengths. Our work was particularly motivated by the *Chandra* X-ray spectrum of SS Cyg in outburst (Mauche 2004). The grating spectra cover the wavelength range 10−130 Å, therefore, to model the observed BL spectra five rings are sufficient. Moreover, even the hottest ring spectrum alone can approximate the integral BL spectrum with a relatively good accuracy (see Fig. 7). All BL spectra of the two grids described above were computed using five rings.

It is important to explore the dependence of the BL model spectra on the BL parameters. For this purpose, we computed spectra of two model grids. In the first one we fixed the relative WD angular velocity $\omega_{WD} = 0.8\,\omega_K$ and investigated how the spectra depend on the WD mass M_{WD}. In the second set we fixed the WD mass $M_{WD} = M_\odot$ and varied the relative WD angular velocity. The obtained results are described below.

A comparison of the computed integral BL spectra for various parameters is shown in Figs. 8−10. The basic differences of the presented spectra are determined by differences in the BL model effective temperatures (see e.g. Fig. 8, top panel). The radial widths of all the computed models are similar (see the same figure and Hertfelder et al. 2013), but the luminosities can
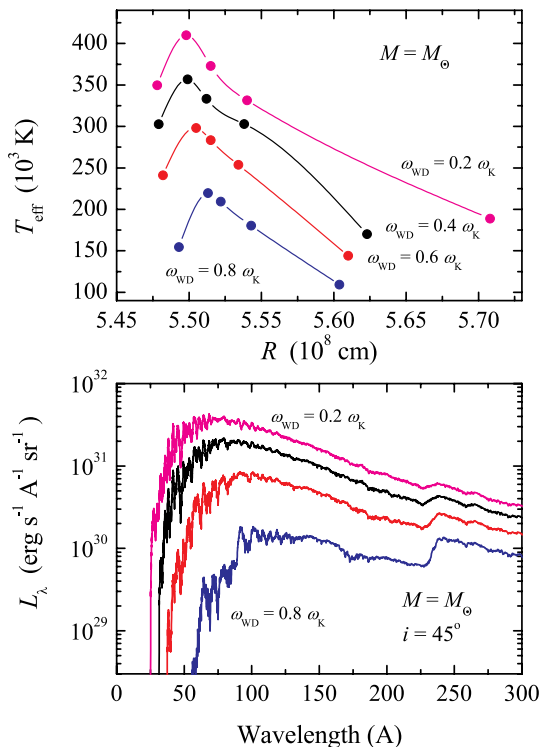
Fig. 8. Effective temperature distributions (*top panel*, the temperatures of the considered rings are marked by dots) and model spectra (*bottom panel*) for the models with different angular velocities (0.2, 0.4, 0.6 and 0.8 ω_K) and fixed WD mass ($M_{WD} = M_\odot$).

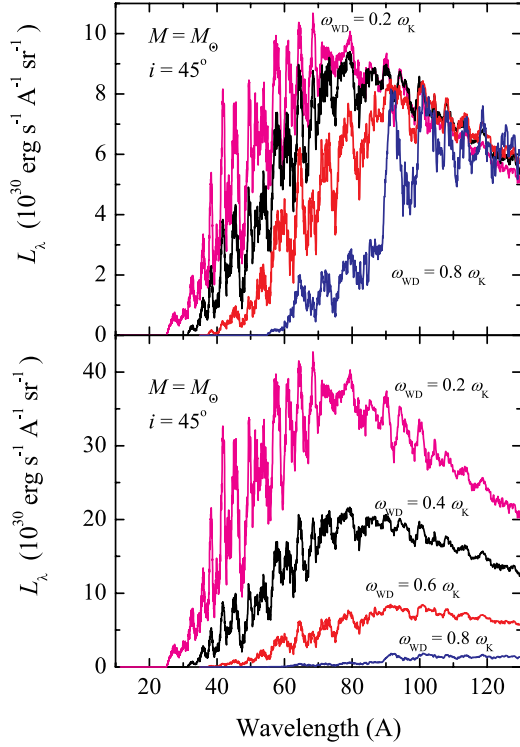**Fig. 9.** Spectra of the same models as in Fig. 8 in the observed wavelength range. The spectra in the *top panel* are normalized to the $\omega_{WD} = 0.6 \omega_K$ model spectrum at 100 Å.
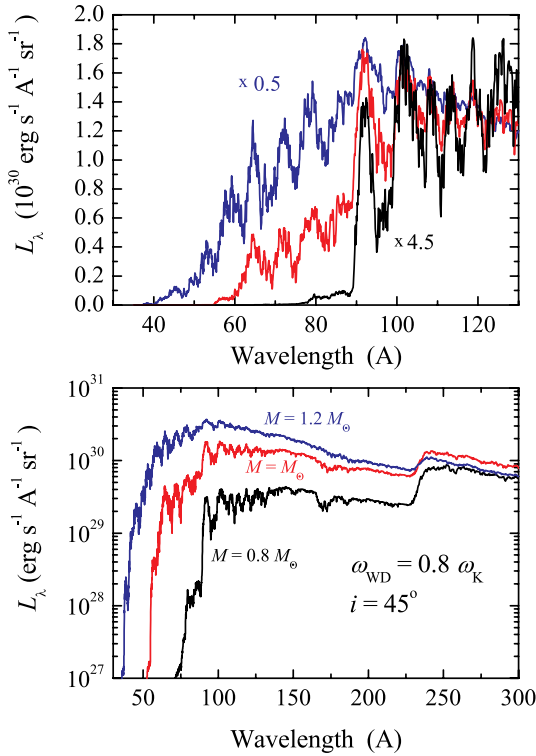

Fig. 10. Comparison of BL model spectra for three WD masses (0.8, 1, 1.2 $M_\odot$) and fixed relative angular velocity ($\omega_{WD} = 0.8 \omega_K$). The spectra in the *top panel* are normalized to the $M_{WD} = M_\odot$ model flux at 100 Å.

change more significantly. So, the BL effective temperatures directly connect with the BL luminosities, which are defined by mass accretion rate $\dot{M}$, WD mass, and relative WD angular velocity ω_{WD}/ω_K (Kluźniak 1987; Kley 1991):

$$L_{BL} = \frac{1}{2} \frac{GM_{WD}\dot{M}}{R_{WD}} \left(1 - \frac{\omega_{WD}}{\omega_K}\right)^2. \qquad (41)$$

All the models considered here have a fixed mass accretion rate. Therefore, luminosities and effective temperatures of these models only depend on WD masses and relative angular velocities. Both of them increase with the WD mass and decrease with the relative angular velocity. Higher BL effective temperatures have to correspond to harder spectra and higher ionization degree of the matter.

Our computations confirm these qualitative conclusions. Emergent spectra of the BL models around a solar mass WD with various relative angular velocities are shown in Fig. 8. The effective temperatures increase with decreasing WD relative angular velocity, and the emergent spectra become harder. As a result, the photo-absorption edges and the intensities of quasi-absorption and quasi-emission features are changing. In particular, the position of a notable spectral short-wavelength roll-off shifts from 60 Å in the spectrum of BL model around the fastest rotating WD up to 25 Å in the spectrum of the BL model around the slowest rotating WD. The same spectra in the 15−130 Å wavelength band on a linear flux scale are shown in Fig. 9. The spectra, which are normalized at 100 Å, are also shown in the top panel of the same Figure to emphasize the changes in the spectral shapes.

We note that some ring models (near the minimum of the surface density distribution) of the BL model around the non-rotating WD ($M_{WD} = M_\odot$, $\omega_{WD} = 0$) did not converge and a corresponding integral BL model spectrum was not computed. The reason is that these rings are effectively optically thin ($\tau_{eff,\nu} = \int_0^{\Sigma_0/2} \sqrt{\sigma_e(\sigma_e + k_\nu)} \, dm < 1$) over a wide wavelength range. We can see that the average Rosseland opacities for the hottest rings for the BL models around slowly rotating WDs are close to pure electron scattering and the input of the "true" opacity k_{kr} is negligible, because $\tau_0 \approx \sigma_e \Sigma_0/2$ (see Table 1). Possibly, the similar effect may exist for other BL models around non-rotating WDs. It could be less important for the BL around WDs with lower masses and could be reduced for lesser mass accretion rates.

The difference between BL spectra computed for the fixed WD relative angular velocity but various WD masses are qualitatively similar (Fig. 10). The spectrum of the BL model around the heaviest WD is harder than the spectra of BL models around less heavy WDs.

4. Comparison with observations

As mentioned in the introduction, there are only four dwarf novae with observed soft X-ray/EUV radiation in outbursts, which can be associated with optically thick BLs. One of them is SS Cyg (Mauche 2004; Suleimanov et al. 2013). Fitting the spectrum gave effective temperature estimations of 190 (250) kK and a bolometric BL luminosity 18(5) × 10³³ erg s⁻¹ for an assumed distance of 160 pc. The bolometric disk luminosity of SS Cyg at the peak of the outburst, $L_D \approx 10^{35}$ erg s⁻¹, was estimated by Mauche (2004) using the same distance and the data published by Polidan & Holberg (1984). We note that the soft X-ray spectrum of SS Cyg was obtained by *Chandra* at the outburst peak, too. The corresponding mass accretion rate

Table 4. Parameters of the strongest emission lines, preliminarily identified in the subtracted spectrum.

λ, Å	Ion	Transition	gf
49.12	S IX	$2p^4\ ^3P_2 - 3d\ ^3D_3^o$	1.12
65.7	Al IX	$2p^3\ ^2P_{3/2} - 3d\ ^2D_{5/2}$	1.33
76.77	Mg VIII	$2p^3\ ^4S^o - 3d\ ^4P$	4.7^a
80.5	Si VI	$2p^5\ ^2P^o - 3d\ ^2P$	2.3^a
83.97	Mg VII	$2p^2\ ^3P - 3d\ ^3D^o$	$\sim 7^b$
85.41	Mg VII	$2p^2\ ^1D - 3d\ ^1F^o$	4.23
88.1	Ne VIII	$2s\ ^2S - 3p\ ^2P^o$	0.6^a
98.26	Ne VIII	$2p\ ^2P_{3/2}^o - 3d\ ^2D_{5/2}$	2.28
106.14	Ne VII	$2p\ ^3P^o - 3d\ ^3D$	4.3^a
107.94	Al V	$2p^5\ ^2P_{3/2}^o - 3d\ ^2D_{5/2}$	1.4

Notes. Part of them could be blends with other lines. Data were taken from the CHIANTI database (Dere et al. 1997). $^{(a)}$ Doublet, the gf values are summed. $^{(b)}$ Triplet, the gf values are summed.

$\dot{M} \approx 1.5 \times 10^{-8}\ M_\odot/\text{yr}$, which was used for the computation of all the BL models in this work, was obtained using this luminosity for the adopted WD parameters, $M_{WD} = M_\odot$ and $R_{WD} = 5.5 \times 10^8$ cm. The corresponding ratio of BL luminosity L_{BL} to disk luminosity L_D is 0.18 (0.05). These values correspond to the fit of the spectrum by a hot stellar atmosphere that is close to Eddington limit (with $\log g = 6.2$, Suleimanov et al. 2013), and the values in brackets were obtained using blackbody fits with broad absorption lines (Mauche 2004). The recent determination of SS Cyg's distance by Nelan & Bond (2013) gave a lesser value, $\sim$110 pc instead of $\sim$160 pc. It reduces the disk and the BL luminosities mentioned before, but does not change their ratio. The low value of L_{BL}/L_D supports the hypothesis about a fast WD rotation in SS Cyg (Mauche 2004). In the ultraviolet spectrum of this CV in quiescence the absorption lines, which are in principle available to determine the WD's projected rotation velocity, were not found (Sion et al. 2010). The most probable reason for this finding are strong emission lines in the UV spectrum of SS Cyg in quiescence (Long et al. 2005), which could mask absorption lines in the WD spectrum. But it is necessary to keep in mind that the BL luminosity estimations are very model dependent and have large uncertainties.

We compare our BL model spectra to the observed *Chandra* spectrum of SS Cyg (Mauche 2004), using the well known normalization for converting the calculated spectra to the spectrum at Earth

$$f_\lambda = \frac{L_\lambda}{d^2}, \qquad (42)$$

where d is the distance. A relatively good fit was obtained for the model spectrum of a BL with parameters $M_{WD} = M_\odot, \omega_{WD} = 0.8\,\omega_K$ for the distance $d \approx 107$ pc and the absorption by the neutral interstellar medium with $N_H \approx 7 \times 10^{19}$ cm^{-2} (Fig. 11). We see that the model spectrum describes some prominent features in the observed spectrum, but there are also some additional features. The subtracted (observed minus BL model) spectrum (Fig. 11, bottom panel) is very similar to a spectrum of an optically thin hot plasma with a strong emission continuum of NeVII and numerous broad emission lines. Part of them are identified (see Fig. 11 and Table 4) as spectral lines with great gf values. It is most probable that the difference spectrum is due to an optically thin outflow, which is projected on the cool WD and the accretion disc, see Fig. 12. We also show in the bottom of Fig. 11 the absorbed (with the same N_H) spectrum of the homogeneous slab computed in LTE approximation with temperature
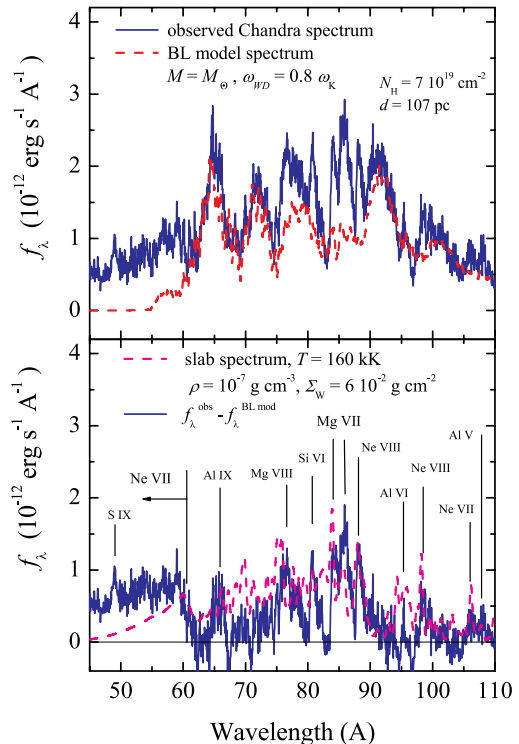

Fig. 11. *Top panel*: comparison of the observed SS Cyg soft X-ray spectrum (solid curve) with the BL model spectrum for a 1 $M_\odot$ WD and relative angular velocity $\omega_{WD} = 0.8\,\omega_K$ (dashed curve). *Bottom panel*: subtracted (observed minus BL model) spectrum (solid curve) together with the homogeneous slab model spectrum (dashed curve). The emission continuum of Ne VII below 60 Å and the strongest identified emission lines are marked.

$T = 160$ kK, density $\rho = 10^{-7}$ g cm^{-3}, and surface density $\Sigma_W = 6 \times 10^{-2}$ g cm^{-2}. The corresponding geometrical thickness of the slab is 6×10^5 cm. The spectrum is computed by the short characteristics method and broadened using a Gauss function with $\sigma = 0.2$ Å. This model slab spectrum cannot fit all the emission details correctly, because the real outflow has to be strongly inhomogeneous, and, probably, the LTE approximation is not correct there. But it reproduces the general shape of the subtracted spectrum supporting our hypothesis. We found that the emission area of this slab is approximately four times greater than the visible model BL area. If we assume that the obtained density of the slab is correct for the averaged density of the outflow, we can estimate a total mass loss rate of $\dot{M}_W \sim \rho v_{esc} S_{BL} \sim 10^{-7}$ g cm$^{-3} \times \sim 10^8$ cm s$^{-1} \times \sim 10^{16} - 10^{17}$ cm^2 $\sim 10^{17} - 10^{18}$ g s^{-1}. This guess is very crude, but, nevertheless, it is comparable with the mass accretion rate, and, therefore, future BL models have to be computed with mass loss taken into account.

However, we have to point out that a recent estimation gave a lesser WD mass in SS Cyg, $M_{WD} = 0.81 \pm 0.18\,M_\odot$ (Bitner et al. 2007) instead of 1 $M_\odot$. We may expect that some BL model around a slower rotating WD with $M_{WD} = 0.8\,M_\odot$ can have similar effective temperatures (and a similar spectrum) as the considered BL model with $M_{WD} = M_\odot$ and $\omega_{WD} = 0.8\omega_K$. Indeed, we find that the spectra of BL models with parameters $M_{WD} = 0.8M_\odot, \omega_{WD} = 0.6\,\omega_K$ and $M_{WD} = M_\odot, \omega_{WD} = 0.8\,\omega_K$ are very similar (see Fig. 13). Therefore the spectrum of the BL model with parameters $M_{WD} = 0.8\,M_\odot, \omega_{WD} \approx 0.6\,\omega_K$ also has to fit the observed SS Cyg soft X-ray spectrum in the outburst
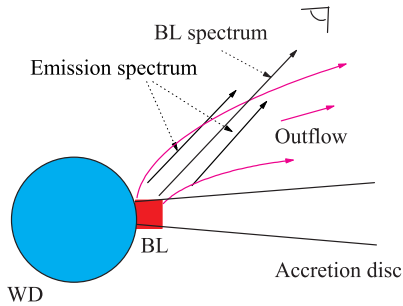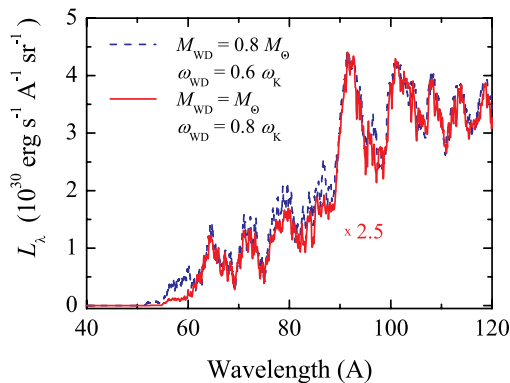
Fig. 12. Scheme of the BL outflow.

Fig. 13. Comparison of the BL model spectra for a 0.8 $M_\odot$ WD and relative angular velocity $\omega_{WD} = 0.6\,\omega_K$ (dashed curve) and for a 1 $M_\odot$ WD and relative angular velocity $\omega_{WD} = 0.8\,\omega_K$ (solid curve). The flux of the latter spectrum is multiplied by 2.5.

with $d \approx 170$ pc. The ratios L_{BL}/L_D are 0.04 and 0.16 for these BL models, respectively, and they are close to the estimations obtained by Mauche (2004) and Suleimanov et al. (2013). Therefore, the BL model spectra computed here can fit the soft X-ray spectrum of SS Cyg in outburst.

The second bright dwarf nova that exhibited a prominent soft X-ray/EUV flux during outburst is U Gem (Cordova et al. 1984; Long et al. 1996). But the properties of this emission differ significantly from the case of SS Cyg. A blackbody fit gives a temperature about 140 kK and a BL luminosity of about 4×10^{34} erg s^{-1} (for the distance 90 pc, Marsh et al. 1990) with the corresponding ratio $L_{BL}/L_D \sim 0.5$ (Long et al. 1996). The earlier X-ray observations performed by the *Einstein* observatory gave similar relations between the blackbody temperatures and the observed fluxes of these CVs' soft X-ray spectra (Cordova et al. 1980a,b, 1984).

The estimated rotation velocity of the WD in this CV is very low (<100 km s^{-1}, Sion et al. 1994) and the derived relative BL luminosity is in accordance with the expected relative BL luminosity (see Eq. (41)). But all 1D BL models including ours predict higher effective temperatures for this luminous BL, at least 200−300 kK, in contradiction with the observed temperature. This means that the BL emitting area in U Gem is about 5−10 times greater than in SS Cyg, i.e. the BL width can be tens of percent of the WD radius instead of a few percent. Therefore, a new BL model is necessary to explain this fact.

A correct theory of optically thick BLs has to explain the observational properties of both dwarf novae. A possible reason could be the 2D nature of BLs around slowly rotating WDs. For example, the BL matter can spread over the WD surface

increasing the radiating area (Kley 1991; Fisker & Balsara 2005; Balsara et al. 2009). Another possible physical mechanism is deposition of a significant part of BL energy deep into the WD (Kippenhahn & Thomas 1978; Godon et al. 1995), as it was also considered for T Tau type stars (Bertout & Regev 1992; Regev & Bertout 1995), with subsequent radiation of this energy by a significant part of the WD surface above and below the equatorial plane. An additional possibility was suggested by Idan & Shaviv (1996), who proposed that a significant part of the energy released in the BL might be carried away by some outflow (wind).

The EUV spectrum of U Gem in outburst is very similar to the soft X-ray spectrum of SS Cyg in outburst. It also shows numerous broad absorption- and emission-like features, but a few strong emission lines are also detected (Long et al. 1996). The latter probably arise in a strong BL wind and they are visible due to a higher inclination of U Gem's orbital plane relative to the line of sight ($i \approx 70°$, Zhang & Robinson 1987) in comparison with the inclination angle of SS Cyg ($i \approx 50°$, Bitner et al. 2007). The even more inclined SU UMa-type dwarf nova OY Car ($i \approx 83°$, Littlefair et al. 2008) shows an EUV spectrum dominated by prominent emission lines in super-outburst as presented by Mauche & Raymond (2000). These authors evaluated the wind mass-loss rate ($\leq 10^{-10}\ M_\odot$ yr^{-1}) and argued that this value cannot be explained by a line-driven disk wind. It is possible that a line-driven BL wind as presented in our calculations can help to resolve this problem. We suggest that radiation-driven winds are much more powerful for BLs around slowly rotating WDs because of much higher effective temperatures at the same emitting area (see, e.g., Table 2). Therefore, such winds could be optically thick like the winds of Wolf-Rayet stars (see, e.g. Nugis & Lamers 2002; Gräfener & Hamann 2005), and the visible BL photospheres could have much greater emitting areas in comparison with the expected BL model sizes. This would lead to significant reduction of the averaged BL effective temperature while saving the bolometric luminosity. This hypothesis can explain the observed properties of the BL in U Gem. We suggest to call this kind of BLs "photospheric radius expanded" (PRE) BLs. A detailed BL wind investigation would be necessary to test these ideas.

5. Conclusions

In this paper we presented the first attempt to compute the soft X-ray/EUV spectra of optically thick BL models in CVs using the model stellar-atmosphere method. We used the 1D hydrodynamic BL models calculated by Hertfelder et al. (2013) for three WD masses (0.8, 1, and 1.2 $M_\odot$) and various values of relative angular velocity (0, 0.2, 0.4, 0.6, and 0.8 ω_K). Two other parameters, the mass-accretion rate $\dot{M} = 1.5 \times 10^{-8}\ M_\odot$ yr^{-1} and the viscosity parameter $\alpha = 0.01$ were fixed. Every BL model is divided into a few rings, and every ring model along the z-direction is computed using the model-atmosphere method. The total BL model spectra are summed over the ring spectra with Doppler effect taken into account.

The effective temperatures of the considered BL model rings range from 100 kK to 400 kK. At these conditions hydrogen and helium are almost fully ionized and highly-charged ions of heavy elements such as carbon, oxygen, neon, magnesium, and silicon determine the opacities and the shape of the model emergent spectra. The local ring spectra with numerous absorption lines of these chemical elements together with absorption edges are smeared by the fast ring rotation and the final model BL spectra show relatively broad absorption- and emission-like

features, which cannot be identified with any individual absorption or emission lines. The absorption-like features arise at the spectral parts with high number densities of strong absorption lines and/or near blue sides of absorption edges. The emission-like features arise at spectral parts with a low number densities of absorption lines and/or near red sides of absorption edges. An additional smoothing of the spectra due to a finite spectral resolution of X-ray instruments has to be also considered to form these prominent features. The predominance of spectral lines in the BL opacities leads to strong BL line-driven winds, which manifest themselves in EUV observations. We developed a simple method to treat approximately the influence of a line-driven wind on the BL model structure. This approach is not self-consistent and it is not sufficiently correct for an investigation of the wind properties, but it offers the possibility to compute the model emergent spectra.

The observed soft X-ray and EUV spectra of the dwarf novae SS Cyg and U Gem in outburst are very similar to the computed model BL spectra and exhibit numerous emission- and absorption-like features (Mauche 2004; Long et al. 1996). Moreover, we reveal that the soft X-ray *Chandra* spectrum of SS Cyg in outburst can be fitted satisfactorily by the spectrum of our BL models with $M_{\rm WD} = M_\odot$, $\omega_{\rm WD} = 0.8\,\omega_{\rm K}$, and $M_{\rm WD} = 0.8\,M_\odot$, $\omega_{\rm WD} = 0.6\,\omega_{\rm K}$. with the interstellar absorption parameter $N_{\rm H} \approx 7 \times 10^{19}$ cm^{-2}, and the distances $\approx$107 and 170 pc correspondingly. The ratio of the observed BL luminosity to the disk luminosity of SS Cyg in outburst is consistent with the model parameters. The subtracted spectrum is a spectrum of a hot optically thin plasma spectrum and could be associated with the outflow from the BL surface with the mass loss rate $\sim 10^{17}$–10^{18} g s^{-1}, which is comparable with the assumed mass accretion rate. Therefore, future BL models have to be computed with the mass loss rate taken into consideration.

On the other hand, the observed EUV flux properties of U Gem in outburst are contradicting our model predictions. We suggest that a powerful radiation-driven wind from U Gem's BL could form an extended photospheric BL surface reducing the averaged effective temperature but saving the bolometric luminosity. The properties of this "photospheric radius expanded" BL could be very similar to the observed U Gem BL properties. Additional extended BL radiation-driven wind investigations are necessary to proof this hypothesis.

References

Balbus, S. A., & Hawley, J. F. 1991, ApJ, 376, 214
Balsara, D. S., Fisker, J. L., Godon, P., & Sion, E. M. 2009, ApJ, 702, 1536
Baskill, D. S., Wheatley, P. J., & Osborne, J. P. 2005, MNRAS, 357, 626
Belyaev, M. A., & Rafikov, R. R. 2012, ApJ, 752, 115
Belyaev, M. A., Rafikov, R. R., & Stone, J. M. 2012, ApJ, 760, 22
Belyaev, M. A., Rafikov, R. R., & Stone, J. M. 2013, ApJ, 770, 67
Bertout, C., & Regev, O. 1992, ApJ, 399, L163
Bitner, M. A., Robinson, E. L., & Behr, B. B. 2007, ApJ, 662, 564
Castor, J. I., Abbott, D. C., & Klein, R. I. 1975, ApJ, 195, 157
Chandrasekhar, S. 1960, Proc. National Academy of Science, 46, 253
Collins, T. J. B., Helfer, H. L., & Van Horn, H. M. 1998, ApJ, 508, L159
Collins, T. J. B., Helfer, H. L., & Van Horn, H. M. 2000a, ApJ, 534, 934
Collins, T. J. B., Helfer, H. L., & Van Horn, H. M. 2000b, ApJ, 534, 944
Cordova, F. A., Chester, T. J., Tuohy, I. R., & Garmire, G. P. 1980a, ApJ, 235, 163
Cordova, F. A., Nugent, J. J., Klein, S. R., & Garmire, G. P. 1980b, MNRAS, 190, 87
Cordova, F. A., Chester, T. J., Mason, K. O., Kahn, S. M., & Garmire, G. P. 1984, ApJ, 278, 739
Dere, K. P., Landi, E., Mason, H. E., Monsignori Fossi, B. C., & Young, P. R. 1997, A&AS, 125, 149
Done, C., Osborne, J. P., & Beardmore, A. P. 1995, MNRAS, 276, 483
Drew, J., & Verbunt, F. 1985, MNRAS, 213, 191
Fisker, J. L., & Balsara, D. S. 2005, ApJ, 635, L69
Frank, J., King, A., & Raine, D. J. 2002, Accretion Power in Astrophysics: 3rd edn. (Cambridge: Cambridge University Press)
Gilfanov, M., Revnivtsev, M., & Molkov, S. 2003, A&A, 410, 217
Godon, P. 1995a, MNRAS, 277, 157
Godon, P. 1995b, MNRAS, 274, 61
Godon, P. 1997, ApJ, 483, 882
Godon, P., & Sion, E. M. 2011, PASP, 123, 903
Godon, P., Regev, O., & Shaviv, G. 1995, MNRAS, 275, 1093
Godon, P., Sion, E. M., Levay, K., et al. 2012, ApJS, 203, 29
Gräfener, G., & Hamann, W.-R. 2005, A&A, 432, 633
Hertfelder, M., Kley, W., Suleimanov, V., & Werner, K. 2013, A&A, 560, A56
Hubeny, I., Hummer, D., & Lanz, T. 1994, A&A, 282, 151
Hummer, D., & Mihalas, D. 1988, ApJ, 331, 794
Ibragimov, A. A., Suleimanov, V. F., Vikhlinin, A., & Sakhibullin, N. A. 2003, Astron. Rep., 47, 186
Idan, I., & Shaviv, G. 1996, MNRAS, 281, 604
Inogamov, N. A., & Sunyaev, R. A. 1999, Astron. Lett., 25, 269
Inogamov, N. A., & Sunyaev, R. A. 2010, Astron. Lett., 36, 848
Jones, M. H., & Watson, M. G. 1992, MNRAS, 257, 633
Kato, S., & Inagaki, S. 1994, PASJ, 46, 289
Kippenhahn, R., & Thomas, H.-C. 1978, A&A, 63, 265
Kley, W. 1989, A&A, 222, 141
Kley, W. 1991, A&A, 247, 95
Kley, W., & Hensler, G. 1987, A&A, 172, 124
Kluźniak, W. 1987, PhD thesis, Stanford University
Kriz, S., & Hubeny, I. 1986, Bull. Astr. Inst. Czechosl., 37, 129
Kudritzki, R.-P., & Puls, J. 2000, ARA&A, 38, 613
Kurucz, R. L. 1970, SAO Special Report, 309
Lanz, T., Telis, G. A., Audard, M., et al. 2005, ApJ, 619, 517
Lewin, W. H. G., van Paradijs, J., & Taam, R. E. 1993, Space Sci. Rev., 62, 223
Littlefair, S. P., Dhillon, V. S., Marsh, T. R., et al. 2008, MNRAS, 388, 1582
Long, K. S., Mauche, C. W., Raymond, J. C., Szkody, P., & Mattei, J. A. 1996, ApJ, 469, 841
Long, K. S., Froning, C. S., Knigge, C., et al. 2005, ApJ, 630, 511
Long, K. S., Brammer, G., & Froning, C. S. 2006, ApJ, 648, 541
Lynden-Bell, D., & Pringle, J. E. 1974, MNRAS, 168, 603
Marsh, T. R., Horne, K., Schlegel, E. M., Honeycutt, R. K., & Kaitchuck, R. H. 1990, ApJ, 364, 637
Mauche, C. W. 1996, in Cataclysmic Variables and Related Objects, eds. A. Evans & J. H. Wood, Astrophys. IAU Colloq., 158, Space Sci. Library, 208, 243
Mauche, C. W. 2004, ApJ, 610, 422
Mauche, C. W., & Raymond, J. C. 2000, ApJ, 541, 924
Mauche, C. W., Raymond, J. C., & Mattei, J. A. 1995, ApJ, 446, 842
Mihalas, D. 1978, Stellar atmospheres (San Francisco: W. H. Freeman and Co.)
Mitsuda, K., Inoue, H., Koyama, K., et al. 1984, PASJ, 36, 741
Mukai, K., Kinkhabwala, A., Peterson, J. R., Kahn, S. M., & Paerels, F. 2003, ApJ, 586, L77
Nagel, T., Dreizler, S., Rauch, T., & Werner, K. 2004, A&A, 428, 109
Narayan, R., Loeb, A., & Kumar, P. 1994, ApJ, 431, 359
Nauenberg, M. 1972, ApJ, 175, 417
Nelan, E. P., & Bond, H. E. 2013, ApJ, 773, L26
Nugis, T., & Lamers, H. J. G. L. M. 2002, A&A, 389, 162
Olson, G. L., & Kunasz, P. B. 1987, J. Quant. Spectr. Rad. Transf., 38, 325
Patterson, J. 1981, ApJS, 45, 517
Patterson, J., & Raymond, J. C. 1985a, ApJ, 292, 550
Patterson, J., & Raymond, J. C. 1985b, ApJ, 292, 535
Piro, A. L., & Bildsten, L. 2004a, ApJ, 616, L155
Piro, A. L., & Bildsten, L. 2004b, ApJ, 610, 977
Polidan, R. S., & Holberg, J. B. 1984, Nature, 309, 528
Popham, R. 1997, ApJ, 478, 734
Popham, R. 1999, MNRAS, 308, 979
Popham, R., & Narayan, R. 1995, ApJ, 442, 337
Pringle, J. E. 1977, MNRAS, 178, 195
Pringle, J. E., & Savonije, G. J. 1979, MNRAS, 187, 777
Prinja, R. K., & Rosen, R. 1995, MNRAS, 273, 461
Proga, D., Stone, J. M., & Drew, J. E. 1998, MNRAS, 295, 595
Rauch, T., Orio, M., Gonzales-Riestra, R., et al. 2010, ApJ, 717, 363

Regev, O. 1983, A&A, 126, 146
Regev, O., & Bertout, C. 1995, MNRAS, 272, 71
Revnivtsev, M. G., & Gilfanov, M. R. 2006, A&A, 453, 253
Revnivtsev, M. G., Burenin, R. A., Tkachenko, A. Y., et al. 2012, Astron. Lett., 38, 238
Revnivtsev, M. G., Suleimanov, V. F., & Poutanen, J. 2013, MNRAS, 434, 2355
Robertson, J. A., & Frank, J. 1986, MNRAS, 221, 279
Robinson, E. L., & Nather, R. E. 1979, ApJS, 39, 461
Shakura, N. I., & Sunyaev, R. A. 1973, A&A, 24, 337
Shaviv, G., & Wehrse, R. 1991, A&A, 251, 117
Sion, E. M., Long, K. S., Szkody, P., & Huang, M. 1994, ApJ, 430, L53
Sion, E. M., Godon, P., Myzcka, J., & Blair, W. P. 2010, ApJ, 716, L157
Suleimanov, V., & Poutanen, J. 2006, MNRAS, 369, 2036
Suleimanov, V., & Werner, K. 2007, A&A, 466, 661
Suleimanov, V. F., Lipunova, G. V., & Shakura, N. I. 2007, Astron. Rep., 51, 549
Suleimanov, V. F., Mauche, C. W., Zhuchkov, R. Y., & Werner, K. 2013, in 18th European White Dwarf Workshop., eds. J. Krzesiński, G. Stachowski, P. Moskalik, & K. Bajan, ASP Conf. Ser., 469, 349
Suleymanov, V. F. 1992, Sov. Astron. Lett., 18, 104

Swank, J. H. 1979, in White Dwarfs and Variable Degenerate Stars, eds. H. M. van Horn, & V. Weidemann, IAU Colloq., 53, 135
Tylenda, R. 1977, Acta Astron., 27, 235
Tylenda, R. 1981, Acta Astron., 31, 267
van der Klis, M. 1989, ARA&A, 27, 517
van der Klis, M. 2000, ARA&A, 38, 717
van Teeseling, A., & Verbunt, F. 1994, A&A, 292, 519
van Teeseling, A., Beuermann, K., & Verbunt, F. 1996, A&A, 315, 467
Velikhov, E. 1959, Sov. Phys. -JETP, 36, 1398
Verner, D. A., & Yakovlev, D. G. 1995, A&AS, 109, 125
Verner, D. A., Ferland, G. J., Korista, K. T., & Yakovlev, D. G. 1996, ApJ, 465, 487
Wade, R. A., & Hubeny, I. 1998, ApJ, 509, 350
Warner, B. 1986, Ap&SS, 118, 271
Warner, B. 2003, Cataclysmic Variable Stars (Cambridge: Cambridge University Press)
Warner, B., & Pretorius, M. L. 2008, MNRAS, 383, 1469
Warner, B., & Woudt, P. A. 2002, MNRAS, 335, 84
Zhang, E.-H., & Robinson, E. L. 1987, ApJ, 321, 813

Astronomy & Astrophysics

Wave mediated angular momentum transport in astrophysical boundary layers

Marius Hertfelder and Wilhelm Kley

Institut für Astronomie und Astrophysik, Abt. Computational Physics, Auf der Morgenstelle 10, 72076 Tübingen, Germany
e-mail: marius.hertfelder@gmail.com

ABSTRACT

Context. Disk accretion onto weakly magnetized stars leads to the formation of a boundary layer (BL) where the gas loses its excess kinetic energy and settles onto the star. There are still many open questions concerning the BL, for instance the transport of angular momentum (AM) or the vertical structure.

Aims. It is the aim of this work to investigate the AM transport in the BL where the magneto-rotational instability (MRI) is not operating owing to the increasing angular velocity $\Omega(r)$ with radius. We will therefore search for an appropriate mechanism and examine its efficiency and implications.

Methods. We perform 2D numerical hydrodynamical simulations in a cylindrical coordinate system (r, φ) for a thin, vertically integrated accretion disk around a young star. We employ a realistic equation of state and include both cooling from the disk surfaces and radiation transport in radial and azimuthal direction. The viscosity in the disk is treated by the α-model; in the BL there is no viscosity term included.

Results. We find that our setup is unstable to the sonic instability which sets in shortly after the simulations have been started. Acoustic waves are generated and traverse the domain, developing weak shocks in the vicinity of the BL. Furthermore, the system undergoes recurrent outbursts where the activity in the disk increases strongly. The instability and the waves do not die out for over 2000 orbits.

Conclusions. There is indeed a purely hydrodynamical mechanism that enables AM transport in the BL. It is efficient and wave mediated; however, this renders it a non-local transport method, which means that models of a effective local viscosity like the α-viscosity are probably not applicable in the BL. A variety of further implications of the non-local AM transport are discussed.

Key words. accretion, accretion disks – hydrodynamics – instabilities – waves – methods: numerical – stars: protostars

1. Introduction

One ubiquitous phenomenon in astrophysics is the accretion of matter on a central object via an accretion disk. This process can be observed for a variety of central objects, such as young stars, compact objects like white dwarfs or neutron stars, and active galactic nuclei. The physics of the accretion disk itself is reasonably well understood. However, the tiny region where the accretion disk connects to the star is still one of the major problems. In this region, called the boundary layer (BL), a smooth connection is established between the disk, which rotates nearly at Keplerian frequency, and the star, which in general rotates much more slowly. It is of great dynamical and thermal importance since the gas undergoes a supersonic velocity drop in a very confined region of a few percent of the stellar radius and loses up to one half of the total accretion energy during that process (Kluźniak 1987).

The BL has been studied extensively for over 40 years, both in an analytical (e.g. Bertout & Regev 1992) and a numerical approach (e.g. Kley & Hensler 1987). Simulations involving the BL around a young star have been performed by Kley & Lin (1996, 1999), including full radiation transport. Most of the work that has been done on the BL (see e.g. Hertfelder et al. 2013, for a brief review of the history) assumes that the gas first slows down in the equatorial plane of the disk and then spreads around the star. This is the classical picture of the BL. However, there

is an alternative theory called the *spreading layer* (Inogamov & Sunyaev 1999, 2010), which was initially developed for neutron stars. Within this concept the gas first spreads around the star because of the ram pressure in the BL and then slows down on the whole surface of the star.

The majority of the simulations of the BL start from the premise that the observed angular momentum (AM) transport in the BL is driven by local turbulent stresses and the authors consequently adopt a α-viscosity model (Shakura & Sunyaev 1973) in their simulations. Sometimes the classical α-model is modified slightly in order to prevent supersonic infall velocities (Kley & Papaloizou 1997) or, for instance, to take into account the radial pressure scale height in the BL (Popham & Narayan 1995). The utilization of a local viscosity model was later justified for the disk by the discovery of the magnetorotational instability (MRI) which creates turbulence that acts like a genuine viscosity on macroscopic scales (Velikhov 1959; Chandrasekhar 1960; Balbus & Hawley 1991, 1998; Balbus 2003; Balbus & Lesaffre 2008). However, as pointed out by Godon (1995) and Abramowicz et al. (1996) and recently shown by Pessah & Chan (2012), if the angular velocity increases with radius, $\mathrm{d}\Omega/\mathrm{d}r > 0$, the MRI is effectively damped out and the associated AM transport oscillates about zero. Since this situation clearly applies for the BL, we do not expect to obtain sufficient AM transport through the MRI. There have been various alternative transport mechanisms proposed, among them the Kelvin-Helmholtz

instability (Kippenhahn & Thomas 1978), the baroclinic insta-
bility (Fujimoto 1993), and the Tayler-Spruit dynamo (Tayler
1973; Spruit 2002; Piro & Bildsten 2004), none of which have
yet been proven to efficiently transport mass and AM in the BL.

In this work, we will focus on the AM transport in the BL
through non-axisymmetric instabilities and therefore carry out
2D simulations in the midplane of the star-disk system using
cylindrical coordinates. Recently, a promising candidate for the
transport has been proposed and investigated in a series of pa-
pers. According to this theory, the steep velocity drop in the
BL is prone to the sonic instability (Glatzel 1988; Belyaev &
Rafikov 2012), which is an instability of a supersonic shear
layer, much like the Papaloizou-Pringle instability (Papaloizou
& Pringle 1984; Narayan et al. 1987). Acoustic waves are ex-
cited in the BL as a consequence of the sonic instability and AM
can be transported by these modes in an efficient way. This has
been demonstrated for 2D flows (Belyaev et al. 2012), 3D flows
in cylindrical coordinates (Belyaev et al. 2013a), and even for
3D magnetohydrodynamical flows (Belyaev et al. 2013b). The
wave mediated AM transport implies that this process is intrisi-
cally non-local since the waves can potentially travel a long way
before they dissipate and release the AM to the fluid. Therefore,
it is problematic to describe the AM transport in the BL by
means of a local viscosity like the α-model. Although the above-
mentioned simulations are already quite sophisticated, the au-
thors make some simplifications that constrain the validity of
their models. This is the point where we step in with this paper
and relax three of the simplifications made. First, we make use
of a realistic equation of state instead of an isothermal one and
propagate the temperature of the system, as well. We use full ra-
diative diffusion in the disk plane and an approximation for the
vertical flux, and hence employ a quasi-3D radiation transport.
Second, we use realistic, state-of-the-art initial models like those
already published in Hertfelder et al. (2013) as a starting point
for the simulations presented here. Third, mass constantly enters
the simulation domain from the outer boundary and thus there is
a net mass flow through the disk, as is the case for a real accre-
tion disk. Because of the high computational costs the treatment
of the radiation brings with it, we perform 2D simulations and
do not yet include magnetic fields. Thus, the next steps will be to
extend the simulations presented here to 3D and also to include
magnetic fields.

The paper is organized as follows. In Sect. 2, the basic phys-
ical model is described. We give an overview of the equations
used for our simulations and present the assumptions we have
made. Furthermore, we briefly review how the AM transport due
to stresses in the fluid can be measured and quantized. Section 3
is devoted to the numerical method that we employ in our simu-
lations. We discuss the numerical code, the initial and boundary
conditions, as well as the model parameters. In Sect. 4 we start
the analysis of the results. We first discuss the sonic instabil-
ity and the acoustic modes that are excited in the BL. Then, in
Sect. 5, we investigate how these instabilities affect the physi-
cal picture of the BL and look deeply into the AM transport and
long-term behavior of our models. We conclude with Sect. 5.

2. Physics

In this section, we present the physical foundations for the sim-
ulations we have performed and that are described later in this
publication. In order to investigate non-axisymmetric behavior
in the disk plane, we utilized the vertically integrated Navier-
Stokes equations. Since the focus of our current work lies on
instability developing in the BL, we describe the flow of a

perturbed, compressible fluid and also the derivation of the re-
sulting Reynolds stresses.

2.1. Two-dimensional equations for a flat disk

In order to obtain a set of 2D Navier-Stokes equations includ-
ing radiation transport, we apply a cylindrical coordinate system
with coordinates (r, φ, z) and integrate the 3D equations over the
vertical coordinate z. The star lies in the center of the coordinate
system and the midplane of the disk coincides with $z = 0$. If we
assume a Gaussian profile for the mass density ρ, we can define
the 2D *surface density* by

$$\Sigma = \int_{-\infty}^{\infty} \rho \, dz = \sqrt{2\pi} \rho(r, \varphi, 0) H, \qquad (1)$$

where we introduce the effective pressure scale height H, which
is a measure of the vertical extent of the disk. Under the assump-
tion of hydrostatic balance and an isothermal equation of state in
the z-direction, the pressure scale height reads

$$H = \frac{c_s}{\Omega_K}, \qquad (2)$$

with c_s and $\Omega_K = \sqrt{GM_*/r^3}$ being the midplane soundspeed
and the Keplerian angular velocity, respectively. The inverse of
$\Omega_K(R_*)$ is proportional to the period of a Keplerian orbit at the
surface of the star, $P_* = 2\pi/\Omega_K(R_*)$. Derivatives with respect to z
are neglected, as is the z-component of the velocity, u_z. Clearly,
this is not a reasonable assumption if one wants to investigate the
overall structure of the BL. However, it is still justified since we
restrict ourselves to the study of non-axisymmetric flow struc-
ture in this work.

The vertically integrated continuity equation reads

$$\frac{\partial \Sigma}{\partial t} + \frac{1}{r}\frac{\partial(r\Sigma u_r)}{\partial r} + \frac{1}{r}\frac{\partial(\Sigma u_\varphi)}{\partial \varphi} = 0. \qquad (3)$$

We express the momenta equations in terms of the conservative
variables and introduce the radial momentum density $s = \Sigma u_r$
and the angular momentum density $h = \Sigma r u_\varphi \equiv \Sigma r^2 \Omega$. These
variables reflect the physically conserved quantities, as opposed
to the primitive variables u_r and u_φ. The conservation of momen-
tum in radial direction is then given by

$$\frac{\partial s}{\partial t} + \frac{1}{r}\frac{\partial(rsu_r)}{\partial r} + \frac{1}{r}\frac{\partial(su_\varphi)}{\partial \varphi} - \Sigma\frac{u_\varphi^2}{r} = -\frac{\partial p}{\partial r} + \frac{1}{r}\frac{\partial(r\sigma_{rr})}{\partial r} + \frac{1}{r}\frac{\partial(\sigma_{r\varphi})}{\partial \varphi}$$
$$-\frac{1}{r}\sigma_{\varphi\varphi} - \Sigma\frac{\partial\Phi}{\partial r}, \qquad (4)$$

and the equation in azimuthal direction reads

$$\frac{\partial h}{\partial t} + \frac{1}{r}\frac{\partial(rhu_r)}{\partial r} + \frac{1}{r}\frac{\partial(hu_\varphi)}{\partial \varphi} = -\frac{\partial p}{\partial \varphi} + \frac{1}{r}\frac{\partial(r^2\sigma_{r\varphi})}{\partial r}$$
$$+\frac{\partial(\sigma_{\varphi\varphi})}{\partial \varphi} - \Sigma\frac{\partial\Phi}{\partial \varphi}. \qquad (5)$$

Here p denotes the vertically integrated pressure $p = \Sigma R_G T/\mu$,
where $R_G = k_B/m_H$ with Boltzmann's constant k_B and the mass
of hydrogen m_H, T is the temperature, and μ is the mean molec-
ular weight; $\Phi = -GM_*/r$ is the gravitational potential (G and M_*
are the gravitational constant and stellar mass). The components
of the vertically integrated viscous stress tensor, σ_{ij}, can be

found in e.g. Masset (2002). The equation for the conservation of energy is given by

$$
\frac{\partial e}{\partial t} + \frac{1}{r}\frac{\partial(reu_r)}{\partial r} + \frac{1}{r}\frac{\partial(eu_\varphi)}{\partial \varphi} = -p\left[\frac{1}{r}\frac{\partial ru_r}{\partial r} + \frac{1}{r}\frac{\partial u_\varphi}{\partial \varphi}\right] + \sigma_{rr}\frac{\partial u_r}{\partial r}
$$
$$
+ \sigma_{r\varphi}\left[\frac{1}{r}\frac{\partial u_r}{\partial \varphi} + r\frac{\partial \Omega}{\partial r}\right] + \sigma_{\varphi\varphi}\left[\frac{\partial \Omega}{\partial \varphi} + \frac{u_r}{r}\right]
$$
$$
- 2\sigma_{SB}T_{eff}^4 - \frac{H}{r}\left[\frac{\partial(rF_r)}{\partial r} + \frac{\partial F_\varphi}{\partial \varphi}\right], \tag{6}
$$

where σ_{SB} and T_{eff} are the Stefan-Boltzmann constant and the effective temperature, and the factor H follows from the vertical integration.

The last line of Eq. (6) incorporates the radiative flux in the flux-limited diffusion approximation,

$$
\mathbf{F} = -K_R\nabla T. \tag{7}
$$

Utilizing this approach, we assume that the BL is optically thick both in the radial and vertical directions, where the inclusion of a flux-limiter also allows for the treatment of optically thin regions. Equation (7) has exactly the same mathematical form as molecular heat conduction in a gas. The effective radiative conductivity K_R is

$$
K_R = \frac{4\lambda ac T^3}{\kappa_R\rho}, \tag{8}
$$

where κ_R, a, and c are the Rosseland mean opacity, the radiation constant and the speed of light, and λ is the flux limiter (Levermore & Pomraning 1981; Levermore 1984). We adopt the formulation given by Kley (1989) for λ. We assume that the disk locally radiates like a blackbody of temperature T_{eff} and associate the vertical flux with the blackbody luminosity divided by the radiating area, $F_z = \sigma_{SB}T_{eff}^4$. The factor 2 in Eq. (6) stems from the fact that the disk has two sides. The vertical flux provides the cooling of the disk, while the other parts of the energy equation generate heat through viscous dissipation (second line in Eq. (6)) or redistribute it in the disk plane (the terms with F_r and F_φ). The effective temperature T_{eff} is evaluated according to Hubeny (1990), who approximates the optical depth in the vertical direction of the disk (see Sect. 5.3). By approximating the flux in the vertical direction as well, we employ a quasi-3D radiation transport.

We also adopt a piecewise prescription for the Rosseland mean opacity, where in each temperature regime κ_R is given by a power-law approximation, $\kappa_R = \kappa_0\rho^a T^b$, as described in Lin & Papaloizou (1985) and Bell & Lin (1994). Each of the regimes is characterized by a prevailing mechanism that dominates the opacity in this region. The parameters κ_0, a, and b for the various opacity regimes are listed in e.g. Müller & Kley (2012).

2.2. Viscosity

In the simulations presented here, we strictly distinguish between the BL and the disk with regard to viscosity. As has already been mentioned in Sect. 1, the AM transport in the disk is mainly driven by turbulent stresses due to the MRI and can therefore be parametrized with the classic α-viscosity approach by Shakura & Sunyaev (1973). The effective kinematic viscosity is written as

$$
\nu = \alpha c_s H \tag{9}
$$

in this ansatz, where α is a dimensionless parameter whose value is derived from MRI simulations. The cause of the AM

in the BL and its investigation is, however, the subject of this work. Consequently, we do not make use of an additional viscosity term in the BL region. The entire AM transport in the BL is therefore due solely to the Reynolds stresses exerted by the gas.

From a numerical point of view, the distinction between the BL and the disk is made by searching for the global maximum of the radial angular velocity profile, $\Omega(r_{max}) = \Omega_{max}$. This has to be done for every angle φ in order to prevent a suppression of non-axisymmetric perturbations. We can then computationally realize the viscosity as pointed out above by utilizing the following conditions:

- if $r < r_{max}$, we set $\alpha = 0$ in Eq. (9) and no viscosity is applied (*BL region*);
- if $r > r_{max}$, α is set to the default value, $\alpha = 0.01$, and the viscous stress tensor does not vanish (*disk region*).

2.3. Reynolds stresses

Gas flows in general can be characterized by a laminar bulk flow with superimposed perturbations. One typical approach is to decompose the flow variables f into an averaged or filtered part $\bar{f}$ and a fluctuating or subfiltered, unresolved part f':

$$
f(\mathbf{r}, t) = \bar{f}(\mathbf{r}, t) + f'(\mathbf{r}, t). \tag{10}
$$

Within the classical Reynolds approach, the averaging is performed over an ensemble of systems, thus $\bar{f}$ is an ensemble mean. In the case of a statistically steady or stationary flow field, or when it is homogeneous, *ergodicity* can be assumed. This means that both a sufficiently long time average over many time scales and a spatial average over many length scales correspond to the ensemble mean. Often, practical flows are inhomogeneous and the ensemble mean is replaced by a time average:

$$
\bar{f}_\tau(\mathbf{r}, t; \tau) = \frac{1}{\tau}\int_{t-\tau}^t f(\mathbf{r}, t')\,dt'. \tag{11}
$$

If, on the other hand, there is a symmetry in at least one direction, as there is in our case, a spatial average is also a viable solution.

The actual average process in the Reynolds decomposition is a simple arithmetic mean over space or time (see Eq. (11)). A more common approach in the case of compressible flows, however, is to use a density-weighted Reynolds average for the filtered part of the variables (Gatski & Bonnet 2013; Peyret 1996; Balbus & Papaloizou 1999). These density-weighted, or *Favre* variables are given by a decomposition, which reads

$$
f = \tilde{f} + f'' \quad \text{with} \quad \tilde{f} = \frac{\overline{\rho f}}{\bar{\rho}}, \tag{12}
$$

where the bar denotes a Reynolds average and the tilde a Favre average.

After performing a decomposition (of any kind) of the flow field, one can then derive the Navier-Stokes equations for the mean or resolved field. They are called the Reynolds-averaged Navier-Stokes (RANS) equations, or, in the case of a Favre mean, the Favre-averaged Navier-Stokes (FANS) equations (e.g. Gatski & Bonnet 2013; Peyret 1996). Those mean field equations contain additional terms, however, that are dependent on the fluctuating part of the flow variables. In many engineering applications where simulations of the mean field are performed, those parts are unknown and have to be dealt with by using appropriate closure relations or models. Here, on the other hand,

we are running direct numerical simulations and solve for the actual values of the flow field variables. From these simulations, we can compute the additional terms, which appear in the averaged equations.

From the FANS equations, we obtain the Reynolds stresses exerted by the fluctuating motion of the gas. For accretion disks, the dominant contribution is given by

$$R_{r\varphi} = \overline{\Sigma u_r u_\varphi} - \overline{\Sigma} \tilde{u}_r \tilde{u}_\varphi, \tag{13}$$

where we have already performed a vertical integration. The quantity $R_{r\varphi}$ appears in the angular momentum Eq. (5), where it adds to $\sigma_{r\varphi}$. We note that for the second part in Eq. (13), it is incorrect to use either the mean values of the laminar flow (i.e. the initial values, when starting from a relaxed model) or assume $\tilde{u}_r \approx 0$. Our simulations showed that the instability-dominated state has other mean values than the laminar flow state, and that both terms in Eq. (13) are approximately of the same order of magnitude. Our simulations also showed that for the quasi-stationary state both temporal and azimuthal averaging procedures yield the same mean values since the evolution of the BL is significantly slower than an orbital period. Therefore, we mostly used azimuthal averaging for the mean values since it is computationally far less expensive.

The vertically integrated Reynolds stress, which has the dimensions of a 2D pressure, can be expressed by a dimensionless parameter α_{Re} via

$$\alpha_{Re} = \frac{R_{r\varphi}}{\Sigma c_s^2}. \tag{14}$$

Comparing the strength of the Reynolds stresses and the viscous stresses, we can identify $R_{r\varphi} = -\sigma_{r\varphi}$ and calculate an effective viscous α_ν from this equation. This relation is given by

$$\alpha_\nu = -\frac{R_{r\varphi}}{\Sigma c_s \ell r \frac{\partial \Omega}{\partial r}}, \tag{15}$$

where ℓ is the turbulent scale height in the BL, which is approximated to be the smaller of the disk scale height H and the radial pressure scale height (see Papaloizou & Stanley 1986; Popham & Narayan 1995).

2.4. Transport of mass and angular momentum

The mass and AM transport in the disk are two important quantities when we are interested in the effectivity of the Reynolds stresses in the BL. Both result from the 1D stationary hydrodynamic equations, where they play the role of eigenvalues. The mass flux is obtained from the continuity equation and reads

$$\dot{M} = 2\pi r \overline{\Sigma u_r}. \tag{16}$$

The angular momentum flux follows from the momentum equation in azimuthal direction and is given by

$$\dot{J} = 2\pi r^2 \overline{\Sigma u_r u_\varphi} - 2\pi r^2 \overline{\sigma}_{r\varphi} + 2\pi r^2 R_{r\varphi}. \tag{17}$$

Most commonly, the AM flux $\dot{J}$ is expressed as a dimensionless parameter j, which is the AM flux normalized to the advective AM flux at the surface of the star:

$$j = \frac{\dot{J}}{\dot{J}_*}, \qquad \dot{J}_* = \dot{M} R_*^2 \Omega_K(R_*). \tag{18}$$

Either flux is defined such that if mass or AM are traveling outward, $\dot{M}$ and $\dot{J}$ are positive. The three terms in Eq. (17) can be identified as the advective AM transport, the viscous transport, and the transport due to Reynolds stresses. Both $\dot{M}$ and $\dot{j}$ are constant with respect to space and time only if the system has reached a stationary state, i.e. $\partial/\partial t = 0$. Then, $\dot{M}$ equals the imposed mass flux that is set as a boundary condition. For non-stationary states, $\dot{M}$ and $\dot{j}$ represent the local mass and AM flux at a certain time.

3. Numerics

3.1. General remarks

We used the code `fargo` (Masset 2000) with modifications of Baruteau (2008) for the simulations presented in this paper. `fargo` is a specialized hydrodynamics code for simulations of an accretion disk in cylindrical coordinates (r, φ) that exploits the advantages of the FARGO algorithm (Masset 2000). The FARGO algorithm is a special method for the azimuthal transport in differentially rotating disks that is able to speed up the simulations by up to one order of magnitude and exhibits a lower numerical viscosity than the usual transport algorithm. The speed-up works best when the velocity perturbations are smaller than the bulk flow in azimuthal direction. Since the average azimuthal velocity $\overline{u}_\varphi(r)$ changes significantly in the course of the simulations, the background rotational profile for the FARGO algorithm is updated at each time step in order to gain full benefit of the method. The algorithm has also been shown to produce valid results when shocks are created in the disk (Masset 2000). The radiative diffusion in the flux-limited approximation (Eq. (7)) is solved implicitly using a successive over-relaxation (SOR) method (see Müller & Kley 2013). The code has been tested and used extensively for a variety of applications. In order to verify its suitability for simulations of the BL, we compared it to the 1D BL code described in Hertfelder et al. (2013) and found a perfect agreement for the 1D models.

3.2. Boundary and initial conditions

To model the BL with a net mass flow through the disk we have implemented specific boundary conditions in `fargo`. At the outer boundary we impose a mass flux $\dot{M}$ which goes into the disk and whose absolute value can be chosen as a parameter. We require the azimuthal velocity to be Keplerian at the outer boundary, $u_\varphi(r_{out}) = r_{out}\Omega_K(r_{out})$. Modeling the inner boundary, i.e. the beginning of the star, is more difficult. Since we are treating the problem in cylindrical geometry in the disk plane, we cannot simultaneously simulate the outer parts of the star. Therefore, we start the simulation domain of all our simulations at $r_{in} = 1R_*$, where R_* is the radius of the chosen star, and set the azimuthal velocity to the velocity of the rigidly rotating star, $u_\varphi(r_{in}) = R_*\Omega_*$, i.e. we impose a no-slip boundary condition in φ-direction. The radial velocity is set to a certain fraction $\mathcal{F}$ of the Keplerian velocity

$$u_r(r_{in}) = -\mathcal{F} r_{in} \Omega_K(r_{in}). \tag{19}$$

This is obviously an outflow BC for the radial velocity at the inner boundary and it is necessary since the matter which is inserted in the domain from the outer boundary must be allowed to leave again at the inner boundary. The factor $\mathcal{F}$ determines how deep the inner boundary r_{in} is located inside the star: the smaller $\mathcal{F}$ is, the deeper the domain ranges into the star. The actual choice of $\mathcal{F}$ is a trade-off between containing a sufficient part of the stellar envelope in the domain and avoiding densities

and temperatures that are too high at the inner boundary to prevent the simulations from being slowed down too much. A value of $\mathcal{F} = 10^{-6}$ is used in our simulations. We have tested different values of $\mathcal{F}$ and found that it does not have any influence on the initial models apart from shifting the radial profiles by a small amount in r. In particular, it does not have an effect on the mass flux through the inner boundary once the initial model is in an equilibrium state. Instead, the density adjusts such that $\dot{M}$ at the inner boundary equals the value at the outer boundary. Apart from the special boundary treatment mentioned above, we impose zero-gradient or Neuman-type boundary conditions for the remaining variables, which means that the normal derivative at the boundary vanishes.

The 2D simulations were started from fully relaxed 1D axisymmetric BL models which were generated using the same methods as in Hertfelder et al. (2013). Those simulations use a classical α-parametrization for the viscosity with a uniform value of $\alpha = 0.01$ both in the disk and the BL. We employed these models to have realistic profiles for the density and temperatures as initial conditions. After the 1D models reached a stationary state we extended them to 2D input data for `fargo` and ran them again with a small number of azimuthal cells until they were fully relaxed. Following this *burn-in* procedure we started the actual simulations from these axisymmetric initial conditions with full resolution in r and φ. Prior to the start, the radial velocity was randomly perturbed by 1% of the Keplerian velocity at the surface of the star. The initial profiles are shown in Fig. 10 below (dashed lines).

3.3. Model parameters

In this paper we focus on the non-axisymmetric instabilities and the AM transport in the BL. We chose the physical system of a BL around a young star, because the ratio of the mass and the radius of the star, M_*/R_*, is much smaller than, for instance, for a white dwarf, which we considered in a previous paper about the BL. This ratio determines the radial scale height in the BL and the smaller H is, the higher the resolution must be in order to resolve the BL correctly. Therefore, the computational costs increase enormously when one goes to more compact objects. However, we expect what we find here to be the generic case.

The young star we consider in this paper has one solar mass, $M_* = M_\odot$, and is three times the radius of the sun, $R_* = 3 R_\odot$. It has an effective temperature of $T_* = 3000$ K which yields a luminosity of $3 L_\odot$. The star is not rotating, i.e. $\Omega_* = 0$, which is slightly below the observations (Cohen & Kuhi 1979), but was chosen for the sake of a large velocity drop. We impose a mass accretion rate of $\dot{M} = 10^{-6} M_\odot/\text{yr}$, which is a typical value for T Tauri stars such as HL Tau (Hayashi et al. 1993; Lin et al. 1994), and is two orders of magnitude smaller than the accretion rate FU Orionis stars can reach in outburst phases (Hartmann et al. 1993). We took $\alpha = 0.01$ for the viscosity parameter in the disk and $\alpha = 0$ for the BL (see Sect. 2.2). We consider the following four simulations for this work.

- Simulation A: it has a resolution of 512×512 and the radial domain ranges from R_* to $2R_*$. This simulation features the lowest resolution of all runs performed.
- Simulation B: this is the reference simulation, and unless stated otherwise, we always refer to it in the text. It has a simulation domain of $[R_*, 2R_*]$ and a resolution of 1024×1024.
- Simulation C: here, the number of grid cells is doubled in each direction and hence the resolution is given by 2048×2048. The simulation time for this resolution is

very high and we are not able to study the long-term evolution for this run.
- Simulation D: in order to ensure that the radial domain in simulations A-C is not too small, we increased it to $[R_*, 5R_*]$. While the first three simulations utilized an arithmetic grid, we chose a logarithmic spacing in radius for this run along with a resolution of 1024×1024.

4. Boundary layer instability

In this section, we will summarize the key features of the sonic instability and its associated acoustic waves in the BL (Glatzel 1988; Belyaev & Rafikov 2012; Belyaev et al. 2012, 2013a) and demonstrate that our models are also prone to the sonic instability.

4.1. Sonic instability

The sonic instability arises in supersonic shear flows and is a non-local instability similar to the Papaloizou-Pringle instability (Papaloizou & Pringle 1984; Narayan et al. 1987; Glatzel 1988). It is the analogue of the classical KH instability in the regime of a supersonic drop in the velocity of a compressible, stratified fluid. The sonic instability has recently been studied in the context of the BL extensively by Belyaev & Rafikov (2012).

There are two ways by which the sonic instability operates: The first is the *overreflection* of sound waves from a critical layer that corresponds to the corotation resonance in a rotating fluid, i.e. the radius where the pattern frequency of the mode matches the rotation frequency of the bulk flow. This mechanism results in a dispersion relation that features several sharp peaks and hence discrete modes are clearly favored, especially if the density contrast across the shear interface is high (see e.g. panel (n) of Fig. 3 in Belyaev & Rafikov 2012). Each mode can be associated with a pseudo-energy, or conserved action (angular momentum), which can leak through the critical layer when a mode is reflected at the corotation resonance (Narayan et al. 1987). The tunneled wave has the opposite sign of the action and, since it is a conserved quantity, the reflected wave must undergo an increase in its action in order to globally compensate for the additional negative action. Thus, the reflected wave is amplified. Furthermore, if a mode is trapped such that it performs multiple reflections at the corotation resonance, this amplification mechanism, called the corotation amplifier (e.g. Mark 1976), eventually leads to instability.

The other destabilizing mechanism is the *radiation* of energy away from the BL. If a mode inside the BL has a negative action density, it becomes even more negative through the radiation mechanism and, consequently, is amplified, which results in further instability. The dispersion relation of this destabilizing mechanism is a smooth function of the wave vector. Therefore, a continuum of modes are associated with it. This mechanism dominates the overreflection for a small density contrast on either side of the interface (see again Fig. 3 of Belyaev & Rafikov 2012).

Each mechanism, the overreflection and the radiation, is most efficient in the regime of large density contrast or equal density, respectively, and they operate together. The growth rates of the sonic instability are approximately $1/P_*$, and the dependence of the growth rate on the density contrast is small, despite the different destabilizing mechanisms. This further distinguishes the sonic instability from the KH instability. In the numerical simulations of the BL, a very high numerical resolution is necessary to correctly reproduce the growth rate of
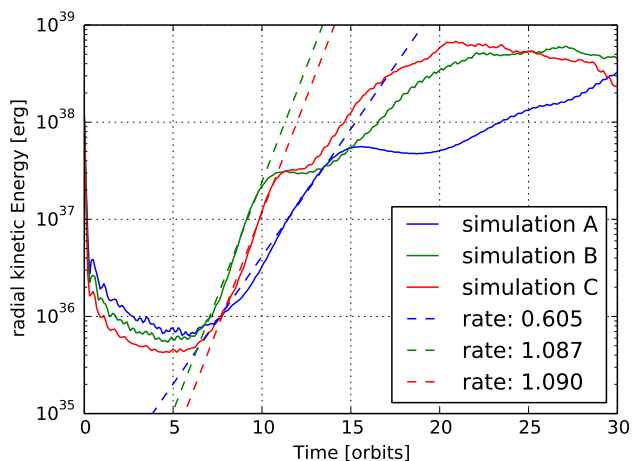
Fig. 1. Total radial kinetic energy as a function of the very first orbits for three simulations mentioned in Sect. 3.3, which differ only in their spatial resolution. At around orbit 5, the sonic instability starts to operate in all three cases, and as a result, the radial kinetic energy rises rapidly. The growth rates were obtained by applying an exponential fit to the first exponential increase.

the sonic instability. Such a high resolution is computationally very demanding and costly, especially for investigations of the long-term evolution of the BL. However, as has been shown by Belyaev & Rafikov (2012) and revisited in Belyaev et al. (2012), a lower resolution merely leads to a slower growth of the instability.

We confirm this point by comparing the growth rates of three simulations with different spatial resolution. Figure 1 shows the evolution of the radial kinetic energy when the sonic instability starts to set in for the three resolutions 512×512, 1024×1024, and 2048×2048. Indeed, the simulation with the lowest spatial resolution underestimates the growth rate by a factor of ∼1.8. However, the simulations with 1024^2 and 2048^2 cells both yield an almost identical growth rate of 1.09 per orbit. The shear layer with positive gradient of Ω is initially resolved with approximately 150 and 300 cells in radial direction, respectively. In simulation A, we only have about 75 cells across the velocity drop. We also verify by Fig. 1 that the growth rates of the sonic instability, which are of the order of 1 per orbit, are actually very high. We will now focus again on our reference simulation, although all simulations behave basically the same. After about ten orbits, the rise of the radial kinetic energy is interrupted briefly and then continues with a slightly different growth rate. The paused increase in the instability and the change in growth rate is due to the change in density and velocity in the shearing region with time. Since the mass inside the BL is delivered from the disk, the density in the vicinity of the velocity drop rises. The velocity itself changes as a result of the initiated angular momentum transport. As has already been mentioned and is elucidated in Belyaev & Rafikov (2012), the growth rate of the sonic instability shows a weak dependence on the density ratio and the modes depend on the slope of the velocity drop, as well. Thus, a change in the instability mechanism can be observed at this time.

We now have a closer look at how the sonic instability manifests itself in the radial velocity and consider Fig. 2 for this purpose. The upper panel is a snapshot taken after five orbits and the lower panel shows u_r at $t = 10$ orbits. In both panels, the velocity is normalized to the Keplerian velocity at the surface of the star. Figure 2a features a distinct boundary at $r_{crit} \approx 1.19$, which

coincides with the inflection point in $\Omega(r)$ and we can clearly see sound waves on either side, propagating away from the boundary. The pattern speed equals the rotation rate of the unperturbed flow at the location of the boundary and thus we associate it with the critical layer, or corotation resonance, which we have already introduced. It is also clearly noticeable that the modes undergo a phase shift across the critical layer. Both features are a clear signature of the sonic instability and we can compare Fig. 2a to Fig. 2 of Belyaev et al. (2012) and Fig. 5a of Belyaev & Rafikov (2012) to verify that our model is indeed unstable to the sonic instability.

Figure 2b depicts the radial velocity five orbits later and the appearance has already noticeably change. The amplitude of the sound waves in the lower panel is at least a factor of 2 larger than that in the upper panel and amounts to a large percentage of the azimuthal velocity. The picture shows a distinct pattern of wave front crossings and reflections for $r < r_{crit}$ and the critical layer at $r_{crit} = 1.19$ has already begun to smear out at this point in time. When the color scale is saturated we recognize three regions where the amplitude of the waves is dropping owing to the wave fronts crossing each other. They lie at $r \approx 1.16, 1.12$, and 1.07. Inside the corotation resonance, the waves are reflected near the inner boundary and at the critical layer, and are thus trapped between the two radii. We have traced three wave fronts with the black lines to illustrate the pattern that is exactly the overreflection mechanism that we have already elucidated. The pattern number of the sonic instability (15 for the simulation shown in Fig. 2) does not depend on details of the inner boundary condition. This has been verified by running the same simulation with identical perturbations with modified boundary conditions, where all variables are kept at their initial values for all time ("do-nothing" BCs). The pattern number is, instead, set by the initial random perturbation. For a different seed of the initial perturbations the pattern number will be different. When the trapped waves undergo a reflection at the critical layer, part of the wave action leaks through the critical layer and has the opposite sign compared to the reflected wave, whose amplitude grows as a consequence of the global conservation of wave action. Thus, the whole process is self-sustaining and even grows with time. The leakage of wave action is also clearly visible in Fig. 2b for $r > r_{crit}$. Now the reason for the change in the growth rate of the sonic instability after about ten orbits (see Fig. 1) becomes apparent: It is simply the overreflection mechanism setting in, gaining in strength, and growing dominant.

4.2. The BL modes

In Sect. 4.1 we described the linear growth regime of the sonic instability and analyzed its manifestation in our models. After only 20–30 orbits the sonic instability saturates and the system remains in the excited state with a radial kinetic energy that is approximately three orders of magnitude larger than before the sonic instability set in. There are still considerable variations in the radial kinetic energy (see Fig. 6); however, we suggest that they a result of a secondary KH like instability that sets in periodically and dies out shortly after. This theory is examined thoroughly in Sect. 5.2.

After the sonic instability has saturated we observe waves that are acoustic in nature propagate through the largest part of the domain. Those modes have been excited by the sonic instability and do not die out for the whole simulation time, which amounts to over 2000 orbits. Considerable effort has been expended by Belyaev & Rafikov (2012) and Belyaev et al. (2012, 2013a) in order to analyze these acoustic modes by means of
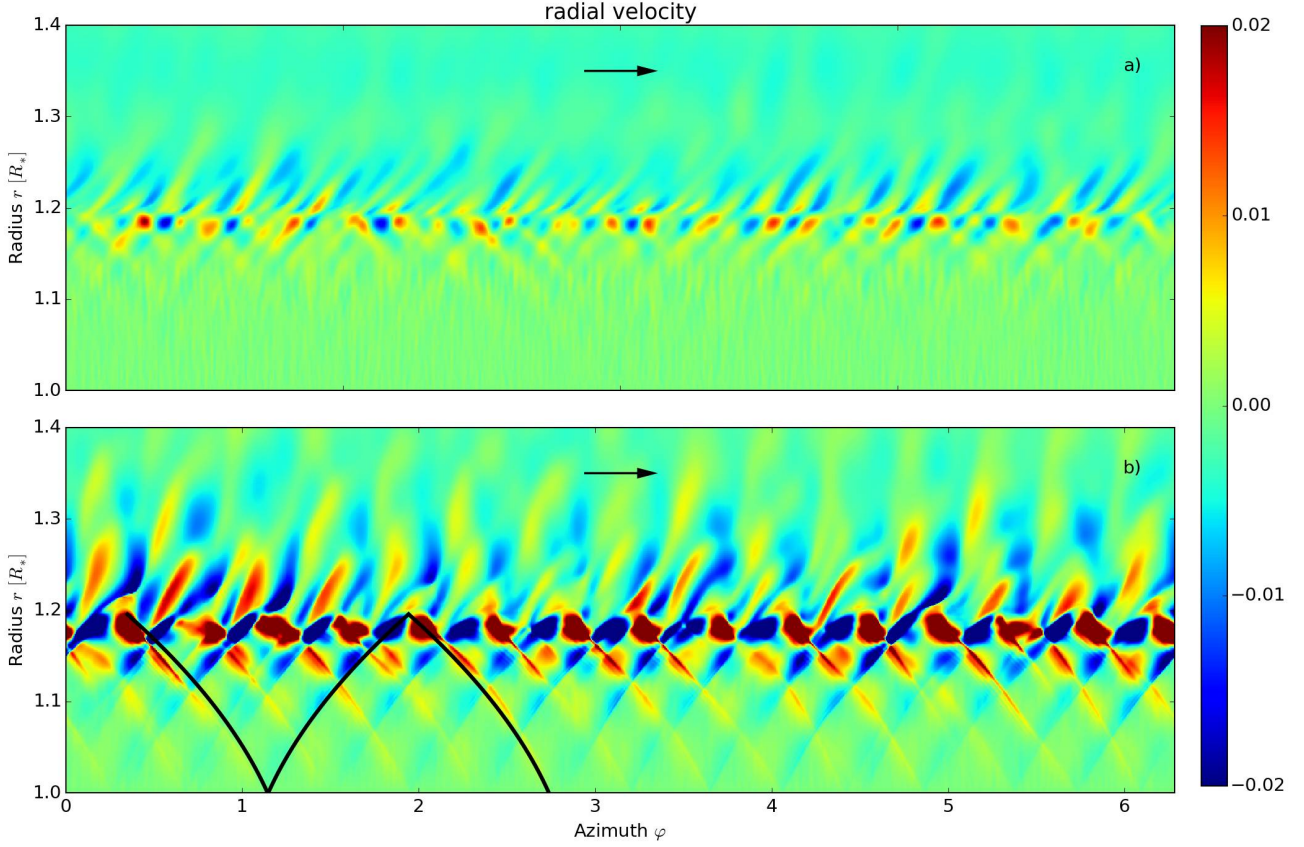
Fig. 2. r-φ plot of the radial velocity in units of $u_K(R_*)$ at $t = 5$ **a)** and $t = 10$ **b)** orbits. The velocity in the *upper panel*, **a)**, has been multiplied by a factor of 2 in order to use the same colormap as below. Both snapshots show the linear stage of the sonic instability and the middle branch in action. The sound waves are propagating toward the inner and the outer edge of the domain in an oblique fashion. The three black lines in panel **b)** illustrate the wavefronts. The arrows denote the direction of the unperturbed azimuthal flow.

linear stability analysis and derive proper dispersion relations. Since this undertaking is quite involved we limit ourselves to reviewing those elements that are crucial for the understanding of our results.

One finds that the acoustic modes of the BL are related to the waves in a plane parallel vortex sheet in the supersonic regime (Belyaev et al. 2013a). For a discontinuous drop of velocity in the isothermal vortex sheet in absence of stratification or rotational effects it can be shown that the linearized Euler equations yield three different expressions for the dispersion relation ω, which are denoted the lower, middle, and upper branch (Belyaev & Rafikov 2012). The three branches differ in the direction of propagation of the modes on either side of the interface (velocity drop) and their general appearance is depicted in Fig. 4 of Belyaev et al. (2013a). The lower and upper branch are very similar to each other. They both show a region where the waves propagate parallel to the interface and a region where the wave vector forms an angle between 0 and $\pi/2$ with respect to the normal vector of the interface. Transferred to the formalism of our models, the modes of the lower branch propagate purely in φ-direction in the BL and both in r and in φ in the disk, where $k_r/k_\varphi \gg 1$, however. For the upper branch, the opposite applies. Modes of the middle branch propagate in an oblique manner both in the disk and in the BL with the same wave vector. Furthermore, the waves undergo a phase shift of π at the interface. This holds true for all branches. The dispersion relations of the three branches of the vortex sheet can then be extended by

including radial stratification and the effects of rotation (Coriolis force) and one can find approximate dispersion relations for a more realistic case of a BL. This was done in Belyaev et al. (2013a) for the isothermal BL. It would be interesting to see how a realistic equation of state and the radiation transport affect the dispersion relations. However, this is beyond the scope of this paper.

Figure 3 is a r-φ plot of the radial velocity after 45 orbits. Three white dashed contour lines of the azimuthal velocity u_φ have been overdrawn. All velocities are, as usual, given in units of the Keplerian velocity at the surface of the star. The image shows a standing wave in azimuthal direction for radii $\lesssim 1.17$ and a wave that propagates into the disk with wave vector components in both r- and φ-directions. Additionally, the amplitude of the wave changes sign at $r \approx 1.17$, i.e. the phase is shifted by $\pi/2$. This pattern is a clear signature of the lower branch of the acoustic modes, which we can observe in action here. The contour lines of u_φ reveal that the interface between the disk and the BL, or in other words the region where the velocity starts to deviate substantially from Keplerian, is strongly deformed. The deformation of the interface is evidently due to the large scale vortices that reside at the base of the BL (see Fig. 3). At $r = 1.2$ the sound speed amounts to $\sim 8\%$ of the Keplerian velocity, whereas the gas rotates with $70\% u_K(R_*)$. Therefore, the azimuthal motion is still nearly ten times super sonic and information about the interface deformation cannot propagate upstream. Hence the oblique shocks, which are clearly visible in the radial
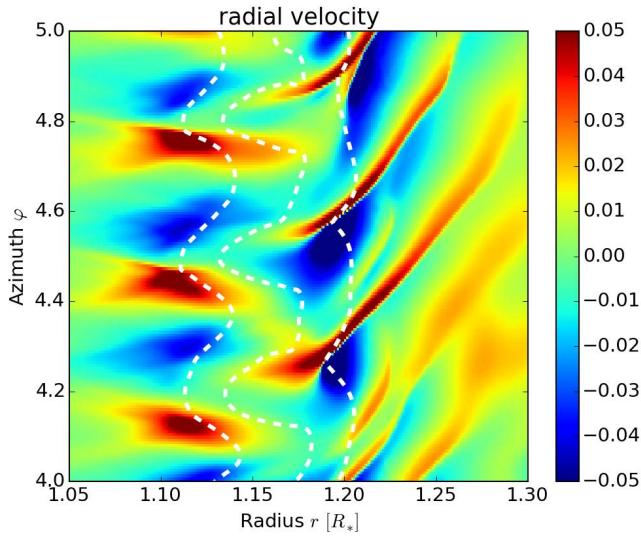
Fig. 3. Two-dimensional plot of the radial velocity u_r at $t = 45$ orbits. The direction of the unperturbed flow is from bottom to top, i.e. in the direction of growing φ. The dashed white lines are contour lines of the azimuthal velocity at the levels $0.15, 0.3$, and 0.7 (from left to right). All velocities are given in units of $u_K(R_*)$. The radial velocity develops a pattern with vortices in the BL and shocks at the top of the BL. This pattern most likely resembles the lower branch of the acoustic modes discussed in Belyaev et al. (2013a).

velocity, have developed. The whole system described above rotates in a prograde way with a pattern speed of $\Omega_p = \omega/m$, where ω is the oscillation frequency in the inertial frame and m the azimuthal wavenumber. For the episode described here (orbit 45), $\Omega_p \approx 0.3$.

The waves of the lower branch, which we find almost exclusively in our simulations, are tightly wound with a leading spiral and we expect $kr/m \gg 1$, where k and m are the radial and azimuthal wave numbers, respectively. Therefore, one can apply the WKB approximation and assume perturbations of the form

$$\delta f \propto \exp\left[i\left(kr + m\varphi - \omega t\right)\right]. \tag{20}$$

A linear stability analysis for a fluid disk with a polytropic equation of state then yields the dispersion relation

$$(\omega - m\Omega)^2 = \kappa^2 + k^2 c_s^2, \tag{21}$$

where $\kappa = \left(\frac{2\Omega}{r}\frac{d}{dr}(r^2\Omega)\right)^{0.5}$ is the epicyclic frequency and $\omega/m = \Omega_p$ (Binney & Tremaine 2008). Of course, Eq. (21) is only an approximation to the dispersion relation of the waves in our fully radiative disk. However, it will mainly be used to explain the wave dynamics in the disk. Furthermore, the WKB approximation is no longer valid in the BL where we have seen that $kr \approx 0$. In the disk we can assume a Keplerian rotation profile, $\Omega \propto r^{-1.5}$, and consequently the epicyclic frequency is real. Therefore, there is a region around the corotation resonance $\Omega = \Omega_p$, flanked by two *Lindblad resonances* $\Omega = \Omega_p \pm \kappa/m$, where k is imaginary and the waves are evanescent. Formally, according to Eq. (21) the wave number k becomes zero at the Lindblad resonances. However, the WKB approximation breaks down at these points since the assumption $kr/m \gg 1$ is no longer valid. Since the whole pattern of waves and interface deformations rotates with a pattern speed $0 < \Omega_p < 1$, there are two corotation resonances, one in the BL and one in the disk, either of them flanked by two Lindblad resonances. Assuming

the disk rotates with Keplerian frequency, we can easily derive the corotation and Lindblad resonance, which are then located at $r_{cor} = \Omega_p^{-2/3}$ and $r_{Lind} = (\Omega_p m/(m \pm 1))^{-2/3}$. The waves or the weak shocks we discussed earlier launched at the BL now propagate into the disk until they reach the Lindblad resonances, where they are reflected and propagate back toward the BL. In the BL the waves might be reflected by Lindblad and corotation resonances as well; however, Eq. (21) is not applicable there. Through this process of consecutive reflections the waves can become trapped between the BL and the disk.

This idea of the trapped modes has been proposed by Belyaev et al. (2012) and was indeed observed in their simulations. In Fig. 3 we do not find such clear evidence for reflected shocks. Reflection of the wave depends, however, on whether the modes are absorbed before they reach the evanescent region in the disk. We observe that the modes in our simulation can only travel until $r \approx 1.5$ before they are substantially damped by shocks, radiation, or viscous damping due to the α-viscosity applied in the disk (see Sect. 2.2). We have run simulations with larger domains in order to investigate a possible influence of the outer boundary on the reflection of the waves. These test runs confirm the early damping of the waves observed in the simulations presented in this work. The effective viscosity in the disk is likely to play a major role in this damping process. The actual interaction between the waves and the MRI turbulence in the disk can, however, only be investigated in real MHD simulations.

In Fig. 4 we plot the velocities u_r and u_φ as a function of (r, φ) at $t = 173$ orbits, a more energetic state than the one depicted in Fig. 3 (see Fig. 6 below). It is immediately apparent that the state at $t = 173$ orbits is far more violent than the situation shown in Fig. 3. The amplitude of the radial velocity has increased by a factor of 2 and the shocks have grown more intense and vigorous. While the general pattern of the radial velocity remains unchanged and still constitutes the lower branch with the vortices at the base of the BL and the outgoing waves at the top of the BL, the wavefronts are now heavily deformed by the shocks. These shocks are a consequence of the strongly distorted interface as can be seen in Fig. 4b. The lines of constant u_φ in the r-φ space (the contours) have a wave-like shape with many irregularities and the transition from zero rotation rate to Keplerian rotation is spread over $\sim 0.2 R_*$ and has broadened considerably. Though the radial velocity is more chaotic in Fig. 4b than in Fig. 3, there is still a dominant mode visible and the azimuthal wave numbers are $m = 14$ and 24, respectively. As we shall see later, the angular momentum transport by the waves is very efficient in this stage.

For completeness, in Fig. 5 we show a r-φ-plot of the radial velocity that spans the whole simulation domain. The snapshot was taken after 200 orbits while the system was in a quiet state. The pattern of the lower branch with its vortices at the base of the BL is clearly visible. We can also see that the waves emerging from the top of the BL are indeed tightly wound and that the spirals are leading. Figure 5 shows another azimuthal wave with $m = 3$ that we had not detected before, which is still a little faint is this figure. Interestingly, Belyaev et al. (2012) also find such a large-scale $m = 3$ global mode in their full 2π simulations. The wavenumber of the high-frequency pattern at the base of the BL is given by $m = 24$.

The middle branch is a transient mode and dominates during the linear growth of the sonic instability. It can be observed in the early stages of the simulation and the oblique wavefronts on either side of the interface are clearly visible in Fig. 2. Both panel a) and b) show features of the middle branch, yet they are more distinct in b). The upper branch, on the other hand, might
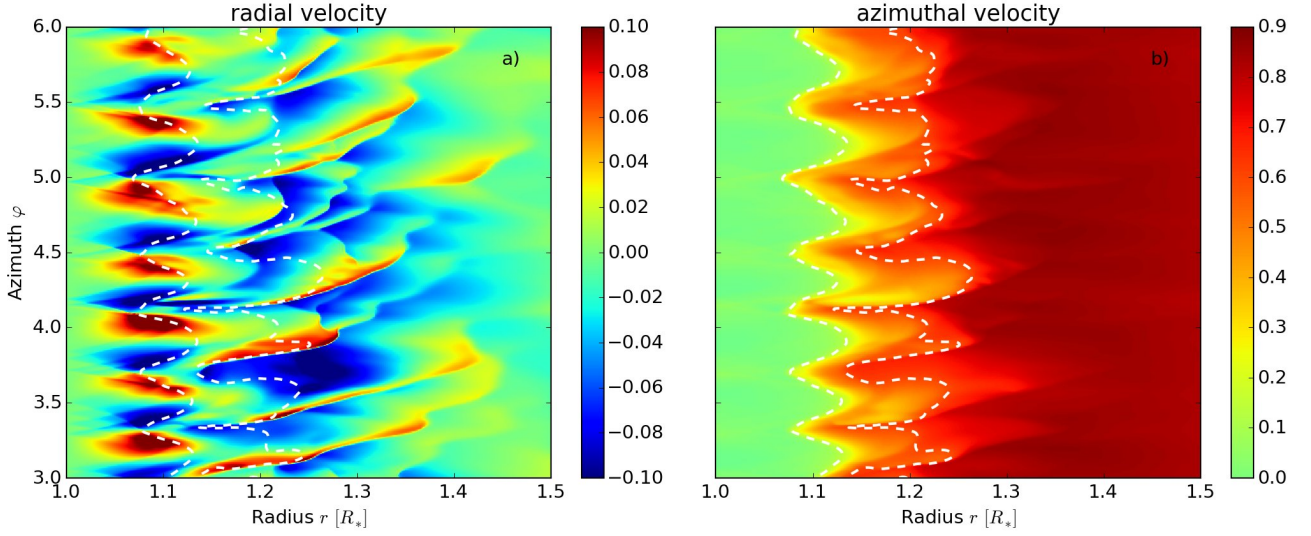
Fig. 4. r-φ plot of the radial velocity **a)** and the azimuthal velocity **b)** at $t = 173$ orbits. Both quantities are given in units of $u_K(R_*)$. The dashed white lines in both plots trace the contour of $u_\varphi = 0.15$ and 0.6 (from left to right). The direction of the unperturbed flow is from bottom to top. The images have been taken at a high activity state and the strong shocks in u_r and the heavy deformation of the interface (see **b)**) are clearly visible.
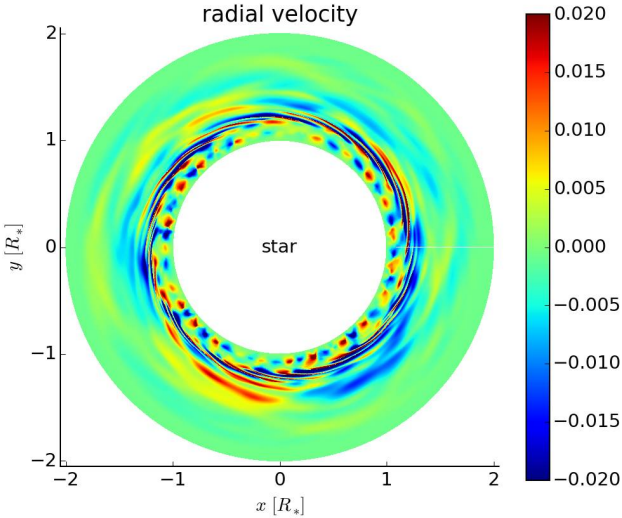

Fig. 5. Full-disk plot of u_r at $t = 200$ orbits. The direction of the unperturbed flow is counterclockwise. The radial velocity is given in units of $u_K(R_*)$.
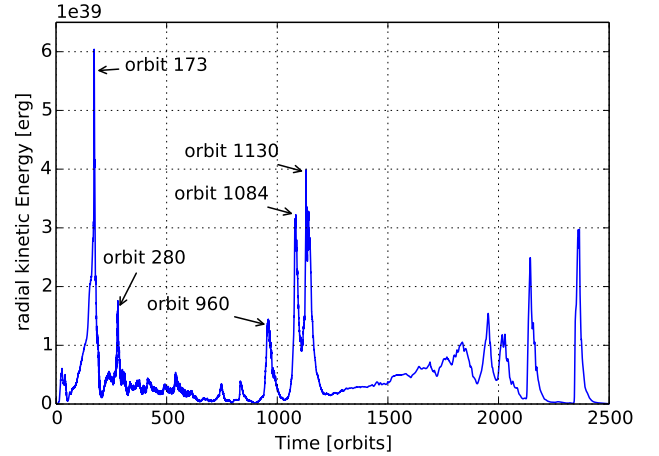
Fig. 6. Temporal evolution of the radial kinetic energy of our reference simulation. The time is given in units of the Keplerian orbit at $r = R_*$, P_*. The switching between quiet and outburst states described in the text is clearly noticeable. We have marked the exact times for some of the outbursts for easier comparison with the text.

be observed during the late times of the simulations. We defer the discussion of this issue to Sect. 5.5.

5. The effects of the instabilities

In the previous section we discuss the hydrodynamical instabilities in the BL in detail. Now we show the implications of the BL instabilities and the physical results of our simulations of the radiative BL around a young star.

5.1. Temporal evolution of the BL

Figure 6 visualizes the total radial kinetic energy, $E_{\rm kin,rad} = \int_{\rm disk} \frac{1}{2}\Sigma u_r^2 \, dA$, for which we summed the radial kinetic energy of every cell in the simulation domain. For a given time, the

radial kinetic energy reflects the strength of the instabilities. Therefore, we can monitor the time-dependence of the instabilities by tracking $E_{\rm kin,rad}$. The reference simulation shows a strongly time-dependent behavior that can be characterized as a recurring series of states of outburst and quiescence. When the kinetic energy reaches a maximum, the instabilities are vigorous and the interface between the BL and the disk is heavily deformed (see Fig. 4). In the quiescence states, on the other hand, the amplitude of the velocity perturbations drops considerably, often by a factor of more than 10, and the interface deformation is less strongly pronounced. The strength of the outbursts does not follow a clear pattern. In the beginning, the outbursts get stronger, with the second outburst at $t \approx 173$ orbits being the most powerful. During this outburst the amplitude of the perturbations in the radial velocity reaches over 20% of the Keplerian velocity at the surface of the star. Thus, the amplitude
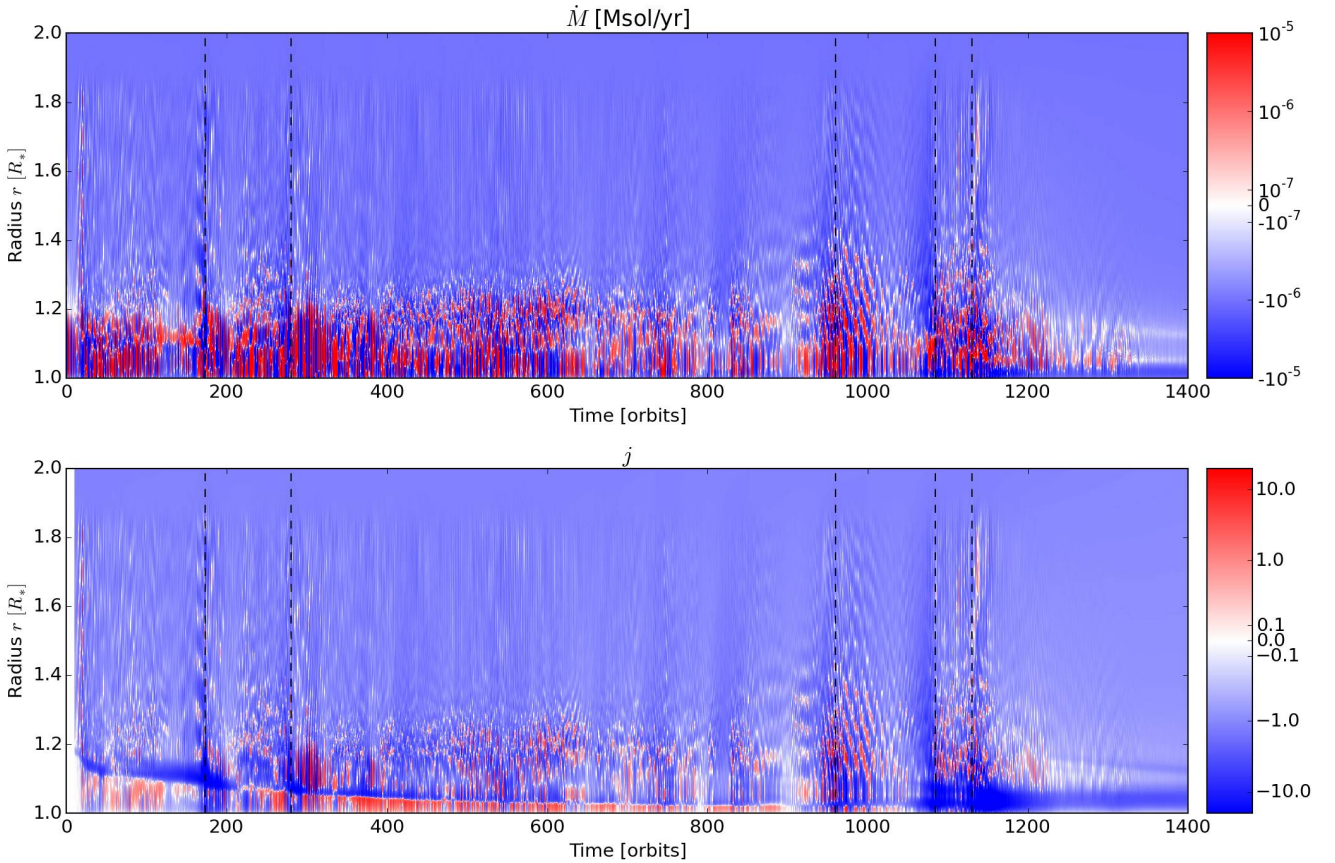
Fig. 7. *Upper panel*: temporal evolution of the mass accretion rate in the radial direction, $\dot{M}(r, t)$, in units of solar masses per year. It is obtained from the mass accretion rate per cell (see Eq. (16)) by integrating over the azimuthal direction. *Lower panel*: visualization of the AM flux normalized to the advective AM flux at the stellar surface (see Eq. (18)), which is also integrated over azimuth. We note that we applied a so-called symlog scaling for the plot, which means that we have a logarithmic scaling for both the positive and the negative values. Only in the vicinity of 0 is the scale linear. A negative value means that mass or AM is transported to the center of the disk. The phases of strong activity in the radial velocity (see Fig. 6, marked with the black dashed lines here) correspond to phases of increased mass and AM transport. The diagonal features in the upper panel are a clear signature of waves, which have alternating signs of mass transport. This sloshing behavior spreads to the AM flux (*lower panel*) via the advective component of j.

of the radial velocity becomes comparable to that in azimuthal direction, or even exceeds it for $r \lesssim 1.1$. The third outburst at $t \approx 280$, which is less intense than the second one, is followed by a longer period of less activity or quiescence during which some small peaks suggest the occurrence of very weak micro-outbursts. After more than 500 orbits, the system starts to go through a series of outbursts again.

The high and low instability states mentioned above correspond to episodic phases of high and low activity in mass accretion and angular momentum transport, as can be seen by comparing Figs. 6 and 7. Figure 7 depicts the time-dependence of the mass accretion rate, Eq. (16), and of the angular momentum transport, Eq. (17), for all radii inside the computational domain. In phases of outbursts, which are marked by the vertical dashed lines, the mass flux through the disk is higher than in the quiescence state. In certain regions, $\dot{M}$ increases by more than two orders of magnitude. In the high activity phases, $\dot{M}$ distinctly rises in the outer parts of the simulation domain as well. The angular momentum transport, j, shows a similar trend. At times of strong instability, the transport of angular momentum, which is mainly directed to the center of the disk, also grows remarkably, quite often by a factor of about 100.

Unlike in a stationary state where mass and AM are transported to the center of the disk (see Eq. (17)), we observe that the transport of mass does not have a preferred direction in certain regions of the simulation domain. We consider for this purpose the upper panel of Fig. 7. There is a clear boundary at $r \approx 1.2-1.3R_*$, which is approximately given by the location of the maximum of Ω and divides the rather organized, inward directed mass flux in the disk from the alternating transport in the BL, where mass is sloshing about back and forth in radius because of the passage of waves which have alternating signs of mass transport. This is clearly visible in the form of the diagonal features in the upper panel of Fig. 7. Thus, the direction of the mass transport in the BL is both a function of time and radius, and the variability with time is on the order of one orbit. After roughly 600 orbits, the strength of the mass transport ceases slightly, only gaining strength again during the subsequent outburst periods. This development matches that of the radial kinetic energy (Fig. 6) where we can also detect a change in activity starting after 600 orbits. After 1200 orbits another major change in the mass transport pattern takes place. The whole system seems to calm down and the sloshing behavior with its frequent changes in direction ceases.
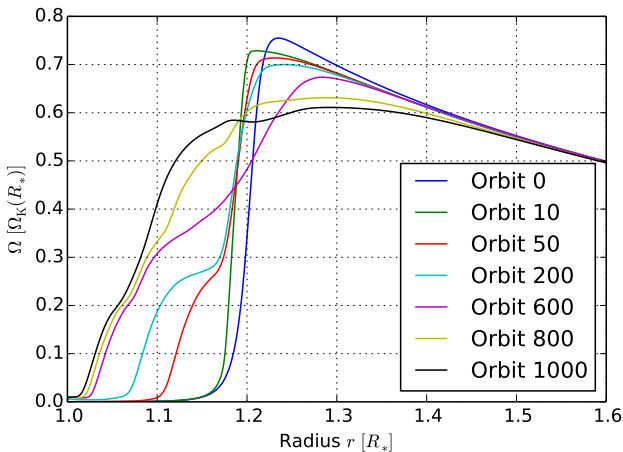
Fig. 8. Velocity in azimuthal direction in units of the Keplerian velocity at the stellar surface for seven different orbits. The curves demonstrate the spin-up of the gas for $r \lesssim 1.2$ and the spin-down for $r \gtrsim 1.2$ over time.

The AM flux does not feature a variability as intense as the mass flux; however, the diagonal features that have also been discussed in the context of $\dot{M}$ are still present. An analysis of the individual components of j confirms that these features arise from the advective part of the AM flux, which shows a sloshing behavior similar to the mass flux. Apart from these features, j assumes mostly negative values (see the lower panel in Fig. 7), meaning that AM is transported inward. This evidence agrees with our expectations that in the disk j is negative for the reasons pointed out earlier. One very distinct feature in the graph of the AM flux is the very pronounced boundary that starts at the beginning of the simulation at r close to $1.2R_*$ and moves inward up to $r \approx 1.025R_*$ during the first 800 orbits. This line can be characterized by an enhanced AM flux in its near vicinity and a shift in direction from inward ($r < r_{\text{line}}$) to outward ($r > r_{\text{line}}$). Figure 8 visualizes the destination of the AM which is accumulated at this interface as a result of transport from both sides. It is spent to spin up the gas at $r \lesssim 1.2$. Hence, the BL is broadened considerably during the course of the simulation. The AM needed for the spin-up of the inner layers is extracted from the faster rotating part at $r \gtrsim 1.2$, which is, consequently, slowed down. By comparing Figs. 7 and 8, we can deduce that the AM transport is the strongest where the gradient of Ω is highest, i.e. where the shearing is strongest.

It can be recognized from Fig. 7 that AM is mostly transported inward although the mass flux is also directed outward. Especially when $\dot{M} > 0$ and large, one would expect a considerable amount of AM to be transported outward along with the matter. Thus, one possibility for the AM flux to still remain negative is that the Reynolds part of Eq. (17) is negative and larger than the advective part (the viscous part is zero in the BL). However, an analysis of several time steps showed that very often the advective AM transport is negative and large while the mass flux is positive and large. This apparent discrepancy between the mass and the AM flux is due to an anti-correlation between the radial and azimuthal velocity. The mass accretion rate periodically points in- and outward, depending on azimuth, owing to the vortices of the radial velocity. The sum of $\dot{M}$ over the whole azimuthal domain for a given radius can therefore be positive (meaning that mass is transported outward). However, according to Eq. (17), the total advective AM flux can easily remain negative if u_φ is smaller at azimuthal locations of
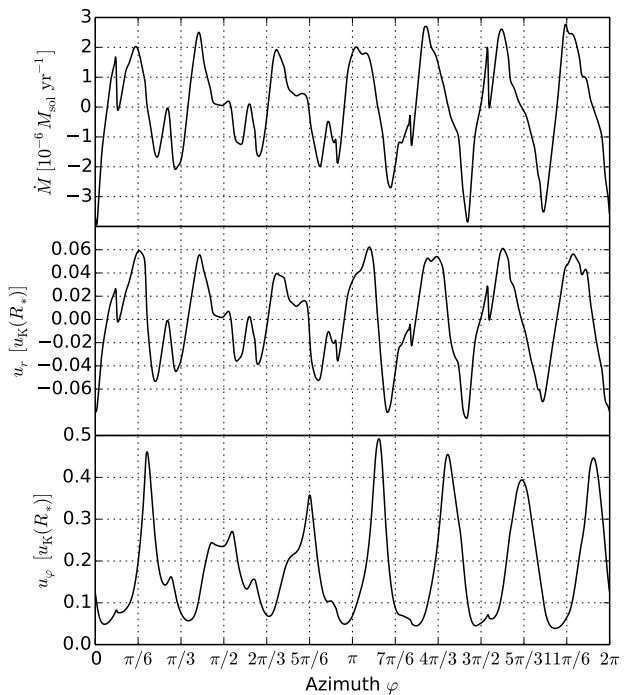

Fig. 9. *Upper panel*: mass accretion rate; *middle panel*: radial velocity; and *lower panel*: azimuthal velocity. All three quantities are plotted as functions of azimuth at the fixed radius $r = 1.12R_*$ after 145 orbits. The upper two curves are shifted in phase with respect to the lower one such that maxima in $\dot{M}$ (nearly) coincide with minima in u_φ.

positive $\dot{M}$ than where it is negative. This is indeed very often the case and we have picked an illustrative example to stress this point (see Fig. 9). It is a snapshot of the mass accretion rate, the radial velocity, and the angular velocity at orbit 145, where we plotted the dependence on azimuth for $r = 1.12R_*$. The figure clearly shows that whenever $\dot{M}(\varphi)$ is positive and large, $u_\varphi(\varphi)$ is small. The comparison between the radial and the azimuthal velocity reveals that the anti-correlation between u_r and u_φ is such that an extreme of the azimuthal velocity coincides with a root of the radial one. Therefore, the two patterns that are similar, although not perfectly equal, are shifted by one quarter of the azimuthal wavelength of the $m = 7$ mode at this annulus.

5.2. Outburst sequence

We now take a closer look at the cause of the periodic outbursts and the behavior of the primitive variables in the disk during such an outburst and we consider Fig. 10 for this purpose. The graphic shows the velocity in azimuthal direction, the surface density, the pressure, and the temperature in the midplane of the disk for five different times that are centered around the outburst at $t = 173$ orbits and are *not* equidistant. These time steps cover the second outburst in Fig. 6. This part of the radial kinetic energy evolution is shown as a zoom-in in the lower right panel of Fig. 10.

At the beginning of the outburst, the surface density has increased quite strongly, especially in the vicinity of $r \approx 1.25$ where it is almost two orders of magnitude higher than at the beginning of the simulation. This pile-up of mass is a result of the fact that mass is constantly entering the BL from the outer disk, but the instabilities in the BL are not yet efficient enough to guide it all through. This situation is universal for all observed
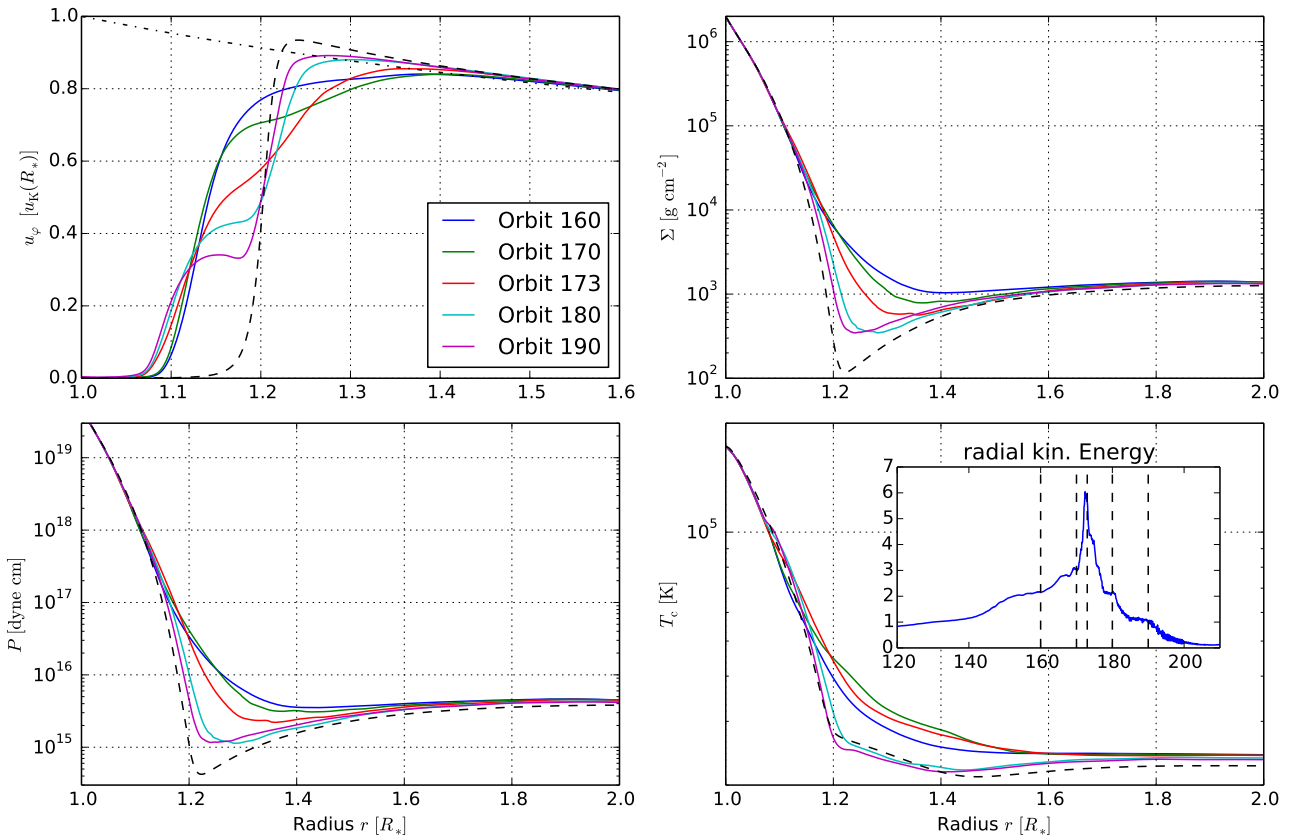
Fig. 10. Azimuthal velocity, the surface density, the pressure, and the midplane temperature for five time steps centered around the second outburst. The dashed lines denote the initial conditions of the simulations. The dash-dotted line in the *upper left panel* gives the azimuthal velocity for pure Keplerian rotation. In the *lower right panel* we have included a zoom-in of Fig. 6 for better identification of the exact location of the plot times.

outbursts, which are preceded by a phase of quiescence during which the activity and the mass transport in the BL are not as strong as in outburst phases. Therefore, the whole process described here using the example of the first outburst can be equally applied to the other outbursts. During the accumulation of the mass just outside the BL, the azimuthal velocity profile is smooth and quasi-stationary. The high amount of mass leads to a high temperature and hence a high pressure, which means that u_φ is remarkably sub-Keplerian in the first half of the domain since the gas is stabilized by pressure.

After a sufficient amount of mass has accumulated, a runaway process sets in during which u_φ and the other quantities change very rapidly. According to Figs. 7 and 10 a great amount of mass is guided through the BL onto the star over such an outburst. The process is initiated outside the BL at about $r \approx 1.3$. The gas is both accelerated and decelerated in azimuthal direction by the Reynolds stresses in and near the BL, with the boundary between the spin-up and spin-down region moving inward with time. Since the effect of the deceleration is much stronger, mass moves inward. As a consequence of the decreasing density, the pressure decreases and the gas is even less stabilized and can accelerate its inward movement. After the density is satisfactorily depleted, the Reynolds stresses decrease and the violent accretion process comes to an end. Then the density grows again because of the lower stresses and the azimuthal velocity is slowly regains its pre-outburst profile.

The variation of the midplane temperature during the outburst phase is consistent with what we have already discussed for the other physical quantities. At the beginning, despite the

decreasing density, the temperature rises for $r \lesssim 1.6R_*$ and even develops a small bump around $r = 1.25R_*$. The increase in temperature is due to the dissipation of energy through the growing Reynolds stresses and indicates the region where the energy release by the waves is largest. This radius is in agreement with what we expected from the plot of the azimuthal velocity if we also take into account that the energy is redistributed by radiative diffusion. Subsequently, the surface density drops more and more and the Reynolds stresses decrease as well. Accordingly, the temperature also drops, and even drops below the level of the initial state. After enough mass has again piled up around the BL, the temperature will rise to its pre-outburst level.

The outburst sequence shown here for the second outburst of the reference simulation is exemplary for the general behavior of outbursts. What we have just discussed might be less clearly visible or even more distinct, depending on the strength of the outburst. However, the mechanism is the same throughout. From simulation C, which has a resolution of 2048×2048, we find that the outburst is far more violent than the one we discussed here. The azimuthal velocity frequently develops an even more pronounced local maximum and minimum for $r < 1.2R_*$ and the depletion of mass is more effective. Thus, it is possible that the instabilities become stronger with increasing resolution. The increasing strength of the outbursts might instead be due to the other modes becoming excited through the initial perturbations, as is typical for classical KH instability.

We propose the following scenario for the physical cause of an outburst such as the one described above. The radial velocity
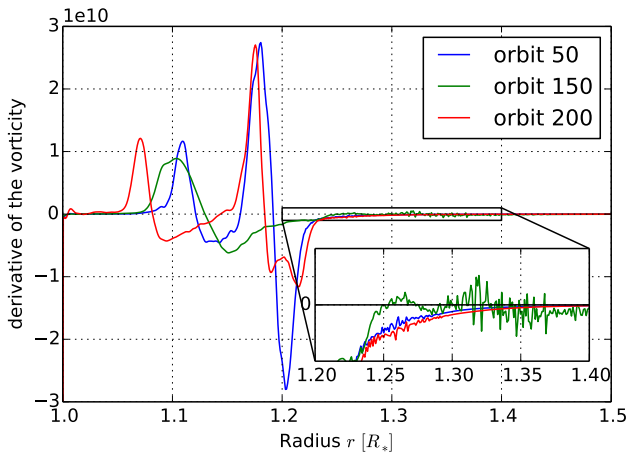
Fig. 11. Derivative of the vorticity, $\partial Z/\partial r$, as a function of radius for orbit 50 (quiet state), orbit 150 (pre-outburst state), and orbit 200 (post-outburst state). The inset is a zoom-in of the region $1.2 \leq r \leq 1.4$ where multiple changes of sign are clearly visible for orbit 150.

Fig. 12. z-component of the vorticity, $\nabla \times \boldsymbol{u}$, at the peak of the second outburst at $t = 172.6$ orbits. The patterns in this image might be indicative of a KH-like instability.

has developed weak shocks at the top of the BL. Every time a fluid element passes through that shock it is slowed down by these oblique shocks. The cumulative effect of all these shock passages leads to a decrease in the azimuthal velocity of the gas and creates a wide plateau in the velocity profile (see e.g. orbit 160 in Fig. 10). Such a flat region with a weak velocity gradient is prone to the classical Kelvin-Helmholtz (KH) instability, which sets in and induces the rapid changes in the BL. In absence of rotation, it follows from *Rayleigh's stability equation* that a necessary condition for instability is the occurrence of an inflection point in the velocity. A stronger form of this condition was given by Fjørtoft (1950), who showed that the velocity profile not only needs to have an inflection point, but also has to satisfy the condition $u''(u-u_s) < 0$ somewhere in the flow, where u_s is the velocity at the inflection point. However, this requirement is only true for parallel flows. A normal-mode analysis of the linearized Euler-equations of a rotating incompressible flow with zero mean radial velocity eventually yields

$$(\omega + \mathrm{i}m\Omega)\left(\frac{\partial^2}{\partial r^2} + \frac{1}{r}\frac{\partial}{\partial r} - \frac{m^2}{r^2}\right)\phi - \mathrm{i}m\frac{1}{r}\frac{\partial Z}{\partial r}\phi = 0 \qquad (22)$$

for 2D disturbances. Here, $\phi(r)$ is the amplitude of a stream function $\psi'(r, \varphi, t) = \phi(r)\exp(\omega t + \mathrm{i}m\varphi)$ such that $u'_r = \mathrm{i}m\phi/r$ and $u'_\varphi = -\partial\phi/\partial r$, where the prime denotes perturbed quantities; $Z = 1/r\,\partial(ru_\varphi)/\partial r$ is the vorticity. Equation (22) is the equivalent of Rayleigh's equation for a rotating fluid. Rayleigh showed that if $\phi = 0$ at two boundaries R_1 and R_2 enclosing the flow, a necessary condition for instability is that the gradient of Z must change sign at least once in the interval $R_1 < r < R_2$ (Drazin & Reid 2004). We take this analogue of Rayleigh's inflection point theorem as a motivation to study the vorticity and its derivative, though Eq. (22) is clearly an idealization of the situation at hand. However, a detailed stability analysis of the RHD equations of a rotating stratified fluid is beyond the scope of this work.

Figure 11 displays the derivative of the vorticity, $\partial Z/\partial r$, for three points in time. At orbit 50, the system is in a state of quiescence (see also Fig. 6). After 150 orbits the second outburst has just started to evolve, and 50 orbits later the system is recovering from the outburst. While the vorticity derivative of the quiet and post-outburst state does not change sign for $r > 1.2R_*$, it does change several times for orbit 150. The region $r > 1.2R_*$ is
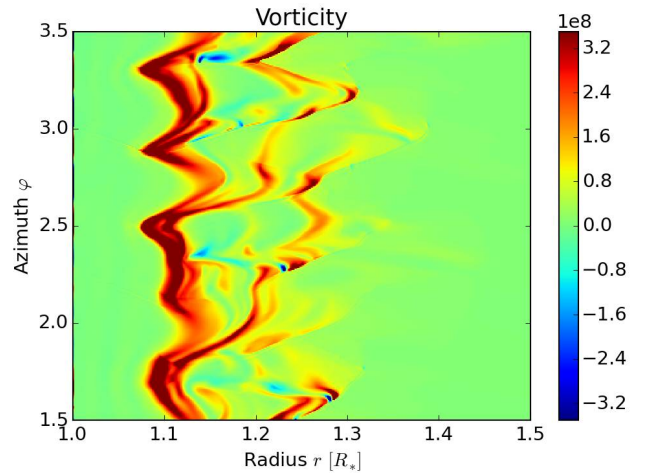
of interest here because this is where the rotation profile is flat. There are, of course, multiple changes of sign for $r < 1.2R_*$ in all curves. However, those points are associated with the strong shearing regions that we have already discussed in Sect. 4. After analyzing several time steps before, during, and after outbursts, we draw the following picture: The consecutive shock passages near the maximum of Ω cause the flow field to adjust such that multiple changes of sign are created in the derivative of the vorticity. Since this is a necessary condition for the instability of a rotating, hydrodynamical flow, it is probable that a classical KH instability develops in the flat regions of the flow. The role, however, that the KH instability plays in the context of the enhanced accretion and AM transport is not yet entirely clear. It might, on the one hand, act as a trigger for a mode of the sonic instability which is excited during the outburst and efficiently drives the accretion. Once a sufficient amount of the mass in the BL has been accreted, the mode can no longer be sustained and the system returns to quiescence. One candidate for this mode might be the upper branch, which we normally do not observe in our simulations. A scenario similar to this option was also discussed in Belyaev et al. (2013a). If, on the other hand, the KH instability itself is responsible for the enhanced accretion, AM should be transported mainly by turbulent stresses, as opposed to the wave transport through the mode mentioned above. We did not find clear signs of turbulence during the outburst, nor did we find evidence of the upper mode. It is, however, plausible that the AM transport is still accomplished by waves and the KH instability might trigger or enhance a mode of the lower branch.

We did find evidence for the existence of a KH instability during the outburst. We consider for this purpose Fig. 12, a 2D image of the z-component of the vorticity $\nabla \times \boldsymbol{u}$ at orbit 172.6, i.e. at the peak of the second outburst. It shows patterns that are commonly associated with the classical KH instability, for instance, the curly arms and the cat's eyes. By analyzing simulation C we find that these patterns become more distinct with increasing resolution (see also Fig. 11 in Belyaev et al. 2012). The KH features are, however, masked to some extent by the waves generated by the main instability. This becomes clear when we investigate the outbursts at later times when the main instability is decreasing. In addition, the flat region where
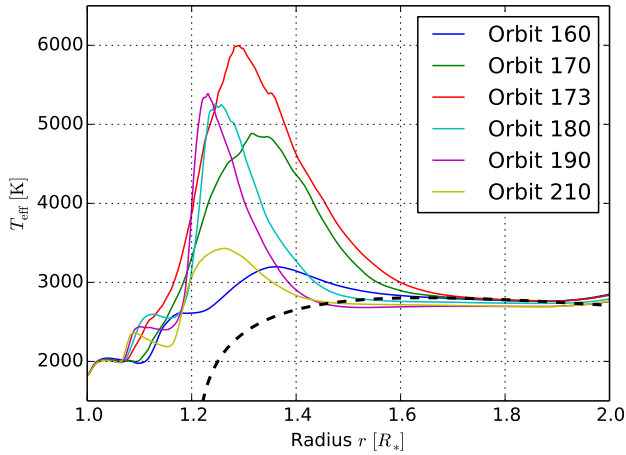
Fig. 13. Azimuthally averaged effective temperature of the BL for six time steps centered around the second outburst (see Fig. 6). $T_{\rm eff}$ increases considerably during the outburst and then declines to approximately the pre-outburst level ~30 orbits after the peak of the outburst. The black dashed line corresponds to the surface temperature of the standard solution of Shakura & Sunyaev (1973).

Fig. 14. 2D plot of the effective temperature of the BL at orbit 173, which marks the peak of the second outburst (see Fig. 6). $T_{\rm eff}$ strongly varies in azimuthal direction and reaches temperatures up to 10 000 K. The curly arms visible for $r < 1.2$ are indicative of a KH-like instability.

we expect KH instability to work occurs in the fast rotating part of the disk. Static grid codes suffer from disadvantages when the fluid is boosted and fluid mixing instabilities can be suppressed (Springel 2010).

5.3. Effective temperature

We now investigate the outburst described in Sect. 5.2 from an observer's point of view and look at the radiation emitted by the BL and the disk. In Fig. 10 we have exclusively considered physical quantities, which are measured in the equatorial plane of the disk, among them the midplane temperature $T_{\rm c}$. If the medium is optically thick, however, the emergent spectrum is dominated by the temperature on the surface of the disk where the vertical optical depth is approximately one, and locally resembles the spectrum of a blackbody radiating with temperature $T_{\rm eff}$. Since we have no knowledge of the vertical structure of the disk, we use the approximation of Hubeny (1990), which is a generalization of the gray atmosphere (e.g. Rybicki & Lightman 1986). The effective temperature can then be calculated with an approximated optical depth in vertical direction (Suleymanov 1992):

$$T_{\rm eff}^4 = T_{\rm c}^4/\tau_{\rm eff}$$
$$\tau_{\rm eff} = \frac{3}{8}\tau_{\rm R} + \frac{\sqrt{3}}{4} + \frac{1}{4\tau_{\rm P}}. \tag{23}$$

Here, $\tau_{\rm R}$ and $\tau_{\rm P}$ ($\tau = \kappa\rho H = 0.5\kappa\Sigma$) are the Rosseland and the Planck mean optical depth, respectively.

Figure 13 shows the effective temperature of simulation B calculated according to Eq. (23). At the beginning of the outburst (orbit 160) the effective temperature features only a slight peak in the BL and the temperature in the BL and in the disk differ at most by 500 Kelvin. The reason why the effective temperature of the BL and the disk are very similar at the beginning of the outburst episode is the following. The system, which is just on the verge of an outburst at this point in time, comes out of a preceding state of quiescence. Therefore, the energy dissipation of the waves is small and the density is rather high owing to the inefficient mass transport. Consequently, both the midplane temperature and the optical depth in the BL are comparable to the disk
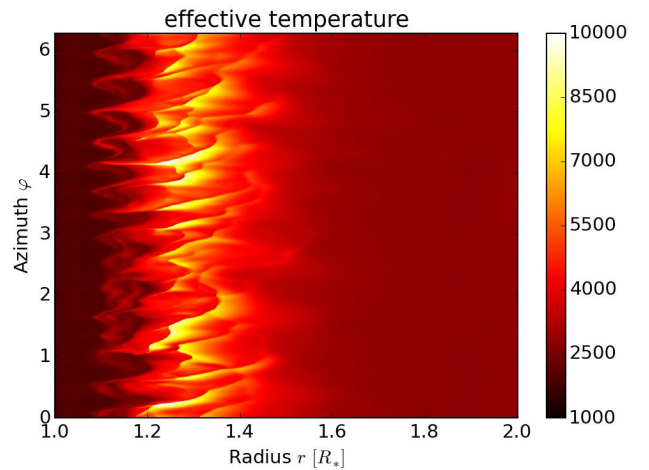
and $T_{\rm eff}$ is only slightly larger in the BL. Over the course of the next 13 orbits, however, the system goes through an episode of effective mass and AM transport, and the midplane temperature increases and the surface density decreases (see Fig. 10). Thus, according to Eq. (23), $T_{\rm eff}$ increases rapidly in the BL yielding a maximum of 6000 K at $r \approx 1.3$, which is twice the temperature in the disk. Care should be taken when comparing $T_{\rm eff}$ in our models with conventional BL models where an α-viscosity has been applied. The latter typically feature a BL that is considerably smaller in radial extent than in the models presented here. The luminosity of the BL, however, does only depend on the physical parameters of the system and must be the same in both models ($\frac{1}{2}GM\dot{M}/R_*$ for a non-rotating star). Since the luminosity is the integral of the flux $F = \sigma_{\rm SB}T_{\rm eff}^4$ over the area of the BL, it follows that the thinner the BL, the higher the effective temperature must be, and vice versa. The relation between the maximum effective temperature in the BL $\theta_{\rm BL}$ and in the disk, $\theta_{\rm d}$, can roughly be estimated by (Lynden-Bell & Pringle 1974)

$$\frac{\theta_{\rm BL}}{\theta_{\rm d}} = 1.56\left(\frac{\delta}{R_*}\right)^{-1/4}, \tag{24}$$

where δ is the width of the thermal BL (see e.g. Regev & Bertout 1995; Popham & Narayan 1995). Equation (24) yields a factor of ~2 for $\delta = 0.3R_*$, which is in good agreement with what we observe in our simulation (see Fig. 13). Also visualized in Fig. 13 (black dashed line) is the surface temperature according to Shakura & Sunyaev (1973), which is given by

$$T_{\rm eff}(r) = \left(\frac{3GM_*\dot{M}}{8\pi r^3 \sigma_{\rm SB}}\left[1 - j\left(\frac{R_*}{r}\right)^{1/2}\right]\right)^{1/4}, \tag{25}$$

where j is the normalized AM flux. We took $j = 1.1$ for Fig. 13, which is the mean normalized AM flux at orbit 160 measured from the simulation. The effective temperature derived from our simulation agrees very well with Eq. (25) in the disk. In the BL, of course, the analytically derived formula fails to capture the rise of the effective temperature.

Another important point for the observational appearance of the BL is the azimuthal dependence of the effective temperature, which is visualized in Fig. 14 for orbit number 173.
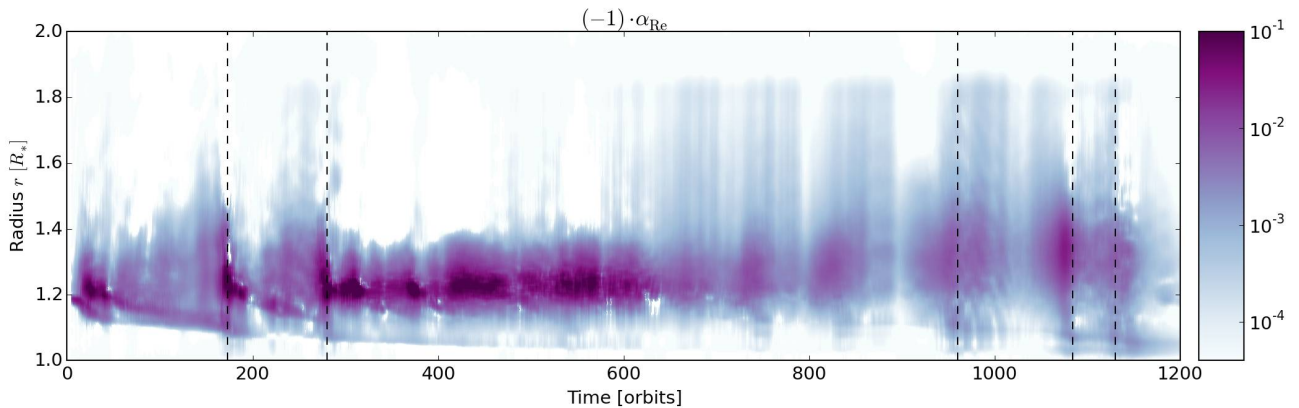
Fig. 15. Time-radius image of α_{Re} spanning several hundred orbits. We note that the values of α_{Re} have been multiplied by (-1) in order to allow for the logarithmic scale. For each point in time the values have been time average over ten orbits. The vertical dashed lines denote the locations of the outbursts mentioned earlier in the text.

We can see from this depiction that T_{eff} reaches temperatures of nearly 10 000 K in the simulation domain which is high, considering the case of a young star. There is strong variation of T_{eff} in φ-direction, especially for the annulus $r \approx 1.3$, which is due to the shocks of the radial velocity that create density perturbations in the surface density and then affect the vertical optical depth and the effective temperature. The φ-dependent pattern of T_{eff} rotates with the pattern speed of the acoustic modes, which is close to the Keplerian velocity, and will express itself in time-dependent variations of the light curve. This is an important point because many systems show light curve oscillations with periods that are close to the orbital period at the surface of the star. In cataclysmic variables, for instance, one observes rapid oscillations called dwarf novae oscillations (DNOs, Warner & Robinson 1972) and quasi-periodic oscillations (QPOs, Patterson et al. 1977). Both phenomena are not yet fully understood and it is tempting to see a connection to the BL modes on the basis of the protostar simulations presented here. However, further research is necessary to clarify this point. We also note that Fig. 14 shows clear indications of KH instabilities. These features are even more pronounced in snapshots of T_{eff} taken before the peak of the second outburst and reinforce the point that a KH-like instability is responsible for the frequent outbursts.

5.4. Angular momentum transport by waves

In Fig. 7 we visualized the total AM flux in the disk, which consists of the advective part, the viscous part in the disk, and the Reynolds part (see Eq. (17)). It is, however, of great interest to see how much the instabilities contribute to the total AM flux and to deduce the efficiency of this transport. As we have described in Sect. 4, the instability in the BL leads to the development of acoustic waves that are launched from the interface and propagate into the disk and the star. As a consequence, AM transport in our models is dominated by acoustic radiation, i.e. sound waves carrying AM. We do not observe any turbulence in our simulations and hence rule out turbulent stresses as a major contribution to the AM flux. Unlike the turbulent stresses, the AM transport by waves is a non-local process. Waves can carry AM of either sign from one point in the domain, e.g. the interface in the BL where they are launched to another point in the disk where they deposit the AM into the fluid through wave dissipation.

Thus, the long-range exchange of angular momentum between regions that are otherwise uncorrelated is possible through the wave transport. This is a major difference from the α-models which yield a local effective viscosity due to a local AM exchange phenomenon, such as turbulence. Therefore, it is questionable whether the processes in the BL can be described by a local prescription like the α-model.

We now analyze the efficiency of the wave mediated AM transport and consider Fig. 15 for this purpose. It shows the dimensionless Reynolds stresses α_{Re}, which has been calculated according to Eq. (14), as a function of radius and time. We can apply this description to the AM transport since waves transport angular momentum exclusively by stresses. The Reynolds stress is evidently very strong with peak values up to the order of unity and it is largest at the top of the BL, at around $r = 1.2$, which is very interesting since in that region Ω reaches its maximum. Thus, our simulations reveal that the stresses are largest around the very point where they would vanish according to a conventional α-viscosity model. Strictly speaking, this renders a local prescription that depends on the shear of the angular velocity inapplicable for the BL. Figure 15 also shows that the AM transport due to the waves includes a large part of the domain, $1.05 \lesssim r \lesssim 1.4$, and spreads out farther into the disk during outbursts. This reinforces the point that the AM transport ultimately generated by the shear in the BL is not confined to the BL, but in fact ranges over long distances. As we saw earlier, the activity rises during outbursts and therefore α_{Re} is enhanced during these periods as well. The value of α_{Re} is almost exclusively negative, meaning that angular momentum is transported toward the star. This behavior is characteristic of the lower branch of the acoustic modes (Belyaev et al. 2013a). We refrain from presenting plots of the parameter α_ν that can be calculated according to Eq. (15) because it is artificial to boil the non-local AM transport down to a local parameter. However, for the sake of completeness, it should be mentioned that Eq. (15) yields values on the order of $10^{-3}-1$ for our models.

Finally, we investigate how the strong AM transport in and around the BL affects the width of the region where the azimuthal velocity rises from stellar rotation to the Keplerian rotation in the disk. Figure 16 depicts the BL thickness as a function of time for all four simulations. The thickness of the BL is defined to be the region in which

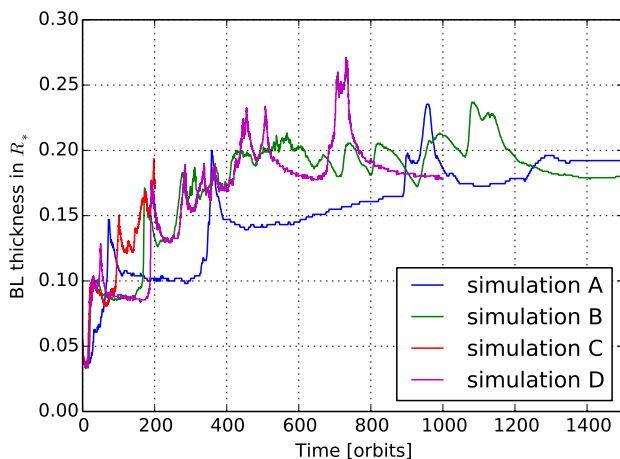$$0.02 < \overline{u_\varphi}(r)/u_{\mathrm{K}}(r) < 0.8. \tag{26}$$

Fig. 16. Width of the BL as a function of time for the four simulations mentioned in Sect. 3.3. The width is calculated from the radii of the region where $0.02 < u_\varphi/u_K < 0.8$. All four simulation settle down to a BL width of approximately 20 percent of the stellar radius. Simulation A approaches this value more slowly and in a slightly different manner, which is due to the very low resolution of this particular simulation (512×512).

The width of the BL increases very rapidly and grows in size by a factor of 2 at the beginning of the simulation, i.e. when the sonic instability has grown to establish an efficient AM transport. After the initial fast growth the width of the BL increases on average linearly over the course of approximately 500 orbits until it settles down at a value of ~$0.2R_*$. We have run additional simulations in order to test the robustness of the BL thickness of 20% of the stellar radius. In these simulations, the initial distance of the velocity drop from the inner edge of the simulation domain has been extended by altering both the parameter $\mathcal{F}$ (see Sect. 3.2) and the point where the computational domain begins. We thereby test whether the thickness is affected by the BL running up against the inner edge of the domain. However, these runs are in perfect agreement with the simulations presented here and saturate at a BL width of ~$0.2R_*$ as well.

There are several spikes in the temporal evolution of the BL width for all three simulations that are clearly associated with the frequent outbursts. During the high activity state the BL broadens considerably in a very short period of time and typically resides at a larger width in the aftermath of the outburst. Because of the high resolution and the resulting long simulation times we can follow the highly resolved simulation only for about 200 orbits. During that time it behaves exactly like the other simulations with the exception that the width of the BL increases much more quickly. This is in good agreement with the fact that the growth rate of the sonic instability depends on the resolution in such a way that it is faster when the resolution is higher (see Sect. 4). Since the BL widens to a large extent, it extends very far into the disk and into the star. The latter means that a consistent simultaneous treatment of the star is required for numerical simulations involving large simulation times. We will discuss this point in detail in the next section.

5.5. The long-term evolution of our simulations

We ran and monitored our reference simulation for over 2000 orbits (see Fig. 6), and the instability and the periodic outbursts do not die out during that time. There is, however, a change in the pattern of the acoustic waves that occurs around orbit 1200, which coincides precisely with the moment when the base of the BL reaches the inner boundary of the simulation domain. We consider this a problematic moment, since it is not possible to treat the star correctly in 2D r-φ simulations. The geometry of the coordinate system inherently gives the star a cylindrical shape in our simulations. In Sect. 3.2 we describe how we treat the inner boundary in order to approximate the beginning of the star and that the radial velocity is set to outflow with a certain velocity at this point. Therefore, we might expect unphysical and artificial processes once the vortices of the acoustic modes reach this point because the radial velocity is fixed to a certain value and an inflow in the domain is not supported. Furthermore, we force the azimuthal velocity to zero at the inner boundary. However, the acoustic modes seem to be quite robust since they do not die out despite the difficulties with the artificial inner boundary. The change in the pattern at orbit 1200 might be due to a switching of the modes to the upper branch, since the spiral arms of the waves are unwinding considerably and changing from leading to trailing. Another 1000 orbits later the process is reversed again and the system switches back to the lower branch.

However, in order to capture the physics correctly at these late stages in time and to still make reliable statements once the BL extends all the way to the surface of the star or even into the star, it is necessary to attach a realistic model of the star to the disk. We consider, for instance, a wave launched in the BL that propagates toward the star. It can penetrate deep into the star before it is stopped by the steep density gradient and dissipates the angular momentum somewhere in the star. On the other hand, many problems arise when the star is treated consistently. The problem must then be simulated in spherical coordinates, i.e. 3D simulations are necessary, and the density varies considerably from the interior of the star to the disk. Simulations of this kind are very demanding from a computational point of view, but also very tempting, and we plan to investigate this problem in the future.

6. Summary and conclusion

We have performed highly resolved, 2D hydrodynamical simulations of the BL surrounding a young star in order to investigate the AM transport driven by instabilities. Extending previous simulations, we have a net mass flow through the disk, we utilized a realistic equation of state, and (within the framework of one-temperature approximation) we included full radiative transfer in the disk plane as well as vertical cooling through an realistic estimate of the vertical optical depth, thereby employing a quasi 3D radiation transport. Moreover, those simulations were started from state-of-the-art 1D models of the BL and thus comprise realistic profiles for the density and temperature. We ran the simulations for over two-thousand orbits in order to study the long-term behavior.

Our simulations confirm that the supersonic velocity drop in the BL is indeed prone to the sonic instability, a kind of supersonic shear layer instability whose subsonic counterpart is the Kelvin-Helmholty instability (Belyaev & Rafikov 2012). Shortly after starting the simulations, the sonic instability sets in and starts to grow rapidly for about 15 orbits. It then saturates and the BL is dominated by acoustic waves that propagate both into the disk and into the star. These acoustic modes manifest themselves in three distinct patterns that can be related to the three branches of the instability of a plane parallel vortex sheet and do not die out for the whole simulation time.

Additionally, the system repeatedly undergoes outbursts where the wave activity as well as the AM and mass transport increase considerably. We argue that these outburst are likely triggered by a secondary KH instability that develops in the flat region of the azimuthal velocity profile due to several changes of sign of the vorticity. Since the effective temperature also shows strong variations during outbursts, they may play an important role in explaining variations in the light curve, such as FU Or-outbursts or DNOs and QPOs in the case of BLs around white dwarfs. It is tempting to associate these phenomena with the outbursts we observe in our simulations; however, this topic must be looked into further in order to draw reliable conclusions. Such an investigation would certainly involve the study of how the outburst reacts to a change in parameters, among other things. It is also vital to perform 3D simulations on this question since there might be a dependence on dimensionality (Belyaev et al. 2013a).

Our main objective in this work was the clarification of the AM transport in unmagnetized astrophysical BLs. We found that the acoustic modes indeed transport AM through the BL and the disk, and that this mechanism is even highly efficient, reaching values for the dimensionless Reynolds stress α_{Re} of ~0.01 in quiet states and up to unity in high activity states (see Fig. 15). Along with AM, mass is also transported efficiently through the domain (see Fig. 7). The BL reacts to the enhanced transport by widening considerably until it reaches a thickness of about $0.2R_*$ (see Fig. 16).

One of the most important elements of wave mediated AM transport is the intrinsic non-locality of this process, i.e. waves can extract AM from one point in the disk and release it in another farther off. There are several implications that emerge from this: Thus far, α-models for the parametrization of the viscosity have been used both in the disk and in the BL, possibly with some corrections for the BL. This prescription is justified in the disk where, under certain conditions, the system is susceptible to the MRI. The MRI leads to turbulence in the gas and angular momentum is transported via turbulent stresses. This is a local process that also depends on the shearing at this point and a local effective viscosity can be derived by the model of Shakura & Sunyaev (1973). Furthermore, it allows for efficient mixing of the gas through the turbulence. In contrast, the AM transport we have investigated in this work does not depend on the local shearing, for instance, but is a non-local mechanism, instead. Therefore, it is doubtful whether a conventional α-model is applicable in the BL, and it will be hard to give a simple parametrization for the AM transport in the BL at all. However, α_{Re} features a rather smooth behavior and might be utilized for a simplified picture of the stresses in the BL. In addition, the mixing in the BL might not be as pronounced as in the disk, which could have important implications concerning the spectrum of the BL.

Connected with the notion of non-local AM transport is the fact that the kinetic energy, which resides in the gas shortly before it is decelerated to stellar rotation, does not need to be released as locally as was previously assumed. Waves also transport energy and release it to the fluid where they are damped or dissipate. This might have important implications for the structure and observational appearance of the BL. We consider, for instance, the alternative BL theory of the *spreading layer* (Inogamov & Sunyaev 1999, 2010) where the gas is not decelerated in the disk midplane but rather in two belts in the northern and southern hemisphere of the star. It is difficult to bring a local viscosity model into accordance with this theory, since the friction on the surface of the neutron star is far too small. The non-local AM transport described in this work could, however, shed new light upon the theory of the spreading layer.

Simulations that investigate both the vertical structure and the non-axisymmetric properties can only be performed in 3D, however. This is a vital extension that should be taken as the next step in order to bring the models closer to reality. In a 3D spherical geometry, it would also be possible to simultaneously model the star, a point that has been illustrated in Sect. 5.5. Another major extension is the inclusion of magnetic fields, i.e. performing magnetohydrodynamical simulations of the BL. It would then be possible to relinquish any viscosity prescription whatsoever and directly simulate the MRI in the disk and the acoustic modes in the BL. There might be important interactions between the turbulent disc and the BL modes and new wave branches might add to the three discussed here. However, the extensions mentioned above will greatly increase the computation time and possibly require more efficient codes and faster hardware.

References

Abramowicz, M., Brandenburg, A., & Lasota, J.-P. 1996, MNRAS, 281, L21
Balbus, S. A. 2003, ARA&A, 41, 555
Balbus, S. A., & Hawley, J. F. 1991, ApJ, 376, 214
Balbus, S. A., & Hawley, J. F. 1998, Rev. Mod. Phys., 70, 1
Balbus, S. A., & Lesaffre, P. 2008, New Astron. Rev., 51, 814
Balbus, S. A., & Papaloizou, J. C. B. 1999, ApJ, 521, 650
Baruteau, C. 2008, Ph.D. Thesis, CEA Saclay
Bell, K. R., & Lin, D. N. C. 1994, ApJ, 427, 987
Belyaev, M. A., & Rafikov, R. R. 2012, ApJ, 752, 115
Belyaev, M. A., Rafikov, R. R., & Stone, J. M. 2012, ApJ, 760, 22
Belyaev, M. A., Rafikov, R. R., & Stone, J. M. 2013a, ApJ, 770, 67
Belyaev, M. A., Rafikov, R. R., & Stone, J. M. 2013b, ApJ, 770, 68
Bertout, C., & Regev, O. 1992, ApJ, 399, L163
Binney, J., & Tremaine, S. 2008, Galactic Dynamics: Second Edition (Princeton University Press)
Chandrasekhar, S. 1960, Proc. National Academy of Science, 46, 253
Cohen, M., & Kuhi, L. V. 1979, ApJS, 41, 743
Drazin, P. G., & Reid, W. H. 2004, Hydrodynamic Stability (Cambridge University Press)
Fjørtoft, R. 1950, Geofys. Publ., Oslo, 17
Fujimoto, M. Y. 1993, ApJ, 419, 768
Gatski, T., & Bonnet, J. 2013, Compressibility, Turbulence and High Speed Flow (Elsevier Science)
Glatzel, W. 1988, MNRAS, 231, 795
Godon, P. 1995, MNRAS, 277, 157
Hartmann, L., Kenyon, S., & Hartigan, P. 1993, in Protostars and Planets III, eds. E. H. Levy, & J. I. Lunine, 497
Hayashi, M., Ohashi, N., & Miyama, S. M. 1993, ApJ, 418, L71
Hertfelder, M., Kley, W., Suleimanov, V., & Werner, K. 2013, A&A, 560, A56
Hubeny, I. 1990, ApJ, 351, 632
Hunter, J. D. 2007, Computing In Science & Engineering, 9, 90
Inogamov, N. A., & Sunyaev, R. A. 1999, Astron. Lett., 25, 269
Inogamov, N. A., & Sunyaev, R. A. 2010, Astron. Lett., 36, 848
Kippenhahn, R., & Thomas, H.-C. 1978, A&A, 63, 265
Kley, W. 1989, A&A, 208, 98
Kley, W., & Hensler, G. 1987, A&A, 172, 124
Kley, W., & Lin, D. N. C. 1996, ApJ, 461, 933
Kley, W., & Lin, D. N. C. 1999, ApJ, 518, 833
Kley, W., & Papaloizou, J. C. B. 1997, MNRAS, 285, 239
Kluźniak, W. 1987, Ph.D. Thesis, Stanford Univ.
Levermore, C. D. 1984, J. Quant. Spectr. Rad. Transf., 31, 149
Levermore, C. D., & Pomraning, G. C. 1981, ApJ, 248, 321

Lin, D. N. C., & Papaloizou, J. 1985, in Protostars and Planets II, eds. D. C. Black, & M. S. Matthews, 981
Lin, D. N. C., Hayashi, M., Bell, K. R., & Ohashi, N. 1994, ApJ, 435, 821
Lynden-Bell, D., & Pringle, J. E. 1974, MNRAS, 168, 603
Mark, J. W. K. 1976, ApJ, 205, 363
Masset, F. 2000, A&AS, 141, 165
Masset, F. S. 2002, A&A, 387, 605
Müller, T. W. A., & Kley, W. 2012, A&A, 539, A18
Müller, T. W. A., & Kley, W. 2013, A&A, 560, A40
Narayan, R., Goldreich, P., & Goodman, J. 1987, MNRAS, 228, 1
Papaloizou, J. C. B., & Pringle, J. E. 1984, MNRAS, 208, 721
Papaloizou, J. C. B., & Stanley, G. Q. G. 1986, MNRAS, 220, 593
Patterson, J., Robinson, E. L., & Nather, R. E. 1977, ApJ, 214, 144
Pessah, M. E., & Chan, C.-k. 2012, ApJ, 751, 48

Peyret, R. 1996, Handbook of Computational Fluid Mechanics (London: Academic Press)
Piro, A. L., & Bildsten, L. 2004, ApJ, 610, 977
Popham, R., & Narayan, R. 1995, ApJ, 442, 337
Regev, O., & Bertout, C. 1995, MNRAS, 272, 71
Rybicki, G. B., & Lightman, A. P. 1986, Radiative Processes in Astrophysics (New York: John Wiley and Sons)
Shakura, N. I., & Sunyaev, R. A. 1973, A&A, 24, 337
Springel, V. 2010, MNRAS, 401, 791
Spruit, H. C. 2002, A&A, 381, 923
Suleymanov, V. F. 1992, Sov. Astron. Lett., 18, 104
Tayler, R. J. 1973, MNRAS, 161, 365
Velikhov, E. 1959, Zhur. Eksptl. i Teoret. Fiz., 36
Warner, B., & Robinson, E. L. 1972, MNRAS, 159, 101

The Boundary Layer in compact binaries

Marius Hertfelder[*]

Institut für Astronomie und Astrophysik, Abt. Computational Physics
Auf der Morgenstelle 10, 72076 Tübingen, Germany
E-mail: marius.hertfelder@gmail.com

The structure and the thermodynamics of the non-magnetic boundary layer (BL) of accretion disks has been an outstanding problem in the field of theoretical astrophysics for years. The BL is a ubiquitous phenomenon that appears in a variety of astrophysical situations and systems where non-magnetic accretion occurs, i.e. where an accretion disk (AD) is present. The AD is an efficient mechanism to transport matter from the exterior of the disk to the gravitating center. Here, at the inner edge of the AD, the circulating matter comes upon the surface of the central object and is decelerated to match the object's rotation rate. During this process, an enormous amount of energy is released from the tiny BL region. This in turn generates hard radiation which can be clearly identified in the observed spectrum of the object. We perform numerical hydrodynamical simulations in order to calculate the luminosity and the spectrum of the BL and its dependence on parameters like the mass, rotation rate or mass accretion rate of the central white dwarf (WD). Therefore, we treat the problem in the one-dimensional, radial slim disk approximation. We employ a classical α-viscosity to account for the turbulence and include cooling from the disk surfaces as well as radial radiation transport. To account for the high temperatures in BLs around WDs, we also consider the radiation energy in a one-temperature approximation. We find that 1D models of the BL are well suited if one is interested in the radiation characteristics of the BL. The BL luminosity directly depends on the varied parameters which makes it possible to draw conclusions about real systems by comparing observations with our synthetic models. Ambiguities concerning different models with identical luminosities can be mitigated by regarding the emitted spectrum. We therefore present a method to gain information about a system by probing the radiation of the BL.

---

[*]Speaker.

arXiv:1702.06726v1 [astro-ph.SR] 22 Feb 2017

1. Introduction

Cataclysmic variables (CVs) are binary systems which are of great interest within the context of accretion physics since one of their main features is the mutual exchange of mass (Paczyński 1971). This leads to the formation of an accretion disk around a roughly solar mass white dwarf (WD) which is fueled by the Roche lobe overflow of the lighter main sequence companion star (Warner 1995; Giovannelli 1985). The accretion disk is an efficient mechanism for the matter to get rid of its angular momentum and travel towards the central WD. During this journey, energy is released due to the fact that the matter is falling deeper into the gravitational potential of the WD (e.g. Shakura & Sunyaev 1973; Lynden-Bell & Pringle 1974; Pringle 1981; Verbunt 1982). Over the whole extent of the disk, about one half of the accretion energy, which is given by

$$L_{\text{acc}} = \frac{GM_*\dot{M}}{R_*} \tag{1.1}$$

($G, M_*, \dot{M}$ and R_* are the gravitational constant, WD mass, mass accretion rate and radius) for non-rotating stars, becomes available. The other half of the energy specified by Eq. (1.1) is stored in terms of kinetic energy of the gas which rotates with Keplerian velocity $\Omega_{\text{K}} = \frac{GM_*}{r^3}$ near the surface of the WD. In order to match the rotation rate of the WD, which is in general much slower or even zero, the gas must be strongly slowed down before it can settle on the stellar surface. During this deceleration, an enormous amount of energy is released in a spatially confined region which is called the BL and has a radial extent of around one percent of the stellar radius for the case of a WD. The resulting UV and soft and hard X-ray emission of these hot BLs has been observed in several CVs (e.g. Cordova et al. 1981a,b; Cordova & Mason 1984). Depending on the mass accretion rate of the WD, the BL can either be optically thin ($\dot{M} \leq 10^{-10}M_\odot/\text{yr}$, Warner 1987) and the radiation will be dominated by soft and hard X-rays (e.g. Mukai & Patterson 2004; Pandel et al. 2003, 2005, King & Shaviv 1984; Shaviv 1987; Narayan & Popham 1993; Popham 1999), or it can be optically thick and emit thermal radiation (see e.g. Cordova et al. 1980; Mauche 2004).

For nearly 50 years now, it has been the goal of many astrophysicists to theoretically reproduce the BL. There have been several approaches to accomplish this task, one of the first being stationary calculations or timescale estimates (Lynden-Bell & Pringle 1974; Pringle 1977; Tylenda 1977, 1981; Pringle & Savonije 1979; Regev 1983). With increasing computational power, the era of numerical hydrodynamics was introduced and the first evolutionary calculations have been performed (Robertson & Frank 1986; Kley & Hensler 1987; Kley 1989a,b, 1991; Godon et al. 1995). The latter authors used a one-dimensional approximation of the BL, which is still a viable approach for certain aims. The gas is assumed to be slowed down in the midplane of the disk before it is spread on the surface of the star. Within this model, considering only the radial dependence of the physical variables, is then sufficient for the calculation of the total radiation emerging from the BL. A modern version of this approach has been presented in Hertfelder et al. (2013) where we included a quasi-two-dimensional radiation transport and special treatment for the radiation field.

Some questions about the BL cannot be answered by the 1D approximation of the BL and therefore, multidimensional models have been pursued as well. Among the first full radiation hydrodynamical simulations were the efforts by Kley (1989a,b, 1991), who did two-dimensional r-ϑ-simulations assuming axisymmetry. Those simulations are apt to investigate the structure of

the BL and the fate of the disk material, i.e. the meridional spreading and the mixing with the stellar material. With the availability of large compute clusters and parallel hydrodynamics codes, simulations of this kind nowadays feature amazing numerical resolutions and long evolution times, while including sophisticated physics and an advanced treatment of radiation (see Hertfelder & Kley 2017, in preparation). However, two-dimensional simulations in the disk plane (r-φ) were of great interest in the recent years. In order to slow down the gas in the BL, some mechanism of angular momentum (AM) transport must be present. In wide parts of the disk, this is done by the magnetorotational instability (MRI), which creates turbulence that acts like a genuine viscosity on macroscopic scales. In this case, the viscosity can be considered using the classical α-prescription by Shakura & Sunyaev (1973). In the BL, though, the source of the observed AM transport is still a matter of ongoing research. Recent simulations revealed the existence of a supersonic instability in the BL, which excites acoustic waves that are able to transport AM and mass (see Hertfelder & Kley 2015, for details). Full three-dimensional simulations have been done sporadically (e.g. Armitage 2002), however, the computational costs for highly resolved models are immense and the simulation times are very long.

In this work, we focus on the BL around a solar mass WD in a cataclysmic variable system. We extent the study presented in Hertfelder et al. (2013) and analyze the luminosity and the compound black body spectrum of the BL as a function of important system parameters such as the mass accretion rate and the stellar rotation rate. Detailed spectra, that also take the vertical structure into account, have been presented in Suleimanov et al. (2014).

2. Model & Physics

The problem is approached in a one-dimensional approximation in a cylindrical coordinate system (r, φ, z). For this purpose, the Navier-Stokes equations have been integrated in the vertical direction and derivatives with respect to the azimuthal direction φ have been dropped due to the assumption of axisymmetry. This approximation is called the *thin disk* approach and the variables depend only on radius and time (r, t). The mass density ρ is replaced by a vertically integrated surface density Σ which can be derived by

$$\Sigma = \int_{-\infty}^{\infty} \rho \, \mathrm{d}z = \sqrt{2\pi} \rho \, (z = 0) H, \tag{2.1}$$

where we assumed a Gaussian profile for ρ in the vertical direction. H is the pressure scale height and thus a measure for the height of the disk. Assuming hydrostatic balance and an isothermal equation of state in z-direction, it reads

$$H = \frac{c_{\mathrm{s}}}{\Omega_{\mathrm{K}}}, \tag{2.2}$$

where c_{s} is the sound speed. In the radial direction we use the ideal gas law for the pressure.

Since radiation pressure and energy are not negligible due to the high temperatures in the BL, we employ the one-temperature radiation transport (see e.g. Flaig et al. 2010), where the two equations for the gas and the radiation energy density are added up. We then propagate the total energy, consisting of gas and radiation energy, in time. This approach is a good approximation for optically thick regions (e.g. Kuiper et al. 2010) and justified since the BLs we are regarding here are optically thick. The radiation energy equation is closed by employing the flux-limited diffusion

3

approximation (FLD; Levermore & Pomraning (1981); Levermore (1984)) for the radiative flux $\vec{F}$ and we adopt the formulation by Levermore & Pomraning (1981) for the flux-limiter λ. The opacity κ is determined using Kramer's law,

$$\kappa = 5 \times 10^{24} \rho T^{-3.5} \, [\text{cm}^2 \text{g}^{-1}], \tag{2.3}$$

with a lower threshold given by Thomson scattering. The disk can cool vertically via a blackbody radiation of temperature T_{eff}, which is calculated from the midplane temperature T by using a generalization of the gray atmosphere for the optical depth in the vertical direction (Hubeny 1990). The exact equations for our model can be found in Hertfelder et al. (2013).

The partial differential equations are discretized on a fixed Eulerian grid using finite differences. For the time propagation, a semi-implicit-explicit scheme is employed since some source terms, especially the viscous ones, require an implicit treatment so that the time step is not restricted too severely. The code (see also Hertfelder et al. 2013) maintains a formal second-order accuracy in time and space and uses a multi step procedure for the time integration (operator splitting), which is controlled by the CFL condition that limits the largest possible time step.

The boundary conditions are implemented such that the disk is fed from the outer radius with a constant rate $\dot{M}$. We impose Keplerian rotation at the outer edge and stellar rotation Ω_* at the inner edge. For the other variables, we assume zero gradient boundary conditions. The models are started from initial profiles given by the disk solution by Shakura & Sunyaev (1973) which have been interpolated to the stellar surface.

2.1 Model Parameters

We focus on the BL around a WD in a cataclysmic variable system. Accordingly, simulations for a WD with $0.6, 0.8$ and 1.0 solar masses have been performed. We assumed different values for the mass accretion rate $\dot{M}$ that range from 10^{-10} up to 10^{-8} solar masses per year. As can be seen from Eq. (1.1), another crucial parameter for the luminosity of the BL is the stellar radius R_*. For WDs, mass and radius are not independent but connected via an inverse relation; i.e. the larger the stellar mass, the smaller the radius. We use the relation from Nauenberg (1972) to determine the exact value of R_*. The stellar rotation rate also plays an important role for the luminosity of the BL. We varied it between 0.0 and $0.9\Omega_{\text{K}}(R_*)$, which corresponds to non-rotating up to nearly break-up velocity. The parameter for the α-viscosity was taken to be 0.01 throughout.

3. Results

3.1 The general structure of the BL

We will begin our discussion of the results by first presenting the basic properties of the BL. For this purpose we adduce the case with $M_* = 0.8 M_\odot$ and $\dot{M} = 10^{-8} M_\odot/\text{yr}$ as a standard model and basis for the parameter variations.

Figure 1 shows the dynamical structure of the BL. On the left hand side, the angular velocity divided by the Keplerian angular velocity is depicted in the region between the stellar surface and the disk. Viewing the situation from the outside to the inside, the gas initially rotates with Keplerian velocity in the disk due to the force balance of gravitational and centrifugal forces. There is a small,
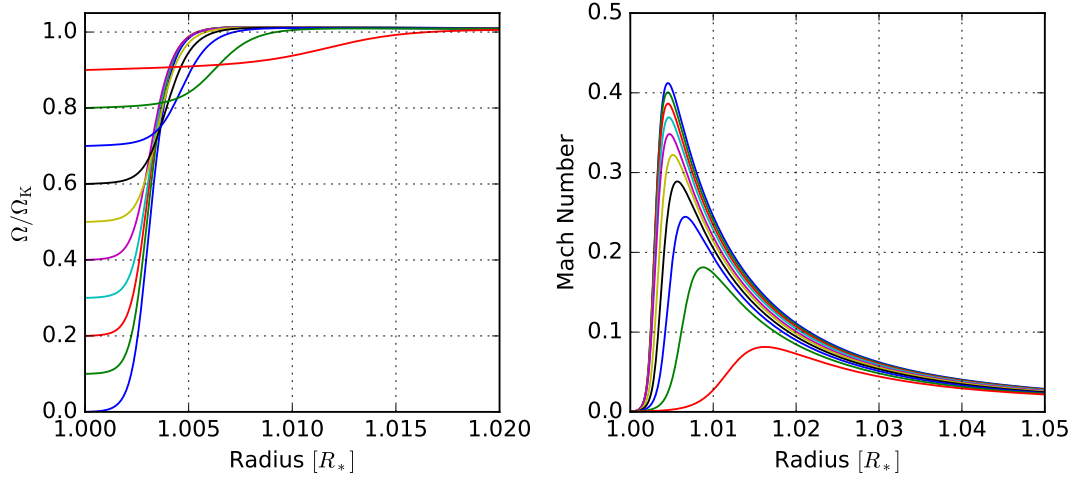
Figure 1: Angular velocity $\Omega = v_\varphi/r$ in terms of the Keplerian angular velocity (*left panel*) and radial Mach number $\mathrm{Ma} = -v_r/c_\mathrm{s}$ (*right panel*) as a function of the radial coordinate in units of R_*. The different colors denote the different stellar rotation rates Ω_* which can be inferred from the left panel at $r = 1$.

additional pressure support since the temperature decreases with increasing radius and thus the gas may rotate sub-Keplerian. This situation changes when the pressure gradient is pointing inwards as we come closer to the BL. Then, the gas rotates slightly super-Keplerian. When entering the BL, the gas reaches the maximum rotational velocity, a point which is called the zero-torque point, since no viscous torques exist at this point due to the vanishing gradient of Ω. Going further inwards, the gas is decelerated smoothly down to the velocity of the stellar surface. Here, it is mainly stabilized by pressure support. The region between the stellar surface and the maximum of Ω is denoted by the *dynamical BL width* and there is a tendency for an increasing BL width with increasing stellar rotation rate.

The radial or infall velocity of the matter is reflected by the Mach number shown in the right panel of Fig. 1. Approaching the BL from the outside, the infall velocity of the gas increases and reaches its maximum at the zero-torque point before it drops rapidly to almost zero at the surface of the star. Thus, there is no shocking of the gas at the stellar surface. The increasing radial velocity is due to the loss of angular momentum caused by friction in the disk and the slower the star spins, the higher is the infall velocity. Apparently no supersonic infall velocities are reached, which is an important issue in connection with the causality (see e.g. Pringle 1977; Popham & Narayan 1992; Kley & Papaloizou 1997). In general, we do not find supersonic infall velocities in any of our models for small values of α.

The thermal structure of the BL is illustrated in Fig. 2 with the surface density Σ (see Eq. 2.1) on the left hand side and the effective temperature on the right hand side. The color coding is analogue to Fig. 1). The plot of the surface density shows that the BL is heavily depleted of gas, Σ decreases by almost two orders of magnitude compared to the disk. The BL can thus be seen as a bottleneck, where the matter has to squeeze through in order to reach the surface of the star. This notion is in accordance with the behavior of the radial velocity: The smaller the surface density
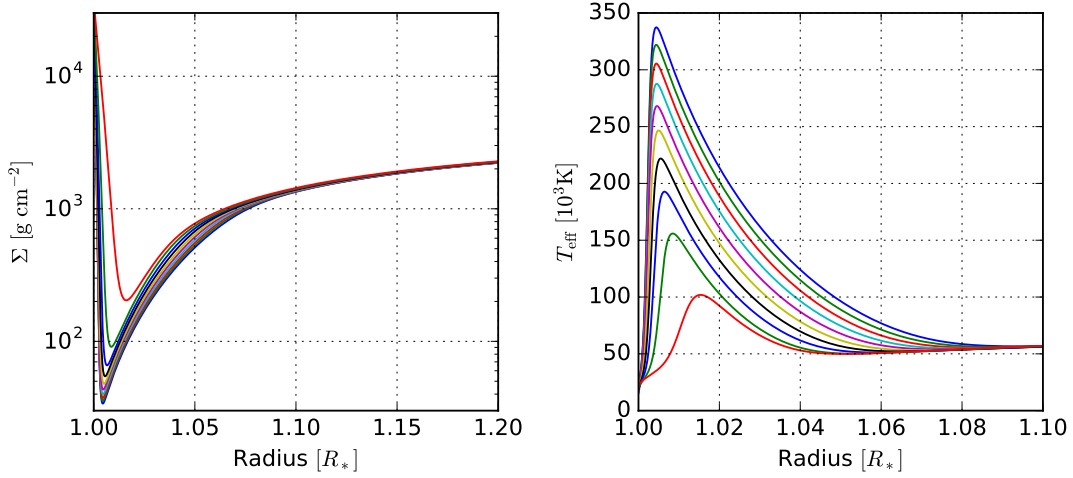
Figure 2: Surface density Σ (*left panel*) and effective or surface temperature T_{eff} (*right panel*). The different colors represent models with different stellar rotation rate and match those of Fig. 1.

becomes, the greater the radial velocity is in order to maintain a constant mass accretion rate,

$$\dot{M} = -2\pi r \Sigma v_r. \tag{3.1}$$

Equation 3.1 can directly be derived from the conservation of mass. Furthermore, the depletion of mass in the BL depends on the stellar rotation rate and is most severe for a non-rotating star. This does not apply for the disk where all models have about the same density. The rapid increase of Σ at $r \approx 1$ marks the beginning of the WD.

Although the physical model presented here is one-dimensional in nature, we can calculate a surface temperature from the midplane temperature by using an appropriate approximation for the vertical structure (see Sec. 2). T_{eff} then represents the temperature of the disk and BL at an optical depth of $\tau \approx 1$ and thus determines the radiation emerging from the system. Figure 2 shows that the surface temperature increases tremendously in the BL, reaching up to almost 350 000 Kelvin. This peak is due to the strong shearing in the BL where the gradient of Ω is large (see Fig. 1) and a great deal of heat is produced through friction. With increasing stellar rotation rate, the maximum value of T_{eff} in the BL shrinks, since the shearing becomes less intense. In the disk, there is no difference between the presented models. The surface temperature shows a second peak at $r \approx 1.41$ with $T_{\text{eff}} = 67152$ Kelvin which is in perfect agreement with the disk solution by Shakura & Sunyaev (1973). Although the region where the energy is produced has a radial extent of only about one percent of the stellar radius, the major peak of T_{eff} spreads over almost 10 percent. The reason is the radial diffusion which transports energy through the disk and the resulting region has been named the *thermal BL* (Regev & Bertout 1995; Popham & Narayan 1995). It is the area from which the BL radiation that can be observed escapes.

3.2 The width of the BL

Table 1 shows the width of the dynamical BL for the reference model. It is defined to be the

ω	$\Delta r \ [R_*]$
0.0	0.0071
0.1	0.0071
0.2	0.0071
0.3	0.0071
0.4	0.0072
0.5	0.0076
0.6	0.0081
0.7	0.0089
0.8	0.0112
0.9	0.0182

Table 1: Width of the boundary layer for the standard model with $M_* = 0.8 M_\odot$, $\dot{M} = 10^{-8} M_\odot/\mathrm{yr}$ and stellar rotation rates $\omega = \Omega_*/\Omega_\mathrm{K}(R_*)$ spanning from 0.0 up to 0.9. By definition, the BL ranges from the surface of the star to the point where $\partial \Omega(r)/\partial r = 0$, i.e. where it has a maximum.

region ranging from the stellar surface, which is at $r \approx 1$ in our simulations, to the zero-gradient point where $\partial \Omega/\partial r = 0$, i.e. the angular velocity has its maximum. This point is not identical with the maximum point of the curves in the left panel of Fig. 1. The width of the BL around a WD is extremely small with values of less than one percent of the stellar radius in most cases. Only for fast rotating WDs is the BL becoming significantly wider. The reason for the narrow BL is the large value of M_*/R_* for WDs which have a mass comparable to our sun but a radius of only a hundredth of the solar radius. This fraction appears in the gravitational force which is, among other parameters, responsible for the temperature and surface density of the disk and the BL. The width is in general governed by the viscosity, which in turn depends on the surface density and the temperature if we employ a α-prescription. Thus, the high ratio of stellar mass and stellar radius in WDs leads to very thin BLs, as opposed to young stars, for instance. This is one of the reasons why BL simulations of WDs are demanding from a computational point of view, since a high numerical resolution has to be applied in order to resolve this small area sufficiently.

With increasing stellar rotation rate, the temperature in the BL decreases, since the gas retains more and more of its angular momentum and less kinetic energy is released. Although a colder BL should be thinner than a hot one (one can think of the heat puffing up the BL), we observe the opposite, namely an increasing BL width (see Table 1). The reason is that the depletion of mass in the BL depends on the rotation rate as well (see Fig. 2, left panel), and Σ is larger for high Ω_*. The complex interplay of surface density and midplane temperature arranges it such that the BL becomes wider. The thermal BL, however, is about ten times larger and diminishes in size with increasing stellar rotation due to the decreasing energy release in the BL.

Figure 3 visualizes the width of the dynamical BL as a function of the WD rotation rate and mass for three different values of the mass accretion rate $\dot{M}$. We will first refer to the graph on the left hand side, where the marker colors correspond to the mass accretion rate and the line color represents the mass of the WD. The reference model is shown with cyan markers and a green dashed line. As has been discussed in connection with Table 1, we recognize a clear trend for an increasing
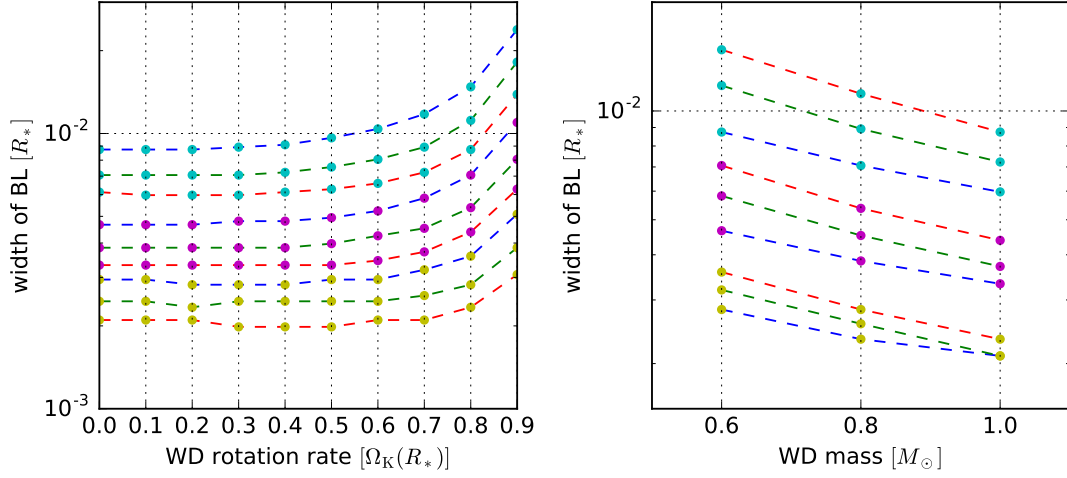
7

Figure 3: The width of the dynamical BL as a function of the WD rotation rate (*left panel*) and the WD mass (*right panel*) in units of the WD radius R_*. The marker color represents the mass accretion rate of the WD in both plots where cyan equals 10^{-8}, magenta 10^{-9} and yellow 10^{-10} solar masses per year. On the left hand side, the line color illustrates the mass of the WD with blue, green and red being $0.6, 0.8$ and $1.0 M_\odot$. On the right hand side, the line color tells the rotation rate of the model and blue, green and red correspond to 0.2, 0.7 and $0.9 \Omega_K(R_*)$, respectively.

BL width with growing stellar rotation rate. This is, however, not the case in some other models considered in Fig. 3. Especially for lower values of the mass accretion rate, the BL might shrink in width before it is getting larger with increasing stellar rotation rate. Consider, for instance, the bottom red line with yellow markers, which corresponds to $1.0 M_\odot, 10^{-10} M_\odot/\text{yr}$, where this behavior is visible. The reverse of the trend is due to the complex interplay of surface density and midplane temperature, which has been mentioned before. Depending on the specific choice of parameters, the BL is either growing continually with increasing rotation rate, or it is shrinking slightly in the beginning before it is widening again. It is impossible to give a general answer to this issue, however, there seems to be a tendency for models with low mass accretion rate and high stellar mass to adopt the latter behavior. Apart from this detail, all models show a similar overall trend: The width is increasing slowly in the beginning and more severely for high stellar rotation rates. Thus, if one is able to identify the width of a BL (e.g. from the radiation characteristics), it helps to distinguish between fast rotating WDs but not between low or non-rotating ones.

The right panel of Fig. 3 shows how the mass of the WD influences the width of the BL. Again, the mass accretion rate is visualized by the differently colored markers. We have picked three stellar rotation rates for each mass accretion rate and WD mass, given by 0.2 (blue line), 0.7 (green line) and 0.8 (red line) times the breakup velocity. Clearly, the BL is shrinking with increasing WD mass. The reason is the increasing gravitational pull, which is enhanced even more by the inverse mass-radius relation for WDs. It arranges it so that the surface density is decreasing and the temperature is increasing with growing WD mass and the width is decreasing, finally. The width of the thermal BL is increasing with M_*, on the other hand, although only weakly. This is due
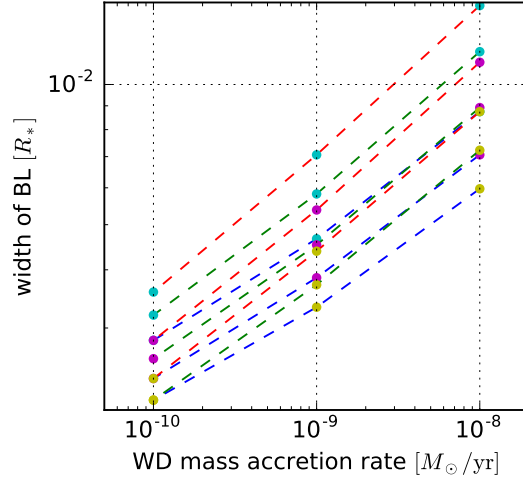
Figure 4: The width of the dynamical BL as a function of the WD mass accretion rate in units of solar masses per year. The marker color represents the mass of the WD and cyan, magenta and yellow correspond to 0.6, 0.8 and 1.0 solar masses, respectively. The line color indicates the rotation rate of the model such that blue, green and red correspond to 0.2, 0.7 and $0.9\Omega_{\mathrm{K}}(R_*)$, respectively.

to the fact that more energy is released with increasing WD mass which is distributed on a wider area. It seems that the dependence on the stellar mass is approximately linear in a logarithmic plot. Thus, as a rule of thumb, we infer that the width of the BL is decreasing exponentially with increasing WD mass.

Finally, we investigate the dependence on the mass accretion rate of the WD and consider Fig. 4 for this purpose. Shown here are the same nine models as in Fig. 3. There is a clear trend for the BL width to grow with increasing mass accretion rate. Again, this is influenced by the surface density and the temperature which are both growing drastically with increasing mass accretion rate since a higher $\dot{M}$ means that more mass accumulates in the disk. Accordingly, the energy dissipation through shear is enhanced and leads to a higher disk temperature. The same holds for the effective temperature and thus the width of thermal BL is growing even more drastically than the dynamical BL. For high stellar rotation rates (red line), the trend is almost linear in the double logarithmic plot of Fig. 4. With decreasing stellar rotation rate, however, the trend seems to deviate slightly from linear. Therefore, while the BL width increases exponentially with the logarithm of the mass accretion rate for high stellar rotation rates, it does only roughly so for lower rotation rates. We note that the width of the BL is in all cases given in units of the stellar radius, which depends on the stellar mass.

3.3 The luminosity of the BL

The luminosity of the BL is of great importance when comparing the results of our simulations with real observations. In our model, the BL and the disk radiate like a black body at each surface point with a temperature that is given by the effective temperature T_{eff}. Therefore, the luminosity
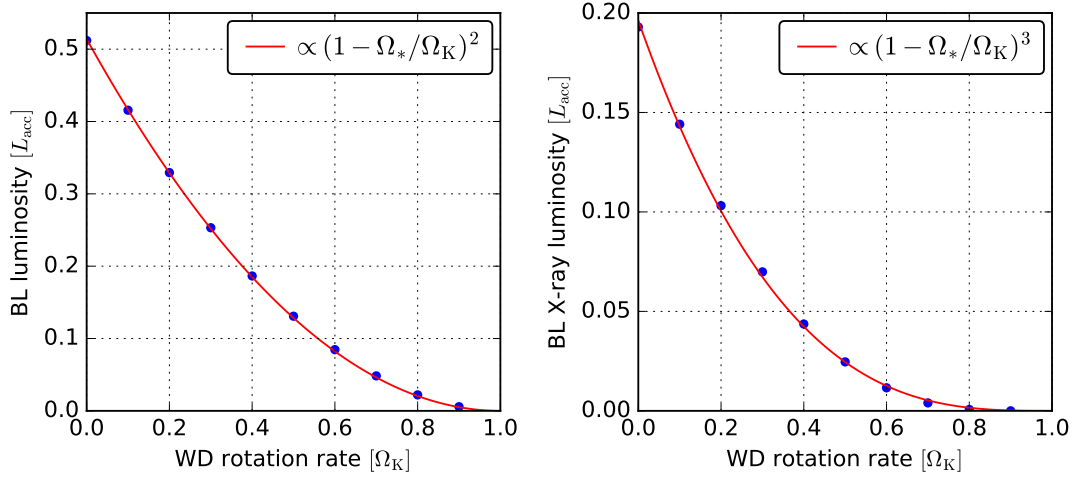
9

Figure 5: The luminosity of the BL as a function of the WD rotation rate. The luminosity is normalized to the total accretion luminosity $L_{\mathrm{acc}} = GM_*\dot{M}/R_*$. The left hand side visualizes the total luminosity of the BL and square fit to the data points. In the right hand side picture, only the X-ray luminosity (0.1 to 10 keV) is taken into account and plotted along with a cubic fit to the data.

of one ring is given by

$$L_i = 2\int_0^{2\pi}\int_{r_i^{\mathrm{L}}}^{r_i^{\mathrm{R}}} \sigma T_{\mathrm{eff},i}^4 \, r\,\mathrm{d}r\,\mathrm{d}\varphi, \tag{3.2}$$

where the factor 2 comes from the two sides of the disk and $r^{\mathrm{L,R}}$ means the left and the right limit of the individual ring. The total BL luminosity is then obtained by summing up all rings up to the point where the disk starts. The end of the BL and the beginning of the disk, respectively, is derived by comparing the effective temperature of our models with the surface temperature given by the standard solution of the accretion disk by Shakura & Sunyaev (1973):

$$T(r) = \left[\frac{3GM\dot{M}}{8\pi r^3\sigma}\left(1 - \left(\frac{R_*}{r}\right)^{1/2}\right)\right]^{1/4} \tag{3.3}$$

The disk of our models is perfectly described by the standard solution and especially Eq. 3.3 and thus we define the thermal BL to extent up to the point where T_{eff} comes to within five percent of the standard solution.

Figure 5 visualizes the luminosity as a function of the stellar rotation rate for the reference model with $0.8M_*$ and $\dot{M} = 10^{-8}M_\odot/$yr. With increasing stellar rotation rate, the luminosity of the BL decreases drastically. This is due to the fact that almost all energy which is released in the BL originates from the difference in kinetic energy of the gas just outside the BL and at the surface of the WD. The faster the star spins, the less the gas is slowed down and less energy becomes free and contributes to the observed luminosity. Thirty years ago, there has been a debate about the relation that ties the luminosity of the BL to the stellar rotation rate (see e.g. Kluźniak 1987; Kley 1991;
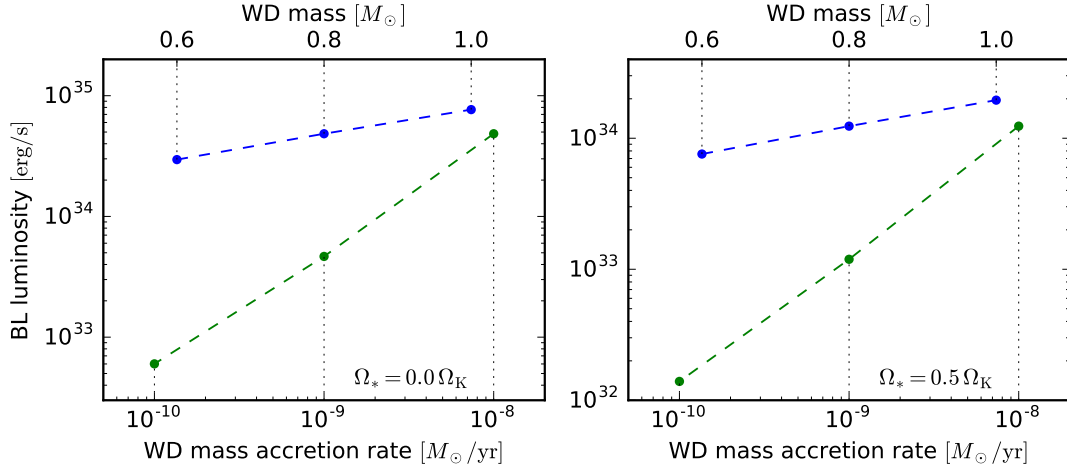
Figure 6: The total luminosity of the BL as a function of the stellar mass M_* and mass accretion rate $\dot{M}$. The green data points visualize the luminosity for the three different mass accretion rates $10^{-10}, 10^{-9}$ and $10^{-8} M_\odot/\mathrm{yr}$ and the blue data points correspond to the mass dependence of the luminosity. The WD is non-rotating in the left panel, $\Omega_* = 0.0\Omega_\mathrm{K}(R_*)$, and has a rotation rate of $\Omega_* = 0.5\Omega_\mathrm{K}(R_*)$ in the right panel.

Popham & Narayan 1995), however, the consent has been to utilize

$$L_\mathrm{BL} = \frac{1}{2} L_\mathrm{acc} \left(1 - \frac{\Omega_*}{\Omega_\mathrm{K}(R_*)} \right)^2 \tag{3.4}$$

as a formula. The functional dependence of Eq. (3.4) almost perfectly describes the data as can be seen from the fit (red curve) in Fig. 5. However, we found from our simulations that the prefactor of $1/2$ is too low and the fit yielded a value of 0.51 for the reference model. This has to do with the definition of the inner disk radius and thus small variations are possible due to different setups.

On the right hand side of Fig. 5 we display the X-ray luminosity of the BL for the energy band between 0.1 and 10 keV. In order to derive $L_\mathrm{BL,X-ray}$, we assume Planck's law for every ring with the temperature $T_\mathrm{eff}(r)$ and integrate over the solid angle and the disk area to obtain the spectral luminosity of the BL. We can then confine the energy interval of interest and calculate the luminosity of that band. For our reference model, the X-ray luminosity of the BL around a non-rotating WD amounts to roughly 40% of the total BL luminosity and drops very fast for increasing stellar rotation because only very high effective temperatures significantly contribute to the X-ray band. The drop is considerably faster than that of the total luminosity and goes with the third power of the stellar rotation rate. Thus, we postulate as a rule of thumb for the X-ray luminosity of the BL the law:

$$L_\mathrm{BL,X} = 0.2 \left(1 - \frac{\Omega_*}{\Omega_\mathrm{K}(R_*)} \right)^3 \tag{3.5}$$

The prefactor might also depend on other parameters of the system. The functional dependence, however, seems to be solid for the cases we simulated within this study.

In Figure 6, we verify the dependence of the luminosity on the WD mass and mass accretion rate, which is given by Eq. (1.1). The green data points and connecting dashed line refer to the
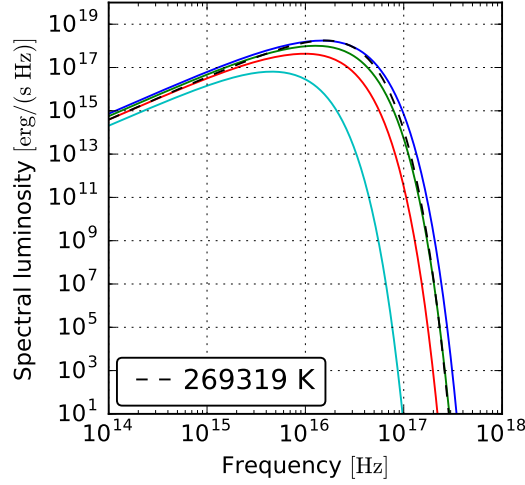
Figure 7: Spectral luminosity L_ν for the reference model ($0.8M_\odot, 10^{-8}M_\odot/\mathrm{yr}$) and a stellar rotation rate of 0.0 (blue), 0.3 (green), 0.6 (red) and $0.9\Omega_\mathrm{K}(R_*)$ (cyan). The black dashed line indicates a fit with a single temperature Planck law.

three different mass accretion rates of $10^{-10}, 10^{-9}$ and 10^{-8} solar masses per year. In the double logarithmic plot the data points lie on one straight line which means that indeed $L_\mathrm{BL} \propto \dot{M}$, independent of Ω_*. Both plots of Fig. 6 differ only in stellar rotation rate. In the left hand side plot, the WD is non-rotating and on the right hand side it rotates with 50% of the breakup velocity. The data points for the three different WD masses $0.6, 0.8$ and $1.0M_\odot$ are situated also on a straight line, though in a semi logarithmic representation. This means that there seems to be a rather weak exponential dependence between BL luminosity and WD mass. We note that mass and radius are not independent due to the mass-radius relation for WDs. Therefore, the exact dependence on stellar mass is rather given by the relation M_*/R_*, which depends on the mass-radius relation. However, for the small mass spectrum observed in WDs, a good first approximation is a linear increase in luminosity with increasing stellar mass.

Finally, in Fig. 7 we show the spectrum of the BL of the reference model which has a 0.8 solar mass WD and a mass accretion rate of 10^{-8} solar masses per year. The spectral luminosity is obtained by imposing Planck's law with temperature T_eff for each ring of the BL and subsequently adding them up while taking into account the area of the ring. In the graph, four different stellar rotation rates, 0.0 (blue), $0.3, 0.6$ and $0.9\Omega_\mathrm{K}(R_*)$ (cyan) are presented. The spectrum becomes considerably harder with decreasing stellar rotation rate which is in accordance with the discussion of the effective temperature shown in Fig. 2. The high energetic part of the spectrum stems from the hottest parts of the thermal BL, i.e. where the maximum of the effective temperature is located. The dashed black line in Fig. 7 indicates a black body fit to the spectrum of the non-rotating WD. To this purpose we tried to approximate the compound BL spectrum by a single temperature Planck law which gives a rough estimate of the shape of the spectrum. In this case, the fit yields a black body temperature of approximately 270 000 Kelvin. This temperature can then be compared with black body fits of real observations.

12

4. Summary and conclusion

In this study, we have presented elaborate one-dimensional simulations of the BL around a WD in a cataclysmic variable system. We employed the thin disk approximation where axisymmetry is assumed and the disk is vertically integrated. The novelty of our model involves the detailed treatment of radiation in that radiation transport in the radial as well as in the vertical direction has been implemented and that the radiation energy has been propagated in time along with the thermal energy. For the purposes considered within this study the 1D approximation is sufficient and, together with observationsi, our results can help to identify system parameters of CVs like SS Aur (Nabizadeh, Balman, Hertfelder 2017, in preparation). There are, however, questions which involve the structure, the mixing or instabilities in the BL that can not be answered withing the realm of the 1D model presented here. One must then perform two- or higher dimensional simulations (e.g. Hertfelder & Kley 2017, in preparation).

The parameter study we presented here comprises models of the BL around WDs of the masses $0.6, 0.8$ and 1.0 solar masses and thus covers the typical mass range of WDs in CVs. For each mass, three mass accretion rates, viz. $10^{-10}, 10^{-9}$ and 10^{-8} solar masses per year, were considered. Finally, for every $M_* $-$\dot{M}$ combination, ten stellar rotation rates were imposed, spanning the whole domain from a non-rotating up to a nearly at break-up velocity rotating WD. Thus, we have run 90 models in total which gave us a good starting point for a thorough parameter study. As a reference model we took the simulation with $0.8 M_\odot$ and $10^{-8} M_\odot$/yr and started by discussing the basic properties of a non-magnetic BL.[1]

The BL connects the disk in which the gas is moving with Keplerian velocity with the stellar surface that in general rotates with a lower velocity and thus the gas looses a good part of its angular momentum and kinetic energy in this region. Our simulations show that the BL takes the form of a bottleneck in order to accomplish this task: The radial infall velocity increases drastically due to the loss of the stabilizing angular momentum and simultaneously the surface density drops considerably in order to maintain the constant mass flux. During the deceleration of the azimuthal velocity component a great deal of energy comes free which is responsible for the sudden rise of the effective temperature in the BL. Temperatures of up to almost 350 000 Kelvin are reached for the non-rotating WD of the reference model. Since the energy originates from the deceleration process, consequently with increasing stellar rotation the maximum temperature of the BL decreases more and more rapidly.

The width of the BL is one of the important parameters that we deeper looked into. At first, we have to distinguish between the terminologies of the dynamical and the thermal BL. The dynamical BL orients itself to the behavior of the angular velocity only and the width is defined to be the region from the stellar surface up to the maximum of $\Omega(r)$. With increasing WD rotation rate, the width of the dynamical BL in general increases as well. However, depending on parameters like stellar mass and mass accretion rate, it is not an uncommon phenomenon that it first shrinks before growing perceptibly. For variations in M_* and $\dot{M}$, the situation is clear: With increasing mass or decreasing mass accretion rate, the dynamical BL becomes considerably thinner. The dynamical width is an important parameter since it defines the region where the energy which is later radiated

---

[1]Due to the high number of simulations it is not possible to include data such as the BL luminosity for each model in this paper. However, numbers not presented here can naturally be requested by email to the author.

13

away is produced. The more confined this region is, the harder the radiation will be. However, in this context it is more convenient to refer to the thermal BL. The radiation produced in the dynamical BL is distributed through radiative diffusion in the radial direction before it can escape from the system. The region where the heat spreads is denoted as the thermal BL and with a radial extent of $\sim 10\%$ of the stellar radius it is roughly ten times as wide as its dynamical counterpart. In contrast to the dynamical BL, the thermal BL becomes smaller with increasing stellar rotation rate. Its width directly influences the spectrum of the BL.

The most important parameter when comparing one-dimensional BL simulations with observations is the luminosity. We confirmed that indeed the BL luminosity decreases quadratically with increasing stellar rotation rate Ω_*. An interesting result arises when considering the X-ray band of the BL luminosity only: In this case, we observe a cubic dependence on the stellar rotation rate. One problem that arises in connection with the BL luminosity is clearly the ambiguity that different models may yield the same total BL luminosity. For instance, a model with high stellar rotation rate but also a high mass accretion rate can yield the same luminosity as a model with a smaller mass accretion rate but also a lower rotation rate. Here, one can step in with the additional information from the X-ray luminosity and utilize the formula we provided for an estimate of the system parameters. Another possibility is given by regarding the spectrum of the BL which will also help to clear up the ambiguity outlined above.

In the end, we want to learn more about systems that can be observed in space. Thus, by combining the insight gained from theoretical simulations and observation we should be able to learn more about its parameters. The approach presented here answers these purposes in that it is elaborated enough to come to unambiguous conclusions by comparing the results with observations, but at the same time it is still fast enough to run a large number of models which are necessary for the parameter hunt.

References

Armitage, P. J. 2002, MNRAS, 330, 895

Cordova, F. A., Jensen, K. A., & Nugent, J. J. 1981a, MNRAS, 196, 1

Cordova, F. A. & Mason, K. O. 1984, MNRAS, 206, 879

Cordova, F. A., Mason, K. O., & Nelson, J. E. 1981b, ApJ, 245, 609

Cordova, F. A., Nugent, J. J., Klein, S. R., & Garmire, G. P. 1980, MNRAS, 190, 87

Flaig, M., Kley, W., & Kissmann, R. 2010, MNRAS, 409, 1297

Giovannelli, F. 1985, Multifrequency Behavior of Galactic Accreting Sources, Frascati Workshop (Edizioni Scientifiche Siderea)

Godon, P., Regev, O., & Shaviv, G. 1995, MNRAS, 275, 1093

Hertfelder, M. & Kley, W. 2015, A&A, 579, A54

Hertfelder, M., Kley, W., Suleimanov, V., & Werner, K. 2013, A&A, 560, A56

Hubeny, I. 1990, ApJ, 351, 632

King, A. R. & Shaviv, G. 1984, Nature, 308, 519

Kley, W. 1989a, A&A, 208, 98

Kley, W. 1989b, A&A, 222, 141

Kley, W. 1991, A&A, 247, 95

Kley, W. & Hensler, G. 1987, A&A, 172, 124

Kley, W. & Papaloizou, J. C. B. 1997, MNRAS, 285, 239

Kluźniak, W. 1987, PhD thesis, , Stanford Univ., (1987)

Kuiper, R., Klahr, H., Dullemond, C., Kley, W., & Henning, T. 2010, A&A, 511, A81

Levermore, C. D. 1984, J. Quant. Spec. Rad. Trans., 31, 149

Levermore, C. D. & Pomraning, G. C. 1981, ApJ, 248, 321

Lynden-Bell, D. & Pringle, J. E. 1974, MNRAS, 168, 603

Mauche, C. W. 2004, in Revista Mexicana de Astronomia y Astrofisica Conference Series, Vol. 20, Revista Mexicana de Astronomia y Astrofisica Conference Series, ed. G. Tovmassian & E. Sion, 174–175

Mukai, K. & Patterson, J. 2004, in Revista Mexicana de Astronomia y Astrofisica Conference Series, Vol. 20, Revista Mexicana de Astronomia y Astrofisica Conference Series, ed. G. Tovmassian & E. Sion, 244–244

Narayan, R. & Popham, R. 1993, Nature, 362, 820

Nauenberg, M. 1972, ApJ, 175, 417

Paczyński, B. 1971, Annu. Rev. Astro. Astrophys., 9, 183

Pandel, D., Córdova, F. A., & Howell, S. B. 2003, MNRAS, 346, 1231

Pandel, D., Córdova, F. A., Mason, K. O., & Priedhorsky, W. C. 2005, ApJ, 626, 396

Popham, R. 1999, MNRAS, 308, 979

Popham, R. & Narayan, R. 1992, ApJ, 394, 255

Popham, R. & Narayan, R. 1995, ApJ, 442, 337

Pringle, J. E. 1977, MNRAS, 178, 195

Pringle, J. E. 1981, Annu. Rev. Astro. Astrophys., 19, 137

Pringle, J. E. & Savonije, G. J. 1979, MNRAS, 187, 777

15

Regev, O. 1983, A&A, 126, 146

Regev, O. & Bertout, C. 1995, MNRAS, 272, 71

Robertson, J. A. & Frank, J. 1986, MNRAS, 221, 279

Shakura, N. I. & Sunyaev, R. A. 1973, A&A, 24, 337

Shaviv, G. 1987, Astrophys. Space Sci., 130, 303

Suleimanov, V., Hertfelder, M., Werner, K., & Kley, W. 2014, A&A, 571, A55

Tylenda, R. 1977, Acta Astron., 27, 235

Tylenda, R. 1981, Acta Astron., 31, 267

Verbunt, F. 1982, Space Sci. Rev., 32, 379

Warner, B. 1987, MNRAS, 227, 23

Warner, B. 1995, Cambridge Astrophysics Series, 28

The vertical structure of the boundary layer around compact objects

Marius Hertfelder[*][1] and Wilhelm Kley[1]

Institut für Astronomie und Astrophysik, Abt. Computational Physics, Auf der Morgenstelle 10, 72076 Tübingen, Germany

ABSTRACT

Context. Mass transfer due to Roche lobe overflow leads to the formation of an accretion disk around a weakly magnetized white dwarf (WD) in cataclysmic variables. At the inner edge of the disk, the gas comes upon the surface of the WD and has to get rid of its excess kinetic energy in order to settle down on the more slowly rotating outer stellar layers. This region is known as the boundary layer (BL).
Aims. In this work we investigate the vertical structure of the BL, which is still poorly understood. We shall provide details of the basic structure of the two-dimensional (2D) BL and how it depends on parameters such as stellar mass and rotation rate, as well as the mass-accretion rate. We further investigate the destination of the disk material and compare our results with previous one-dimensional (1D) simulations.
Methods. We solve the 2D equations of radiation hydrodynamics in a spherical (r-ϑ) geometry using a parallel grid-based code that employs a Riemann solver. The radiation energy is considered in the two-temperature approach with a radiative flux given by the flux-limited diffusion approximation.
Results. The BL around a non-rotating WD is characterized by a steep drop in angular velocity over a width of only 1% of the stellar radius, a heavy depletion of mass, and a high temperature ($\sim 500\,000$ K) as a consequence of the strong shear. Variations in Ω_*, M_*, and $\dot{M}$ influence the extent of the changes of the variables in the BL but not the general structure. Depending on Ω_*, the disk material travels up to the poles or is halted at a certain latitude. The extent of mixing with the stellar material also depends on Ω_*. We find that the 1D approximation matches the 2D data well, apart from an underestimated temperature.
Conclusions.

Key words. accretion, accretion disks – hydrodynamics – methods: numerical – white dwarfs – binaries: close

1. Introduction

Accretion of matter onto a non-magnetized star is accompanied by the formation of a boundary layer (BL) where the Keplerian rotation rate of the disk smoothly connects to the stellar rotation rate, that is, in general, much smaller. In the BL, up to $\sim 50\%$ of the total accretion luminosity is liberated in a spatially very confined region. In this publication we focus on the BL around a white dwarf (WD) that resides in a cataclysmic variable (CV) system. The BL around a WD typically has a radial extent of $\lesssim 1\%$ of the stellar radius (Lynden-Bell & Pringle 1974; Hertfelder et al. 2013). The extent of the energy released in the BL depends on the rotation rate of the WD. When the gas enters the BL from the outer parts of the disk, it gradually gets rid of one half of the accretion energy during its inward drift through the disk. The other half of the energy gained by falling into the gravitational potential of the star is stored in terms of kinetic energy. The difference of the kinetic energy at this point and on the surface of the star of each gas particle is liberated in the BL and radiated away in the form of soft and hard X-ray and UV emission (e.g., Cordova et al. 1981a,b; Cordova & Mason 1984). Therefore, the slower the star spins, the higher the energy output of the BL. Apart from the stellar mass and radius, another parameter that heavily influences the radiation characteristics of the BL is the mass-accretion rate $\dot{M}$, which can vary over a wide range for CVs. If it is relatively low, $\dot{M} \leq 10^{-10} M_\odot/\text{yr}$ (Warner 1987),

the BL is optically thin and very high temperatures of the order 10^8 K are reached, resulting in soft and hard X-ray emission (e.g., Mukai & Patterson 2004; Pandel et al. 2003, 2005, King & Shaviv 1984; Shaviv 1987; Narayan & Popham 1993; Popham 1999). Higher mass-accretion rates lead to optically thick BLs with lower temperatures of about 10^5 K (Pringle 1977; Syunyaev & Shakura 1986; Popham & Narayan 1995) in which case the radiation is mostly thermalized (see e.g., Cordova et al. 1980; Mauche 2004).

From a numerical point of view, the BL problem has initially been approached by timescale estimates and stationary calculations (Lynden-Bell & Pringle 1974; Pringle 1977; Tylenda 1977, 1981; Pringle & Savonije 1979; Regev 1983). With increasing computational power, evolutionary simulations became viable and made the investigation of the temporal evolution and non-stationary phenomena possible (Robertson & Frank 1986; Kley & Hensler 1987; Kley 1989a,b, 1991). Godon et al. (1995) performed one-dimensional simulations, where axial symmetry is assumed and the equations are integrated over the vertical (z) direction. This procedure is known as the thin-disk approach and provides a good first approximation for the BL problem. In a previous paper series we performed (one-dimensional) 1D simulations including vertical cooling, radiation transport, and the treatment of the radiation energy, and calculated detailed emergent spectra from these models (Hertfelder et al. 2013; Suleimanov et al. 2014).

---

[*] e-mail: `marius.hertfelder@gmail.com`

In this paper we consider the problem in two-dimensional (2D) spherical coordinates. As in the 1D case, we still assume axisymmetry in order to get rid of the φ-coordinate. We conduct full radiation hydrodynamics simulations, where the radiation energy is treated in the two-temperature approximation (Kuiper et al. 2010; Commerçon et al. 2011), which means that an additional evolutionary equation for the radiation energy is considered. Since the BLs we study here are mostly optically thick, we employ the flux-limited diffusion approximation (Levermore & Pomraning 1981; Levermore 1984) for the radiative flux. We use realistic boundary conditions with a vertically spread mass inflow at the outer edge of the simulation domain (disk) and a sophisticated initial model, which is constructed from different 1D codes (see Sec. 3.2). Our studies are hence related to the work by Kley (1989a,b, 1991) but can span much longer dynamic timescales and feature a much higher resolution due to the parallel code and the available computing power. Multidimensional simulations of the BL have also been done by Fisker & Balsara (2005); Fisker et al. (2006), although only for the adiabatic case, or Balsara et al. (2009), who used a simplified energy dissipation function without radiation transport. Kley & Lin (1996, 1999) also did full radiation hydrodynamics simulations for protostars and studied the evolution of FU Orionis outbursts in protostellar disks, and Babkovskaia et al. (2008) studied the BL around neutron stars in low-mass X-ray binaries. Magnetic fields have been included in 2D by Küker et al. (2003) and in three dimensions (3D) by Armitage (2002). In both cases, however, only low resolution and short dynamical timescales have been presented. Romanova et al. (2012), for example, performed 3D magnetohydrodynamical simulations and also considered magnetospheric accretion but did not include radiation transport.

Simulations in the disk plane have been performed by Belyaev et al. (2012, 2013a,b); Hertfelder & Kley (2015); Philippov et al. (2016); Belyaev (2017) in order to investigate the transport of mass and angular momentum (AM) in the BL. Since it has been shown that due to the increase of the angular velocity Ω with radius, the magnetorotational instability (MRI, Velikhov 1959; Chandrasekhar 1960) is ineffective in the BL (Godon 1995; Abramowicz et al. 1996; Pessah & Chan 2012), alternative concepts are currently being looked into. A promising candidate is the AM transport by acoustic waves excited by the sonic instability (Glatzel 1988; Belyaev & Rafikov 2012).

A different approach to describe the interface between the star and the disk was pursued by Inogamov & Sunyaev (1999, 2010) who introduced the concept of the spreading layer (SL). The SL is a 1D, vertical approximation for the deceleration of disk material on the stellar surface, which is connected to the disk by a 2D transition region. The main difference with the radial BL model is, that the rotating gas is spread on the star where it is then decelerated by turbulent interaction with colder stellar layers beneath it. As a consequence, the SL radiation emerges from two rings on the northern and southern hemisphere of the star. This concept was originally developed for neutron stars and later adapted to WDs in CVs (Piro & Bildsten 2004b,a). (Suleimanov & Poutanen 2006) extended the model for the effects of general relativity and different chemical compositions of the accreted matter.

In this publication, we want to study the vertical structure and the long-term evolution of the BL around a WD. A high resolution is employed in order to monitor the polar spreading and mixing of the disk material on the stellar surface. We decipher whether or not the results show indications of a SL and compare the midplane profiles with 1D simulations as presented in Hertfelder et al. (2013).

The paper is organized as follows. In Sect. 2 we present the basic physical model and list the equations used for production and postprocessing. Section 3 is dedicated to the numerical background of our work. We describe the code, boundary and initial conditions and how we constructed the models, which are shown and detailed in Sect. 4. We finish with Sect. 5, where we discuss the results and come to a conclusion.

2. Physics

In this section, we present the physical foundations for the simulations we have performed and that are described later in this publication. In order to investigate the vertical structure of the BL we use the Navier-Stokes equations in spherical coordinates (r, ϑ, φ) and assume symmetry in the azimuthal direction. We therefore drop all derivatives with respect to the azimuthal coordinate φ but do hold on to the momentum equation in the corresponding direction.

2.1. Vertical structure equations

The conservation of mass is represented by the continuity equation, which is given by

$$\frac{\partial \rho}{\partial t} + \nabla \cdot (\rho \boldsymbol{u}) = 0, \tag{1}$$

where ρ and $\boldsymbol{u} = (u_r, u_\vartheta)$ are the gas density and velocity, respectively. The equations for the momentum conservation are conveniently expressed in terms of the physically conserved quantities s, g, and h. We therefore introduce the radial momentum density $s = \rho u_r$, the polar momentum density $g = \rho r u_\vartheta$ and the angular momentum density $h = \rho r u_\varphi \sin \vartheta = \Omega r^2 \sin^2 \vartheta$. With regards to these variables, the momentum equations read

$$\frac{\partial s}{\partial t} + \nabla \cdot (s\boldsymbol{u}) = \rho \left(\frac{u_\vartheta^2}{r} + \frac{u_\varphi^2}{r} \right) - \frac{\partial p}{\partial r} + \nabla \cdot \boldsymbol{\sigma}_r + \frac{1}{r}\sigma_{rr} - \rho \frac{\partial \Psi}{\partial r} \tag{2}$$

for the radial direction,

$$\frac{\partial g}{\partial t} + \nabla \cdot (g\boldsymbol{u}) = \rho \cot \vartheta\, u_\varphi^2 - \frac{\partial p}{\partial \vartheta} + \nabla \cdot (r\boldsymbol{\sigma}_\vartheta) - \cot \vartheta\, \sigma_{\varphi\varphi} \tag{3}$$

for the polar direction and

$$\frac{\partial h}{\partial t} + \nabla \cdot (h\boldsymbol{u}) = \nabla \cdot (r \sin \vartheta\, \boldsymbol{\sigma}_\varphi) \tag{4}$$

for the azimuthal direction. In the above equations p denotes the gas pressure $p = \frac{\rho R_G T}{\mu}$, where $R_G = \frac{k_B}{m_H}$ with Boltzmann's constant k_B and the mass of hydrogen m_H, T is the gas temperature and μ is the mean molecular weight. $\Psi = -\frac{GM_*}{r}$ is the gravitational potential and G and M_* are the gravitational constant and the mass of the star, respectively.

The viscous stress tensor is denoted by σ and can be displayed in a coordinate-system-independent way by means of the covariant formulation

$$\sigma_{ij} = \eta \left(u_{i;j} + u_{j;i} - \frac{2}{3} u^k_{;k} g_{ij} \right), \tag{5}$$

where $u_{m;n}$ and $u^m_{;n}$ are the co- and contravariant derivative of the m-th component of the velocity with respect to n, while g_{ij} is the metrical tensor of the coordinate system and η is the dynamic viscosity. We note that Eq. (5) gives the covariant components

of the stress tensor that have to be translated to physical components by employing the metric coefficients. The same applies for the co- and contravariant formulation of the velocity. For details of this procedure as well as an insight into tensor calculus we refer the interested reader to classical textbooks such as Arfken & Weber (2005) or Mihalas & Mihalas (1984). The latter book also contains a summary of the individual physical components of σ in spherical coordinates. The vector representations of the stress tensor in Eqs. (2-4) are given by $\boldsymbol{\sigma}_r = (\sigma_{rr}, \sigma_{r\vartheta}, \sigma_{r\varphi})$ ($\boldsymbol{\sigma}_\vartheta$ and $\boldsymbol{\sigma}_\varphi$ similarly) and the divergence is calculated accordingly.

The equation for the conservation of energy is given by

$$\frac{\partial e}{\partial t} + \nabla \cdot (e\boldsymbol{u}) = -p\nabla \cdot \boldsymbol{u} + \Phi - \kappa_P \rho c \left(a_R T^4 - E\right), \tag{6}$$

where $e = \rho\varepsilon = \rho c_V T$ is the internal energy of the gas (ε and c_V are the specific internal energy and heat capacity, respectively), and Φ is the viscous dissipation function which relates to the stress tensor via $\Phi = (\sigma\nabla)\boldsymbol{u} = \frac{1}{2\eta}\text{Tr}\,(\sigma^2)$ (see e.g., Mihalas & Mihalas 1984). The last term in brackets on the right-hand side of equation Eq. (6) accounts for the heating and cooling through the energy exchange between the gas and the radiation field due to emission and absorption processes, and E denotes the radiation energy density, which is also evolved in time in our model. The according equation reads:

$$\frac{\partial E}{\partial t} + \nabla \cdot \boldsymbol{F} = \kappa_P \rho c \left(a_R T^4 - E\right). \tag{7}$$

Here, $\boldsymbol{F}$ is the radiative flux and κ_P, c, and a_R are the Planck mean opacity, the speed of light, and the radiation constant. The approach that incorporates two coupled equations for the gas energy (6) and the radiation energy density (7), respectively, is called the two-temperature approximation (Kuiper et al. 2010; Commerçon et al. 2011).

In order to close the set of equations, we need an assumption for the radiative flux $\boldsymbol{F}$. Here we use the flux-limited diffusion approximation (Levermore & Pomraning 1981; Levermore 1984, FLD) where the radiative flux is given by

$$\boldsymbol{F} = -\frac{c\lambda}{\kappa_R \rho}\nabla E, \tag{8}$$

with the Rosseland mean opacity κ_R and the flux limiter λ. The flux limiter mediates between optically thick regions, where radiation and matter are in thermal equilibrium, and optically thin regions, where photons can travel much farther before they interact with matter. In our simulations we utilize the formulation of the flux limiter given by Minerbo (1978) where λ is calculated by

$$\lambda(R) = \begin{cases} \frac{2}{3 + \sqrt{9 + 12R^2}} & 0 \le R \le \frac{3}{2} \\ \frac{1}{1 + R + \sqrt{1 + 2R}} & \frac{3}{2} \le R \le \infty \end{cases}, \tag{9}$$

with

$$R = \frac{|\nabla E|}{\kappa_R \rho E}. \tag{10}$$

The Rosseland mean opacity is further determined following Kramer's law,

$$\kappa = \kappa_0 \left(\frac{\rho}{\text{g cm}^{-3}}\right)\left(\frac{T}{\text{K}}\right)^{-3.5}, \tag{11}$$

where $\kappa_0 = 5 \times 10^{24}\,\text{cm}^2\,\text{g}^{-1}$, which we also use for the Planck mean opacity (see also Bitsch et al. 2013). As a lower threshold, we consider a constant opacity $\kappa_{\text{Thomson}} = 0.4\,\text{cm}^2\,\text{g}^{-1}$ which accounts for free-electron scattering processes at very high temperatures (Thomson scattering).

2.2. Viscosity

As has been discussed in Sect. 1, the driving mechanism for angular momentum transport in the BL is still a matter of ongoing research. We do not yet have a suitable prescription to implement the wave-mediated AM transport in the equations of hydrodynamics without directly simulating it. This, however, is not feasible for the kind of simulations presented in this publication, considering the huge demand of computational resources for highly resolved, three dimensional radiation hydrodynamics simulations (see e.g., Hertfelder & Kley 2015). We therefore employ the classic α-prescription by Shakura & Sunyaev (1973), which considers turbulent stresses in the accretion disk responsible for the observed AM transport and parametrizes them according to

$$\nu = \alpha c_s H, \tag{12}$$

where $\nu = \eta/\rho$ is the kinematic viscosity and $c_s = \sqrt{\gamma\frac{p}{\rho}}$ is the sound speed. H is a length scale that stands for the maximum eddy size of the turbulence. We define it according to Papaloizou & Stanley (1986):

$$\frac{1}{H^2} = \frac{1}{H_d^2} + \frac{1}{H_r^2}. \tag{13}$$

By employing Eq. (13) for the length scale, we account for the fact that in the BL the radial pressure scale height H_r becomes smaller than the vertical one. The relations for the scale heights read

$$H_d = \frac{c_s}{\Omega_K} \quad \text{and} \quad H_r = \frac{p}{|dp/dr|}, \tag{14}$$

where $\Omega_K = \sqrt{GM_*/r^3}$ is the Keplerian angular velocity. Inside the star, which is included, to a lesser extent, in our simulations, we apply a constant small viscosity $\nu_{\text{const}} = 10^{12}\text{cm}^2/\text{s}$ in the low-density region above the disk, no viscous heating occurs.

2.3. One-dimensional disks and stellar structure equations

In Sect. 3 we describe in detail the workflow we used in order to create the vertical models of the BL. Apart from the actual 2D simulations, the initial conditions also involve 1D disk profiles as well as a simple representation of the star. The underlying equations shall be presented here in short.

The 1D disk profiles are created using the thin disk approximation where the Navier-Stokes equations are vertically integrated and azimuthal symmetry is assumed. The 3D equations are thus reduced to depend only on the time t and the cylindrical radius $R = r \cdot \sin\vartheta$. The mass density ρ is replaced by the surface density Σ during the vertical integration. Since a Gaussian profile is assumed for the vertical density stratification of the disk, we can recalculate the midplane mass density from the results of the 1D simulations and approximate the vertical density and temperature structure. The equations of the slim disk approach and details about the code we used to obtain the 1D profiles can be found in Hertfelder et al. (2013).

The outermost layers of the star are obtained from the radial hydrostatic equilibrium and flux conservation:

$$\frac{dp}{dr} = -\frac{\rho GM_*}{r^2} \tag{15}$$

$$r^2 F = R_*^2 \sigma_{\text{SB}} T_*^4 = \text{const.} \tag{16}$$

Here, $F = F_{\text{rad}} + F_{\text{conv}}$ is the stellar flux, which consists of a radiative and a convective part, T_* is the effective temperature of the star (i.e., T at the optical depth $\tau = 1$) and σ_{SB} is the Stefan-Boltzmann constant. All other quantities are identical to the ones described earlier. We neglect the convective flux in Eq. (16) since we found that it is sufficient to only use the radiative flux to obtain a robust starting model for the star that can be plugged into the full 2D simulation. The two stellar structure equations are coupled ordinary differential equations that can be solved for $\rho(r)$ and $T(r)$. The radius of the star R_* is determined from the mass-radius relation for white dwarfs by Nauenberg (1972).

3. Numerics

3.1. General remarks

We mainly used the code PLUTO (Mignone et al. 2007) for the simulations presented in this publication. In PLUTO, the conservation laws Eqs. (1,2 - 4,6) are discretized on a static grid using the finite volume (FV) formalism where volume averages evolve in time. A high-resolution shock-capturing (HRSC) scheme is applied, with the algorithm being based on a reconstruct–solve–average (RSA) strategy. This means, that the variables are interpolated to the cell interfaces where subsequently a Riemann problem is solved for the two discontinuous states. Finally, the system is evolved in time using the fluxes computed by the Riemann solver. In order to approximate the variables at the cell interfaces, we used the piecewise parabolic method (PPM, 5th order), which is known to handle curvilinear coordinates and nonuniform grid spacing more correctly than other implemented methods[1]. The code retains a global 2nd-order accuracy as fluxes are computed at the interface midpoints. PLUTO offers a variety of slope limiters for the reconstruction step that differ in diffusivity. We have found that for our problem it is adept to start with a more diffusive limiter (minmod-limiter) and switch to the least diffusive monotonized central difference limiter (MC-limiter) once the simulation converges to the equilibrium. The Riemann problem is solved using the approximative HLLC solver, which is a Harten, Lax, Van Leer method that also considers the contact discontinuity. Finally, a dimensionally unsplit third-order TVD Runge-Kutta scheme with a variable time step based on the Courant-Friedrichs-Lewy condition (Courant et al. 1928) is employed for the temporal integration. The code has been tested and used extensively for a variety of applications[2].

Since we also considered the evolution of the radiation energy density (Eq. 7), we made use of the additional module by Kolb et al. (2013). Here, an additional step is performed after the non-radiative part has been accomplished. In this step, the radiation energy is solved together with the corresponding absorption-emission term in the gas energy equation. This results in a system of two coupled differential equations (see also Commerçon et al. 2011). Since radiation processes typically happen on much shorter timescales than hydrodynamical processes, an explicit treatment of these equations would confine the time step severely and render the method impractical. Therefore, an implicit scheme is applied to handle the radiative part. The resulting system of equations, which is partially linearized following Commerçon et al. (2011), is solved using the matrix solver from the PETSc library. For our problem, the improved stabilized version of the biconjugate gradient squared method (KSPIBCGS) in connection with a block jacobian or `hypre` preconditioner has turned out to be a fast and reliable combination. A variety of tests have been performed in order to confirm the correctness of the implementation and applicability of the method (Kolb et al. 2013). Due to the fact that the radiation module as described above can only handle 3D problem setups, we have modified it to support one and two dimensions, as well, and have redone the test cases.

3.2. Initial conditions

During the preparations and the first runs we noticed that PLUTO is quite susceptible to crashes due to negative density or pressure. In the BL problem, large density contrasts appear between the star-disk system and the virtually empty space above the disk, where high radial infall velocities are reached. However, the closer the initial model[3] matches the equilibrium state, the more stable the simulations are. Thus, we developed a strategy where we build the full problem step by step from smaller subproblems and perpetually construct initial models from the results of the preceding step. We outline this approach below:

We begin by constructing the very outer layers of the star. For that purpose the stellar structure Eqs. (15, 16) are solved for $\rho(r)$ and $T(r)$ using a fourth-order Runge-Kutta integrator. The integration starts at $r = 1$ and is performed outwards. The initial density $\rho(r = 1)$ is varied until we obtain $T = T_*$ at optical depth $\tau = 1$. Then, the integration starts at $r = 1$ again and is performed inwards. The simulation domain of the star spans [0.99, 1.01] and a large number of grid cells is needed due to the large gradients.

The following step entails calculating a radial 1D profile for the disk; we use our self-developed code, which solves the partial differential equations on a fixed Eulerian, staggered grid using a semi-implicit-explicit time stepping scheme with operator splitting (see also Stone & Norman 1992). In contrast to the simulations performed in Hertfelder et al. (2013) we do not simulate the BL, but only the disk for this step. Therefore we shift the inner boundary to $r = 1.1$ and require the azimuthal velocity to be Keplerian while we impose zero-gradient boundary conditions for all other variables. The outer boundary resides at $r = 5$ and the BCs remain unchanged. After the 1D disk has reached its equilibrium state we switch to the PLUTO code, load in the 1D profiles and extrapolate them by using a Gaussian vertical stratification. The disk simulation is now 2D with a domain that spans from $\vartheta = 0$ to $\pi/2$. We run the PLUTO code until the 2D disk has reached a stationary state.

Finally, we join together the ingredients mentioned above. The domain now ranges from 0.99 to 5 in radius with 1118 logarithmically spaced grid cells and from 0 to $\pi/2$ with 1000 grid cells in polar angle. The number of cells has been chosen such that each cell is approximately quadratic. The stellar structure model and the 2D disk are loaded in and the small region [1, 1.1] in radius that has no yet been simulated is simply extrapolated from the disk. In this region, the BL starts to build immediately after starting the full 2D simulation.

We have chosen the aforementioned procedure since it minimizes the time effort and maximizes the chances for a successful run without crashes. Another obvious way to pursue would be to simulate 1D BL profiles and attach these to the star and extend them to 2D. This approach is, however, much more time consuming and the initial model is less stable.

---

[1] See `plutocode.ph.unito.it/files/userguide.pdf`
[2] See `plutocode.ph.unito.it/Publications.html`

[3] In general, the boundary conditions play a more important role within the Navier-Stokes equations than the initial conditions.

3.3. Boundary conditions and density floor

At the outer boundary at $r = 5$, mass is continuously entering the domain, representing the mass flux $\dot{M}$ through the disk. Numerically this is accomplished by manipulating the flux into the outermost active cells that is actually calculated by the Riemann solver. We spread the mass influx over a vertical extent assuming a Gaussian profile whose width is determined through the disk height that comes out of the 1D disk simulation. The influx is realized such that the mass-accretion rate $\dot{M}$ is a simple runtime input parameter. The inflowing matter further receives an azimuthal momentum so that u_φ matches the Keplerian velocity at the outer boundary. The radiation energy density at the outer boundary is fixed at a value corresponding to $T = 100$ K. In the disk, we impose a no-flux condition since the radial transport is very small. The other quantities are implemented with zero-gradient BCs. Above the disk, the outer radial boundary is closed to prevent additional mass from falling in.

The inner boundary at $r = 0.99$ is a rigid wall where the radial and polar velocities equal zero. The azimuthal velocity is implemented as an input parameter so we can easily change the rotation rate of the star Ω_*. For the radiation energy density, the radiative flux of the star at the inner domain edge is used as a boundary condition. All other variables are again implemented using zero-gradient or Neuman-type boundary conditions, which means that the normal derivative at the boundary vanishes. At the polar axis ($\vartheta = 0$) and in the equatorial plane ($\vartheta = \pi/2$) we apply symmetry conditions (vanishing gradients) as boundary conditions.

We apply a lower threshold for the density of 5×10^{-14} g/cm^3, which is approximately ten orders of magnitude smaller than the disk midplane density. It is effective in the empty area above the disk and prevents negative densities due to infalling material. The density floor, however, also causes a flat density structure in this region. Along with the small radiation energy density above the disk, the computation of the flux-limiter becomes inaccurate and flux barriers develop that prevent the cooling of the disk. Since this process is unphysical, we reset the flux-limiter to $1/3$ in areas of low ρ and E in order to maintain a radiative flux towards the domain boundary. Since the ambient region is dynamically unimportant due to its low density, this intervention does not affect the validity of the model.

3.4. Model parameters

In this publication, we are interested in the structure of the BL around a weakly magnetized white dwarf, a situation that is frequently found in cataclysmic variable systems. White dwarfs in CVs typically have masses in the range of one solar mass and effective temperatures of $T_* \sim 50\,000$ K (e.g., Sion et al. 2010, for SS Cygni). We leave the effective temperature fixed at $50\,000$ K. The radial scale height of the star grows with T_* and it is easier to simulate a star with a larger scale height since a lower resolution may be chosen. The mass of the WD, on the other hand, is one parameter that we have varied during our research. Analogous to Hertfelder et al. (2013), we considered three masses, $M_* = 0.8 M_\odot$, $1.0 M_\odot$ and $1.2 M_\odot$. Alongside the mass, the radius of the WD is the crucial parameter that determines the strength of the gravitational pull. We used the mass-radius relation from Nauenberg (1972) in order to calculate R_*, which, for instance, yields $R_* \approx 5.6 \times 10^8$ cm for $M_* = 1.0 M_\odot$. An equatorial radius increase for rapidly rotating WDs is automatically taken into account in the simulations. The WD rotation rate Ω_* itself is an important parameter that we vary from $0.0\Omega_K$ (non-rotating) up to

$0.9\Omega_K$ for fast rotating stars. Ω_* determines the amount of kinetic energy that the gas loses before meeting the star and therefore the total luminosity of the BL. The last parameter that we modify is the mass-accretion rate $\dot{M}$, which can comprise several orders of magnitude in CVs. We consider mass-accretion rates of $\dot{M} = (10^{-8} - 10^{-10}) M_\odot/$yr. Furthermore, we took $\alpha = 0.01$ for the viscosity parameter and $\gamma = 5/3$ (monoatomic ideal gas) for the adiabatic index. The gas is assumed to consist of completely ionized hydrogen, so we adopt $\mu = 0.5$ for the mean molecular weight.

4. Results

4.1. The basic structure of the 2D BL

We begin the presentation of the results by discussing the general structure and basic properties of the 2D BL. For this purpose we adopt the parameter set of $M_* = 0.8 M_\odot$, $\dot{M} = 10^{-8} M_\odot/$yr, $\Omega_* = 0.0\Omega_K$ as our reference model which serves as the starting point for our analysis. The measured mass-accretion rate of the reference model is nearly constant throughout the domain. The maximum deviation from the imposed value is below 10%. This also applies to the simulations mentioned later in the text. Typically the models reach a state where the general flow structure remains steady after some tens of orbits. It does, however, take a few hundred orbits for the temperature to settle down to the equilibrium value and for the mass-accretion rate to exactly match the imposed value. All models presented in this paper are virtually in a steady state.

The thermal structure of the BL after 688 orbits is illustrated in Fig. 1 with the mass density ρ on the left hand side (a) and the temperature T on the right hand side (b). Additional contour lines are added to panel (a) in order to clarify the structure of the disk. We first discuss the density structure of the reference model. A heavy depletion of mass is observed directly in front of the stellar equator and the density decreases by approximately two orders of magnitude compared to the disk. This region, which connects the disk with the stellar surface, is called the BL. Due to the decreasing density and increasing infall velocity, it resembles a bottleneck where matter has to go through before it can come to rest on the star. At the surface of the star, the density rises rapidly with decreasing distance from the center and is several orders of magnitude larger than in the disk, which begins on the other side of the BL. The density in the disk is highest in the equatorial plane and decreases like a Gauss function in the vertical direction until it reaches the density floor. This area is represented in the plot by the dark blue color-coding. The gas from the disk accumulates in an equatorial shell around the star, which is barely visible since it is very thin. This is an indication for efficient radiative cooling of the gas that is heated up in the BL. The thin layer of disk material floats on the stellar surface and slowly spreads towards the poles. After almost 700 orbits it reaches a latitude of $\sim 35°$ and continues to crawl towards the pole. One orbit is given by the time needed for a point on the stellar surface to make a full rotation, $T = 2\pi/\Omega_K(R_*) \approx 11.5$ s.

The temperature distribution of the gas is visualized in Fig. 1 (b). The main feature is the peak in the equatorial plane at $r \approx 1$ with a temperature of almost $550\,000$ K. It is the consequence of the strong shearing in the BL due to the abrupt drop of the angular velocity. The shearing component of the stress tensor is the dominant part for the dissipation, and the heat production is proportional to the square of the shear. At the maximum of the angular velocity at $r = 1.0065$, the shear vanishes since the gradient is zero, $\partial\Omega/\partial r = 0$ (*zero-torque point*). Thus the heat
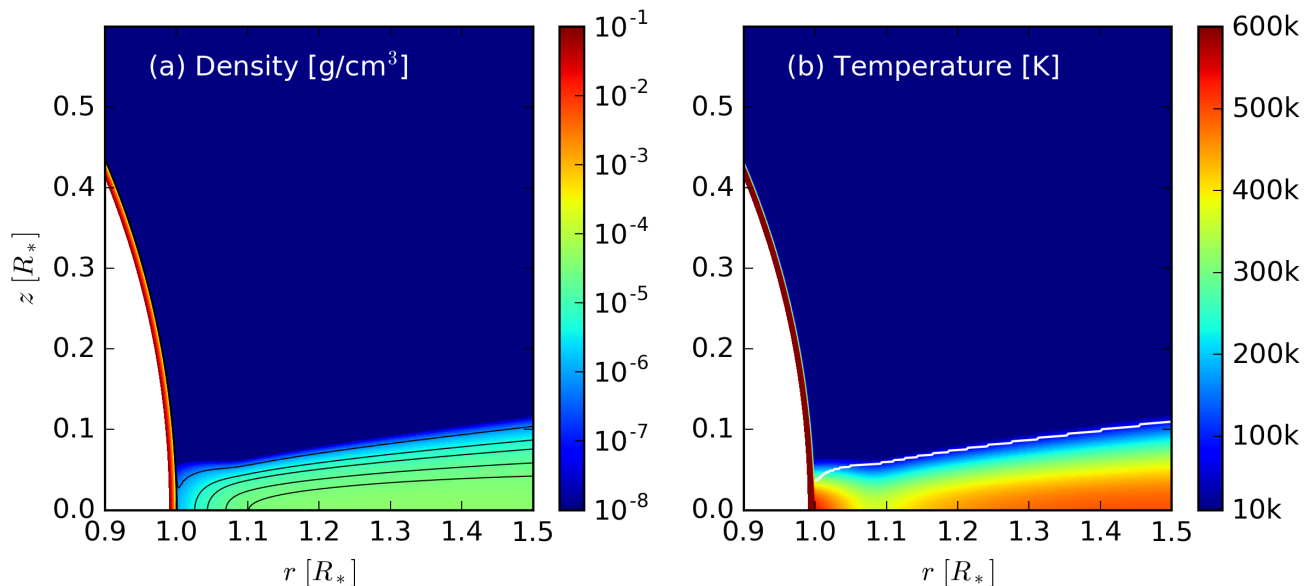
Fig. 1. Density (a) and temperature (b) for the reference model as a function of radius *r* and vertical coordinate *z* in cgs units at orbit 688. Contour lines for the levels $(0.8, 5, 10, 20, 30) \times 10^{-6} \mathrm{g/cm^3}$ are overlaid in the plot of the density (a). The white line in panel (b) denotes the points where the optical depth is unity, $\tau = 1$.
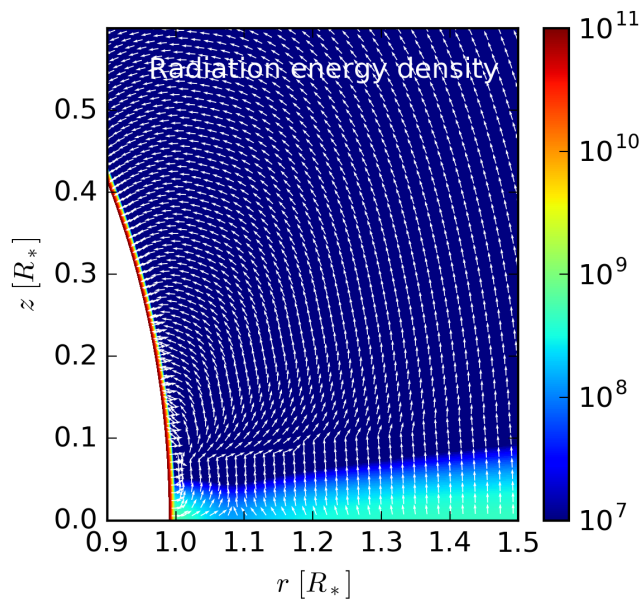

Fig. 2. Radiation energy density *E* of the reference model in $\mathrm{g/(cm\,s^2)}$ as a function of radius and height for the inner part of the accretion disk at orbit 688. The arrows denote the direction of the radiative flux as specified in Eq. (8).

production declines for greater radii $r \gtrsim 1$ before it rises again in the accretion disk. This minimum of *T* is visible at $r \approx 1.1$ in the equatorial plane in Fig. 1 (b). The location of the minimum does, however, not coincide with the zero-torque point because of the transport of energy mainly through radiation. Moreover, the cooling rate strongly depends on the density, which changes drastically in this region and thus also influences the tempera-

ture distribution. Another important point is that due to the high radial velocities in this area, the components σ_{rr} and $\sigma_{\varphi\varphi}$ also become important concerning the heat production. It is therefore a complex interplay of several factors that arranges the temperature here. In the disk, beyond $r = 1.1$, the midplane temperature increases again because of the ever-present shear of a differentially rotating accretion disk. It peaks at $r = 1.51$ and $T = 495\,857$ K and decreases again for larger radii with a slope approximately proportional to $r^{-1/2}$ due to the influence of the BL. For larger radii $r \gg 1$, *T* approaches the $r^{-3/4}$ variation of the standard disk solution. In the vertical direction, the disk can cool efficiently and hence the temperature drops rapidly to a few thousand K. The temperature of the low-density material above the disk decreases with radius.

The radiation energy density *E* shows the same features as the gas temperature since the medium is mainly optically thick in the disk and BL. The energy dissipation in the BL also leads to a drastic increase in radiation energy density. In addition to *E*, Fig. 2 visualizes the radiative flux *F* which is computed according to Eq. (8). At around $r \approx 1.1$ there is also a minimum in *E* that lies between the BL and the disk in the equatorial plane. Due to the gradient of the radiation energy density inwards and outwards from this minimum, there is considerable radiation transport towards the point $r \approx 1.1$. The energy produced in the BL is therefore transported outwards by radiation. Also some part of the energy produced in the disk is transported inwards. Thus there is a significant redistribution of energy both from the BL and from the disk to a wider region of about 10 percent of the stellar radius in radial extent. This region is called the *thermal BL* (Regev & Bertout 1995; Popham & Narayan 1995). In the disk, the cooling from the surface is accounted for by the radiation transport in the vertical direction, which is indicated by the nearly vertical arrows pointing upwards in Fig. 2. Directly above the BL, the radiative flux is very strong and pushes the disk surface flux outwards. At higher stellar latitudes, Fig. 2 shows that the flux is directed towards the star. This unexpected behavior

is probably a consequence of the small density in the corona and the numerical problems for the radiation transport associated with the density floor. However, this region does not influence the structure or the thermodynamics of the BL.

In Fig. 3 (a) the dynamic structure of the star-BL-disk system is displayed. The density is shown as an orientation for the velocity vectors that visualize the direction and the magnitude of the flow. The disk shows a steady slow inflow towards the star. The inflow velocity is larger near the disk surface than in the midplane. As the gas approaches the stellar surface it is considerably sped up. This is clearly visible in Fig. 3 (b), where the radial velocity u_r in the disk midplane is shown in red. The infall of material is accelerated until $r \approx 1.05$ and then rapidly decelerated as the matter comes to the surface of the star. The peak of u_r corresponds to a Mach number of approximately 0.25, so the infall occurs subsonically for our chosen value of α, which is important for causality reasons (e.g., Pringle 1977). Due to the friction in the disk, the gas loses angular momentum and its stabilizing force so that the infall velocity increases. As a consequence, the density in this region must decrease accordingly in order to maintain a constant mass-accretion rate through the disk. The mass flux through concentric spherical shells of radius r is given by

$$\dot{M} = -4\pi r^2 \rho u_r. \tag{17}$$

Thus, if the velocity becomes larger, the density must decrease. $\dot{M}$ can be derived from Eq. (1) assuming a stationary state ($\partial_t = 0$). Also shown in Fig. 3 (b) is the angular velocity Ω, which describes the rotation of the gas around the star. In the disk, the gas rotates with Keplerian frequency and there is a force balance between the gravitational force of the star and the centrifugal force of the circular motion. Additional forces arising through pressure gradients are, in general, small in the disk and influence Ω only slightly. As the gas approaches the stellar surface, it is decelerated and smoothly connects to the rotation rate of the star, which is zero in this case. The deceleration happens very fast and causes a supersonic velocity drop over a range of less than one percent of the stellar radius. Here, the stabilization of the gas switches from centrifugal to pressure support. The large gradient of Ω during the velocity drop is responsible for the heat production in the BL and drives the high temperature observed in the thermal BL. In contrast, by definition the *dynamical BL* is the region from the stellar surface to the maximum of Ω (zero-torque point) and it is extremely small for BLs around WDs. In this case, the width amounts to $\Delta r = 0.01$. We begin to measure the BL width when the angular velocity deviates by more than 1% from the stellar-rotation rate. Only the velocities, especially u_r and u_φ, vary considerably on a scale of the order of the dynamical BL width ($\sim 1\%R_*$). For the other quantities, it is usually not necessary to resolve the dynamical BL in the figures since no rapid changes happen (see e.g., Fig. 3 (b) vs. Fig. 6, lower panels). From an observational point of view, the thermal BL is the essential region. However, if we compare the dynamics or the width of the BL, we refer to the dynamical BL.

Once the gas has reached the surface of the star, it has lost almost all of its angular and radial momentum and has settled to a dense shell in the equatorial plane. It is slowly driven to the poles of the star. Above the disk we set the velocities to zero whenever the density floor is applied. We thus limit the velocity of the inevitably infalling gas since it dissipates energy when it shocks on the surface of the star or the disk and heats up the low-density regions. Therefore, no velocity arrows are visible in the dark blue regions of Fig. 3.

We now compare the reference model with the results of the 1D approach where the BL equations in cylindrical coordinates are vertically integrated and axisymmetry is assumed (see Hertfelder et al. 2013). The vertically integrated density (*surface density*), which is extracted from the 2D data by integrating vertically at constant spherical radius, is similar for the two approaches. In the disk, the differences are small ($\lesssim 5\%$). The only significant deviation ($\sim 40\%$) is given in the BL where the 1D model predicts a surface density that is slightly too low. The temperature deviates by approximately 50 000 K or 10% throughout the domain, see Fig. 4. In order to be sure that the reason for this mismatch is not given by a non fully relaxed 2D midplane temperature, we looked at snapshots of different times and found that in the equatorial plane, the model is in thermal equilibrium. We conclude that the 1D approximation slightly underestimates the disk temperature. Apart from the general deviation, the overall trend is well reproduced. The 1D approach insufficiently approximates the vertical structure of the disk. This leads to a lower temperature as well as a lower disk height. In the 1D model, thus, the disk is too thin. This is a consequence of the vertical cooling, which relies on an approximation of the vertical optical depth analog to a gray atmosphere. If the estimate for the vertical optical depth is too low, the cooling is more efficient and, hence, the temperature in the equatorial plane lower. The dynamical structure of the 1D model matches the 2D simulation very well. The shape of Ω and the width of the BL are virtually identical for the two different approaches. The infall velocity is also a close match, though it is slightly larger in the BL since the surface density is smaller (see Eq. 17).

Figure 5 shows the surface temperature of the BL and the disk. In the 1D radial approximation, the surface temperature is derived from the midplane temperature by employing the estimate for the vertical optical depth $\tau_{\rm eff}$ by Hubeny (1990):

$$T_{\rm c}^{\rm 1D} = \sqrt[4]{\tau_{\rm eff}} T_{\rm surface}^{\rm 1D}. \tag{18}$$

For the 2D model, the radiation temperature is computed according to

$$T_{\rm rad} = \left(\frac{E}{a}\right)^{1/4}, \tag{19}$$

where a is the radiation constant. The surface temperature is then obtained by evaluating $T_{\rm rad}$ in an optical depth of $\tau = 1$. Since the line of constant $\tau = 1$ approximately equals the visible surface, the surface temperature is a measure for the radiation emitted by the system. The 1D and the 2D approaches yield remarkably similar values of $T_{\rm surf}$ (Fig. 5). The peak of the 2D surface temperature is slightly shifted towards the star since the BL of the 2D model lies closer to the star than in the 1D case (see also Fig. 4). The peak is marginally lower and the descent less steep. In the 2D model, the thermal BL is thus slightly wider and less hot than in the 1D approximation. In the disk, both models decrease to about 55 000 K and the radiation is comparable to the WD. The 2D surface temperature is not as smooth as the 1D counterpart and shows frequent edges and small spikes. The reason is, that, coming from above, the density in the disk rapidly rises to the point where $\tau = 1$ and the number of grid cells in this region is limited. By increasing the resolution at the transition to the disk, the smoothness of the profile could be improved.

4.2. The influence of the WD rotation

The rotation rate of the WD is an important parameter since it determines the amount of energy released in the BL. With increasing stellar rotation rate, the amount of kinetic energy that is
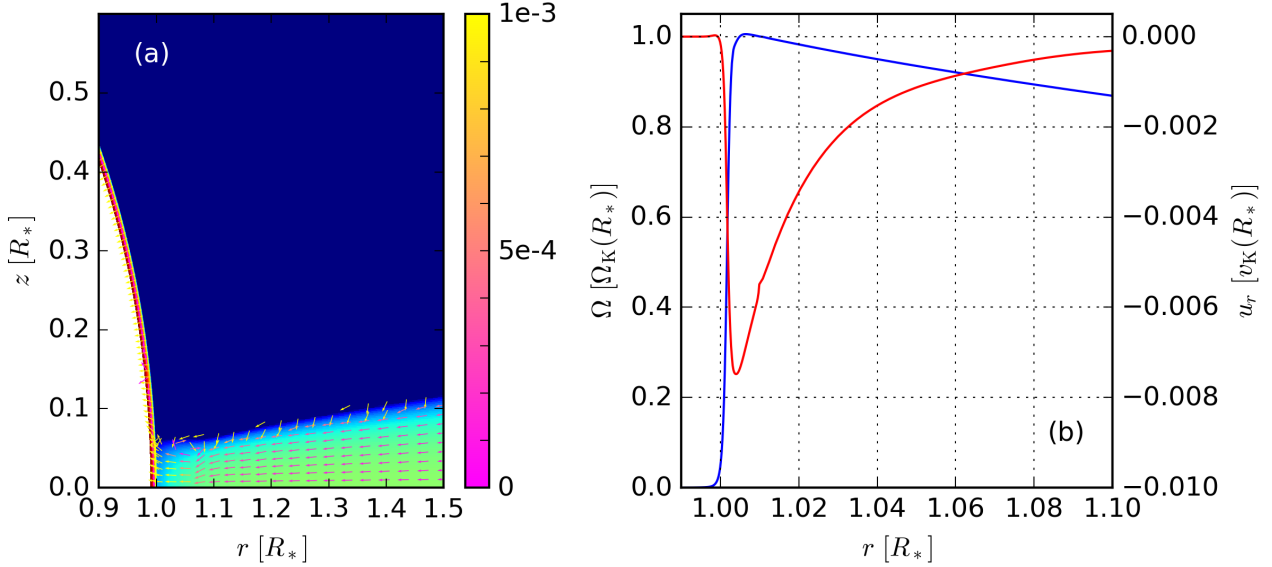
Fig. 3. (a) The density as shown in Fig. 1 as an orientation for the over plotted velocity vectors. The color-bar indicates the absolute value of the velocity of each vector in units of $v_K(R_*)$. Only the radial and polar component of the velocity vector have been taken into account. (b) The angular velocity $\Omega = u_\varphi/r$ (blue) and the radial velocity u_r (red) in the equatorial plane as a function of the radius r. The y-axis on the left-hand side refers to Ω and the y-axis on the right-hand side refers to u_r. All velocities are normalized to the Keplerian (angular) velocity at the surface of the star, $v_K(R_*) = \sqrt{GM_*/R_*}$. Both snapshots are taken after a time of 688 orbits.
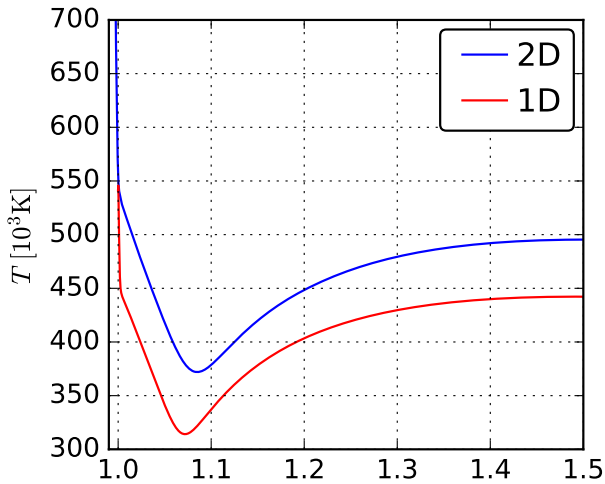
Fig. 4. Midplane temperature T as a function of radius. We compare the results from 1D (red) and 2D (blue) simulations. A general deviation of about 10% is due to an insufficient approximation of the vertical optical depth in the 1D approach.
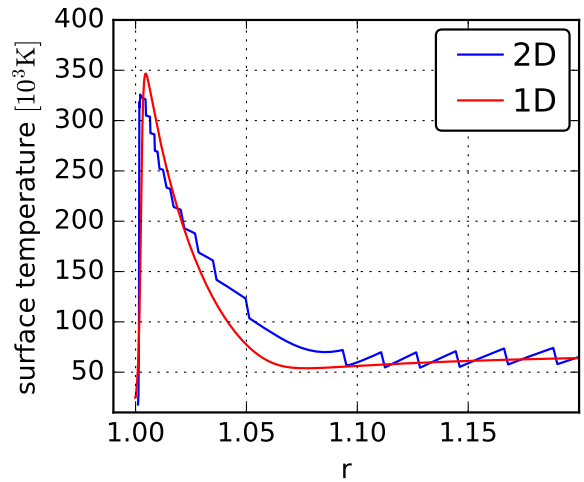
Fig. 5. The surface temperature as a function of radius for the 1D radial model and the 2D model. In the latter, the radiation temperature T_{rad} is calculated following Eq. (19) and the surface temperature of the disk and BL is given by T_{rad} at an optical depth of $\tau = 1$.

transformed into heat in the BL decreases. The luminosity of the BL decreases quadratically with increasing stellar rotation rate,

$$L_{BL} = \frac{1}{2}L_{acc}\left(1 - \frac{\Omega_*}{\Omega_K(R_*)}\right)^2, \tag{20}$$

where $L_{acc} = GM_*\dot{M}/R_*$ is the total accretion luminosity. Equation (20) can be derived theoretically (Popham & Narayan 1995) and has been verified numerically (Hertfelder 2017).

We considered five different stellar rotation rates ranging from non-rotating up to nearly break-up rotation velocity. The differences between these models are illustrated in Fig. 6 where the midplane radial dependency of the angular velocity, radial
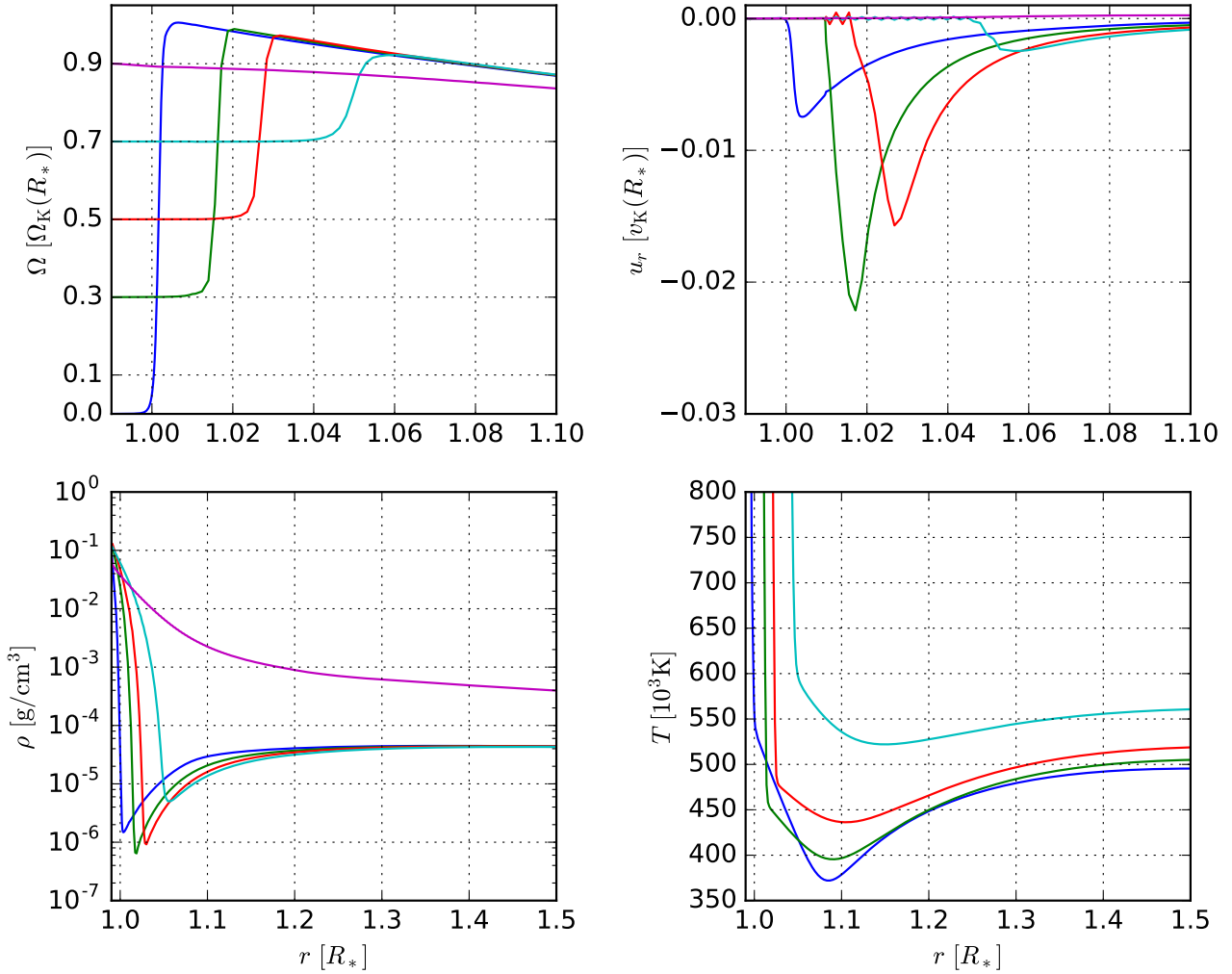
Fig. 6. Angular velocity Ω and radial velocity u_r (both in dimensionless units) and density ρ and temperature T in cgs units. All variables show the radial dependency in the equatorial plane. The different colors denote the different stellar rotation rates of $0, 0.3, 0.5, 0.7$ and 0.9 times the Keplerian angular velocity at the stellar surface. The snapshots are taken after 688, 251, 248, 263 and 253 orbits. The blue lines correspond to the reference model.

velocity, density and temperature are shown. The angular velocity Ω decreases smoothly from Keplerian rotation in the disk to the stellar-rotation rate. The faster the star spins, the more the dynamical BL is shifted to greater radii since the star increases its equatorial radius due to the centrifugal force imposed by its rotation. For a WD that spins at 70% of Ω_K, the equatorial radius increase amounts to already $\sim 4\%$ of the stellar radius. Also, the dynamical BL width becomes larger with increasing stellar rotation; $\Delta r = 0.01, 0.015, 0.016, 0.025$ for $\Omega_* = 0.0, 0.3, 0.5, 0.7\Omega_K(R_*)$. The reason for the increasing BL width is the complex interplay of density and temperature, both of which influence the viscosity, which ultimately governs the width of the BL. In the disk, the angular velocity of all models is nearly Keplerian, with a small deviation due to the outward pointing pressure gradient, which adds as a stabilizing force.

The infall velocity u_r shows a behavior which is not expected from 1D BL simulations where the maximum of the radial velocity decreases with rising rotation rate (e.g., Hertfelder et al. 2013). In contrast, the 2D simulations propose a trend where the

peak of u_r first increases significantly before decreasing again. The turnaround point seems to be in the range of $\Omega_* \approx 0.3$ and only for a high stellar rotation rate of $\Omega_* = 0.7$ is the peak smaller than in the non-rotating model. Here it would certainly be interesting to run additional models with different Ω_* to investigate the trend in depth. Apart from the peak behavior, the shape of u_r reflects our expectations. Coming from the disk, u_r is small and increases as the BL is approached. In the BL, it peaks and then decreases rapidly as the stellar surface is encountered. Although two models peak at a higher infall velocity than the reference model, the infall is still well sub-sonic.

The unexpected behavior of the rotating models continues to occur in the density and the temperature. While in 1D models there is a clear trend that the (surface) density increases and the temperature decreases as the star spins up, Fig. 6 points towards a different picture. The density in the BL for the $\Omega_* = 0.3$ case is smaller than in the non-rotating model. The same applies for the model where the star rotates at half of the break-up velocity. The trend of each $\rho(r)$ curve, however, is in perfect agreement with

the non-rotating model. The temperature, instead of decreasing with increasing rotation rate, seems to rise at first glance. Important, though, is the BL temperature which corresponds to the region directly in front of the steep rise as we enter the star. Here, the non-rotating model has a higher temperature than the 0.3 and 0.5 cases, which is in agreement with Eq. (20). The 0.7 model deviates from this picture since the equatorial radius increase is already very pronounced. The cause for the increased infall velocity in the rotating models is unclear. Perhaps the lack of a stabilizing pressure force due to a lower BL temperature is responsible for the accelerated inflow. As has been mentioned earlier, ρ will adjust to the radial velocity such that the mass flux remains constant, see Eq. (17). This could also explain the lower density in these cases. In general, however, the inflow velocity should be proportional to the loss of angular momentum and thus be higher for lower Ω_*. This point remains to be clarified through further investigation. The temperature of the $\Omega_* = 0.9$ model is not visible in Fig. 6 since it is larger than 800 000 K throughout the plotted region due to the high density.

A special case is given by the model with a stellar rotation rate of 0.9. Due to the high rotation rate of the star, the system has reached a state where matter is fed into the disk by the star and transported outwards by the disk. This phenomenon is called a *decretion disk*. The radial velocity is pointing outwards throughout the disk. Due to this exotic state of the disk, no BL is formed and the density and temperature are much higher than in the other cases since the hot stellar material is transported outwards. We find that a decretion disk is formed in each model that has a rotation rate of 0.9 and therefore exclude those cases from our further analysis.

For the models with a rotating star we found that the material does not continue its journey to the poles unhindered as was the case for the non-rotating star. We investigate the polar spreading of the material, which depends on the stellar rotation rate, in detail in Sec. 4.4.

4.3. Dependency on stellar mass and mass-accretion rate

We now investigate to what extent the stellar mass and the mass-accretion rate of the system influence the structure of the BL. To this end, we consider the following models (see also Table 1): For the $\dot{M}$-study, we leave the stellar mass fixed at $M_* = 0.8 M_\odot$ and compare three different mass-accretion rates, $10^{-8}, 10^{-9}$, and $10^{-10} M_\odot/\mathrm{yr}$. We then fix $\dot{M}$ at $10^{-8} M_\odot/\mathrm{yr}$ and change the stellar mass to 0.8, 1.0, and $1.2 M_\odot$. All models feature a non-rotating WD.

The upper two panels of Fig. 7 show the density ρ and the temperature T in the equatorial plane as a function of radius for three different mass-accretion rates. With decreasing $\dot{M}$ the density also drops significantly. A difference of two orders of magnitude in mass-accretion rate leads to a density drop of one and 1.5 orders of magnitude in the disk and in the BL, respectively. A similar trend applies to the temperature, which also decreases with ceasing mass-accretion rate. Here we find a factor of more than three between the temperature in the disk with an accretion rate of 10^{-10} and 10^{-8} solar masses per year. While the hottest model reaches over 500 000 K in the BL, the coldest model lies at only roughly 150 000 K, apart from the interesting peak, which we discuss later. The more mass is transported through the disk, the more massive the disk will grow and hence the density increases with $\dot{M}$. This behavior is also reflected in the disk height, which increases along with $\dot{M}$. Due to the higher disk density, the depletion of mass in the boundary layer is less severe for the high $\dot{M}$ case as well. There are two major reasons

Table 1. Width of the boundary layer for a parameter variation of the stellar mass and the mass-accretion rate. By definition, the BL ranges from the surface of the star to the point where $\partial\Omega(r)/\partial r = 0$, that is, where it has a maximum.

M_* [$M_\odot$]	$\dot{M}$ [$M_\odot$/yr]	Δr [R_*]	sim. time [orbits]
0.8	1×10^{-8}	0.0100	688
0.8	1×10^{-9}	0.0066	604
0.8	1×10^{-10}	0.0048	395
1.0	1×10^{-8}	0.0084	395
1.2	1×10^{-8}	0.0064	387

for the increasing temperature: On the one hand, the total accretion luminosity scales linearly with the mass-accretion rate:

$$L_{\mathrm{acc}} = \frac{GM_*\dot{M}}{R_*}. \tag{21}$$

It describes the total amount of energy the gas loses in the disk and the BL around a non-rotating star per time. Thus, the higher the mass-accretion rate, the higher the energy production and also the temperature, since there is simply more material in the disk, which produces heat through shearing. On the other hand, a higher disk density amplifies the energy dissipation. In the BL, again, the increase in temperature is more distinct than in the disk.

With decreasing mass-accretion rate, an interesting feature arises for the temperature in the BL. In the zoom-in box of Fig. 7, which magnifies the BL region [0.99, 1.03], small peaks for 10^{-9} and $10^{-10} M_\odot/\mathrm{yr}$ are visible, which seem to grow larger with decreasing $\dot{M}$. Those temperature peaks directly reflect the heat production in the BL where the dissipation rate has its maximum and are also observed in 1D simulations (e.g., Hertfelder et al. 2013). Since at this location the density is very low due to the peak of the radial velocity, the matter cannot cool efficiently enough. The radiation transport depends on the opacity, which strongly depends on the density and the temperature. The lower the mass-accretion rate, the smaller also the density and the transport of energy away from this region by radiation, thus cooling this region down, becomes more and more difficult. Therefore this peak grows more pronounced with decreasing $\dot{M}$.

In the lower two panels of Fig. 7, the midplane density and temperature for the three different stellar masses are presented. The density plot confirms, that a higher stellar mass leads to higher density in the disk and in the BL. The variation is roughly exponentially and equally pronounced in the disk and the BL. With increasing stellar mass, the radius of the WD decreases due to the inverse mass-radius relation. This causes a non-linear variation of gravity and the disk height for high-mass WDs is considerably smaller than for lower-mass WDs. Since the mass-accretion rate remains fixed, the amount of mass transported through the disk also remains constant and thus the density increases with M_*. According to Eq. (21) and in combination with the higher density, the temperature also increases strongly. For the case of a very massive 1.2 solar mass WD, the one million K temperature mark is reached. Again, the temperature in the BL grows stronger than in the disk with increasing M_*. A peak in the BL is not visible due to the high mass-accretion rate and the effective radiative cooling. For reference, we state the radii for the WDs of masses 0.8, 1.0, and $1.2 M_*$ which amount to $7.1 \times 10^8, 5.6 \times 10^8$, and 4×10^8 cm, respectively.

The dynamical structure does not significantly change with the stellar mass or the mass-accretion rate and can be de-
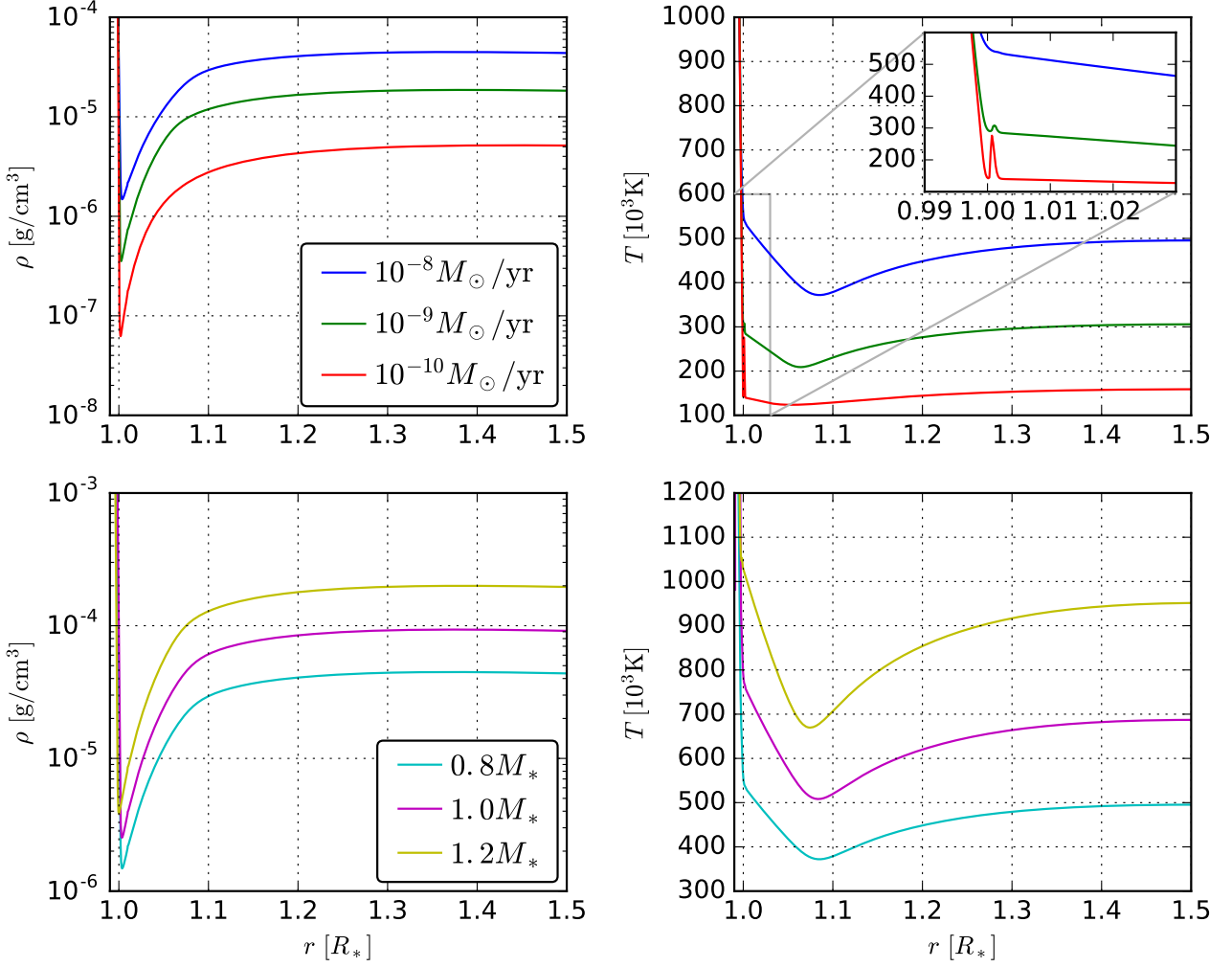
Fig. 7. Density and temperature in the equatorial plane as a function of radius. In the upper two panels the variables are displayed for three different mass-accretion rates. The plot of the temperature has an additional zoom box to make the thin peaks in the BL more visible. The lower two panels show ρ and T for three different stellar masses.

scribed by the general flow structure of the reference model (see Sec. 4.1). The width of the BL, however, depends on $\dot{M}$ and M_* as can be extracted from Table 1. There is a clear trend for all stellar masses that the BL shrinks with decreasing mass-accretion rate. The width further decreases with increasing stellar mass. High mass-accretion rates lead to broader BLs since the density and the temperature are larger and consequently the BL hotter. This effect is reinforced by the inefficient radiation transport in the BL for low mass-accretion rates, which prevents a more distinct expansion. When considering the stellar masses, however, higher densities and temperatures cause quite the opposite, namely a shrinking BL width. Here, we have to take into account the increased gravitational pull, which dominates in this case and drags the disk as close as possible to the stellar surface. Several factors contribute to the width of the BL and it is therefore difficult, to come to a unique conclusion without running simulations. The radial velocities and Mach numbers are almost identical, apart from the slight radial shift due to the different BL

widths. We also observe an unhindered, slow polar spreading of the disk material shell in all models.

4.4. Polar spreading and mixing

In Fig. 8, the destination of the disk material on the stellar surface is visualized. To this purpose, we have added a tracer in the equatorial plane just short of the stellar surface in the simulations. The tracer behaves like a scalar quantity for which an advection equation is solved. It thus illustrates in which direction the material from the disk is going. Along with the tracer we have added the line of constant $\tau = 2/3$ with a dotted black line that is approximately the visible surface of the star. Four different stellar rotation rates are given.

In Figure 8 (a) the situation is shown for the reference model with the non-rotating WD. As was mentioned earlier, the disk material is gathered in a very thin shell that slowly moves to the poles. Since the WD is not rotating and the material has been completely depleted of its angular momentum near the midplane,
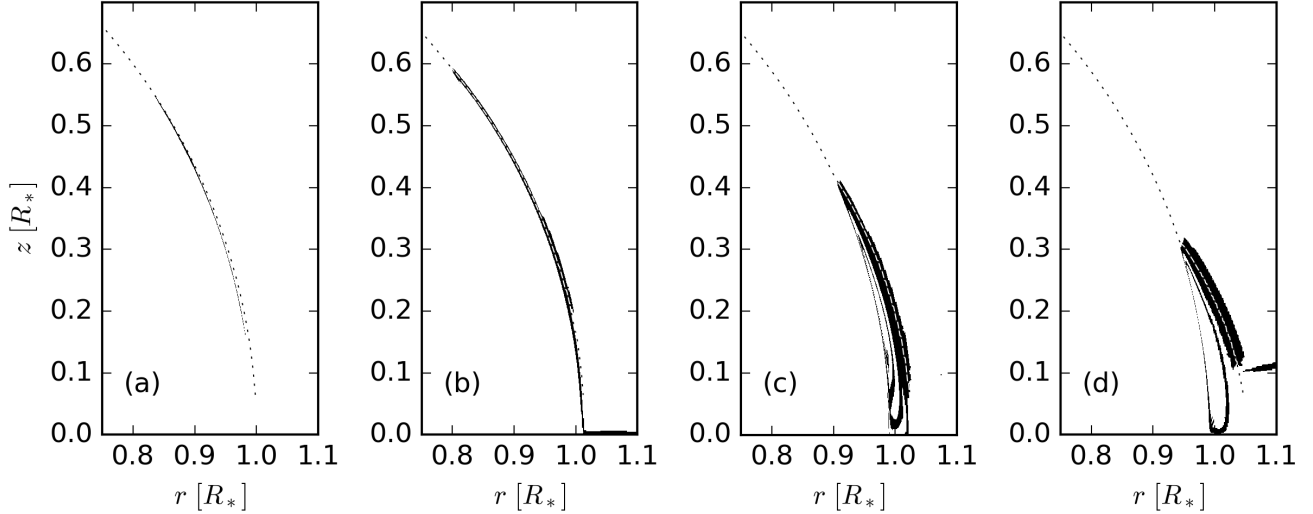
Fig. 8. Black and white image of the tracer, which has been inserted in the equatorial plane in order to visualize the mixing and polar spreading of the disk material of a $0.8M_\odot$ WD with $\dot{M} = 10^{-8}M_\odot/$yr. The plots differ in the stellar-rotation rate, which is given by 0.0 (a, orbit 688), 0.3 (b, orbit 251), 0.5 (c, orbit 248) and $0.7\Omega_K(R_*)$ (d, orbit 263). The dotted black line denotes the optical depth of $\tau = 2/3$.
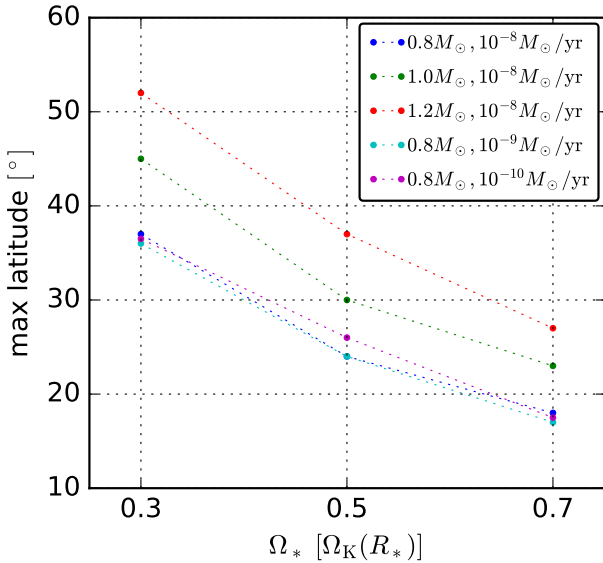

Fig. 9. The maximum latitude reached by the disk material on its way to the pole as a function of the stellar-rotation rate. The different curves correspond to different choices of stellar mass and mass-accretion rate (see legend). The maximum latitude angle is measured towards the equatorial plane and is given in degrees.

the surface of the WD is an equipotential area. The gas is pushed up towards the poles by the pressure that has developed in the midplane at $r \approx 1$ due to the deceleration of the disk. On the WD surface, the movement is slowed down by friction. If the viscosity v_{const} of the WD is reduced, we observe that the material reaches the poles faster than in the reference model. In these cases, we can actually follow the simulation for the time that is needed for the gas to reach the pole. However, the choice of an

overly small v_{const} is problematic since it prevents the BL from building up in the first place. For the rotating models it is especially important that v_{const} is large enough so that the WD rotates like a solid body. We have found that $v_{const} = 10^{12}$cm^2/s is a good choice for this purpose.

The picture changes when the star begins to rotate. In this case, there is a centrifugal barrier that initially prevents the gas from leaving the midplane. However, the pressure force in the equatorial plane is large enough to overcome this barrier and push the material towards the pole. At a certain latitude, an equilibrium of pressure and centrifugal force is established and the movement is halted. This situation is illustrated in panels (b) - (d) of Figure 8, where the WD rotates with $30\%, 50\%$, and 70% of $\Omega_K(R_*)$. Since with increasing stellar rotation rate the centrifugal force increases and the pressure force decreases, the maximum latitude shrinks considerably.

The mixing of the stellar and disk material also becomes more pronounced with increasing rotation rate. In all three cases where the WD spins at a non-zero rate, the $\tau = 2/3$ is engulfed in a mixture of material from the disk and the star. Therefore it is to be expected that the radiation of the star is reprocessed in regions partly dominated by disk material; material that might have a composition different from the stellar mixture in some cases. This situation occurs, however, only for a part of the star and two caps at the poles, which increase in size as the star spins up and remain untouched by the disk material.

Figure 9, where the maximum latitude as a function of Ω_* is shown, visualizes how the spreading is influenced by M_* and $\dot{M}$. The trend of the polar spreading of material decreasing with stellar radius from Fig. 8 is confirmed by Fig. 9 for various combinations of stellar mass and mass-accretion rate. The gas faces a centrifugal barrier when traveling to the poles due to the fact that it retains an increasing amount of angular momentum with growing stellar rotation rate when reaching the stellar surface. The viscosity on the stellar surface on regions off the equatorial plane is far too low to decelerate the material efficiently and rid it of its excess angular momentum. This also explains the unhindered slow movement of the disk gas in the non-rotating case.

Figure 9 further suggests that an increase in stellar mass leads to a considerable growth of the maximum latitude. The rotational velocity on the surface of the star is proportional to $\sqrt{M_*/R_*}$ and thus is growing with increasing stellar mass. This means that a point on the equator of a $1.2M_\odot$ WD that rotates with 30% of the break-up velocity moves at almost 2000 km/s, whereas for a $0.8M_\odot$ WD the velocity is only about 1200 km/s. The important quantity for the polar spreading, however, is the angular momentum, which scales $\propto \sqrt{M_*R_*}$ on the surface and thus decreases with increasing stellar mass due to the inverse mass-radius relation of WDs. The material can therefore reach higher latitudes on the WD. The mass-accretion rate, on the contrary, does not seem to influence the polar spreading at all. The small deviations between the blue, cyan, and magenta curves in Fig. 9 are probably due to inaccuracies in measurement. There is therefore no increased pressure force to drive the material further to the poles for increasing mass-accretion rate. The angular momentum of the gas remains the key issue in the polar spreading. It would be interesting to investigate the shape of the Ω_* dependence of the maximum latitude further, however, with only three data points per curve we feel that an interpretation beyond the general trend is too speculative. We leave that issue for future studies.

In all of the simulations we have performed, the disk material is decelerated in the midplane and the radiation of the BL emerges in proximity to the stellar equator. The situation depicted in Fig. 2 also holds true for increasing stellar rotation rate Ω_* and only the amount of dissipated energy decreases. The disk material that finally spreads towards the poles has the same rotational velocity as the stellar surface. Therefore, we do not observe a spreading layer (SL) as mentioned in Inogamov & Sunyaev (1999, 2010), where the rotating material first spreads on the star and is decelerated and radiates within two rings above and beyond the equator. The latitude of these rings depends on the mass-accretion rate. However, we also do not detect any such changes in the BL when the mass-accretion rate is varied (for instance Fig. 9).

5. Summary and conclusion

For this publication we have performed 2D simulations of the non-magnetic BL around WDs in CVs in a spherical geometry assuming axisymmetry. The hydrodynamical model based on the Navier-Stokes equations is extended by an additional equation for the radiation energy, which is closed using the flux-limited diffusion approach. We employ Kramer's opacity, which suits the temperatures found in the inner disk around WDs and utilize a modified α-prescription for the viscosity, which also takes into account the radial scale height in the BL. A total of 45 models have been prepared in a complex way (see Sec. 3.2) and run with varied M_* $(0.8, 1.0, 1.2M_\odot)$, $\dot{M}$ $(10^{-8}, 10^{-9}, 10^{-10}M_\odot/\text{yr})$ and Ω_* $(0.0, 0.3, 0.5, 0.7, 0.9\Omega_K(R_*))$. Each model features a high resolution (~ 1.1 million cells) and has been run for several hundred orbits, both of which are unprecedented, especially when considering the elaborate physics included in the model. The downside of this advanced setup are simulation times of $\gtrsim 1$ week with 560 parallel cores on the most recent cluster hardware. However, this can be coped with thanks to the availability of high-performance computing centers in Baden-Württemberg, Germany.

We found that in the BL the angular velocity of the gas decreases smoothly from the Keplerian rotation in the disk towards the non-rotating stellar surface. Due to the loss of stabilization by angular momentum, the infall velocity of the gas increases and peaks in the BL. This goes along with a severe depletion of mass

which is characteristic for the BL and suggests the picture of a bottleneck. Since the gas loses a great amount of energy before coming to rest on the star, very high temperatures of $\sim 550\,000$ K for a $0.8M_*$ WD with a mass accretion of $10^{-8}M_*/\text{yr}$ are reached. Whereas the dynamical BL, that is, the region where Ω drops to Ω_*, is very small ($\lesssim 1\%R_*$), the area over which the dissipated energy is radiated away is considerably larger ($\sim 10\%R_*$). This is of particular interest for the observational appearance of the BL, since a wider region means less hard radiation. The radiative flux further reveals that the hottest (i.e., closest to the star) part of the disk also contributes to the thermal BL. This might lead to an overestimated Ω_* since the BL dissipation is assumed slightly too large when comparing observations with synthetic BL models.

By increasing the stellar-rotation rate, the general structure of the BL does not change. The angular velocity still smoothly connects to the surface velocity and the density and temperature in the BL are small and large, respectively. The dynamical width, however, increases due to the changing viscosity which is governed by the temperature. One open question remains with the infall velocity that, against our expectations, increases with rising Ω_* at first and decreases only for $\Omega_* \gtrsim 0.3$. An interesting case is found for the high stellar-rotation rate of $0.9\Omega_K(R_*)$ throughout the M_*, $\dot{M}$ parameter space. Here, a decretion disk is formed and material from the star is transported outwards through the disk. In general, the stellar-rotation rate is an important parameter since it determines the amount of energy liberated and radiated away in the BL and can in principle be identified by analyzing the BL luminosity from observations. There is, however, an ambiguity in that different choices of Ω_*, M_*, and $\dot{M}$ can lead to similar luminosities, which complicates this process. One way to circumvent this difficulty entails measuring the BL X-ray luminosity along with the bolometric luminosity since Hertfelder (2017) has recently shown that the X-ray luminosity scales $\propto \Omega_*^3$ as opposed to the $\propto \Omega_*^2$ dependency of the total luminosity.

The mass-accretion rate and the stellar mass both affect the BL such that a higher value leads to an increase in density and temperature. In the first case, the higher amount of mass in the disk due to the higher accretion rate and hence the increased dissipation is responsible for the rise in density and temperature. In the other case, a higher M_* intensifies the gravitational pull on the material. A process which is supported by the inverse mass-radius relation of WDs. The width of the BL decreases with increasing stellar mass or decreasing mass-accretion rate for the same reasons. The height of the disk also follows this trend. Intriguingly, with decreasing mass-accretion rate a thin but pronounced temperature peak within the dynamical BL becomes visible due to an inefficient radiative cooling under these conditions. At these mass-accretion rates, the BL starts to become optically thin. The value matches other studies, which give a threshold of about $10^{-10}M_\odot/\text{yr}$ for an optically thin BL (e.g., Warner 1987). Whether or not the peak becomes higher and more pronounced with further decreasing mass-accretion rate, as well as whether or not this finally results in soft and hard X-ray emission from the BL, should be investigated through future studies.

Due to its complexity and resource consumption, the BL is still frequently treated in a 1D approximation (see for instance Hertfelder et al. 2013; Hertfelder 2017). We found that this approach is well justified if the right conclusions are drawn from the results. Insight into the vertical structure or the interplay between BL and star is clearly inaccessible by this method. The radiation and luminosity, however, can be deduced even from 1D models, especially since the surface temperatures are almost

Article number, page 13 of 15

identical. One must bear in mind, though, that the 1D model predicts an overly low midplane temperature and disk height due to an insufficient approximation of the vertical optical depth. Apart from this drawback and a small artificial radial shift, the midplane profiles are amazingly similar between the two different approaches. Because of the vastly reduced simulation time (∼ hours), 1D models are to be preferred for luminosity calculations, for instance.

The results further indicate that the polar spreading, that is, the motion of the disk material in the direction of the poles of the star, depends on the rotation rate. For a non-rotating star, a dense shell creeps towards the poles and does not come to rest before reaching them. With increasing rotation rate, the maximum latitude reached by the gas recedes due to the angular momentum that the gas is not able to get rid of on the slippery stellar surface at higher latitudes. Also, the mixing with the stellar material becomes more pronounced with increasing stellar rotation and the gas from the disk comes to rest on and around the observable surface. As a consequence, the stellar radiation might be reprocessed in a mixture of star and disk material and carry away the spectral features of both. We note, however, that in our setup, differences in the mean molecular weight of the accreted and WD material and gravitational settling are not taken into account. While variations in mass-accretion rate have little or no influence on the polar spreading, a higher stellar mass leads to higher maximum latitudes. The angular momentum at the stellar surface for a fixed rotation rate (e.g., $0.3\Omega_K(R_*)$) decreases with increasing stellar mass due to the inverse mass-radius relations of WDs. Thus for regular relations, as for instance in young stars, the maximum latitude is likely to decrease with increasing stellar mass. Our simulations show no indication of a deceleration of the disk material above (or beyond) the stellar equator for any chosen parameter set. Therefore, we can rule out the concept of the SL for our setup. It remains to be investigated whether or not this picture changes when a different mechanism for the viscosity is employed (e.g., Belyaev & Rafikov 2012).

In general, our results are in good agreement with Kley (1991) who performed simulations of the BL around a solar mass WD. We find a slightly smaller BL width for comparable parameters. This is, however, probably a consequence of small differences in the applied viscosity prescription. Furthermore, we do not detect the extremely hot corona (∼ 10^8 K) above the disk found in Kley (1991). In contrast, this region has a temperature of only ∼ 10^4 K, which is probably too low and a consequence of the simplified radiation treatment in the optically thin corona. The author also mentions that if a turbulent ansatz for the viscosity is taken (similar to Eq. 12), the flow shows a strong time variability with an irregular and eddy-like structure. The question is raised of whether this is a consequence of inconsistencies with initial conditions or a general feature of accretion disk flows. Analyzing our simulations, we believe now that this is a transient phenomenon due to some involuntary initial perturbations, which disappears after several orbits of simulation time. A higher numerical resolution also mitigates this problem. We can, however, not rule out that, for a specific choice of parameters, a real physically unstable state develops. Instabilities are more likely found in the disk plane though (e.g., Hertfelder & Kley 2015). More recently, Balsara et al. (2009) conducted simulations of the BL around a WD with a strong focus on the outer stellar layers. They varied the α parameter and found optically thick BLs that extend to more than 30° to either side of the disk plane after a short time. While we also find optically thick BLs for $\alpha = 0.01$ and high mass-accretion rates, the inflation of the BL is absent in our simulations and both the disk and the BL

are rather thin, as is expected around a compact object. The unphysical treatment of the dissipated energy most likely causes the behavior observed in Balsara et al. (2009). We also did not detect gravity waves or Kelvin-Helmholtz instabilities although the outer stellar layers are included and are highly resolved in our setup.

The non-magnetic BL has been investigated in a 1D radial approximation (Hertfelder et al. 2013), in a 2D cylindrical approach in order to examine the instabilities in the disk plane (Hertfelder & Kley 2015), and finally in the current paper in a 2D spherical geometry that reveals the vertical structure. The mammoth task that still remains to be accomplished is the combination of the latter two. Full 3D simulations will reveal how the AM transport by the BL instability influences the vertical structure and vice versa. Sadly, this lies beyond what is computationally feasible at this time since a high resolution in all three coordinate directions is necessary (especially in the azimuthal direction) and particularly the 3D radiation transport will slow down the simulations considerably. There are, however, other open questions in connection with the BL such as the influence of magnetic fields or the role of the BL around protoplanets in disks which can be tackled in a 1D or 2D approach.

References

Abramowicz, M., Brandenburg, A., & Lasota, J.-P. 1996, MNRAS, 281, L21
Arfken, G. B. & Weber, H. J. 2005, Mathematical methods for physicists 6th ed. (Academic Press)
Armitage, P. J. 2002, MNRAS, 330, 895
Babkovskaia, N., Brandenburg, A., & Poutanen, J. 2008, MNRAS, 386, 1038
Balsara, D. S., Fisker, J. L., Godon, P., & Sion, E. M. 2009, ApJ, 702, 1536
Belyaev, M. A. 2017, ApJ, 835, 238
Belyaev, M. A. & Rafikov, R. R. 2012, ApJ, 752, 115
Belyaev, M. A., Rafikov, R. R., & Stone, J. M. 2012, ApJ, 760, 22
Belyaev, M. A., Rafikov, R. R., & Stone, J. M. 2013a, ApJ, 770, 67
Belyaev, M. A., Rafikov, R. R., & Stone, J. M. 2013b, ApJ, 770, 68
Bitsch, B., Crida, A., Morbidelli, A., Kley, W., & Dobbs-Dixon, I. 2013, A&A, 549, A124
Chandrasekhar, S. 1960, Proceedings of the National Academy of Science, 46, 253
Commerçon, B., Teyssier, R., Audit, E., Hennebelle, P., & Chabrier, G. 2011, A&A, 529, A35
Cordova, F. A., Jensen, K. A., & Nugent, J. J. 1981a, MNRAS, 196, 1
Cordova, F. A. & Mason, K. O. 1984, MNRAS, 206, 879
Cordova, F. A., Mason, K. O., & Nelson, J. E. 1981b, ApJ, 245, 609
Cordova, F. A., Nugent, J. J., Klein, S. R., & Garmire, G. P. 1980, MNRAS, 190, 87
Courant, R., Friedrichs, K., & Lewy, H. 1928, Math. Ann., 100, 32
Fisker, J. L. & Balsara, D. S. 2005, ApJ, 635, L69
Fisker, J. L., Balsara, D. S., & Burger, T. 2006, New A Rev., 50, 509
Glatzel, W. 1988, MNRAS, 231, 795
Godon, P. 1995, MNRAS, 277, 157
Godon, P., Regev, O., & Shaviv, G. 1995, MNRAS, 275, 1093
Hertfelder, M. 2017, ArXiv e-prints
Hertfelder, M. & Kley, W. 2015, A&A, 579, A54
Hertfelder, M., Kley, W., Suleimanov, V., & Werner, K. 2013, A&A, 560, A56
Hubeny, I. 1990, ApJ, 351, 632
Hunter, J. D. 2007, Computing In Science & Engineering, 9, 90
Inogamov, N. A. & Sunyaev, R. A. 1999, Ast. Lett., 25, 269

Inogamov, N. A. & Sunyaev, R. A. 2010, Astron. Lett., 36, 848
King, A. R. & Shaviv, G. 1984, Nature, 308, 519
Kley, W. 1989a, A&A, 208, 98
Kley, W. 1989b, A&A, 222, 141
Kley, W. 1991, A&A, 247, 95
Kley, W. & Hensler, G. 1987, A&A, 172, 124
Kley, W. & Lin, D. N. C. 1996, ApJ, 461, 933
Kley, W. & Lin, D. N. C. 1999, ApJ, 518, 833
Kolb, S. M., Stute, M., Kley, W., & Mignone, A. 2013, A&A, 559, A80
Kuiper, R., Klahr, H., Dullemond, C., Kley, W., & Henning, T. 2010, A&A, 511, A81
Küker, M., Henning, T., & Rüdiger, G. 2003, ApJ, 589, 397
Levermore, C. D. 1984, J. Quant. Spectr. Rad. Transf., 31, 149
Levermore, C. D. & Pomraning, G. C. 1981, ApJ, 248, 321
Lynden-Bell, D. & Pringle, J. E. 1974, MNRAS, 168, 603
Mauche, C. W. 2004, in Revista Mexicana de Astronomia y Astrofisica Conference Series, Vol. 20, Revista Mexicana de Astronomia y Astrofisica Conference Series, ed. G. Tovmassian & E. Sion, 174–175
Mignone, A., Bodo, G., Massaglia, S., et al. 2007, ApJS, 170, 228
Mihalas, D. & Mihalas, B. W. 1984, Foundations of radiation hydrodynamics (Oxford University Press, New York)
Minerbo, G. N. 1978, J. Quant. Spectr. Rad. Transf., 20, 541
Mukai, K. & Patterson, J. 2004, in Revista Mexicana de Astronomia y Astrofisica Conference Series, Vol. 20, Revista Mexicana de Astronomia y Astrofisica Conference Series, ed. G. Tovmassian & E. Sion, 244–244
Narayan, R. & Popham, R. 1993, Nature, 362, 820
Nauenberg, M. 1972, ApJ, 175, 417
Pandel, D., Córdova, F. A., & Howell, S. B. 2003, MNRAS, 346, 1231
Pandel, D., Córdova, F. A., Mason, K. O., & Priedhorsky, W. C. 2005, ApJ, 626, 396
Papaloizou, J. C. B. & Stanley, G. Q. G. 1986, MNRAS, 220, 593
Pessah, M. E. & Chan, C.-k. 2012, ApJ, 751, 48
Philippov, A. A., Rafikov, R. R., & Stone, J. M. 2016, ApJ, 817, 62
Piro, A. L. & Bildsten, L. 2004a, ApJ, 616, L155
Piro, A. L. & Bildsten, L. 2004b, ApJ, 610, 977
Popham, R. 1999, MNRAS, 308, 979
Popham, R. & Narayan, R. 1995, ApJ, 442, 337
Pringle, J. E. 1977, MNRAS, 178, 195
Pringle, J. E. & Savonije, G. J. 1979, MNRAS, 187, 777
Regev, O. 1983, A&A, 126, 146
Regev, O. & Bertout, C. 1995, MNRAS, 272, 71
Robertson, J. A. & Frank, J. 1986, MNRAS, 221, 279
Romanova, M. M., Ustyugova, G. V., Koldoba, A. V., & Lovelace, R. V. E. 2012, MNRAS, 421, 63
Shakura, N. I. & Sunyaev, R. A. 1973, A&A, 24, 337
Shaviv, G. 1987, Ap&SS, 130, 303
Sion, E. M., Godon, P., Myzcka, J., & Blair, W. P. 2010, ApJ, 716, L157
Stone, J. M. & Norman, M. L. 1992, ApJS, 80, 753
Suleimanov, V., Hertfelder, M., Werner, K., & Kley, W. 2014, A&A, 571, A55
Suleimanov, V. & Poutanen, J. 2006, MNRAS, 369, 2036
Syunyaev, R. A. & Shakura, N. I. 1986, Soviet Astronomy Letters, 12, 117
Tylenda, R. 1977, Acta Astron., 27, 235
Tylenda, R. 1981, Acta Astron., 31, 267
Velikhov, E. 1959, Zhur. Eksptl. i Teoret. Fiz., 36
Warner, B. 1987, MNRAS, 227, 23

5 | CONCLUSION

In this chapter, a brief overview of the results obtained within the scope of this thesis is given. I will highlight the most important findings of the publications presented in Chapter 4. For further details which are not mentioned here, the reader is referred to the respective publications.

5.1 IMPLICATIONS FOR THE RADIAL APPROXIMATION

Within the one-dimensional radial approach, simulations of the BL around a WD in a cataclysmic variable system have been performed (Hertfelder et al., 2013; Hertfelder, 2017). The thin disk approximation, in which axisymmetry is assumed and the disk is vertically integrated, is employed. We extent previous 1D models by the inclusion of radiation transport in the radial and the vertical direction and by considering the radiation energy as an additional quantity which is propagated in time.

The results provide a picture of the BL which can be described as a bottleneck. When the material approaches the stellar surface, the surface density decreases considerably. Simultaneously, the radial infall velocity increases so that a constant mass flux is maintained. It reaches its maximum in the BL (see Figs. 1 & 2 in Hertfelder 2017 and Figs. 1-5 in Hertfelder et al. 2013). During the deceleration of the azimuthal velocity component, a great deal of energy is released which causes a sudden rise of the effective temperature in the BL (see Fig. 2, right panel, in Hertfelder 2017). Temperatures of up to almost $350\,000$ K are reached for a non-rotating $0.8 M_\odot$ WD with a mass accretion rate of $10^{-8} M_\odot/\text{yr}$. With increasing stellar rotation rate, the maximum temperature of the BL decreases since the gas retains more and more kinetic energy.

Based on the surface temperature, the luminosity of the BL models is computed (cf. Eq. 3.2 in Hertfelder 2017). In the radial model, the BL and the disk radiate like a black body at each surface point with a temperature that is given by T_{eff}. The luminosity decreases quadratically with increasing stellar rotation rate Ω_*. In addition to this well known result, we could show that, if only the luminosity in the X-ray band (0.1-10 keV) is considered, a cubic dependence is found (see Fig. 5.1):

$$L_{\text{BL,X}} = 0.2 L_{\text{acc}} \left(1 - \frac{\Omega_*}{\Omega_K(R_*)} \right)^3 \tag{5.1}$$

L_{acc} is the total accretion luminosity, see Eq. (1.4). The different scaling of the total and the X-ray luminosity provides a way to overcome the ambiguity which arises when synthetic BL models are compared to observations: A model with high stellar rotation rate but also a high mass accretion rate can yield the same luminosity as a model with a smaller mass accretion rate but
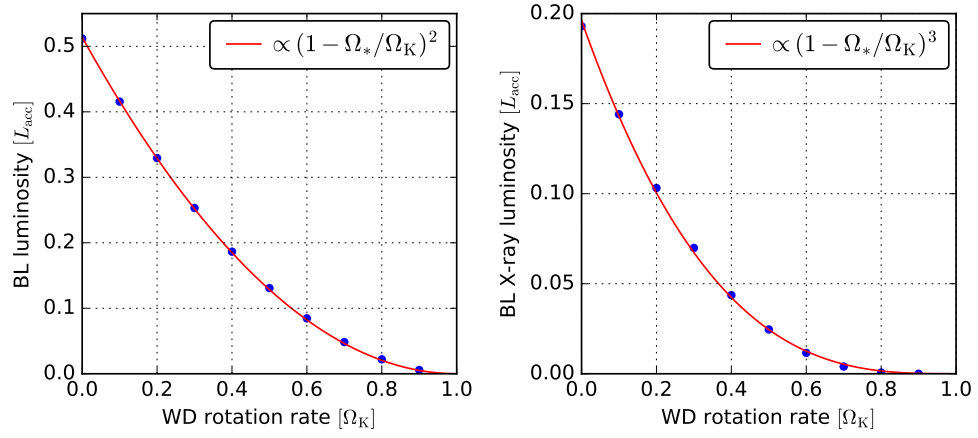
Figure 5.1: The luminosity of the BL as a function of the WD rotation rate. The luminosity is normalized to the total accretion luminosity (see Eq. 1.4). The left panel visualizes the total luminosity of the BL and a square fit to the data points. In the right panel, only the X-ray luminosity (0.1-10 keV) is taken into account and plotted along with a cubic fit to the data. The WD has $0.8 M_\odot$ and $\dot{M} = 10^{-8} M_\odot/\mathrm{yr}$. From Hertfelder (2017).

also a lower rotation rate. The factor of 0.2 in Eq. (5.1) is independent of Ω_*, but varies with the stellar mass and mass accretion rate.

Extending the analysis of the BL radiation, the spectral luminosity can be obtained by imposing Planck's law with temperature T_{eff} for each ring of the BL and subsequently adding them up while taking into account the area of the ring. The spectrum becomes considerably harder with decreasing stellar rotation rate (see Fig. 7 in Hertfelder 2017) since the maximum of T_{eff}, which is responsible for the high energetic part of the spectrum, increases. The compound BL spectrum can be approximated by a single temperature Planck law which gives an estimate of the shape of the spectrum and can be compared to observations. This study is currently in progress in collaboration with the group of Prof. Balman of the Middle East Technical University in Ankara.

A more sophisticated approach to calculate spectra of the BL has been pursued in Suleimanov et al. (2014) which constitutes the first comprehensive attempt to model the soft X-ray/EUV spectra of optically thick BLs in CVs. The 1D hydrodynamic BL models which have been calculated in Hertfelder et al. (2013) are employed as the basis for the computation of a vertical structure using the stellar-atmosphere method. Doppler broadening and Limb darkening are taken into account when deriving the total BL model spectra from the individual rings.

We find that, at conditions present in the BL, the opacity and the shape of the emergent spectra are determined by highly-charged ions of heavy elements such as carbon, oxygen, neon, magnesium and silicon. Hydrogen and helium are almost fully ionized. The final model BL spectra feature relatively broad absorption- and emission-like characteristics which arise from numerous lines of heavy elements smeared by the fast ring rotation. It was further pointed out that the predominance of spectral lines in the BL opac-
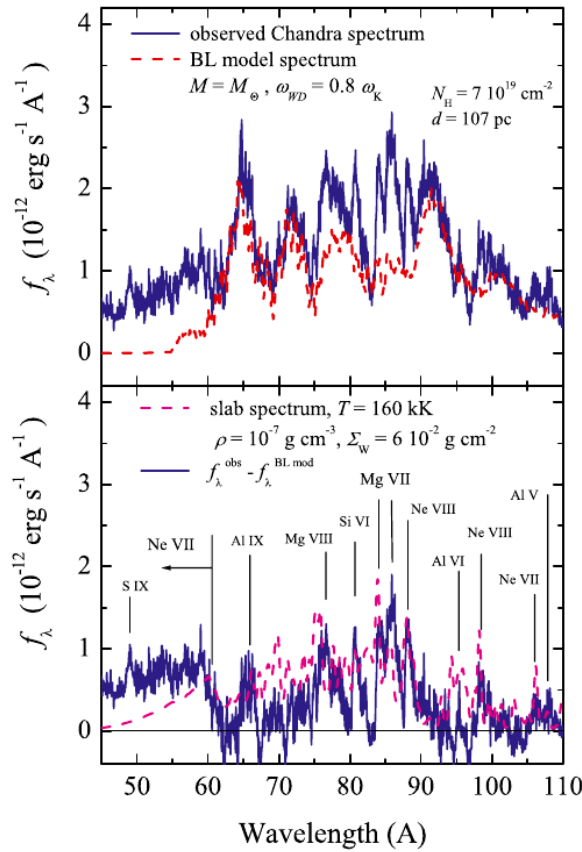
Figure 5.2: *Top panel*: Comparison of the observed SS Cyg soft X-ray spectrum (solid curve) with the BL model spectrum for a $1M_\odot$ WD with rotation rate $\Omega_* = 0.8$ (dashed curve). *Bottom panel*: Subtracted (observed minus BL model) spectrum (solid curve) together with the homogeneous slab model spectrum (dashed curve). The emission continuum of Ne VII below 60 Å and the strongest identified emission lines are marked. From Suleimanov et al. (2014).

ities leads to strong line-driven winds which manifest themselves in EUV observations.

The key result of Suleimanov et al. (2014) is that the observed soft X-ray and EUV spectrum of the dwarf nova SS Cyg in outburst is very similar to the computed model BL spectrum. It also exhibits various absorption- and emission-like features (Mauche, 2004a; Long et al., 1996). We show that the soft X-ray *Chandra* spectrum can be fitted by two model spectra (see Fig. 5.2):

- $M_* = M_\odot, \dot{M} = 1.5 \times 10^{-8} M_\odot/\text{yr}, \Omega_* = 0.8$, distance ≈ 107 pc

- $M_* = 0.8 M_\odot, \dot{M} = 1.5 \times 10^{-8} M_\odot/\text{yr}, \Omega_* = 0.6$, distance ≈ 170 pc

Also, the ratio of observed BL luminosity to the disk luminosity is consistent with the above models. The ambiguity arises due to the unknown distance of SS Cyg which, if known, could rule out one of the above models.

The workflow described in Hertfelder et al. (2013) and Suleimanov et al. (2014), or in Hertfelder (2017) and the forthcoming publication in collaboration with METU, demonstrates how theory (numerical simulations) and
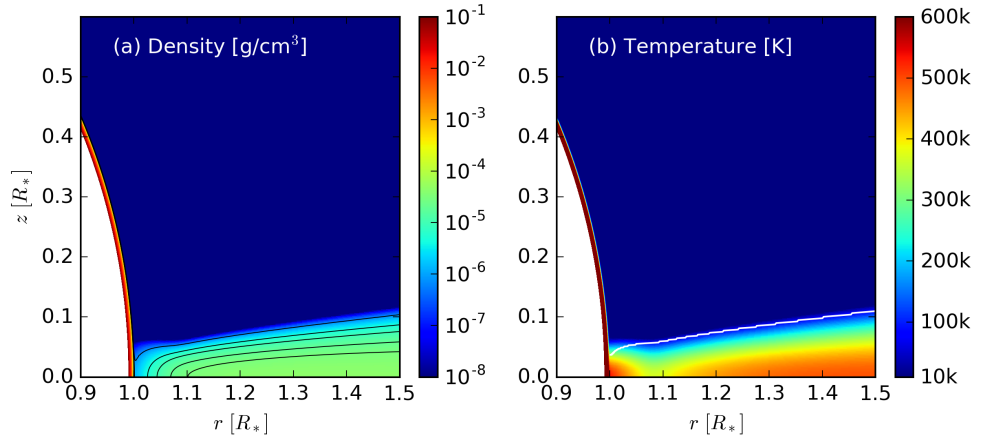
Figure 5.3: Density (a) and temperature (b) for the standard model $(0.8 M_\odot, 10^{-8} M_\odot/\text{yr}$, non-rotating) as a function of radius r and vertical coordinate z in cgs units at orbit 688. Contour lines for the levels $(0.8, 5, 10, 20, 30) \times 10^{-6} \text{g/cm}^3$ are overlaid in the plot of the density. The white line in panel (b) denotes the points where the optical depth is unity, $\tau = 1$. From Hertfelder and Kley (2017).

observations can be jointly utilized in order to reveal important characteristics of real astrophysical objects. One-dimensional radial models will play an important role in this facet of BL research in the future. Their clear advantage is the relative simplicity and short simulation times. After a few hours, a steady state with a constant mass and angular momentum flow is reached (see Figs. 9 & 10 in Hertfelder et al. 2013). Recently, the validity of the 1D approach has been confirmed by two-dimensional simulations (Hertfelder and Kley, 2017). We found that the 1D model predicts a too low midplane temperature and disk height due to an insufficient approximation of the vertical optical depth. The surface temperatures, however, are almost identical (see Figs. 4 & 5 in Hertfelder and Kley 2017). Therefore, the radiation and luminosity of the BL can be deduced also from 1D models. Insight into the vertical structure, though, is clearly inaccessible by this method.

5.2 IMPLICATIONS FOR THE VERTICAL STRUCTURE

In order to overcome the drawback of the 1D approach, two-dimensional simulations to clarify the vertical structure of the BL have been conducted in Hertfelder and Kley (2017). These models focus on the BL around a WD and feature a high resolution (~ 1.1 million grid cells) and large simulation times (hundredth of orbits). They extent the few 2D BL studies that have been performed until today (e.g. Kley, 1991; Balsara et al., 2009).

The BL structure and dynamics in the equatorial plane is well described by the 1D radial approximation. Figure 5.3 shows the vertical structure of the disk, the BL and the star. The picture of the bottleneck is confirmed by the 2D simulations. Directly in front of the star, a considerable depletion of mass occurs. The temperature, however, has a distinct maximum located next to
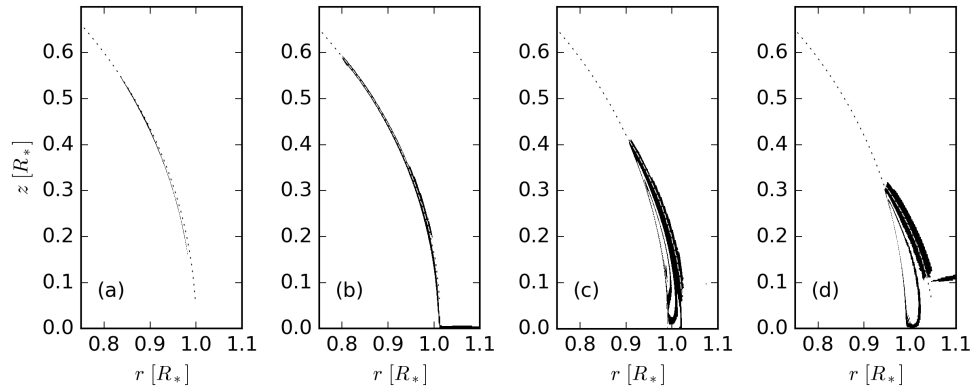
Figure 5.4: B/w coding of the tracer which has been inserted in the equatorial plane in order to visualize the mixing and polar spreading of the disk material for the standard model. The plots differ in the stellar rotation rate, which is given by $\Omega_* = 0.0, 0.3, 0.5$ and 0.7 ((a) through (d)). The dotted black line denotes the optical depth of $\tau = 2/3$. From Hertfelder and Kley (2017).

the stellar equator. Very high temperatures of $\sim 550\,000$ K are reached for the standard model ($0.8 M_\odot, 10^{-8} M_\odot/$yr, non-rotating). The width of the region, where the angular velocity drops to zero, is only about 1% of the star. Visualizations of the radiation energy and the flux vectors show, however, that the energy generated in the BL is partly transported outwards and radiated away over a larger region of $\sim 10\%$ of the stellar radius (see Fig. 2 in Hertfelder and Kley 2017). This redistribution, along with the thermalization in an optically thick BL, is responsible that the BL radiation is less hard despite the enormous energy dissipation.

The mass accretion rate and the stellar mass both affect the BL such that a higher value leads to an increase in density and temperature. The width of the BL and the disk height decrease with increasing M_* and $\dot{M}$. A growing peak in the midplane temperature directly in front of the star is found with decreasing mass accretion rate (see Fig. 7 in Hertfelder and Kley 2017). Under these conditions, the radiative cooling becomes more and more inefficient and the heat generated in the BL cannot be transported away. This marks the threshold to the case of an optically thin BL where the radiation is not thermalized and very hard. The stellar rotation rate does not change the general structure of the BL considerably. The luminosity decreases as described in Hertfelder (2017) and visualized in Fig. 5.1. Somewhere around $\Omega \approx 0.9$, however, the disk changes its state and forms a decretion disk, where mass is transported outwards. The transition towards a decretion disk is possibly a two-dimensional phenomenom since it is not observed in 1D simulations (see also Popham and Narayan, 1991).

In Hertfelder and Kley (2017), we could show for the first time that the polar spreading, i.e. the motion of the disk material in direction of the poles of the star, depends on the stellar rotation rate and decreases with growing Ω_* (see Fig. 5.4). The reason for this trend is the growing angular momentum barrier that prevents the material from reaching too high latitudes. Thus, with increasing stellar mass, the polar spreading also increases.
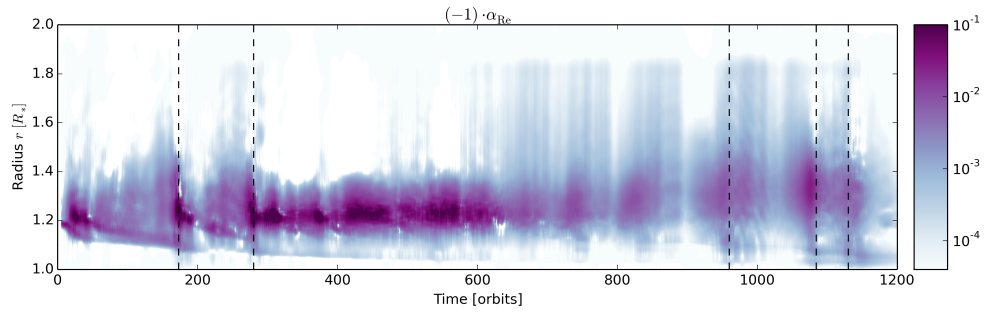
Figure 5.5: Time-radius image of α_{Re} spanning several hundred orbits. We note that the values of α_{Re} have been multiplied by (-1) in order to allow for the logarithmic scale. For each point in time the values have been time averaged over ten orbits. The vertical dashed lines denote the locations of outbursts. From Hertfelder and Kley (2015).

This is, however, only true for an inverse mass-radius relation (WDs) where the angular momentum at the stellar surface decreases with increasing mass. Furthermore, a pronounced mixing with the stellar material is observed for a non-zero rotation rate. As a consequence, the stellar radiation will be reprocessed in a mixture of star and disk material and carry away the spectral features of both. A special case is observed for a non-rotating WD: A dense shell creeps slowly up to the poles beneath the observable surface and does not come to rest before reaching the poles. Another major result is that our simulations show no indication of a deceleration of the disk material above the stellar equator for any chosen parameter set. Therefore, we can rule out the concept of the Spreading Layer for our setup.

5.3 IMPLICATIONS FOR THE VISCOSITY IN THE BL

For the investigation of the viscosity mechanism, we conducted highly resolved, two-dimensional simulations of the BL surrounding a young star (Hertfelder and Kley, 2015). In this part of the project, we chose a protostar since the ratio M_*/R_* is smaller than for a WD and lower resolution in radial direction can be chosen. This increases the amount of orbits that can be simulated within a reasonable physical time. Recent simulations were extended by including a net mass flow through the disk, utilizing a realistic equation of state and employing a quasi three-dimensional radiation transport. The simulations were started from radial 1D models similar to Hertfelder et al. (2013).

We could confirm that the supersonic velocity drop in the BL is susceptible to the sonic instability, a kind of supersonic shear layer instability whose subsonic counterpart is the Kelvin-Helmholtz instability. The sonic instability governs the BL for the first ~ 15 orbits (see Fig. 2 in Hertfelder and Kley 2015), saturates and hands over control to the acoustic modes. They are persistent acoustic waves that propagate both into the disk and into the star (see Figs. 3-5 in Hertfelder and Kley 2015). The acoustic modes efficiently transport angular momentum and mass through the BL and the disk. Fig-

ure 5.5 shows the dimensionless Reynolds stress α_{Re} which reaches values up to unity in high activity states.

An important consequence of the findings of Hertfelder and Kley (2015) is that there is considerable evidence that the AM transport in the BL is an intrinsically non-local process. Waves can extract AM from one point in the disk and release it in another one farther off. Energy is released to the fluid where the waves are damped or dissipate. The non-locality of the process means that the popular α-prescription is probably not applicable in the BL, since the AM transport does not depend on the local shearing. Direct simulations of the wave mediated AM transport are computationally too expensive if another aspect of the BL is examined[1]. Therefore it is desirable to find a prescription similar to the α-model. We come to the conclusion that α_{Re} might be a good candidate for this task. The width of the BL reacts to the wave mediated AM transport with an increase compared to classical α-viscosity simulations (see Fig. 8 in Hertfelder and Kley 2015).

Another interesting feature we found during this study is that the system repeatedly undergoes outbursts where the wave activity as well as the AM and mass transport increase considerably (e.g. Fig. 7 & 14 in Hertfelder and Kley 2015). These outbursts are likely triggered by a secondary Kelvin-Helmholtz instability that develops in plateaus of the azimuthal velocity profile due to several changes of sign of the vorticity. The effective temperature also shows strong variations during outbursts. These might play an important role in explaining light curve variations such as FU Ori outbursts or DNOs and QPOs in the case of WDs.

---

1 For this reason, the effects of the MRI are condensed into the α-viscosity.

6 | OUTLOOK

In this thesis I presented a comprehensive approach to address several questions about the non-magnetic BL of accretion disks. Although many answers emerged from this effort, some aspects of the BL still remain to be researched through future studies.

Regarding the one-dimensional radial model, it would be desirable to investigate the value of the prefactor in Eq. (5.1) by conducting a large parameter study. Thereby one can perhaps find an explicit dependence on the stellar mass and mass accretion rate or at least produce a table with the according values. Then also the absolute value of the X-ray luminosity could be calculated for arbitrary parameter combinations. In Suleimanov et al. (2014) we found that the temperatures in combination with the disk material leads to strong BL line-driven winds. Through comparison with real observations, a mass loss rate of $\sim 10^{17}$-10^{18}g/s due to the outflow from the BL surface was derived. Since these values are comparable with the assumed mass accretion rate, future BL models should be computed with the mass loss taken into consideration. It should be investigated whether the mass loss can be consistently included in the 1D radial model and how this might be accomplished. Finally, since our 2D simulations revealed a pronounced mixing of material from the disk with stellar gas, the spectral properties of this mixture could be considered for the emergent spectra.

Concerning multidimensional simulations of the BL, several interesting tasks could be realized. The vertical structure of the 2D BL around a WD should be investigated for conditions in which an optically thin BL is expected ($\dot{M} \lesssim 10^{-10} M_\odot$/yr). Perhaps the treatment of the radiation energy and the radiative flux must be adjusted for this case. A major task will be the inclusion of the wave mediated AM transport in the investigation of the vertical structure. For this purpose, three-dimensional simulations with extraordinary numerical resolution in each coordinate direction would have to be conducted in order to capture both the instability/acoustic waves and the stellar and BL scale heights. We have attempted such simulations, however, they are computationally not feasible at this time. In connection with the BL viscosity, it is tempting to associate phenomena like FU Ori outbursts, DNOs or QPOs with outbursts seen in our simulations. This topic must be further investigated in order to draw reliable conclusions. Such an investigation would certainly involve the study of how the outburst reacts to a change in parameters, among other things. It is also vital to perform 3D simulations on this question since there might be a dependence on dimensionality (Belyaev et al., 2013a).

In order to examine the vertical structure in the light of the wave mediated AM transport, another approach would involve finding an apt prescription for the macroscopic effects of this transport. We suggest the dimensionless Reynolds stress α_{Re} as a starting point for this endeavor. However, since we

are dealing with a non-local process, it is unclear if an ad-hoc prescription can approximate the consequences of this process, at all. Furthermore, the concept of the SL should be reconsidered in the light of the wave mediated AM transport.

Finally, a major extension is the inclusion of magnetic fields. This means that magnetohydrodynamical simulations of the BL including radiation transport have to be conducted. It would then be possible to relinquish any viscosity prescription whatsoever and directly simulate the MRI in the disk and the acoustic modes in the BL. There might be important interactions between the turbulent disk and the BL modes and new wave branches might add to the three non-magnetic ones. Moreover, by including a stellar dipole field, the influence of magnetic fields on the vertical structure of the BL could be investigated. However, these extensions will greatly increase the computation time and possibly require more efficient numerical methods and codes.

ACKNOWLEDGMENTS

BIBLIOGRAPHY

M. Abramowicz, A. Brandenburg, and J.-P. Lasota. The dependence of the viscosity in accretion discs on the shear/vorticity ratio. *MNRAS*, 281:L21, July 1996.

P. J. Armitage. Turbulence and Angular Momentum Transport in Global Accretion Disk Simulation. *ApJL*, 501:L189, July 1998. doi: 10.1086/311463.

P. J. Armitage. Magnetic activity in accretion disc boundary layers. *MNRAS*, 330:895–900, March 2002. doi: 10.1046/j.1365-8711.2002.05152.x.

N. Babkovskaia, A. Brandenburg, and J. Poutanen. Boundary layer on the surface of a neutron star. *MNRAS*, 386:1038–1044, May 2008. doi: 10.1111/j.1365-2966.2008.13099.x.

S. A. Balbus. Enhanced Angular Momentum Transport in Accretion Disks. *Annu. Rev. Astro. Astrophys.*, 41:555–597, 2003. doi: 10.1146/annurev.astro.41.081401.155207.

S. A. Balbus and J. F. Hawley. A powerful local shear instability in weakly magnetized disks. I - Linear analysis. II - Nonlinear evolution. *ApJ*, 376:214–233, July 1991. doi: 10.1086/170270.

S. A. Balbus and J. F. Hawley. Instability, turbulence, and enhanced transport in accretion disks. *Rev. Mod. Phys.*, 70:1–53, January 1998. doi: 10.1103/RevModPhys.70.1.

S. A. Balbus and P. Lesaffre. The effects of Prandtl number on black hole accretion flows. *New Astron. Rev.*, 51:814–818, May 2008. doi: 10.1016/j.newar.2008.03.010.

D. S. Balsara, J. L. Fisker, P. Godon, and E. M. Sion. Simulations of the Boundary Layer Between a White Dwarf and Its Accretion Disk. *ApJ*, 702:1536–1552, September 2009. doi: 10.1088/0004-637X/702/2/1536.

S. V. W. Beckwith, A. I. Sargent, R. S. Chini, and R. Guesten. A survey for circumstellar disks around young stellar objects. *AJ*, 99:924–945, March 1990. doi: 10.1086/115385.

M. A. Belyaev. Incompressible Modes Excited by Supersonic Shear in Boundary Layers: Acoustic CFS Instability. *ApJ*, 835:238, February 2017. doi: 10.3847/1538-4357/835/2/238.

M. A. Belyaev and R. R. Rafikov. Supersonic Shear Instabilities in Astrophysical Boundary Layers. *ApJ*, 752:115, June 2012. doi: 10.1088/0004-637X/752/2/115.

M. A. Belyaev, R. R. Rafikov, and J. M. Stone. Angular Momentum Transport and Variability in Boundary Layers of Accretion Disks Driven by Global

Acoustic Modes. *ApJ*, 760:22, November 2012. doi: 10.1088/0004-637X/760/1/22.

M. A. Belyaev, R. R. Rafikov, and J. M. Stone. Angular Momentum Transport by Acoustic Modes Generated in the Boundary Layer. I. Hydrodynamical Theory and Simulations. *ApJ*, 770:67, June 2013a. doi: 10.1088/0004-637X/770/1/67.

M. A. Belyaev, R. R. Rafikov, and J. M. Stone. Angular Momentum Transport by Acoustic Modes Generated in the Boundary Layer. II. Magnetohydrodynamic Simulations. *ApJ*, 770:68, June 2013b. doi: 10.1088/0004-637X/770/1/68.

A. Brandenburg. Disc turbulence and viscosity. In M. A. Abramowicz, G. Bjornsson, and J. E. Pringle, editors, *Theory of Black Hole Accretion Disks*, page 61, 1998.

A. Brandenburg. The Inverse Cascade and Nonlinear Alpha-Effect in Simulations of Isotropic Helical Hydromagnetic Turbulence. *ApJ*, 550:824–840, April 2001. doi: 10.1086/319783.

A. Brandenburg, A. Nordlund, R. F. Stein, and U. Torkelsson. Dynamo-generated Turbulence and Large-Scale Magnetic Fields in a Keplerian Shear Flow. *ApJ*, 446:741, June 1995. doi: 10.1086/175831.

J. K. Cannizzo, A. W. Shafter, and J. C. Wheeler. On the outburst recurrence time for the accretion disk limit cycle mechanism in dwarf novae. *ApJ*, 333:227–235, October 1988. doi: 10.1086/166739.

S. Chandrasekhar. The Stability of Non-Dissipative Couette Flow in Hydromagnetics. *Proceedings of the National Academy of Science*, 46:253–257, February 1960. doi: 10.1073/pnas.46.2.253.

F. A. Cordova, J. J. Nugent, S. R. Klein, and G. P. Garmire. The HEAO-A2 soft X-ray survey of dwarf novae in outburst. *MNRAS*, 190:87–97, January 1980.

R. H. Durisen, A. P. Boss, L. Mayer, A. F. Nelson, T. Quinn, and W. K. M. Rice. Gravitational Instabilities in Gaseous Protoplanetary Disks and Implications for Giant Planet Formation. *Protostars and Planets V*, pages 607–622, 2007.

J. A. Eisner, L. A. Hillenbrand, J. M. Carpenter, and S. Wolf. Constraining the Evolutionary Stage of Class I Protostars: Multiwavelength Observations and Modeling. *ApJ*, 635:396–421, December 2005. doi: 10.1086/497161.

G. J. Ferland, G. H. Pepper, S. H. Langer, J. MacDonald, J. W. Truran, and G. Shaviv. The mystery of the missing boundary layer. *ApJL*, 262:L53–L58, November 1982. doi: 10.1086/183910.

J. L. Fisker and D. S. Balsara. Simulating the Boundary Layer between a White Dwarf and Its Accretion Disk. *ApJL*, 635:L69–L72, December 2005. doi: 10.1086/499159.

J. L. Fisker, D. S. Balsara, and T. Burger. The accretion and spreading of matter on white dwarfs. *New Astron. Rev.*, 50:509–515, October 2006. doi: 10.1016/j.newar.2006.06.009.

J. Frank, A.R. King, and D.J. Raine. *Accretion Power in Astrophysics*. Cambridge University Press, 2002. ISBN 9780521629577. URL http://books.google.de/books?id=GGM_t-xn8ocC.

M. Y. Fujimoto. The Evolution of Accreting Stars with Turbulent Mixing. *ApJ*, 419:768, December 1993. doi: 10.1086/173528.

C. F. Gammie. Numerical models of accretion disks. In S. S. Holt and T. R. Kallman, editors, *American Institute of Physics Conference Series*, volume 431 of *American Institute of Physics Conference Series*, pages 99–107, April 1998. doi: 10.1063/1.55861.

F. Giovannelli. *Multifrequency Behavior of Galactic Accreting Sources*. Frascati Workshop. Edizioni Scientifiche Siderea, 1985. URL http://books.google.de/books?id=vm0HNQAACAAJ.

F. Giovannelli, S. Gaudenzi, C. Rossi, and A. Piccioni. Orbital parameters of SS Cygni. *Acta Astron.*, 33:319–330, 1983.

W. Glatzel. Sonic instabilities in supersonic shear flows. *MNRAS*, 231:795–821, April 1988.

P. Godon. On the turbulent viscosity prescription in accretion discs. *MNRAS*, 277:157–162, November 1995.

A. A. Goodman, P. J. Benson, G. A. Fuller, and P. C. Myers. Dense cores in dark clouds. VIII - Velocity gradients. *ApJ*, 406:528–547, April 1993. doi: 10.1086/172465.

L. Hartmann, S. Kenyon, and P. Hartigan. Young stars - Episodic phenomena, activity and variability. In E. H. Levy and J. I. Lunine, editors, *Protostars and Planets III*, pages 497–518, 1993.

J. F. Hawley. Global Magnetohydrodynamical Simulations of Accretion Tori. *ApJ*, 528:462–479, January 2000. doi: 10.1086/308180.

J. F. Hawley. Global Magnetohydrodynamic Simulations of Cylindrical Keplerian Disks. *ApJ*, 554:534–547, June 2001. doi: 10.1086/321348.

J. F. Hawley and J. H. Krolik. Global MHD Simulation of the Inner Accretion Disk in a Pseudo-Newtonian Potential. *ApJ*, 548:348–367, February 2001. doi: 10.1086/318678.

J. F. Hawley, C. F. Gammie, and S. A. Balbus. Local Three-dimensional Magnetohydrodynamic Simulations of Accretion Disks. *ApJ*, 440:742, February 1995. doi: 10.1086/175311.

J. F. Hawley, C. F. Gammie, and S. A. Balbus. Local Three-dimensional Simulations of an Accretion Disk Hydromagnetic Dynamo. *ApJ*, 464:690, June 1996. doi: 10.1086/177356.

M. Hertfelder. The Boundary Layer in compact binaries. *ArXiv e-prints*, February 2017.

M. Hertfelder and W. Kley. Wave mediated angular momentum transport in astrophysical boundary layers. *A&A*, 579:A54, July 2015. doi: 10.1051/0004-6361/201526005.

M. Hertfelder and W. Kley. The vertical structure of the boundary layer around compact objects. *ArXiv e-prints*, May 2017.

M. Hertfelder, W. Kley, V. Suleimanov, and K. Werner. The boundary layer in compact binaries. *A&A*, 560:A56, December 2013. doi: 10.1051/0004-6361/201322542.

I. Hubeny. Vertical structure of accretion disks - A simplified analytical model. *ApJ*, 351:632–641, March 1990. doi: 10.1086/168501.

N. A. Inogamov and R. A. Sunyaev. Spread of matter over a neutron-star surface during disk accretion. *Ast. Lett.*, 25:269–293, May 1999.

N. A. Inogamov and R. A. Sunyaev. Spread of matter over a neutron-star surface during disk accretion: Deceleration of rapid rotation. *Astron. Lett.*, 36:848–894, December 2010. doi: 10.1134/S1063773710120029.

C. Jaschek and A. E. Gómez. The Frequency of Spectroscopic Binaries. *PASP*, 82:809, August 1970. doi: 10.1086/128966.

H. Jeffreys. *The earth: its origin, history and physical constitution*. University Press, 1924. URL http://books.google.de/books?id=j71NAAAAMAAJ.

S. Kato and S. Inagaki. A non-local description of turbulent stress tensor in accretion disks. *Publ. Astron. Soc. Jpn*, 46:289–299, June 1994.

A. R. King and G. Shaviv. X-ray emission from non-magnetic cataclysmic variables. *Nature*, 308:519–521, April 1984. doi: 10.1038/308519a0.

A. R. King, J. E. Pringle, and M. Livio. Accretion disc viscosity: how big is alpha? *MNRAS*, 376:1740–1746, April 2007. doi: 10.1111/j.1365-2966.2007.11556.x.

R. Kippenhahn and H.-C. Thomas. Accretion belts on white dwarfs. *A&A*, 63:265–272, February 1978.

W. Kley. Radiation hydrodynamics of the boundary layer in accretion disks. I - Numerical methods. *A&A*, 208:98–110, January 1989a.

W. Kley. Radiation hydrodynamics of the boundary layer in accretion disks. II - Optically thick models. *A&A*, 222:141–149, September 1989b.

W. Kley. On the influence of the viscosity on the structure of the boundary layer of accretion disks. *A&A*, 247:95–107, July 1991.

W. Kley and G. Hensler. Two-dimensional numerical models of the boundary layer of accretion disks in cataclysmic variables. *A&A*, 172:124–142, January 1987.

W. Kley and D. N. C. Lin. The Structure of the Boundary Layer in Protostellar Disks. *ApJ*, 461:933, April 1996. doi: 10.1086/177115.

W. Kley and D. N. C. Lin. Evolution of FU Orionis Outbursts in Protostellar Disks. *ApJ*, 518:833–847, June 1999. doi: 10.1086/307296.

W. Kley and J. C. B. Papaloizou. Causal Viscosity in Accretion Disc Boundary layers. *MNRAS*, 285:239–252, February 1997.

W. Kluźniak. PhD thesis, , Stanford Univ., (1987), 1987.

W. Kluzniak and J. R. Wilson. Hard X-ray spectra from gap accretion onto neutron stars. *ApJL*, 372:L87–L90, May 1991. doi: 10.1086/186030.

M. Küker, T. Henning, and G. Rüdiger. Magnetic Star-Disk Coupling in Classical T Tauri Systems. *ApJ*, 589:397–409, May 2003. doi: 10.1086/374408.

C. D. Levermore. Relating Eddington factors to flux limiters. *J. Quant. Spec. Rad. Trans.*, 31:149–160, February 1984. doi: 10.1016/0022-4073(84)90112-2.

C. D. Levermore and G. C. Pomraning. A flux-limited diffusion theory. *ApJ*, 248:321–334, August 1981. doi: 10.1086/159157.

F. K. Liu, F. Meyer, and E. Meyer-Hofmeister. Dwarf novae in quiescence: the relationship between disk evaporation and accretion onto a white dwarf. *A&A*, 300:823, August 1995.

F. K. Liu, F. Meyer, E. Meyer-Hofmeister, and V. Burwitz. Low heat conduction in white dwarf boundary layers? *A&A*, 483:231–237, May 2008. doi: 10.1051/0004-6361:20079260.

K. S. Long, C. W. Mauche, J. C. Raymond, P. Szkody, and J. A. Mattei. EUVE Observations of U Geminorum in Outburst. *ApJ*, 469:841, October 1996. doi: 10.1086/177832.

D. Lynden-Bell and J. E. Pringle. The evolution of viscous discs and the origin of the nebular variables. *MNRAS*, 168:603–637, September 1974.

S. P. Maran. *The astronomy and astrophysics encyclopedia*. Cambridge University Press, 1992.

I. G. Martinez-Pais, F. Giovannelli, C. Rossi, and S. Gaudenzi. An optical time-resolved spectroscopic study of SS Cygni. 1: Quiescence. *A&A*, 291: 455–467, November 1994.

D. Y. Martynov. *Course of general astrophysics. Text-book for students of astronomy.* Nauka, Moskva, 1971.

C. W. Mauche. Chandra Low Energy Transmission Grating Spectrum of SS Cygni in Outburst. *ApJ*, 610:422–426, July 2004a. doi: 10.1086/421438.

C. W. Mauche. A Simple, Unifying Model of the Extreme Ultraviolet Spectra of Dwarf Novae in Outburst. In G. Tovmassian and E. Sion, editors, *Revista Mexicana de Astronomia y Astrofisica Conference Series*, volume 20 of *Revista Mexicana de Astronomia y Astrofisica Conference Series*, pages 174–175, July 2004b.

M. V. Medvedev and R. Narayan. Self-similar Hot Accretion Flow onto a Neutron Star. *ApJ*, 554:1255–1267, June 2001. doi: 10.1086/321385.

F. Meyer and E. Meyer-Hofmeister. Accretion disk evaporation by a coronal siphon flow. *A&A*, 288:175–182, August 1994.

K. Mukai and J. Patterson. XMM-Newton and Optical Observations of WZ Sagittae in Quiescence. In G. Tovmassian and E. Sion, editors, *Revista Mexicana de Astronomia y Astrofisica Conference Series*, volume 20 of *Revista Mexicana de Astronomia y Astrofisica Conference Series*, pages 244–244, July 2004.

R. Narayan. A flux-limited model of particle diffusion and viscosity. *ApJ*, 394:261–267, July 1992. doi: 10.1086/171578.

R. Narayan and R. Popham. Hard X-rays from accretion disk boundary layers. *Nature*, 362:820–822, April 1993. doi: 10.1038/362820a0.

R. Narayan, P. Goldreich, and J. Goodman. Physics of modes in a differentially rotating system - Analysis of the shearing sheet. *MNRAS*, 228:1–41, September 1987.

R. Narayan, A. Loeb, and P. Kumar. Casuality in strong shear flows. *ApJ*, 431:359–279, August 1994. doi: 10.1086/174490.

C. Obach and W. Glatzel. On the boundary layer of accretion discs. *MNRAS*, 303:603–610, March 1999. doi: 10.1046/j.1365-8711.1999.02278.x.

J. E. Owen and K. Menou. Disk-fed Giant Planet Formation. *ApJL*, 819:L14, March 2016. doi: 10.3847/2041-8205/819/1/L14.

B. Paczyński. Evolutionary Processes in Close Binary Systems. *Annu. Rev. Astro. Astrophys.*, 9:183, 1971. doi: 10.1146/annurev.aa.09.090171.001151.

D. Pandel, F. A. Córdova, and S. B. Howell. X-ray and ultraviolet observations of the dwarf nova VW Hyi in quiescence. *MNRAS*, 346:1231–1241, December 2003. doi: 10.1111/j.1365-2966.2003.07199.x.

D. Pandel, F. A. Córdova, K. O. Mason, and W. C. Priedhorsky. X-Ray Observations of the Boundary Layer in Dwarf Novae at Low Accretion Rates. *ApJ*, 626:396–410, June 2005. doi: 10.1086/429983.

J. Papaloizou and E. Szuszkiewicz. A Comparison of One-Dimensional and Two-Dimensional Models of Transonic Accretion Discs around Collapsed Objects. *MNRAS*, 268:29, May 1994.

J. C. B. Papaloizou and J. E. Pringle. The dynamical stability of differentially rotating discs with constant specific angular momentum. *MNRAS*, 208: 721–750, June 1984.

J. C. B. Papaloizou and G. Q. G. Stanley. The structure and stability of the accretion disc boundary layer. *MNRAS*, 220:593–610, June 1986.

J. Patterson. The evolution of cataclysmic and low-mass X-ray binaries. *ApJS*, 54:443–493, April 1984. doi: 10.1086/190940.

M. E. Pessah and C.-k. Chan. On Hydromagnetic Stresses in Accretion Disk Boundary Layers. *ApJ*, 751:48, May 2012. doi: 10.1088/0004-637X/751/1/48.

A. A. Philippov, R. R. Rafikov, and J. M. Stone. Spreading Layers in Accreting Objects: Role of Acoustic Waves for Angular Momentum Transport, Mixing, and Thermodynamics. *ApJ*, 817:62, January 2016. doi: 10.3847/0004-637X/817/1/62.

A. L. Piro and L. Bildsten. Spreading of Accreted Material on White Dwarfs. *ApJ*, 610:977–990, August 2004a. doi: 10.1086/421763.

A. L. Piro and L. Bildsten. A Spreading Layer Origin for Dwarf Nova Oscillations. *ApJL*, 616:L155–L158, December 2004b. doi: 10.1086/426501.

J. B. Pollack, O. Hubickyj, P. Bodenheimer, J. J. Lissauer, M. Podolak, and Y. Greenzweig. Formation of the Giant Planets by Concurrent Accretion of Solids and Gas. *Icarus*, 124:62–85, November 1996. doi: 10.1006/icar.1996.0190.

R. Popham. A boundary layer origin for dwarf nova oscillations. *MNRAS*, 308:979–983, October 1999. doi: 10.1046/j.1365-8711.1999.02782.x.

R. Popham and R. Narayan. Does accretion cease when a star approaches breakup? *ApJ*, 370:604–614, April 1991. doi: 10.1086/169847.

R. Popham and R. Narayan. Supersonic infall and causality in accretion disk boundary layers. *ApJ*, 394:255–260, July 1992. doi: 10.1086/171577.

R. Popham and R. Narayan. Accretion disk boundary layers in cataclysmic variables. 1: Optically thick boundary layers. *ApJ*, 442:337–357, March 1995. doi: 10.1086/175444.

R. Popham and R. Sunyaev. Accretion Disk Boundary Layers around Neutron Stars: X-Ray Production in Low-Mass X-Ray Binaries. *ApJ*, 547:355–383, January 2001. doi: 10.1086/318336.

M. L. Pretorius, B. Warner, and P. A. Woudt. Dwarf nova oscillations and quasi-periodic oscillations in cataclysmic variables - V. Results from an extensive survey. *MNRAS*, 368:361–370, May 2006. doi: 10.1111/j.1365-2966.2006.10123.x.

J. E. Pringle. Soft X-ray emission from dwarf novae. *MNRAS*, 178:195–202, January 1977.

J. E. Pringle. Accretion discs in astrophysics. *Annu. Rev. Astro. Astrophys.*, 19:137–162, 1981. doi: 10.1146/annurev.aa.19.090181.001033.

J. E. Pringle and G. J. Savonije. X-ray emission from dwarf novae. *MNRAS*, 187:777–783, June 1979.

O. Regev and C. Bertout. Asymptotic models of accretion disc boundary layers. *MNRAS*, 272:71–79, January 1995.

B. Reipurth. FU Orionis eruptions and early stellar evolution. In L. V. Mirzoian, B. R. Pettersen, and M. K. Tsvetkov, editors, *Flare Stars in Star Clusters, Associations and the Solar Vicinity*, volume 137 of *IAU Symposium*, pages 229–251, 1990.

J. A. Robertson and J. Frank. A numerical study of two-dimensional accretion flows. *MNRAS*, 221:279–309, July 1986.

M. M. Romanova, G. V. Ustyugova, A. V. Koldoba, and R. V. E. Lovelace. MRI-driven accretion on to magnetized stars: global 3D MHD simulations of magnetospheric and boundary layer regimes. *MNRAS*, 421:63–77, March 2012. doi: 10.1111/j.1365-2966.2011.20055.x.

T. Sano, S.-i. Inutsuka, N. J. Turner, and J. M. Stone. Angular Momentum Transport by Magnetohydrodynamic Turbulence in Accretion Disks: Gas Pressure Dependence of the Saturation Level of the Magnetorotational Instability. *ApJ*, 605:321–339, April 2004. doi: 10.1086/382184.

N. I. Shakura and R. A. Sunyaev. Black holes in binary systems. Observational appearance. *A&A*, 24:337–355, 1973.

N. I. Shakura and R. A. Sunyaev. The theory of an accretion disk/neutron star boundary layer. *Adv. Space Res.*, 8:135–140, 1988. doi: 10.1016/0273-1177(88)90396-1.

S. L. Shapiro and S. A. Teukolsky. *Black holes, white dwarfs, and neutron stars: The physics of compact objects*. 1983.

G. Shaviv. The boundary layer in cataclysmic variables. *Astrophys. Space Sci.*, 130:303–314, February 1987. doi: 10.1007/BF00655010.

H. C. Spruit. Dynamo action by differential rotation in a stably stratified stellar interior. *A&A*, 381:923–932, January 2002. doi: 10.1051/0004-6361:20011465.

S.W. Stahler and F. Palla. *The Formation of Stars*. Wiley, 2005. ISBN 9783527405596. URL https://books.google.de/books?id=Cx98QgAACAAJ.

M. H. R. Stoll and W. Kley. Vertical shear instability in accretion disc models with radiation transport. *A&A*, 572:A77, December 2014. doi: 10.1051/0004-6361/201424114.

J. M. Stone and J. E. Pringle. Magnetohydrodynamical non-radiative accretion flows in two dimensions. *MNRAS*, 322:461–472, April 2001. doi: 10.1046/j.1365-8711.2001.04138.x.

J. M. Stone, J. F. Hawley, C. F. Gammie, and S. A. Balbus. Three-dimensional Magnetohydrodynamical Simulations of Vertically Stratified Accretion Disks. *ApJ*, 463:656, June 1996. doi: 10.1086/177280.

V. Suleimanov and J. Poutanen. Spectra of the spreading layers on the neutron star surface and constraints on the neutron star equation of state. *MNRAS*, 369:2036–2048, July 2006. doi: 10.1111/j.1365-2966.2006.10454.x.

V. Suleimanov, M. Hertfelder, K. Werner, and W. Kley. Modeling the EUV spectra of optically thick boundary layers of dwarf novae in outburst. *A&A*, 571:A55, November 2014. doi: 10.1051/0004-6361/201423724.

R. A. Syunyaev and N. I. Shakura. Disk Accretion onto a Weak Field Neutron Star - Boundary Layer Disk Luminosity Ratio. *Soviet Astronomy Letters*, 12: 117, April 1986.

R. J. Tayler. The adiabatic stability of stars containing magnetic fields-I.Toroidal fields. *MNRAS*, 161:365, 1973.

R. Tylenda. The continuous radiation emitted by accretion discs in cataclysmic binaries - The dwarf nova SS CYG during outburst and the old novae V 603 AQL and RR PIC. *Acta Astron.*, 27:235–249, 1977.

R. Tylenda. Viscous Boundary Layer and Hard X-Rays from Dwarf Novae. *Acta Astron.*, 31:267, 1981.

T. S. van Albada and A. Blaauw. Définition de l'objet "étoile double": On the frequency distribution of separations and mass ratios of early-type double stars. In J. Dommanget, editor, *On the Evolution of Double Stars*, page 44, 1967.

E.P. Velikhov. Stability of an ideally conducting liquid flowing between rotating cylinders in a magnetic field. *Zhur. Eksptl. i Teoret. Fiz.*, 36, May 1959.

F. Verbunt. Accretion disks in stellar X-ray sources - A review of the basic theory of accretion disks and its problems. *Space Sci. Rev.*, 32:379–404, 1982. doi: 10.1007/BF00177448.

B. Warner. Absolute magnitudes of cataclysmic variables. *MNRAS*, 227: 23–73, July 1987.

B. Warner. Cataclysmic variable stars. *Cambridge Astrophysics Series*, 28, 1995.

B. Warner. Rapid Oscillations in Cataclysmic Variables. *PASP*, 116:115–132, February 2004. doi: 10.1086/381742.

B. Warner and P. A. Woudt. DNOs and QPOs in Cataclysmic Variables. In J.-M. Hameury and J.-P. Lasota, editors, *The Astrophysics of Cataclysmic Variables and Related Objects*, volume 330 of *Astronomical Society of the Pacific Conference Series*, page 227, August 2005.

S. J. Weidenschilling. Aerodynamics of solid bodies in the solar nebula. *MNRAS*, 180:57–70, July 1977.

C. F. v. Weizsäcker. Die Rotation kosmischer Gasmassen. *Zeitschrift Naturforschung Teil A*, 3:524, 1948.

H. W. Yorke and P. Bodenheimer. The Formation of Protostellar Disks. III. The Influence of Gravitationally Induced Angular Momentum Transport on Disk Structure and Appearance. *ApJ*, 525:330–342, November 1999. doi: 10.1086/307867.